EFFECTIVE INTERACTION AND THE REACTIONS ^{7}Li$(p,p')^7$Li(478 keV) AND ^{7}Li$(p,n)^7$Be(431 keV)†

P. J. Locard,* S. M. Austin, and W. Benenson
Department of Physics, Michigan State University, East Lansing, Michigan
(Received 28 August 1967)

The total cross sections for the reactions ^{7}Li$(p,p')^7$Li(478 keV) and ^{7}Li$(p,n)^7$Be(431 keV) have been measured for proton energies between 23 and 52 MeV and compared with the predictions of a microscopic model of the reaction. The spin-flip, isospin-flip part of the effective interaction is found to be essentially independent of energy, whereas the pure central part appears to decrease with increasing energy.

In the distorted-wave theory of inelastic scattering the transition amplitude has the form[1,2]

$$T_{fi} = \int \chi_f^{(-)*}(\vec{r}) \langle \Psi_f | V_{\text{eff}} | \Psi_i \rangle \chi_i^{(+)}(\vec{r}) d\vec{r}.$$

The χ_i and χ_f are distorted waves describing the elastic process and are generated from optical-model parameters which fit the elastic scattering from the target nucleus. This expression neglects particle exchange.

If one wishes to obtain detailed spectroscopic information, one must use a microscopic model in which Ψ_f and Ψ_i are shell model states and V_{eff} is the effective interaction causing the transition from Ψ_i to Ψ_f. Except at energies well above 100 MeV, where one can with good accuracy set V_{eff} equal to the free nucleon-nucleon interaction,[3] there is no simple way to determine V_{eff} from external information.[2,4] For this reason it is difficult to isolate properties of the nuclear wave function from uncertainties in V_{eff}. Several authors[2,4,5] have suggested that in this situation one should attempt to determine V_{eff} from a comparison of experiments with theory in cases where the wave functions are known. The present Letter describes a measurement of V_{eff} and an attempt to make the first determination of its energy dependence.

The reactions

$$^7\text{Li} + p \rightarrow {}^7\text{Li}(478\text{ keV}) + p,$$

$$^7\text{Li} + p \rightarrow {}^7\text{Be}(431\text{ keV}) + n,$$

leading to the mirror first excited states of ^{7}Li and ^{7}Be, are well suited for investigations of V_{eff}. These states have $J^\pi = \frac{1}{2}^-$; so the angular distributions of the de-excitation gamma rays are isotropic in the rest frame of the recoiling nucleus. In addition, these states are the highest energy particle-stable states; so they are not fed with appreciable probability by gamma-ray transitions from above. For these reasons a measurement of the intensity of the de-excitation gamma ray at a single angle is a measure of the total cross section for the reactions.[6] This method enables one to measure the total cross section of a (p,n) reaction in a case for which standard techniques would not have sufficiently high resolution.

Protons from the Michigan State University sector-focused cyclotron bombarded a 59 mg/cm^2 thick, self-supporting target rolled from natural lithium metal. The gamma radiation was detected in a 3-cm^3 Ge(Li) detector which was placed at the largest possible angle (166°) from the beam to reduce the Doppler broadening of the peaks and the neutron background. At each energy, spectra were recorded both with the target in the beam and with the target removed to permit the subtraction of backgrounds which did not originate in the target. Figure 1 shows spectra taken at 25 and 52 MeV.

The cross sections obtained after correction for the relative detection efficiency of the 431- and 478-keV gamma rays and normalization to a total ^{7}Li$(p,p')^7$Li(478 keV) cross section measured at 24.4 MeV[7] are shown in Fig. 2.

In order to relate these results to an effective interaction, V_{eff} is assumed to have the form[1,2,5]

$$V_{\text{eff}} = \sum_i t_i,$$

where t_i is the scattering amplitude from the

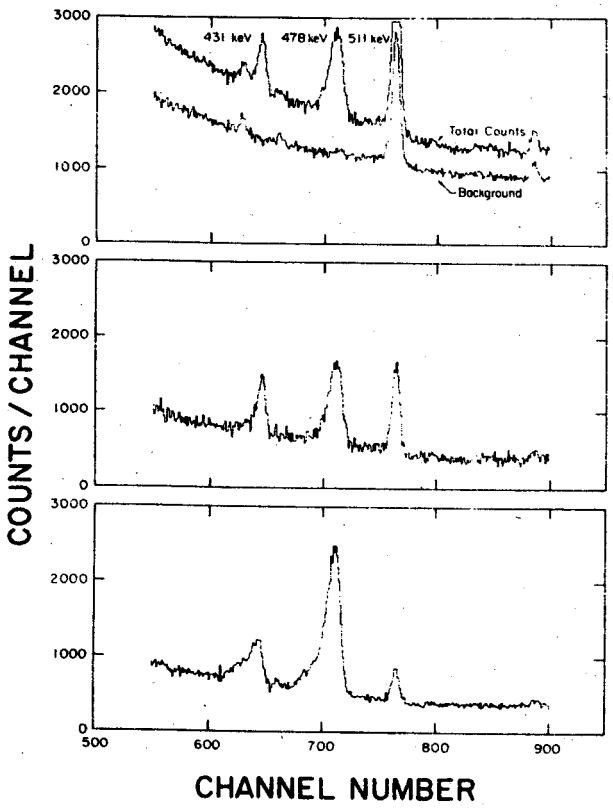

FIG. 1. Gamma-ray spectra taken at 25 (bottom) and 52 (middle and top) MeV. The peaks at 431 and 478 keV arise from the reactions ^{7}Li(p,p'), ^{7}Li(478 keV), and ^{7}Li(p,n)^{7}Be(431 keV), respectively, while the 511-keV peak arises from β^+ annihilation. Other peaks appear also in the background not associated with the target and can be traced to proton-induced reactions in the beam pipe and Faraday cup. The detector resolution was about 5 keV, but the 431- and 478-keV peaks are Doppler broadened.

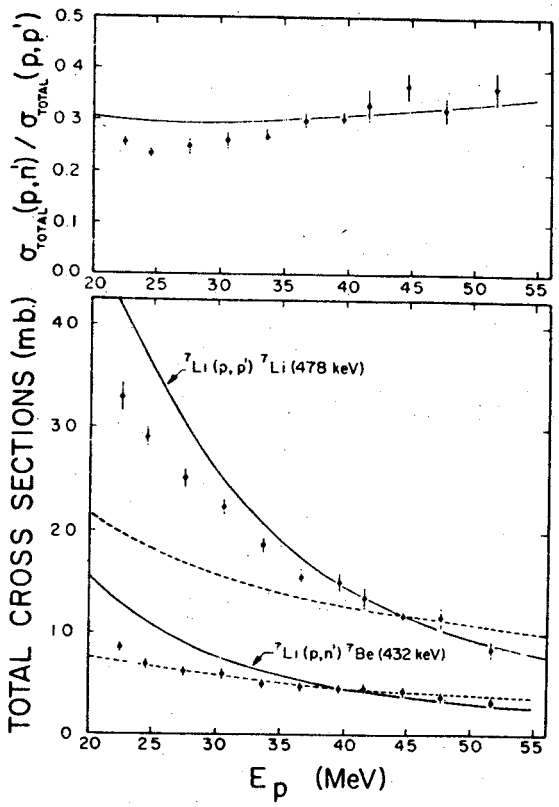

FIG. 2. Total cross sections for the reactions ^{7}Li(p,p')^{7}Li(478 keV) and ^{7}Li(p,n)^{7}Be(431 keV). The top graph shows the ratios of these cross sections with their statistical errors and the lower graph shows the cross sections normalized to Ref. 7 plotted with their total errors (exclusive of normalization errors). The dashed and solid curves are theoretical predictions discussed in the text.

ith target nucleon and

$$t_i = V_{00} + V_{10}\vec{\sigma}\cdot\vec{\sigma}_P + V_{01}\vec{\tau}_i\cdot\vec{\tau}_P + V_{11}(\vec{\sigma}_i\cdot\vec{\sigma}_P)(\vec{\tau}_i\cdot\vec{\tau}_P).$$

The operators $\vec{\sigma}_P$ and $\vec{\sigma}_i$ are the Pauli spin operators for the projectile and struck particle, respectively, and the τ's are the analogous operators for the isospin. In this parametrization of V_{eff} the subscripts on the V_{ST} are the transferred spin S and isospin T. McManus et al.[5,8] have obtained the V_{ST} from a fit to the Hamada-Johnson nucleon-nucleon potential. In this case the interactions are local and complex, and have a Yukawan radial dependence. Each V_{ST} has a different strength and range, both of which are energy dependent. Other authors[2] have fitted inelastic scattering data by varying the strength of a real, Yukawan potential with a range of 1.0 F.

The selection rules allow eight amplitudes [labeled by (L, S, J, T): the transferred orbital, spin, and total angular momentum, and the transferred isospin] to contribute to the (p,p') cross section while four contribute to the (p,n) reaction. As a first step we calculated all of these terms in the zero-range plane-wave impulse approximation using the t_i of McManus et al.[5,8] Harmonic-oscillator wavefunctions with a length parameter $b = 1.72$ F[9] were used in the L-S coupling limit. The results are shown as solid curves in Fig. 2. Since plane-wave calculations are not expected to predict the magnitudes of the cross sections correctly, the curves have been normalized to the (p,p') cross section at 44.7 MeV. These

curves indicate that both the ratio of the cross sections and the energy dependence are given approximately by the interactions of McManus.

These calculations fit the data somewhat better than one might expect considering the crudeness of the model. To determine whether this is fortuitous we have made some preliminary distorted-wave calculations using the same wave functions and the finite-range McManus interaction. These calculations give cross sections that are roughly correct in magnitude. They agree with the plane-wave calculation in the identification of which terms are the most important contributors to the cross sections and in the energy dependence of the cross sections. However, the ratio of the (p,n) to the (p,p') cross sections is about 0.6, roughly twice the experimental value. This effect can be traced to the fact that the $(LSJT)=(2020)$ amplitude is smaller relative to other amplitudes in the distorted-wave calculations. Since this amplitude is more important in the (p,p') reaction, it appears that the inclusion of a quadrupole enhancement which might arise from core polarization effects[10] would decrease the discrepancy.

Both the plane- and distorted-wave calculations show that a single V_{ST} dominates the cross sections. In the (p,p') reaction V_{00} contributes 70% of the cross section while V_{11} accounts for 90% of the cross section in the (p,n) reaction. Although the percentages presumably depend upon the choice of wave function, we may regard the two processes as rough measures of V_{00} and V_{11}, respectively. Under the assumption that V_{00} and V_{11} are real, independent of energy, and have a Yukawan shape with a range of 1.0 F, distorted-wave calculations give the dashed curves shown in Fig. 2. The strengths of the potentials required to fit the total cross sections at 44.7 MeV are $V_{00}=90$ MeV and $V_{11}=15$ MeV. A comparison of the results of the calculation with the data shows that V_{00} should be taken to be energy dependent. At 25 MeV a strength of 113 MeV would fit the data. The shape of the angular distribution calculated with $V_{00}=113$ MeV at 25 MeV is in fair agreement with the data of Crawley and Austin[7] at 24.4 MeV. There is no evidence for an energy dependence of V_{11}.

Other analyses[2,10] of inelastic scattering data have given values of V_{00} between 100 and 200 MeV depending upon whether or not core polarization was taken into account. A value of V_{11} of 7 MeV (assumed range of 1.4 F) has been derived from measurements of the $^{14}C(p,n)$ cross sections near 14 MeV.[11] An analysis of inelastic scattering from ^{208}Pb gives a value of 10 MeV.[10]

We are continuing the distorted wave analysis with an emphasis on the use of form factors which account for the core polarization of ^7Li.[10]

The authors wish to thank Professor H. McManus and Mr. F. Petrovitch for many illuminating conversations and for assistance with the calculations, and Dr. T. Tamura and Dr. R. Haybron for making available their distorted-wave code. We also wish to thank M. J. Kolata for putting this code into operation at Michigan State University. Useful discussions were held with Professor G. M. Crawley. We are grateful to Mr. S. H. Fox, Mr. R. A. Paddock, and Mr. I. Proctor for assistance in taking the data.

Note added in proof.—The value of V_{11} given in this paper is in good agreement with an analysis of measurements of the total cross section for the reaction $^6Li(p,p')^6Li$ to the $T=1$ second excited state.[12] In this case V_{11} is the only term which contributes to the cross section.

---

†Work supported in part by the National Science Foundation.

*On leave from the Laboratoire de Chimie Nucléaire et Radioactivité, Centre d'Etudes Nucléaires de Grenoble, Grenoble, France.

[1]G. R. Satchler, Nucl. Phys. 55, 1 (1964); 77, 481 (1966).

[2]G. R. Satchler, Nucl. Phys. A95, 1 (1967).

[3]R. M. Haybron and H. McManus, Phys. Rev. 136, B1730 (1964).

[4]H. McManus, Brookhaven National Laboratory Report No. BNL 948, 1965 (unpublished), Vol. I, p. 175.

[5]F. Petrovitch, D. Slanina, and H. McManus, Michigan State University Report No. MSPT-103, 1967 (unpublished).

[6]The gamma radiation is not quite isotropic in the laboratory frame. This introduces an error of less than 3.5% for the proton energies of this experiment.

[7]G. M. Crawley and S. M. Austin, in Proceedings of the International Conference on Nuclear Physics, Gatlinburg, Tennessee, September, 1966 (to be published).

[8]H. McManus, F. Petrovitch, and D. Slanina, Bull. Am. Phys. Soc. 12, 12 (1967).

[9]A. Johansson, Phys. Letters 24B, 29 (1967).

[10]G. R Satchler, to be published.

[11]C. Wong, J. D. Anderson, J. McClure, B. Pohl, V. A. Madsen, and F. Schmittroth, to be published.

[12]P. J. Locard, S. M. Austin, W. Benenson, and G. M.

Crawley, meeting of the Division of Nuclear Physics of the American Physical Society, Madison, Wisconsin, 23-25 October 1967 (Bull. Am. Phys. Soc., to be published), paper No. AD13.

Reprinted from THE PHYSICAL REVIEW, Vol. 167, No. 4, 963–970, 20 March 1968
Printed in U. S. A.

Study of Reactions $^{10}B(p,d)^{9}B$ and $^{11}B(p,d)^{10}B$†

L. A. KULL* AND E. KASHY
Cyclotron Laboratory, Michigan State University, East Lansing, Michigan
(Received 11 September 1967)

Excited states of ^{9}B and ^{10}B were studied by means of the (p,d) reaction, using 33.6-MeV incident protons. Deuteron groups were observed corresponding to strongly excited levels in ^{9}B at 0.0-, 2.35-, 7.1-, and 11.75-MeV excitation and in ^{10}B at 0.0-, 0.72-, 1.76-, 2.15-, 3.57-, 4.75-, 5.10-, and 6.04-MeV excitation. Small deuteron yields were observed corresponding to excited states in ^{9}B at 2.8- and 14.6-MeV excitation and ^{10}B at 6.57- and 7.5-MeV excitation. The angular distribution for the elastic scattering of 33.6-MeV protons from ^{10}B was measured and fitted with an optical-model calculation to provide parameters for a distorted-wave Born-approximation (DWBA) analysis of the (p,d) data. Angular distributions were taken for all the levels strongly excited in the (p,d) reaction, and the results compared to a DWBA calculation. Spectroscopic factors were extracted and compared with theoretical intermediate-coupling calculations in the $1p$ shell and with other (p,d) and (d,t) results. Spin assignments were made for the levels of ^{9}B strongly excited in the (p,d) reaction. Difficulties in matching the shapes of the experimental angular distributions to DWBA calculations for pickup and stripping reactions involving light nuclei are discussed.

INTRODUCTION

THIS paper describes the results from the reactions $^{11}B(p,d)^{10}B$ and $^{10}B(p,d)^{9}B$, using a 34-MeV incident proton beam. It represents the continuation of a study of neutron pickup reactions on $1p$ shell nuclei; an earlier paper describes the results of (p,d) reactions at an incident proton energy of 34 MeV with targets of ^{6}Li, ^{7}Li, and ^{9}Be.[1]

The (p,d) reactions on ^{10}B and ^{11}B have been investigated previously with incident proton energies in the range 11 to 155 MeV.[2–4] However, a considerable amount of additional information could still be obtained by using a sufficiently high incident-proton energy and a solid-state detector system with good resolution capabilities. With this arrangement, the observable range of excitation energy in the residual nucleus included those levels known to be strongly excited in this reaction, and angular distributions for these states have been measured. Spectroscopic factors were extracted from the data and compared to the theoretical calculations of Kurath[5] and Balashov.[6]

EXPERIMENTAL METHOD

The experimental setup for these measurements was the same as that described in a previous paper.[1] A proton beam with an energy of 33.6±0.2 MeV was extracted from the Michigan State University cyclotron. The reaction products were detected by a ΔE-E counter telescope; the E counter was a 3-mm-thick lithium-drifted silicon detector, and the ΔE counter was a silicon surface-barrier detector with a thickness of 270 μ. The energy resolution obtained was 160 keV for the $^{11}B(p,d)^{10}B$ deuteron spectra and 120 keV for the $^{10}B(p,d)^{9}B$ deuteron spectra. The apparatus used to measure the elastic scattering of protons from ^{10}B was identical to that described in an earlier paper.[1]

The ^{10}B target was purchased from the Nuclear Division of the Oak Ridge National Laboratory. It consisted of a self-supporting boron foil, isotopically enriched to 92.15% ^{10}B, with a thickness of 165±5 $\mu g/cm^2$. The ^{11}B target was made by evaporating isotopically enriched boron (98.05% ^{11}B) on a carbon backing ~50 $\mu g/cm^2$ thick, using an electron gun. Since the Q value for the reaction $^{12}C(p,d)^{11}C$ is ~7.2 MeV more negative than the Q value for $^{11}B(p,d)^{10}B$, deuterons from the carbon backing do not interfere with the observation of the strongly excited levels of ^{10}B. In addition to these targets, natural-boron targets were made using a suspension of finely ground natural boron (80.22% ^{11}B and 19.78% ^{10}B) in a polystyrene binder. The natural-born targets were used to obtain the ratio of the ground-state cross sections for the $^{11}B(p,d)^{10}B$ and $^{10}B(p,d)^{9}B$ reactions; this ratio was then used together with the $^{10}B(p,d)^{9}B$ data to normalize the differential cross sections from the $^{11}B(p,d)^{10}B$ reaction data, and yielded a value of 53±4 $\mu g/cm^2$ for the thickness of the ^{11}B deposited on the carbon backing.

EXPERIMENTAL RESULTS

$^{10}B(p,d)^{9}B$

A deuteron-energy spectrum from the reaction $^{10}B(p,d)^{9}B$ is shown in Fig. 1. Deuteron groups were observed corresponding to strongly excited levels of ^{9}B at 0.0, 2.35, 7.1, and 11.75 MeV, and small deuteron yields were noted corresponding to weakly excited levels at 2.8 and 14.6 MeV (Fig. 2). The very broad, weakly excited level observed with a ^{9}B excitation energy (E_x) of 14.6 MeV may correspond to the level observed at E_x=14.9 MeV in the same reaction, using 156-MeV

† Work supported in part by the National Science Foundation.
* Present address: Gulf General Atomic, San Diego, Calif.
[1] L. Kull, Phys. Rev. 163, 1066 (1967).
[2] T. Lauritsen and F. Ajzenburg-Selove, Nucl. Phys. 78, 1 (1966).
[3] D. Bachelier *et al.*, J. Phys. (Paris) C1, 51 (1966).
[4] University of Minnesota Linac Laboratory Progress Report, 1964, p. 61 (unpublished).
[5] D. Kurath (private communication).
[6] V. V. Balashov, A. N. Boyarkina, and I. Rotter, Nucl. Phys. 59, 417 (1964).

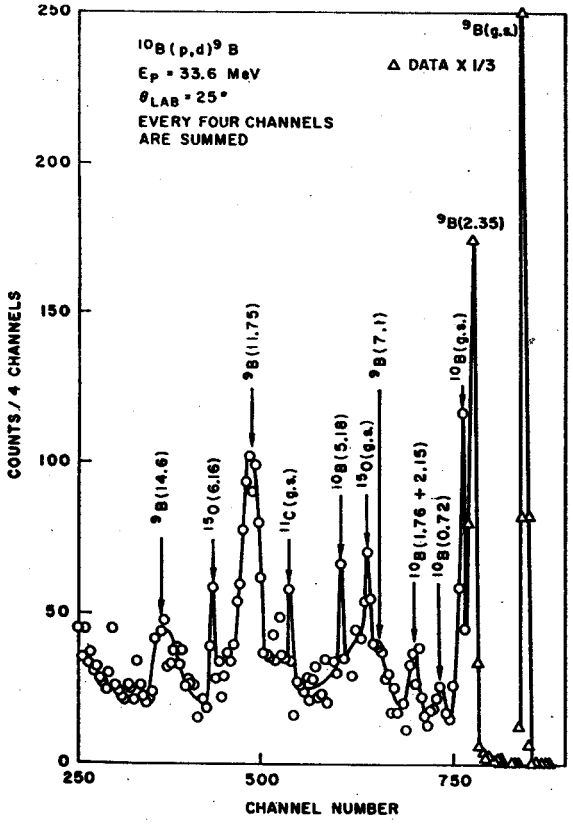

FIG. 1. ^{10}B$(p,d)^{9}$B deuteron spectrum at 25°. Deuteron groups corresponding to levels of ^{10}B are excited by the reaction ^{11}B$(p,d)^{10}$B and arise from an 8% ^{11}B impurity in the target. The counts have been summed for every four channels in order to show more clearly yields corresponding to ^{9}B levels at 7.1- and 14.6-MeV excitation.

protons.[3] With the higher incident proton energy, however, the 14.9-MeV level was reported to be strongly excited, with a cross section comparable to that of ground state at forward angles, whereas the present 34-MeV data show the 14.6-MeV level to have a cross section $\sim\frac{1}{10}$ that of the ground state at forward angles.

The two known positive-parity ^{9}B states at excitation energies of 1.5 MeV ($J^{\pi}=\frac{1}{2}^{+}$) and 2.83 MeV ($J^{\pi}=\frac{3}{2}^{+}$, $\frac{5}{2}^{+}$) [2,7] are of special interest, since their presence in the spectra could denote evidence of 2s-1d shell admixtures in the ground-state wave functions of stable nuclei with $A\leq 10$.[1] No evidence was found for the excitation of the 1.5-MeV level, which corresponds to the 1.67-MeV level of ^{9}Be($J^{\pi}=\frac{1}{2}^{+}$); however, results from the ^{10}B$(p,d)^{9}$B reaction using 11-MeV protons show a level at 1.7 MeV very weakly excited by what appears to be a compound-nucleus mechanism.[8] While the 1.7-MeV level is not observed in this investigation, the present 34-MeV data do not rule out the possibility of the same degree of excitation.

A small deuteron group (E_x=2.8 MeV) with a differential cross section of approximately 120 μb/sr was

[7] G. D. Symons, Phys. Letters 18, 142 (1965).
[8] E. F. Farrow and H. J. Hay, Phys. Letters 11, 50 (1964).

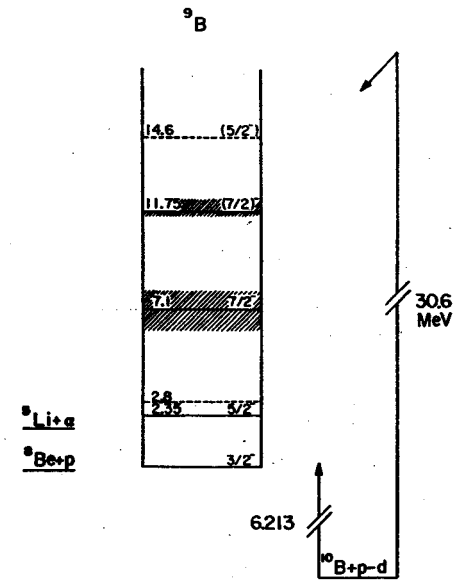

FIG. 2. Energy-level diagram of ^{9}B showing levels of ^{9}B excited in the ^{10}B$(p,d)^{9}$B reaction. Weakly excited levels are indicated with a dashed line.

observed at about 30° (center-of-mass angle), but it was difficult to follow over an extended range of forward angles because of the masking effect of levels arising from an ^{11}B impurity in the target (see Fig. 1). At 60°,

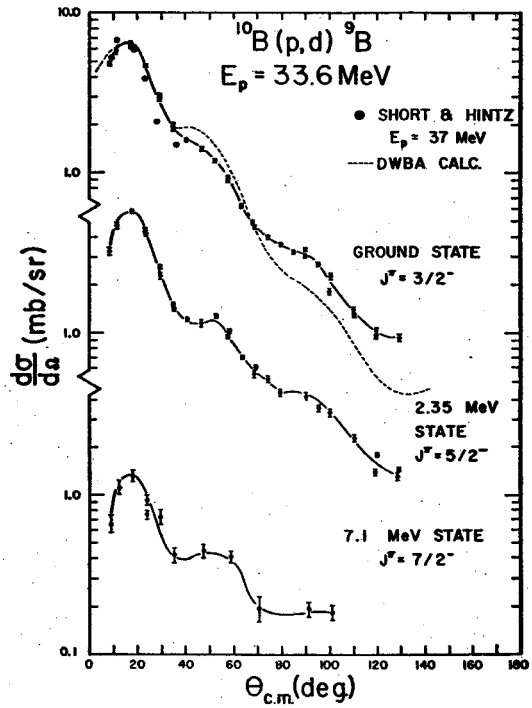

FIG. 3. ^{10}B$(p,d)^{9}$B angular distributions for deuteron groups corresponding to ^{9}B levels at 0.0, 2.35, and 7.1 MeV. The error bars only represent statistics, and the solid lines are drawn in to guide the eye. The dashed line shows the results of a DWBA calculation. Data points from work done at E_p=37 MeV (Ref. 4) are also shown.

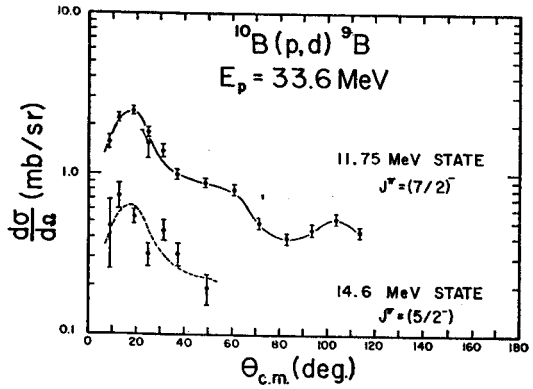

FIG. 4. $^{10}B(p,d)^{9}B$ angular distributions for deuteron groups corresponding to ^{9}B levels at 11.75 and 14.6 MeV. The dashed line drawn through the 14.6-MeV data points has the same shape as the line drawn through the 11.75-MeV data points

where it would not be masked by the deuteron groups arising from the ^{11}B impurities, it was not observed. This could signify a rapidly decreasing cross section typical of a direct-reaction process, and therefore opens the possibility for an observable $2s$-$1d$ shell admixture in the ground-state wave function of ^{10}B. The evidence, however, is scanty at best, and the only definite conclusion one can draw is that any $2s$-$1d$ admixture in the ^{10}B ground state is very small.

There are two previously reported states in ^{9}B at 11.62-MeV ($J^\pi=?$) and at 12.06-MeV excitation ($J^\pi=\frac{1}{2}^-, \frac{3}{2}^-$).[2] A single strong deuteron group was observed corresponding to an excitation energy of 11.75 MeV in ^{9}B. If the 12.06-MeV state has $J^\pi=\frac{1}{2}^-$, it would not be excited by a direct-reaction process due to angular-momentum selection rules. In this case, the single observed level has a measured excitation energy of

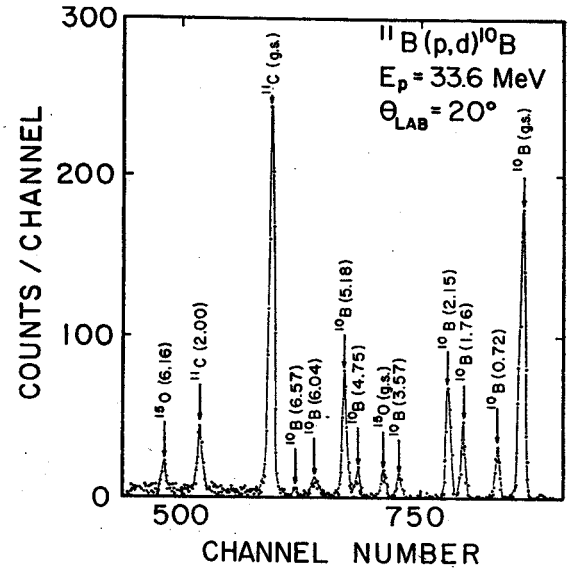

FIG. 5. $^{11}B(p,d)^{10}B$ deuteron spectrum at 20°. The target consisted of 54 $\mu g/cm^2$ of ^{11}B on a carbon backing 50 $\mu g/cm^2$ thick.

TABLE I. Measured ^{9}B excitation energies and widths for deuteron groups observed in the reaction $^{10}B(p,d)^{9}B$.

Excitation energy (MeV)	Width (MeV)
0.0	~0
2.35±0.02	
7.1 ±0.2	1.95±0.2
11.75±0.1	0.80±0.05
14.6 ±0.2	1.35±0.2

11.75±0.1 MeV, as compared with a previously determined energy of 11.62±0.1 MeV.[2] However, if the 12.06-MeV level has $J^\pi=\frac{3}{2}^-$ and is excited in the reaction, it would cause the centroid of the doublet peak to be shifted up in excitation energy from the strongly excited level at 11.62 MeV to the observed value of 11.75 MeV. The first explanation is more attractive, since the deuteron group shows no sign of a doublet structure over a wide range of angle, and the observed width of 800±50 keV is close to the previously reported width for the 11.62-MeV level of 700±100 keV.[2]

Strongly excited levels of ^{9}B at 0.0-, 2.35-, 7.1-, and 11.75-MeV excitation all have angular distributions with shapes characteristic of $l_n=1$ pickup (see Figs. 3 and 4), so that the parity of these levels is negative. Poor statistics for the 14.6-MeV-level data do not allow the definite assignment of the picked-up neutron's orbital angular momentum; however, the dashed curve in Fig. 4 is approximately the same shape as that observed for the 11.75 state and shows that an $l_n=1$ as-

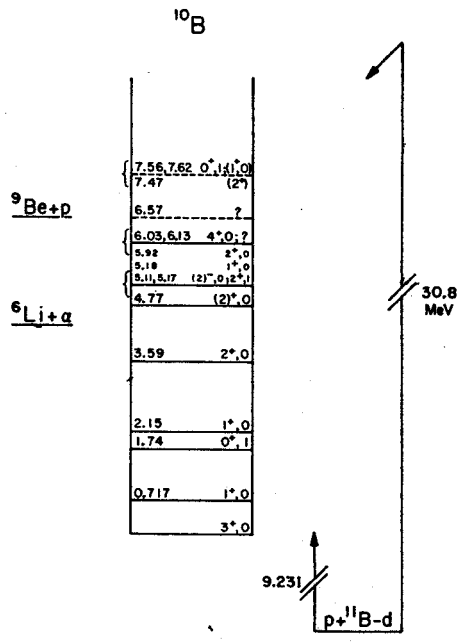

FIG. 6. Energy-level diagram of ^{10}B showing previously known levels (Ref. 2) excited in the $^{11}B(p,d)^{10}B$ reaction. Levels indicated with a dashed line are weakly excited by the reaction; the brackets indicate groups of levels which could not be separated with the energy resolution obtained in these measurements.

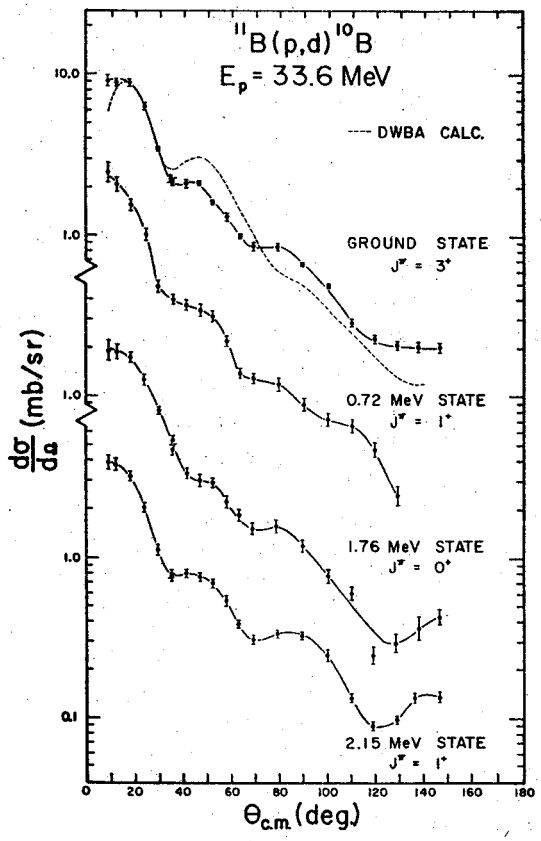

FIG. 7. ^{11}B$(p,d)^{10}$B angular distributions for deuteron groups corresponding to ^{10}B excitation energies of 0.0, 0.72, 1.67, and 2.15 MeV. The dashed line shows the results of a DWBA calculation.

signment is a reasonable possibility for the state. Total-angular-momentum assignments for all the observed states have been made on the basis of the measured spectroscopic factors for these levels and will be discussed in the next section. Table I is a list of the measured excitation energies and linewidths for the observed levels of ^{9}B.

^{11}B$(p,d)^{10}$B

The deuteron-energy spectrum from the ^{11}B$(p,d)^{10}$B reaction (see Fig. 5) shows deuteron groups corresponding to strongly excited levels of ^{10}B with excitation energies of 0.0, 0.72, 1.76, 2.15, 3.57, 4.75, 5.18, and 6.04 MeV; weakly excited levels of ^{10}B with excitation energies of 6.57 and 7.5 MeV were also observed. The deuteron group corresponding to a ^{10}B excitation energy of 5.18 MeV could correspond to known levels[2] of ^{10}B at 5.17-MeV ($J^\pi=2^+$), 5.18-MeV ($J^\pi=1^+$), and 5.11-MeV ($J^\pi=2^-$) excitation (Fig. 6). The 5.11-MeV level should only be weakly excited, since it can only be excited in the direct-reaction process by pickup of a $2s$-$1d$ shell neutron. The 5.17- and 5.18-MeV levels can both be excited by a direct-reaction mechanism, and deuteron groups from the two could not be separated with the 160-keV energy resolution obtained in this experiment.

The deuteron group corresponding to 6.04-MeV excitation energy in ^{10}B could correspond to previously observed levels at 5.92-MeV ($J^\pi=2^+$), 6.03-MeV ($J^\pi=4^+$), and 6.13-MeV ($J^\pi=?$) excitation.[2] The level at 6.03 MeV cannot be excited by a direct-reaction process due to angular-momentum selection rules; hence principal contributions to this group are from the 5.92- and 6.13-MeV levels. No evidence was found for the excitation of negative-parity states at 7.0-MeV ($J^\pi=1^-$), 7.8-MeV ($J^\pi=1^-$), and 8.1-MeV ($J^\pi=2^-$) excitation.[2] Any yield to these states was not masked by strongly excited positive-parity states, so that no direct evidence for sizable $2s$-$1d$ admixtures in the ground-state wave function of ^{11}B was found in this work.

The angular distributions for the ^{10}B levels at 0.0-, 0.72-, 1.76-, 2.15-, 3.57-, and 4.75-MeV excitation have shapes characteristic of the direct pickup of a $1p$ shell neutron (see Figs. 7 and 8). The deuteron groups corresponding to ^{10}B excitation energies of 5.18 and 6.04 MeV have similar angular distributions. This indicates that contributions to the 5.18-MeV group from the 5.11-MeV level ($J^\pi=2^-$) are indeed small, as previously con-

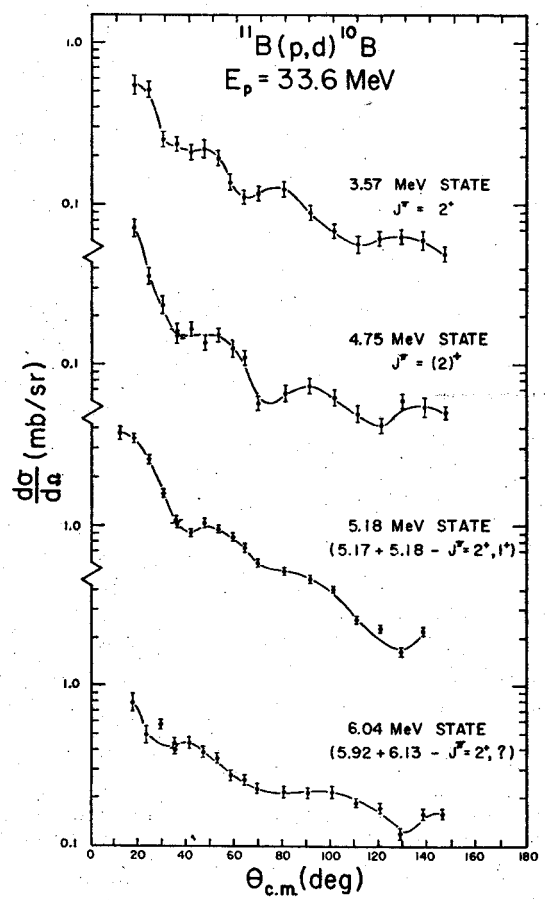

FIG. 8. ^{11}B$(p,d)^{10}$B angular distributions for the deuteron groups corresponding to ^{10}B excitation energies of 3.57, 4.75, 5.18, and 6.04 MeV.

jectured, and that if the 6.04-MeV group contains contributions from the 6.13-MeV level ($J^{\pi}=?$), the parity of this level is probably positive.

It was previously reported for reaction $^{7}Li(p,d)^{6}Li$ that the slopes of the angular distributions[1] first peaks for the ^{6}Li $T=0$ states at 0.0 and 2.15 MeV were steeper than those of the ^{6}Li $T=1$ states at 3.57 and 5.38 MeV.[1] No such effect was noted in comparing the angular distributions for the ^{10}B $T=0$ states at 0.72 and 2.15 MeV and the ^{10}B $T=1$ state at 1.76 MeV. The differential cross section for the transition to the ^{10}B $T=1$ level at 1.76 MeV does not fall off more rapidly beyond the first maximum than those transitions to the neighboring $T=0$ levels at 0.72 and 2.15 MeV. Such an effect was reported for these levels in the $^{11}B(d,t)^{10}B$ reaction with $E_d=11.8$ MeV.[9]

$^{10}B(p,p)^{10}B$

The angular distribution for the elastic scattering of 33.6-MeV protons from ^{10}B was measured with a proton-energy resolution of 500 to 600 keV (see Fig. 9). Proton groups corresponding to the ground state and the 0.72-MeV state of ^{10}B could not be resolved; however, data from the elastic scattering of protons from ^{10}B at incident energies of 19[10] and 185 MeV[11] show the cross section of the 0.72-MeV level to be 1 to 2% as large as that of the ground state. Since ^{11}B constituted only 8% of the target, its effect on the cross section was assumed to be small and was neglected. This is not a serious omission, assuming that the ^{10}B and ^{11}B elastic-proton distributions do not differ appreciably in shape and magnitude. The accuracy of the absolute differential cross sections is 6 to 9%.

ANALYSIS

The ABACUS computer code[12] was used to fit the measured angular distribution for the leastic scattering of protons from ^{10}B. The optical potential used was of the form

$$U=U_c-Vf(r,R,a_R)-i4a_IW\frac{d}{dr}f(r,R,a_I)$$
$$-\frac{1}{(m_\pi c)^2}\frac{V_{so}}{r}\frac{d}{dr}f(r,R,a_R). \quad (1)$$

Here $f(r,R,a)=1/(e^x+1)$, $x=(r-RA^{1/3})/a$, and U_c is the Coulomb potential from a uniformly charged sphere of radius $RA^{1/3}$ F. The best fit to the data is shown in Fig. 9, and the optical parameters used are given below.[13]

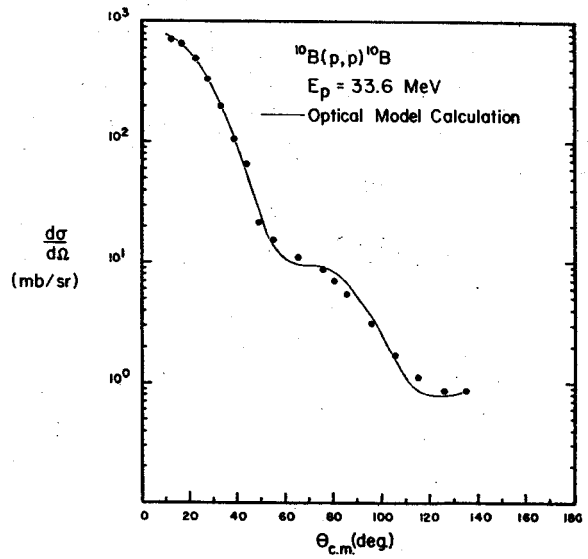

FIG. 9. $^{10}B(p,p)^{10}B$ angular distribution. The solid line shows the results of an optical-model calculation.

The DWBA calculations were carried out using the Macefield computer code. Parameters for the picked-up neutron were $a_n=0.65$ F, $R_n=1.25A^{1/3}$ F; no spin-orbit term was included in the potential. The deuteron optical parameters[14] were obtained from an outside source,[15] with a volume-absorption term instead of the surface term given in Eq. (1). One set of optical parameters was used for both the $^{10}B(p,d)^{9}B$ and $^{11}B(p,d)^{10}B$ DWBA calculations.

It was impossible to get reasonable fits to the experimental (p,d) angular distributions using the deuteron optical parameters given above. However, if the deuteron imaginary well is increased by a factor of 4, reasonable fits were obtained, as can be seen in Figs. 3 and 7. This same effect was observed in the (p,d) reactions with ^{6}Li, ^{7}Li, and ^{9}Be.[1] The increase in the deuteron-well depth varied the amplitude of the first peak of the differential cross section by less than 20% in all cases.

The same difficulties were also encountered in attempting to fit data from (d,p) reactions with $1p$ shell nuclei[16] at an incident deuteron energy of $\sim$20 MeV. In this case, reasonable fits to the data were obtained by using a cutoff radius[17] in the DWBA calculations. It was found, however, that the amplitude of the first peak of the differential cross section varied strongly as a function of the cutoff radius. Roughly, the amplitude of the first peak of angular distribution had two maxima; the first maximum appeared at a cutoff radius of 0 F and the

[9] H. Fuchs and R. Santo, Phys. Letters **24B**, 234 (1967).
[10] G. Schrank, E. K. Warburton, and W. W. Daehnick, Phys. Rev. **127**, 2159 (1962).
[11] D. Hasselgren, P. U. Renberg, O. Sundberg, and G. Tibell, Nucl. Phys. **69**, 81 (1965).
[12] E. H. Auerbach, Brookhaven National Laboratory Report No. BNL-6562, 1962 (unpublished).
[13] Proton optical parameters: $V=53.99$ MeV, $W=6.22$ MeV, $V_{so}=6.31$ MeV, $R=1.097$ F, $a_R=0.548$ F, $a_I=0.644$ F.
[14] Deuteron optical parameters: $V=83.5$ MeV, $W=14.94$ MeV, $V_{so}=0.0$, $R=1.33$ F, $a_R=a_I=0.65$ F.
[15] D. Dehnhard, G. C. Morrison, and Z. Vager, in *Proceedings of the International Conference on Nuclear Physics, Gatlinburg, Tennessee, 1966* (Academic Press Inc., New York, 1967).
[16] R. H. Siemssen, Bull. Am. Phys. Soc. **12**, 479 (1967).
[17] L. L. Lee, J. P. Schiffer, B. Ziedman, G. R. Satchler, R. M. Drisko, and R. H. Bassel, Phys. Rev. **136**, B971 (1964).

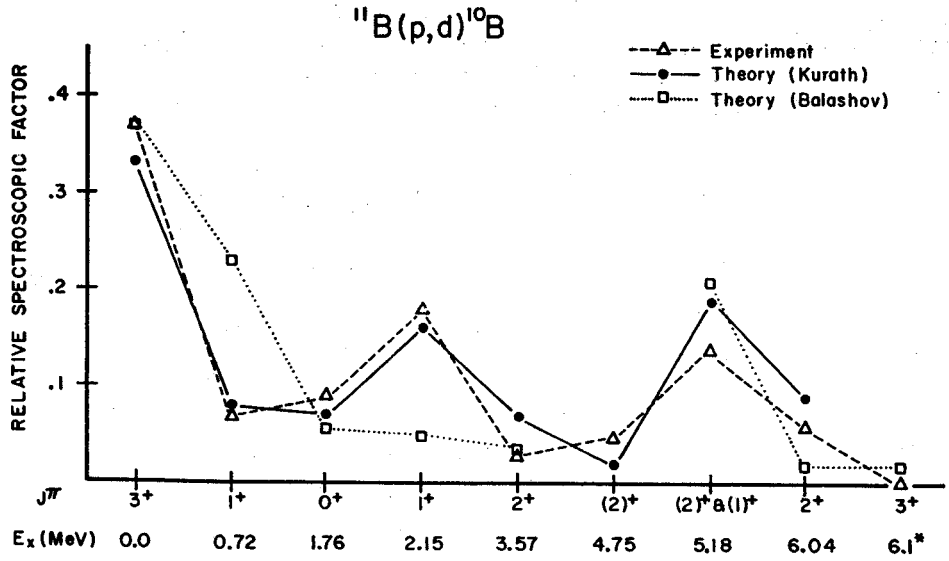

FIG. 10 Theoretical and experimental spectroscopic factors from the reaction $^{11}B(p,d)^{10}B$. A weakly excited $J^\pi=3^+$ level near 6.1-MeV excitation (indicated by an asterisk) is predicted by both Kurath and Balashov, but was not observed experimentally.

second at a cutoff radius from 3 to 5 F. The cross section of this peak varied by a factor of about 3 between the two maxima. Cutoff radii corresponding to the second maximum were used in the subsequent DWBA calculations, in which reasonable fits to the data were obtained.

The concern about the behavior of the amplitude of this forward-angle peak arises because the spectroscopic factor is assumed to be directly proportional to the ratio of the maxima of the DWBA and experimental angular distributions at forward angles. If the parameters of the DWBA calculation are varied in order to produce theoretical results which bear a reasonable resemblance (in shape) to the experimental data, the effect of these variations on the amplitude of the angular distribution's forward-angle peak must be considered in deciding just how meaningful the extracted spectroscopic factors are.

In summary, neither method of obtaining fits to the data explains the reason for the anomalous behavior of the DWBA in the case of light nuclei. The effect is large and reproducible, and it has been observed in the case of (d,p) and (p,d) reactions at several different bombarding energies. It deserves further study in that it may be pointing out weaknesses in the DWBA calculations which are especially emphasized in the case of light nuclei.

SPECTROSCOPIC FACTORS

Experimental spectroscopic factors were obtained by comparing the relative magnitudes of the characteristic $l_n=1$ peaks in the DWBA calculation and the experimental data. Theoretical spectroscopic factors were obtained from the coefficients of fractional parentage calculated by Kurath, using an intermediate-coupling model for the $1p$ shell nuclei[5]; a second set of theoretical spectroscopic factors was obtained from the calculations of Balashov.[6] The theoretical and experimental relative spectroscopic factors were obtained by normalizing the sum of the observed spectroscopic factors for each reaction to 1. More details concerning the method used to extract experimental spectroscopic factors and the expression used to obtain the theoretical spectroscopic factors from the coefficients of fractional parentage can be found in an earlier paper.[1]

Relatively good agreement is obtained between the theoretical calculations of Kurath and the experimentally obtained spectroscopic vactors for the $^{11}B(p,d)^{10}B$ reaction (see Fig. 10). Somewhat poorer agreement is obtained with the calculations of Balashov; in particular, there is a marked difference between the calculated and experimental spectroscopic factors for the 0.72- and 2.15-MeV levels of ^{10}B. Both Balashov and Kurath predict a weakly excited level ($J^\pi=3^+$) around 5–6-MeV excitation in ^{10}B. There are three known levels in the region 6.5–7.0-MeV excitation in ^{10}B with unknown spins and parities.[2] None was observed to be excited by the (p,d) reaction; however, the deuteron yield may have been very small and lost in the background. The spectroscopic factor for the deuteron group observed at a ^{10}B excitation energy of 6.04 MeV was calculated, assuming that only a 2^+ state contributed to the yield, whereas, as mentioned previously, the energy resolution could not have separated contributions from a previously observed level of ^{10}B at 6.13 MeV.

Spectroscopic factors have now been extracted for the $^{11}B(p,d)^{10}B$ reaction at incident proton energies of 18.9,[18] 155,[3] and 33.6 MeV; they have also been extracted for the $^{11}B(d,t)^{10}B$ reaction at an incident deuteron energy of 21.6 MeV.[15] The results are shown in Fig. 11, where the spectroscopic factors for the deuteron group corresponding to a ^{10}B excitation energy of 5.16 MeV have been extracted, assuming that only the 5.17-MeV level of ^{10}B ($J^\pi=2^+$) contributes to the yield. In all these experiments, however, the energy resolution was not good enough to separate out contributions to the observed deuteron yield from the 5.18-

[18] J. Legg, Phys. Rev. 129, 272 (1962).

MeV level of ^{10}B ($J^{\pi}=1^{+}$). Contributions to the observed deuteron group from both levels were assumed in the calculation shown in Fig. 10. The experimental spectroscopic factor for the 5.16-MeV level of ^{10}B extracted from the $E_p=155$-MeV work also contains contributions from the 4.77-MeV level of ^{10}B ($J^{\pi}=2^{+}$), which was not resolved.

The spectroscopic factor for the 2.15-MeV level of ^{10}B obtained from the work at $E_p=18.9$ MeV appears likely to be in error, as its value is significantly different from a closely grouped series of results from (p,d) experiments performed at widely different energies, from Kurath's theoretical calculations, and from a (d,t) experiment (see Fig. 11). It was on the basis of the work done at $E_p=18.9$ MeV that a previous investigation proposed an isotopic-spin dependence in the (p,d) and (d,t) reactions, which would account for significant differences in the observed spectroscopic factors for the 2.15- and 0.72-MeV levels of ^{10}B [15]; the present work does not support this contention.

With the above-mentioned 2.15-MeV datum point ignored, a mean spectroscopic factor was calculated from the experimental data for each ^{10}B level; the results are shown in Table II.

From these results, the following general conclusions appear to be valid: (1) Relative spectroscopic factors obtained over a wide range of incident energies using a variety of DWBA procedures agree to within 15–20%. (2) Spectroscopic factors obtained from the (d,t) reaction are not significantly different from those obtained with (p,d) reactions. (3) Kurath's calculations agree with the experimental spectroscopic factors to within ~20%. (4) A reasonable absolute error for the spectroscopic factors obtained in this work falls somewhere in the region of 15–20%.

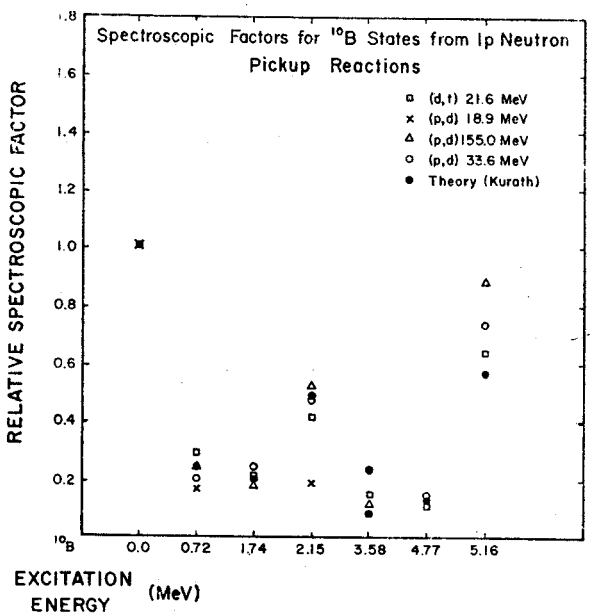

FIG. 11. A comparison of theoretical and experimental spectroscopic factors for ^{10}B states from $1p$ neutron pickup reactions. The spectroscopic factors for the ground state have been normalized to 1.

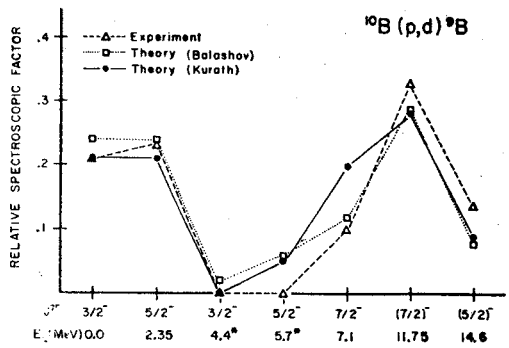

FIG. 12. Theoretical and experimental spectroscopic factors for the reaction $^{10}B(p,d)^{9}B$. Weakly excited levels near 4.4- and 5.7-MeV excitation (indicated by asterisks) are predicted by both Kurath and Balashov, but were not observed experimentally.

Note, however, that $^{7}Li(d,t)^{6}Li$ [19] data analyzed using the plane-wave Born approximation (PWBA) shows a possible isotopic-spin dependence in the spectroscopic factor for the 3.57-MeV level of ^{6}Li ($T=1$) when compared with results from $^{7}Li(p,d)^{6}Li$. Unfortunately, the consistency of the observed effect could not be checked, as results for the 5.36-MeV level of ^{6}Li ($T=1$) were inconclusive. In another case, a comparison of the results from the $^{9}Be(d,n)^{10}B$ and $^{9}Be(^{3}He,d)^{10}B$ reactions has shown that smaller relative spectroscopic factors for the $T=1$ states are extracted from the (d,n) reaction than from the $(^{3}He,d)$ reaction.[20] There is therefore some evidence for an isotopic-spin dependence in spectroscopic factors which is not included in the present theories, but the absence of any evidence for isotopic-spin effects in the present work indicates that the origin of the observed irregularities is not easily isolated.

Experimental and theoretical spectroscopic factors for the reaction $^{10}B(p,d)^{9}B$ are shown in Fig. 12. The ^{9}B levels at 4.4 and 5.7 MeV have been predicted theoretically by both Kurath and Balashov, but have not been observed experimentally. The predicted yields are small, however, and the peaks may have been lost in the high background because of three-body breakup.

The ^{9}B levels at 0.0, 2.35, 7.1, and 11.75 MeV have all been determined to have negative parity, while the

TABLE II. Average differences of spectroscopic factors from mean values of the experimental data.

Spectroscopic factors from	Average difference from mean values
(p,d) reactions	15%
(d,t) reactions	18%
Theoretical calculation (Kurath)	20%

[19] E. W. Hamburger and J. R. Cameron, Phys. Rev. **117**, 781 (1960).

[20] R. H. Siemssen, G. C. Morrison, B. Zeidman, and H. Fuchs, Phys. Rev. Letters **16**, 1050 (1966).

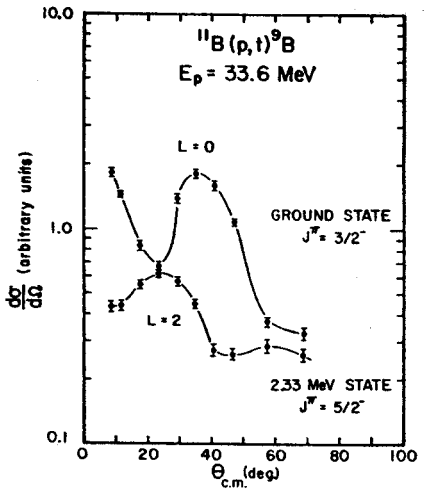

FIG. 13. ^{11}B$(p,t)^{9}$B angular distributions for the 0.0- and 2.33-MeV levels of ^{9}B.

^{9}B level at 14.6 MeV has been tentatively identified as having negative parity. Assuming the experimental spectroscopic factors agree with theoretical calculations to within ~20%, the spins for the observed levels were assigned by comparing the theoretical and experimental results (see Fig. 12).

Additional evidence to support these assignments was obtained from triton-energy spectra for the reaction ^{11}B$(p,t)^{9}$B. These spectra were taken with the same ^{11}B targets used in the ^{11}B$(p,d)^{10}$B reaction work, with the particle identification system adjusted to detect tritons. Angular distributions were measured for the ground state and the 2.33-MeV state of ^{9}B and are shown in Fig. 13. These data are in agreement with results from the ^{11}B$(p,t)^{9}$B reaction with E_p=40 MeV.[21] The shapes of the angular distributions can be explained with the following simple model for the (p,t) reaction. When the incident proton picks up two neutrons as a pair from ^{10}B, they must be in the singlet state with a total spin $S=0$, and the orbital angular momentum of the pair must be even from symmetry considerations ($L=0$, 2, 4, $\cdots$). Using this simple picture, the ground-state distribution for ^{11}B$(p,t)^{9}$B has a characteristic shape for the pickup of a dineutron with orbital angular momentum $L=0$. This means that the ground state of ^{9}B can only have the assignment $J^\pi=\frac{3}{2}^-$, in agreement with the ^{10}B$(p,d)^{9}$B work. The angular distribution for the 2.33-MeV state has a characteristic shape for the pickup of a dineutron with $L=2$, allowing for spin and parity assignment of $J^\pi=\frac{7}{2}^-$, $\frac{5}{2}^-$, $\frac{3}{2}^-$, or $\frac{1}{2}^-$. These values do not contradict the previous $J^\pi=\frac{5}{2}^-$ assignment for this state.

Note also that the assignments for the levels at 0.0, 2.35, and 7.1 MeV also coincide with the spin assignments for isobaric analog levels of ^{9}Be at 0.0-, 2.43-, and 6.6-MeV excitation.[2] There is therefore a significant amount of supplementary evidence to support the spin and parity assignments which were made on the basis of agreement between experimental and theoretical spectroscopic factors.

SUMMARY

The shapes of the experimental angular distributions for pickup and stripping reactions with light nuclei consistently disagree with DWBA calculations which use optical parameters obtained from elastic-scattering experiments. Two different methods have been used to adjust the theoretical calculations in order to obtain reasonable fits to the data: (1) The strength of the imaginary deuteron well was increased by a factor of 3 or 4 in the (p,d) calculations[1,22]; (2) a cutoff radius was used in the (d,p) calculations.[16] At the present time, there is no apparent theoretical justification for either method.

The same relatively good agreement between experimentally obtained spectroscopic factors and the intermediate-coupling calculations of Kurath was found for the reaction ^{11}B$(p,d)^{10}$B as has been observed previously for the reactions ^{7}Li$(p,d)^{6}$Li and ^{9}Be$(p,d)^{8}$Be.[1] On the basis of this general accord observed between the intermediate-coupling model and experiment, spin assignments were made for the observed negative-parity levels of ^{9}B by comparing the data from the ^{10}B$(p,d)^{9}$B reaction with the model predictions. No evidence was observed for any sizable $2s$-$1d$ admixture in the ground-state wave functions of ^{10}B and ^{11}B.

A comparison of spectroscopic factors from the reaction ^{11}B$(p,d)^{10}$B with proton energies in the range 19 to 155 MeV with those from the reaction ^{11}B$(d,t)^{10}$B with E_d=21.6 MeV shows no significant difference between the experimental results. The comparison also indicates that relative spectroscopic factors can be determined to within 15–20%.

No noticeable difference in the shapes of angular distributions for the neighboring $T=0$ and $T=1$ states of ^{10}B was observed which could be interpreted as an isotopic-spin effect, nor were there any significant differences noted in the (p,d) or (d,t) spectroscopic factors to the $T=1$ levels of ^{10}B which could be correlated to a difference in isotopic spin. Some recent investigations of other reactions report effects in spectroscopic factors and angular distributions which are interpreted as an isotopic-spin dependence not included in the present DWBA theory. The present work shows that the observation of isotopic-spin effects is limited to specific cases, and adds to the collection of data from which some obvious patterns of regularities has yet to be recognized.

ACKNOWLEDGMENTS

The authors would like to express their thanks to C. Barrows for assistance in taking the data, and to Dr. G. Crawley for helpful discussions of the results.

[21] G. Reynolds, J. R. Maxwell, and N. M. Hintz, Bull. Am. Phys. Soc. **10**, 439 (1965).
[22] N. S. Chant, P. S. Fisher, and D. K. Scott, Nucl. Phys. **A99**, 669 (1967).

NUCLEAR INSTRUMENTS AND METHODS 58 (1968) 245–252; © NORTH-HOLLAND PUBLISHING CO.

DESIGN CONSIDERATIONS FOR A SEPARATED TURN ISOCHRONOUS CYCLOTRON

M. M. GORDON*

Cyclotron Laboratory, Michigan State University, East Lansing, Michigan, U.S.A.

Received 3 October 1967

The objective of this machine is the production of large proton currents at energies from 200 to 1000 MeV with clear turn separation so that 100% beam extraction is achieved. Each stage of the cyclotron consists of a "ring" of identical magnet sectors interspersed with an appropriate set of rf acceleration cavities. The beam is injected from a linac thereby eliminating the central region problems associated with present isochronous cyclotrons. As a result of the narrow magnet gaps, the machine has relatively strong axial focusing throughout. The orbital frequency is high enough so that the beam can be accommodated within the space charge limits. Additional small third harmonic cavities provide for a "flat-top" on the resultant voltage wave form thereby allowing a relatively large phase width in the accelerated beam. Conditions for achieving clear turn separation are analysed and found feasible. For a reasonable total number of turns, the isochronous field trimming requirements are quite tractable. Tentative design figures are presented and compared with the present Separated Orbit Cyclotron (SOC) designs.

1. Introduction

During the past few years the proposed Separated Orbit Cyclotron (SOC) designs have evolved toward a machine more closely resembling a conventional isochronous cyclotron. The question then arises as to whether it might be desirable to design an SOC directly in terms of an isochronous cyclotron. The present paper discusses the main features of such a design and shows that the lack of phase stability in such a machine is not a serious limitation. Our information on present SOC designs comes from a paper by Martin at the 1966 Cyclotron Conference in Gatlinburg[1]).

The Separated Turn Isochronous Cyclotron (STIC) considered here should have all the desirable features of the present SOC designs, namely, the capability of producing currents in the 50–100 mA range with clear turn separation such that 100% extraction can be achieved. The STIC would consist of a "ring" of identical magnet sectors interspersed with rf acceleration cavities. The following is a list of its overall features which will be discussed in more detail in the succeeding sections.

1. As in present SOC designs, beam injection would be from a linac (say, 10 MeV) since only such an injector can yield currents in the 50 mA range with the required beam qualities. Such injection eliminates the central region of the cyclotron with its tremendous disadvantages.

2. The magnet gap would be small (about 5 cm) so that relatively high ν_z values ($\gtrsim 1$) could readily be achieved over the entire acceleration region. As a result of the isochronism condition ν_r values would be close to γ. Thus, these ν values would be about three times smaller than for present SOC designs. The magnet gap, however, would be unobstructed by focusing elements. The number of magnet sectors is not crucial and would be determined by engineering considerations (magnet and cavity design, as well as inflection and deflection problems).

3. The orbital frequency f_0 would be in the 6–8 MHz range, which is two to four times higher than in present SOC designs. Since the space charge limits are proportional to $(f_0\nu)^2$, the increase in f_0 would compensate for the decrease in ν in this respect. For a given energy the machine radius is inversely proportional to f_0 so that the STIC would be 2–4 times smaller than present SOC designs.

4. Present SOC designs require a radius gain per turn R_1 of 20–30 cm; since the magnet gap is unobstructed, the STIC could have R_1 as small as 4–5 cm and still achieve clear turn separation. Since the required energy gain per turn E_1 is proportional to (f_0R_1), the STIC would have a lower E_1 than present SOC designs.

5. In addition to the main rf cavities (50 MHz), one or more third harmonic (150 MHz) cavities would be included so as to yield a "flat-top" to the resultant voltage wave form. (These third harmonic cavities would supply only 12–14% of the net voltage.) This flat-topping would permit the acceleration, for example, of a 50° phase width in the beam with a resultant fractional radius spread of only 0.4%.

6. Assuming, for example, a beam with 1.5 cm intrinsic radial width and 50° phase width, and assuming $R_1 = 4$ cm, then a clear turn separation of 1 cm could be achieved provided the number of turns τ is less than 100. Even with beam fluctuation effects taken into account, this turn separation is quite adequate for a deflection system initiated by an electrostatic deflector, and should guarantee 100% beam extraction.

* Most of this work was carried out during August, 1966, at the Oak Ridge National Laboratory; this work has also been partially supported by the National Science Foundation.

7. The phase acceptance of the STIC decreases as the number of turns increases and a phase acceptance of 70°, for example would restrict the number of turns to $\lesssim 30$. By contrast, the present SOC designs have a phase acceptance of 90°. However, the resultant STIC beam would have a smaller radial width and energy spread.

8. In the absence of phase stability the STIC requires some care in the magnetic field trimming; however, if the number of turns τ is in the 50–100 range, this problem should be quite tractable. If h is the harmonic ratio of rf to orbital frequency, then the phase excursion can be kept within $\pm 2.5°$ provided $h\tau < 650$, considering the present state of magnet technology.

There are at present a number of cyclotrons operating in the proton energy range up to 60 MeV and in the next few years this range will be extended up to 100 or 125 MeV. As a consequence, it seems highly desirable that the first stage SOC be designed with an upper energy of about 200 MeV. Such a goal might be achieved with an STIC design and the resultant machine would be smaller than the proposed 10–50 MeV SOC. Most of the analysis given here will apply equally well to a "meson factory" designed for much lower currents (~ 0.1 mA).

2. Turn separation

An absolute spatial separation of turns is essential for 100% beam extraction which, in turn, is a necessity for a machine producing 50–100 mA currents. However, it must be kept in mind that this turn separation is required only at extraction (and inflection). Since turn separation is extremely expensive, it should be kept as small as possible consistent with the 100% extraction goal. For an extraction system initiated by an electrostatic deflector, turn separation as small as 1–3 mm should be sufficient. However, since the turn separation must be sufficiently large to accommodate beam fluctuations (sect. 3), we shall assume here a design goal of 1 cm for the turn separation.

A basic element in considerations of turn separation is the intrinsic radial width of the beam $\Delta_i R$ at a given phase ϕ. This width is determined by the size of the beam injected into the cyclotron from the linac. If $\Delta_i R$ is small, then turn separation is more easily achieved; however, space charge limits are proportional to the cross sectional area of the beam, so that an appropriate beam size must be chosen by balancing these two effects.

If the peak radius gain per turn (turn spacing) is R_1, then the turn separation δ is given by:

$$\delta = R_1 - \Delta_\phi R - \Delta_i R, \tag{1}$$

where $\Delta_\phi R$ is the spread in radius resulting from the finite phase width of the beam. This $\Delta_\phi R$ is proportional to the number of turns τ; that is,

$$\Delta_\phi R / R_1 = \tau g(\phi), \tag{2}$$

where $g(\phi)$ is a function of the phase ϕ and is characteristic of the rf voltage wave form. For example, for a simple sinusoidal wave form, $g(\phi) = 1 - \cos\phi$; however, as will be shown later, if a third harmonic component is added thereby "flat-topping" the wave form, then $g(\phi)$ can be kept quite small over a relatively large phase range. Thus,

$$\delta = R_1[1 - \tau g(\phi)] - \Delta_i R; \tag{3}$$

therefore, an essential prerequisite for turn separation is:

$$\tau g(\phi) < 1. \tag{4}$$

This condition restricts the phase acceptance for a given number of turns, or conversely, the number of turns for a given phase acceptance.

If we assume $\delta = 1$ cm, $\Delta_i R = 1.5$ cm, and $R_1 = 4$ cm, then from eq. (4),

$$\tau g(\phi) < 0.375. \tag{5}$$

As will be shown later, for $\Delta\phi = 50°$, this requires $\tau < 100$, while for $\Delta\phi = 70°$, the requirement is $\tau < 25$. The specific numbers given here, and in the remainder of this paper, serve mainly for elucidation and should not be construed as well thought-out design figures.

The intrinsic radial width $\Delta_i R$ results from the combined effect of the radial beam width w_i and the energy spread δE_i at injection. The latter causes a net beam spread $\delta_i r$ given by:

$$\delta_i r = \tfrac{1}{2} R_i (\delta E_i / E_i), \tag{6}$$

where R_i and E_i are the initial radius and energy of the beam at injection. In addition, acceleration produces adiabatic damping of the radial beam width by a factor γ^{-1}. Combining these effects then yields:

$$\Delta_i R = (w_i + \delta_i r)/\gamma. \tag{7}$$

Assuming $w_i = 1$ cm, $R_i = 86$ cm at 10 MeV (from table 1 in sect. 3) and $(\delta E_i)/E_i = 1\%$ (i.e., $\delta E_i = 100$ keV at $E_i = 10$ MeV), then $\Delta_i R = (1.43 \text{ cm})/\gamma$; the factor γ^{-1} reduces this $\Delta_i R$ to 1.2 cm at 200 MeV, and to 0.7 cm at 1000 MeV. Thus, the adiabatic damping of $\Delta_i R$ substantially counteracts the increase in $\Delta_\phi R$ with τ, and also mitigates the effect of beam fluctuations on turn separation. Note that at inflection ν_r is close to unity, so that the term $\delta_i r$ in eq. (7) does not influence the radial width at the end of the first turn; thus, the

amount of turn separation available for clearing the inflector electrode is simply:

$$\delta_{in} = R_1 - w_i, \tag{8}$$

and for the numbers given above, $\delta_{in} = 3$ cm, which should be quite ample.

3. Energy, radius and turn number

For an isochronous magnetic field corresponding to the orbital frequency f_0, the mean orbit radius R is given by:

$$R = \beta(c/\omega_0), \tag{9}$$

where $\omega_0 = 2\pi f_0$ and $\beta = v/c$; for example, if $f_0 = 8$ MHz, then $c/\omega_0 = 5.964$ m. Thus, the value of f_0 determines the size of the machine.

The peak energy-gain per turn E_1 is related to f_0 and R_1 through the formula:

$$E_1 = (m_0c^2)(\beta\gamma^3)\omega_0 R_1/c, \tag{10}$$

where $\beta\gamma^3 = \gamma^2(\gamma^2-1)^{\frac{1}{2}}$, and $\gamma = 1 + E/(m_0c^2)$, and E is the kinetic energy. Since $\beta\gamma^3$ increases rapidly with E, if E_1 is constant, then R_1 decreases rapidly with E. However, a large R_1 is needed only at extraction; consequently, as in present SOC designs, it is much more feasible to consider a machine design with constant, or nearly constant, R_1. We shall assume then a constant value for R_1.

Table 1 gives values for E_1, R and τ as a function of E for $f_0 = 8$ MHz and $R_1 = 4$ cm. The values of τ are obtained from the formula:

$$\tau = (R - R_i)/R_1, \tag{11}$$

assuming injection at 10 MeV. Although the values of E_1 are large by normal cyclotron standards, they are somewhat smaller than those for present SOC designs; however, the real question is whether appropriate rf cavities can be designed within the available space. (As discussed in sec. 5, about 50% of the circumference would be available for such cavities.)

TABLE 1

$f_0 = 8$ MHz; $R_1 = 4$ cm.

E(MeV)	E_1(MeV)	R(m)	τ
10	0.941	0.86	0
20	1.36	1.21	9
50	2.31	1.87	25
100	3.30	2.55	42
200	5.24	3.38	63
350	11.16	4.09	81
500	17.18	4.52	91.5
1000	48.54	5.22	109

Clearly, the specification of f_0 and R_1 fixes the main characteristics of the machine. The numbers in the table seem reasonably appropriate for a first-stage 10–200 MeV STIC, which would then have 63 turns. For a second-stage 200–1000 MeV STIC, a lower frequency could be tolerated; for example, with $f_0 = 6$ MHz the given values of E_1 would be multiplied by $\frac{3}{4}$ while the given R and τ values would be multiplied by $\frac{4}{3}$, so that the number of turns in this stage would be 61 rather than 46.

The energy spread in the beam $\Delta_\phi E$ due to the finite phase width is given by:

$$\Delta_\phi E = (\Delta_\phi R/R_1)E_1, \tag{12}$$

and assuming constant R_1, it follows that

$$\Delta_\phi E/E_f = \gamma_f(\gamma_f+1)(1-\beta_i/\beta_f)g(\phi), \tag{13}$$

where the subscripts "i" and "f" refer to the initial (injection) and final values. As a result of isochronism the initial energy spread δE_i at injection will persist; however, this δE_i will usually be negligible compared to $\Delta_\phi E$. Assuming as in sect. 2, $\Delta_\phi R = 1.5$ cm, then, for example, $(\Delta_\phi E)/E_f = 0.98\%$ at $E_f = 200$ MeV, and 1.84% at 1000 MeV, using the numbers in the table.

Fluctuations in the rf voltage produce corresponding fluctuations in the final beam radius R_f which can seriously affect the definition of the beam position relative to the deflector septum. Assuming a fractional voltage variation $(\delta V_0)/V_0$, then:

$$\delta R_f = \tau R_1(\delta V_0/V_0). \tag{14}$$

For example, taking $(\delta V_0)/V_0 = \pm 10^{-3}$, and using the numbers in the table above, gives $\delta R_f = \pm 0.25$ cm for $E_f = 200$ MeV, and ± 0.44 cm at 1000 MeV. Such fluctuations reduce the effective turn separation at extraction; using the preceding numbers this reduction would be 0.50 cm at 200 MeV and 0.88 cm at 1000 MeV. The turn separation δ calculated in the preceding section must be large enough to withstand such reductions. In addition, these fluctuations increase the effective width of the beam within the deflector channel and this channel must be designed accordingly.

4. Rf voltage wave form

Most of the rf cavities in the STIC would operate at the same frequency as the linac injector (say, 50 MHz); in addition, one or more cavities would operate at three times this frequency (i.e., 150 MHz). These third harmonic cavities would serve to "flat-top" the resultant rf voltage wave form (this is an old idea which, I am told

was first proposed by Rossi in 1939). With a proper phasing of all these cavities, the net energy-gain per turn will be given by:

$$dE/d\tau = V_0(\cos\phi - \lambda\cos 3\phi)$$
$$= V_0[(1+3\lambda)u - 4\lambda u^3], \quad (15)$$

where $u = \cos\phi$. The parameter λ specifies the fraction of the voltage contributed by the third harmonic cavities; if $\lambda > \frac{1}{9}$, then the peak of this wave form splits into two peaks with a shallow valley between. In this case the peak energy-gain per turn occurs for $\phi = \phi_0$ given by:

$$12\lambda(u_0)^2 = 1+3\lambda, \quad (16)$$

where $u_0 = \cos\phi_0$. The peak energy-gain per turn E_1 is then given by:

$$E_1 = V_0(8\lambda)(u_0)^3; \quad (17)$$

and,

$$dE/d\tau = E_1 v(\phi), \quad (18)$$

with:

$$v(\phi) = \tfrac{3}{2}(u/u_0) - \tfrac{1}{2}(u/u_0)^3.$$

Assuming as before, that the peak radius-gain per turn R_1 has a constant value, then:

$$dR/d\tau = R_1 v(\phi), \quad (19)$$

and

$$R(\phi) = \tau R_1 v(\phi),$$

provided ϕ remains constant (isochronism). Corresponding to the definitions in sect. 2, it follows then that:

$$\Delta_\phi R = R(\phi_0) - R(\phi) = \tau R_1 g(\phi), \quad (20)$$

where

$$g(\phi) = 1 - v(\phi) \quad (21)$$
$$= [(u/u_0)-1]^2\{1+(\tfrac{1}{2}u/u_0)\}.$$

Fig. 1 shows a plot of $g(\phi)$ vs ϕ for $\phi_0 = 20°$. It is clear from this figure that for $|\phi| < 28°$, then $g(\phi) < 0.0063$. If this $g(\phi)$ range were acceptable with regard to the turn separation condition of eq. (3), then the phase acceptance in this case would be 56°. The third harmonic obviously makes an enormous improvement since, if it were absent, the same phase range would yield $g(\phi)$ values as large as 0.12. Note that the curve for $g(\phi)$ in fig. 1 is an "inverted image" of the voltage wave form $v(\phi)$.

For a given g_0 the problem is to determine the value of λ such that $g(\phi) \leqq g_0$ over the largest possible range of ϕ values. Examination of the form of $g(\phi)$ reveals that the solution consists in finding λ such that:

$$g_0 = g(0) = g(\tfrac{1}{2}\Delta\phi), \quad (22)$$

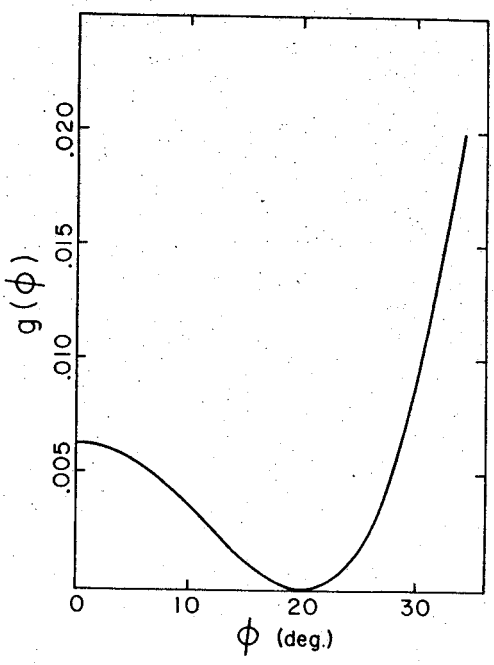

Fig. 1. Typical curve showing fractional energy spread $g(\phi)$ as a function of phase ϕ produced by third harmonic "flat-topping" of the voltage wave form.

for which $g(\phi) \leqq g_0$ over the phase range $-\frac{1}{2}\Delta\phi \leqq \phi \leqq +\frac{1}{2}\Delta\phi$. For a given phase acceptance $\Delta\phi$, the correct value of λ can be calculated from:

$$\lambda = [1+2\cos(\tfrac{1}{2}\Delta\phi)]^{-2}; \quad (23)$$

with this λ value, u_0 can be obtained from eq. (16), and then g_0 from eq. (21) with $u = 1$. This procedure was employed to construct table 2 which presents values of g_0, ϕ_0, λ and V_0/E_1 for $\Delta\phi$ values from 30° to 90°.

TABLE 2

$\Delta\phi$	g_0	ϕ_0	λ	V_0/E_1
30	0.00045	10.58	0.1163	1.1311
35	0.00084	12.33	0.1183	1.1332
40	0.00145	14.07	0.1206	1.1355
45	0.00235	15.81	0.1233	1.1380
50	0.00362	17.53	0.1264	1.1406
55	0.00537	19.25	0.1300	1.1432
60	0.00771	20.96	0.1340	1.1458
65	0.01079	22.66	0.1385	1.1483
70	0.01476	24.35	0.1437	1.1505
75	0.01979	26.02	0.1495	1.1524
80	0.02611	27.67	0.1560	1.1539
85	0.03394	29.31	0.1633	1.1546
90	0.04355	30.94	0.1716	1.1545

Clearly, the value of g_0 increases rapidly with $\Delta\phi$. The following approximate formula (obtained by expansion) gives fairly accurate results for most cases of interest:

$$g_0 = (1.5)\varepsilon^2(1+2\varepsilon), \tag{24}$$

where

$$\varepsilon = \sin^2(\tfrac{1}{4}\Delta\phi).$$

Corresponding to the condition of eq. (4) the maximum possible number of turns may be defined as $\tau_{max} = (g_0)^{-1}$ for a given $\Delta\phi$. Thus, for $\Delta\phi = 30°$, $\tau_{max} = 2200$, while for $\Delta\phi = 70°$, $\tau_{max} = 70$.

The values of λ given in table 2 indicate that the third harmonic would furnish only 12–14% of the net voltage supplied by the main harmonic cavities. Assuming 180° symmetry, a 3 to 1 cavity ratio would yield an 8-sector machine, while a 4 to 1 cavity ratio would yield a 10-sector machine. For the same two cavity ratios, 120° symmetry would require 12 and 15 sector machines, respectively. Since the third harmonic cavities are relatively small, it may be possible to use the sectors they occupy for inflection and deflection; such a design would avoid the necessity of "blank" sectors and would thereby ease the problem of achieving a prescribed E_1 within the allotted space.

The foregoing discussion assumes a constant value for λ and such a condition would probably be quite difficult to achieve in practice. Fortunately, this condition is not essential to the proper functioning of the third harmonic. The purpose of the third harmonic is to subtract energy (and hence, radius) from the particles at $\phi = 0$ while leaving those at $\phi = 30°$ unaffected. Since turn separation is required only at extraction, it is only the cumulative effect of the third harmonic over all the turns which is significant; that is, this cumulative effect must be such as to minimize the variation in final radius with phase. Since the voltage on the third harmonic cavities is an independent parameter, for a given cavity design this voltage can be adjusted in practice so as to yield the desired effect. Suppose then that λ (and also R_1) are functions of the radius r; from eq. (19) the number of turns τ will be given by:

$$\tau(R_f) = \int \{R_1 v(\lambda,\phi)\}^{-1} dr, \tag{25}$$

where the integration extends from the initial radius R_i to the final radius R_f. Considering R_i and τ as fixed parameters, this equation then provides a relationship between R_f and ϕ which depends on the amplitudes of the variation in R_1 and λ with radius; consequently, these amplitudes can be adjusted and their values set such that the change in R_f over the prescribed phase range $\Delta\phi$ is minimized.

5. Magnet design

During the past ten years a sizable reservoir of knowledge and experience has accumulated relevant to the magnet design problems associated with sectored cyclotrons. These tools include: procedures for mapping magnetic fields with considerable speed and accuracy; computer programs for calculating magnetic field corrections, focusing frequencies, and other pertinent orbit properties; and techniques for assembling trim coil data so as to accurately reproduce prescribed magnetic fields. The magnet design work required for the STIC could make direct use of this theoretical and technological progress. We shall present here only the most elementary design considerations relative to the magnet structure for the STIC. The magnet design problems can be defined quite readily, but their detailed solutions can be achieved only through model magnet studies.

If isochronous conditions obtain, then the average magnetic field along the orbit B_{av} is given by:

$$B_{av} = (m_0\omega_0/e)\gamma; \tag{26}$$

for example, for an orbital frequency $f_0 = 8$ MHz, then $(m_0\omega_0/e) = 5.248$ kG. Consider a magnet sector whose gap is small (e.g., 5 cm) compared to the distance between sectors. Let $B(r)$ be the field within the gap at a given radius, and let $\Delta\theta$ be the angular width of the magnet sector at this radius; then the average field is given approximately by:

$$B_{av} = \rho(r)B(r), \tag{27}$$

where:

$$\rho = N(\Delta\theta)/(2\pi), \tag{28}$$

and N is the number of sectors. Combining these results then yields:

$$B(r) = (m_0\omega_0/e)\{\gamma(r)/\rho(r)\}. \tag{29}$$

In order to avoid saturation effects, $B(r)$ should be less than about 18 kG; assuming such a restriction, then a lower limit is placed on ρ for a given f_0 and final energy. For example, with $f_0 = 8$ MHz and $B < 18$ kG, the following restriction is obtained:

$$\rho(r) > 0.29\gamma(r). \tag{30}$$

Furthermore, if $B(r) = 18$ kG at all radii, then ρ would increase from 0.30 to 0.36 over a 10–200 MeV energy range, and from 0.36 to 0.62 for a 200–1000 MeV energy range.

As in present SOC designs, the cyclotron acceleration

cavities would operate at the same rf frequency as the linac injector, and variation of the final proton energy would be accomplished through two mechanisms. First, there would be a provision for extracting the beam on successive turns; and second, there would be a provision for changing the orbital frequency to different subharmonics of the rf frequency. Thus, the magnets should have sets of trim coils capable of precisely adjusting the field to match the spectrum of orbital frequencies covering the range of final energy variation desired.

The value of ν_r will be approximately equal to γ (provided $N > 2\gamma$) and will therefore vary from 1.01 to 2.06 as E varies from 10 to 1000 MeV. Clearly, the number of turns is so small ($\lesssim 100$) and the ν_r change so rapid in this type of machine that all nonlinear resonances can safely be ignored. Indeed, even the linear resonances may be insignificant provided a modicum of precaution is taken; however, a more detailed investigation would be required to establish this point. If the rf acceleration process produces a significant perturbation of the orbits near the $\nu_r = 1$ or $\nu_r = 2$ resonance, then the magnet plus cavity structure should possess 180° or 120° minimum symmetry in order to avoid this perturbation; however, if these perturbations are insignificant, then no special symmetry would be required.

The axial focusing frequency ν_z can be expressed as follows:

$$\nu_z^2 = -(\beta\gamma)^2 + F + S, \tag{31}$$

where F represents the edge (Thomas) focusing, and S represents the spiral focusing[1] (which is roughly proportional to F). For the narrow gap magnets considered here, F is given approximately by:

$$F = \rho^{-1} - 1; \tag{32}$$

when this is inserted, the above equation for ν_z^2 becomes:

$$\nu_z^2 = -\gamma^2 + \rho^{-1} + S. \tag{33}$$

Assuming that no spiral focusing is required ($S = 0$), the following value of ρ is obtained:

$$\rho = (\nu_z^2 + \gamma^2)^{-1}, \tag{34}$$

so that small ρ values would be required to produce $\nu_z \gtrsim 1$. However, as noted above, a lower limit is imposed on ρ by the condition that the field within the magnet gap does not exceed about 18 kG. As in the previous example above, if $\rho = 0.3\gamma$, then ν_z ranges from 1.53 down to 1.13 over the energy range from 10 to 200 MeV; since these ν_z values are quite good, no spiral focusing would be needed in this case; in addition, since $\rho < 0.36$, at least 60% of the circumference would be available for inserting rf cavities. Since the axial width of the beam varies as $(\gamma\nu_z)^{-\frac{1}{2}}$, a decrease in ν_z with E is not serious provided the decrease is not too large. A 200–1000 MeV STIC would probably operate at a lower orbital frequency (i.e., $f_0 = 4$–6 MHz) so that smaller ρ values could then be tolerated; nevertheless, such a machine would undoubtedly require some spiral focusing. Since nonlinear resonances are ignorable, spiral focusing has no disadvantages in itself; however, a spiraled magnet structure might complicate the design and fabrication of the magnets and rf cavities.

The same conclusions can be drawn regarding axial resonances as were set forth above for radial resonances. On the question of coupling resonances, again only the linear coupling resonances are significant and these resonances (along with the other linear resonances) should be studied in detail in connection with a specific magnet design. For the conditions which obtain in the STIC, one can safely expect resonance problems to be quite manageable.

6. Phase excursions

If the magnetic field is perfectly matched to the rf frequency, then the ideal condition of isochronism obtains and the rf phase ϕ of the protons remains fixed at its initial value throughout the acceleration. Such a condition cannot be perfectly achieved in practice, so that the ions will undergo phase excursions as a result. The phase acceptance ϕ treated in sect. 4 assumes the absence of phase excursions; consequently, if phase excursions do occur, then the actual phase acceptance must be lowered in order to accommodate these excursions. Since it is important to achieve the largest possible phase acceptance in practice, the phase excursions should be restricted to a small fraction of $\Delta\phi$. This restriction could readily be sustained in the STIC since the number of turns is relatively so small. Under these conditions, the absence of phase stability represents only a minor handicap.

Let h be the integral harmonic ratio of the rf frequency to the orbital frequency (i.e., $\omega_{rf} = h\omega_0$); then the phase change per turn is given by:

$$d\phi/d\tau = 2\pi h(\Delta\omega)/\omega, \tag{35}$$

where ω is the actual proton angular velocity, and $\Delta\omega = \omega - \omega_0$. If this is combined with eq. (19) and integrated, the result is:

$$\Delta s(\phi) \doteq 2\pi h \int (\Delta\omega/\omega)(dr/R_1), \tag{36}$$

where the integration extends from R_i to R, and $\Delta s(\phi)$ is the resultant change in the function:

$$s(\phi) = \int v(\phi)\,d\phi \qquad (37)$$

$$= (V_0/E_1)[\sin\phi - \tfrac{1}{3}\lambda\sin 3\phi],$$

and $(V_0)/E_1$ depends only on λ via eq. (17). The frequency error can be translated into a corresponding field error ΔB_{av} at a particular radius through the relation:

$$\Delta\omega/\omega = \Delta B_{av}/(\gamma^2 B_{av}), \qquad (38)$$

and since $\gamma > 1$, a given fractional field error corresponds to a smaller fractional frequency error.

If only small phase excursions are considered, then eq. (36) can be accurately approximated by:

$$\phi(R) - \phi(R_i) = 2\pi h \int (\Delta\omega/\omega)(dr/R_1). \qquad (39)$$

The initial phase $\phi(R_i)$ can be set to the correct value by adjustments in the injection mechanism. Furthermore simply by adjusting the gross magnet excitation, the maximum and minimum values of $\phi(R)$ can be equalized. For example, suppose the resultant $\phi(R)$ is given by:

$$\phi(R) - \phi(R_i) = (\delta\phi)\sin[\tfrac{3}{2}\pi(R-R_i)/(R_f-R_i)], \qquad (40)$$

where $\delta\phi$ is the maximum phase excursion. This $\phi(R)$ variation is about the worst form which could be achieved in practice; it therefore serves very well the purpose of the present argument. Differentiating this equation and eq. (39) above, the following result is obtained:

$$\Delta\omega/\omega = \varepsilon_0 \cos[\tfrac{3}{2}\pi(R-R_i)/(R_f-R_i)], \qquad (41)$$

with,

$$\delta\phi = \tfrac{4}{3}h\tau\varepsilon_0, \qquad (42)$$

where

$$\tau = (R_f - R_i)/R_1.$$

Magnetic fields can now be measured with an error of only a few tenths of a gauss; in addition, B_{av} can be determined with even greater accuracy since it consists of an average over many individual measurements. The main problem then is to design a set of trim coils which will accurately produce the desired variation of field with radius.

If $\delta\phi$ is restricted to $\delta\phi < 2.5°$, then the phase acceptance will be reduced by at most 5° out of about 50°. In this case, eq. (42) yields:

$$h\tau\varepsilon_0 < 0.033. \qquad (43)$$

Assuming average fields of order 10 kG, then it should be possible to achieve values of ε_0 as small as 0.5×10^{-4}, considering the present state of magnet technology. Inserting this ε_0, the following condition results:

$$h\tau < 650. \qquad (44)$$

Thus, if the product of the harmonic ratio h and the number of turns τ satisfies this condition, it should be possible to keep the phase acceptance within 5° of the ideal $\Delta\phi$ values considered in sect. 4. For the 10–200 MeV machine discussed previously, with $f_0 = 8$ MHz, h would be about 6 and τ about 63, in which case $h\tau \cong 378$, which easily satisfies the above condition; for a 200–1000 MeV machine with $f_0 = 6$ MHz, h would be about 8 and τ about 61 so that $h\tau \cong 488$, which again satisfies this condition. For the 500 MeV cyclotron being built at ETH in Zurich, it may be noted[2]) that $h\tau \cong 1800$ (i.e., $h = 6$, $\tau \cong 300$).

7. Space charge effects

The protons in a beam form a space charge distribution and the Coulomb repulsion between the protons acts counter to the magnetic focusing forces so as to reduce the effective focusing frequencies. For machine currents in the 50 mA range, these space charge effects can be very substantial.

Consider a single, isolated turn of the beam, and assume cylindrical symmetry, then the decrease in ν^2 (i.e., either ν_r^2 or ν_z^2) resulting from space charge repulsion is given by:

$$-\delta\nu^2 = \frac{0.6\pi}{938}[(c/\omega_0)^2 I/\{(\beta\gamma^3)AD\}], \qquad (45)$$

where A (cm^2) is the cross sectional area of the beam, (c/ω_0) (m) is the cyclotron length unit, I (A) is the time-average current, and $D = (\Delta\phi)/2\pi$ is the duty factor (i.e., I/D is the instantaneous current). The space charge current limit is that current for which $\delta\nu^2 = \nu^2$; thus, this limit is proportional to:

$$(\beta\gamma^3)(f_0\nu)^2 AD.$$

As a result of the $(\beta\gamma^3)$ factor, space charge limitations decrease rapidly with increasing energy and are therefore most serious at or near injection. Assuming injection at 10 MeV, and assuming the following beam properties:

$$\begin{aligned} I &= 0.065\text{ A};\\ c/\omega_0 &= 5.964\text{ m}\ (f_0 = 8\text{ MHz});\\ A &= 2\text{ cm}^2;\\ D &= \tfrac{1}{8}\ (\text{i.e., } \Delta\phi = 45°); \end{aligned}$$

then the above formula yields:

$$\delta\nu^2 = -0.13. \qquad (46)$$

Hence, if $\nu = 1$ in the absence of space charge, then this $\delta\nu^2$ would yield a net value of $\nu = 0.93$, which is quite tolerable; conversely, for $\nu = 1$, the space charge current limit would be about 500 mA.

The formula (45) given above will be reasonably accurate when the width of a turn is small compared to the distance between adjacent turns. Assuming a uniform radius-gain per turn, then as the turn spacing decreases, $\delta\nu_r^2 \to 0$ since the space charge forces in the radial direction will tend to cancel; under the same conditions, $\delta\nu_z^2$ will tend toward a value twice that given by eq. (45). Nevertheless, the above results indicate that currents in the 50–100 mA range can be successfully injected into the STIC provided a reasonable choice of machine parameters has been made.

The longitudinal space charge effect has been treated by Welton[3]) who showed that these effects can be corrected by a small shift in the phase of the third harmonic voltage relative to the main harmonic voltage.

I am indebted to J. A. Martin and R. E. Worsham for their helpful suggestions and discussions during my sojourn at the Electronuclear Research Division of the Oak Ridge National Laboratory.

References

[1]) J. A. Martin, IEEE Trans. Nucl. Sci. NS-13, no. 4 (1966) 288.
[2]) J. P. Blaser and H. A. Willax, ibid. 194.
[3]) T. A. Welton, Sector-focused cyclotrons, Nucl. Sci. Ser. Report no. 26, NAS-NRC-656 (Wash. D.C., 1959) 192.

NUCLEAR INSTRUMENTS AND METHODS 58 (1968) 327–341; © NORTH-HOLLAND PUBLISHING CO.

THEORETICAL AND EXPERIMENTAL BEAM STUDIES FOR THE MICHIGAN STATE UNIVERSITY CYCLOTRON*

R. E. BERG†, H. G. BLOSSER and M. M. GORDON

Michigan State University, East Lansing, Michigan, U.S.A.

Received 28 July 1967

Numerical orbit studies using Michigan State University cyclotron fields have been performed to determine the validity of use of the separated longitudinal equations of motion under conditions obtained in actual cyclotron operation. These results have been applied in a systematic study of phase measurement procedures using frequency and trim coil detuning. Direct experimental measurements were performed to determine the phase and phase width of the beam, as well as the betatron oscillation frequencies ν_r and ν_z, as a function of radius. From the phase history data the radial dependence of the rf dee voltage has been obtained, and the nominal initial phase φ_0 has been determined to be $+20° \pm 1°$ for the MSU central region geometry. Use of necessary computer calculations with this result gives an rf starting time τ_0 of $-28° \pm 1°$ for maximum beam intensity. Results of experimental measurements are compared with pre-computed orbit behavior where possible.

1. Introduction and summary

The Michigan State University cyclotron is a multiparticle variable-energy machine with a proton energy range from 23 MeV to 56 MeV. Operating parameters for the machine have been thoroughly documented and will be discussed herein only as necessary[1–4]).

This paper presents the results of a series of theoretical and numerical investigations of some useful diagnostic procedures involving detuning of either frequency or magnetic field, which are employed with sectored cyclotrons, followed by comparison of measured beam properties in the MSU cyclotron obtained using these and other procedures with numerical results obtained using orbit programs.

Operating points for the MSU cyclotron are precomputed using a program called SETOP[5]) through a method consisting of three basic steps:

1. Interpolation in measured magnetic field data to obtain complete fields at an arbitrary excitation;
2. Least-squares fitting of the isochronous average field with the concentric circular trim oil fields;
3. Calculation of an operating rf frequency so as to minimize the energy spread of the beam in a single turn at extraction.

Properties of orbits in the resulting MSU cyclotron fields have been investigated using a precise orbit integration program known as CYCLONE[6]); orbit properties obtained from CYCLONE are compared with results from the approximations obtained with the separated longitudinal equations, which have been used in the operating point calculations. The program which integrates the longitudinal equations, called PHINAL[7]) has been incorporated the operating point program SETOP.

CYCLONE utilizes exact median plane equations of motion to track accelerated orbits in the magnetic field specified by the operating point program. Details of the electric field are accounted for in three ways, depending on the level of significance of the electric field:

a. source-to-puller region, in which the electric field is obtained from a large-scale model electrolytic tank including exclusively this region;

b. "rf focusing" region, in which the finite width of the accelerating gaps is obtained by using a more complete electrolytic tank to obtain the electric fields covering approximately the first four turns;

c. the main acceleration region, in which the electric field is approximated by a time-dependent step-function potential.

CYCLONE also includes provisions for both an electrostatic deflector and a magnetic channel, and thus is capable of computing the behavior of orbits in the cyclotron from ion source through the complete extraction system; however, for this work no extraction studies have been performed.

Using CYCLONE in combinations with various other orbit programs, a theoretical investigation has been made of certain procedures used regularly for beam diagnostic work. Particular attention has been devoted to problems involved in use of the Smith-Garrent phase measurement procedure[8]) and modifications thereof.

Several important beam properties were obtained through analysis of experimental measurements:

1. Phase history of the beam as a function of radius.
2. Phase width of the beam as a function of radius.
3. Dee voltage variation with radius.

Also, from the phase history data, a value of the

* Work supported by the National Science Foundation.

† National Science Foundation Cooperative Graduate Fellow; Present address: Department of Physics and Astronomy, University of Maryland, College Park, Maryland.

nominal starting phase was obtained by extrapolation. Comparison of families of CYCLONE orbits with experimentally observed phase history data allowed extraction of the rf starting time for peak beam current. Use of the phase analysis procedure "in reverse" to set the main magnetic field is discussed as it is applied to the MSU cyclotron. In addition a radial differential probe and a multi-fingered axial probe were employed to obtain the radial and axial betatron oscillation frequencies. Results of experimental measurements of 1. phase history; 2. phase width; 3. dee voltage 4. initial phase and rf starting time; 5. radial focusing frequency and 6. axial focusing frequency are presented, in excellent agreement with results obtained from independent orbit calculations.

2. Analysis of diagnostic procedures

Of particular interest is the limitation on the validity of the separate longitudinal equations of motion imposed by actual conditions of cyclotron operation. In many cases it is more convenient to use the longitudinal equations than to resort to more detailed and tedious integration of the exact equations, and the limitations of the approximate theory become significant. Errors in the approximate theory arise primarily from the off-centeredness of the orbits which leads to: 1. coupling effects between the radial and longitudinal motion; and 2. failure of the normal radius vs energy relation, which becomes quite evident when the ions gain negligible energy during a precession cycle. These errors will be shown to be exceedingly small for conditions of normal operations of the MSU cyclotron. Discrepancies between the approximate theory and exact orbit integration arise primarily from coupling effects which are essentially incalculable except through such orbit integrations; these discrepancies lead to limitations in the application of the methods discussed only in special circumstances.

Possible problems in actual practice arise from: 1. encounter of resonances, or, in the case of trim coil adjustment, introduction of additional resonances, which results in large centering errors and violates the assumptions necessary to separate the longitudinal equation of motion by introducing coupling terms and non-uniqueness of the radius-energy function; and 2. in the case of trim coil diagnostics, further deviation is introduced into the radius-energy function due to the average field variation.

The problems outlined here are of special concern to the operating point calculations used at MSU for two primary reaons: 1. the operating point set-up procedure makes use of the device of trim coil detuning to set the main field and 2. in order to set the main field precisely and determine the rf frequency precisely, it is necessary to know the starting phase with substantial precision.

TABLE 1
Comparison of energy and phase vs turn number for central ray particles in a 42 MeV field using: a. separated longitudinal equations of motion (PHINAL) and b. numerical integration of the exact radial equations of motion (CYCLONE).

	PHINAL		CYCLONE		
Turn	E (MeV)	φ (deg)	E (MeV)	φ (deg)	$\Delta F(E)$ (keV)
0	0.000	12.0	0.000	–	–
10	1.991	−5.1	1.962	−5.4	−1.0
20	3.975	−7.8	3.948	−7.8	0.0
30	5.952	−8.9	5.927	−8.8	+0.4
40	7.919	−11.1	7.897	−10.7	+1.8
50	9.871	−13.4	9.852	−13.1	+1.0
60	11.808	−14.6	11.792	−14.2	+1.4
70	13.740	−14.9	13.727	−14.6	+1.0
80	15.669	−15.4	15.658	−14.9	+1.8
90	17.591	−16.2	17.582	−16.0	+0.6
100	19.504	−17.2	19.497	−16.8	+1.4
110	21.406	−18.6	21.399	−18.4	+0.6
120	23.290	−20.3	23.283	−20.0	+1.0
130	25.154	−21.8	25.147	−21.7	+0.2
140	27.001	−22.8	26.993	−22.6	+0.8
150	28.841	−22.9	28.831	−22.9	0.0
160	30.688	−21.7	30.675	−21.6	+0.4
170	32.558	−19.2	32.542	−19.3	−0.4
180	34.466	−14.9	34.447	−15.0	+0.4
190	36.418	−8.4	36.399	−8.5	−0.4
200	38.411	+2.7	38.392	+2.5	−0.6
210	40.356	+23.0	40.348	+22.8	−0.6

An example indicating the accuracy of the longitudinal equations under ideal circumstances is given in table 1 for a 42 MeV proton field; energy and phase are tabulated as a function of turn number (at 10 turn intervals) for actual integrated orbits obtained from another computer program known as PHINAL by integrating the separated longitudinal equations:

$$\sin\varphi(E) = \sin\varphi_0 + (2\pi/E_1)\times \times \int_0^E \{(\omega/\omega_0)-1\}\,\mathrm{d}E = \sin\varphi_0 + F(E)/E_1, \quad (1)$$

$$\mathrm{d}E/\mathrm{d}N = E_1\cos\varphi, \quad (2)$$

where $\varphi(E)$ is the particle phase with respect to the rf accelerating voltage, ω is the particle frequency, ω_0 is the rf frequency (first harmonic acceleration), E_1 is the maximum energy gain per turn (at $\varphi = 0$) and the $(\omega_0/\omega)-1$ values are obtained from pre-computed equilibrium orbit data. The integrated orbit in this case possessed a radial oscillation amplitude of approxi-

mately one millimeter; this behavior can be readily obtained on the MSU cyclotron by proper adjustment of central region parameters. Also given in table 1 is the quantity $\Delta F(E)$, which is the difference between the $F(E)$ values obtained from the two methods of integration. The small amplitude of $\Delta F(E)$ indicates the quality of the agreement between the two computational methods; the fact that $\Delta F(E)$ oscillates with a period corresponding to the radial precession cycle (roughly 20 turns) indicates that the small errors present result from centering effects, particularly in the central region and at large radii. Errors as small as those in the table 1 are of negligible effect in setting up the cyclotron. This result and the results of other examples verify the validity of the longitudinal equation under ideal conditions, and validate its general use in diagnostic procedures.

2.1. Frequency detuning

The actual cyclotron beam consists of particles with phase distributed about some central ray whose phase is $\varphi_c(r)$. When eqs. (1) and (2) are valid, the width of the beam in $\sin\varphi$ is constant. If the phase of any part of the accelerating beam reaches the limits $\pm 90°$ ($\sin\varphi = \pm 1$), it is lost, decelerating inward to machine center. In particular, when the central ray of a beam just reaches the 90° limit at a given radius, this can be observed using an integrating beam probe as a reduction of the beam to half amplitude at that radius.

Use of frequency variation as a tool in determination of beam phase history was first proposed by Garren and Smith. Writing the longitudinal equation and introducing a new rf frequency ω', the following relation is obtained:

$$\sin\varphi'(E) = \sin\varphi(E) + 2\pi\{(\omega'-\omega_0)[E+F(E)]/(\omega_0 E_1)\}, \tag{3}$$

where $\varphi'(E)$ is the phase obtained with the new rf frequency and $\varphi(E)$ is the undisplaced phase with the operating freqnecy ω_0. If frequencies ω_+ and ω_- are defined, which drive the phase to $\sin\varphi = +1$ and -1 respectively, one can obtain the relation:

$$\sin\varphi(R) = \{2\omega_0 - \omega_+(R) - \omega_-(R)\}/\{\omega_+(R) - \omega_-(R)\}, \tag{4}$$

where R can be chosen to be the radius at the probe azimuth. Thus, at a given radius, determination of the frequencies which drive the central ray out of phase with the rf accelerating voltage (or equivalently, which reduce the beam to half intensity) allow calculation of the phase of the undisplaced central ray at that radius.

Table 2
Energy vs radius as a function of rf frequency in the 42 MeV field; such data establish the uniqueness of the radius as a function of energy within limits of experimental measurement, and validate the method of frequency detuning described.

rf freq. (Mc)	19.06	19.07	19.09	19.11	19.12
E (MeV)	R''	R''	R''	R''	R''
10	13.560	13.561	13.529	13.508	13.524
15	16.458	16.464	16.461	16.457	16.456
20	–	18.912	18.876	18.838	18.861
15	–	21.033	21.040	21.028	–
30	–	–	23.024	–	–

Ideally, determination of the phase in this manner depends only upon the condition that all quantities (such as starting phase, dee voltage and field) are constant in time. However, several limitations appear

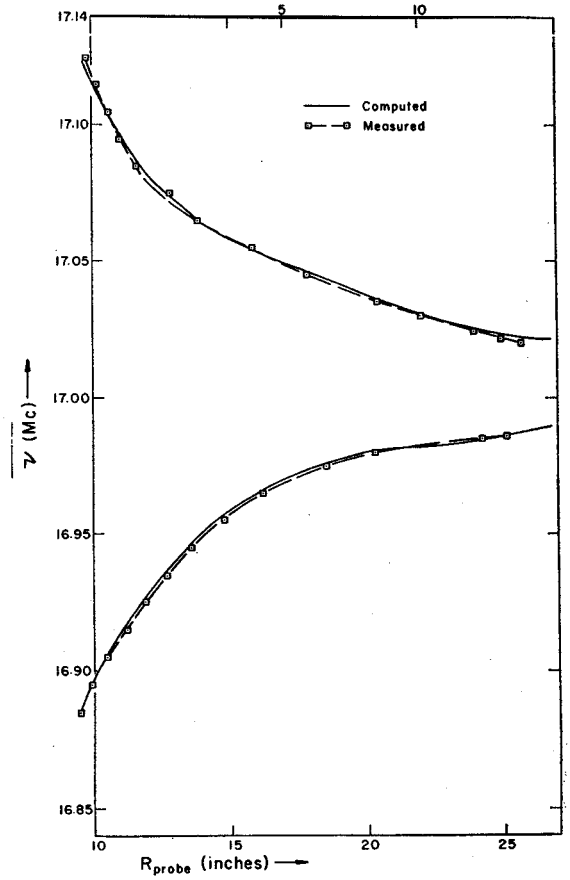

Fig. 1. Computed and measured envelopes of frequency vs radius required to reduce beam intensity to half maximum for the 25 MeV proton field.

in practice. First, centering of the beam places stringent limits on the accuracy of the method. For a beam with 6 mm radial oscillation amplitude, the phase at which the central ray reaches its maximum radius at the angle of the probe can be as small as 65°. Reduction of the radial oscillation amplitude to below 1 mm raises the phase at which the orbit reaches its maximum radius to above 85°.

One assumption used in obtaining eq. (4) is that the radius is a function of energy alone and not of turn number frequency; this assumption has been verified by calculations summarized in table 2 for the 42 MeV proton field from results of a family of CYCLONE orbits. The effect of the small radial oscillation can be seen directly in the variation of radius at a particular energy, and the necessity of minimizing this effect becomes apparent. The conditions shown here are essentially identical to those obtained in the operation of the MSU cyclotron. It should be noted that the oscillation is introduced through the starting conditions and is not amplified by detuning of the system. It should also be noted that, due to the gap crossing resonance[9]), it is not possible to center the beam at all radii simultaneously; therefore, starting conditions have been used which center the beam at large radii where the turn density is greatest.

Another limitation in applying the frequency detuning method at large radii arises from the particular shape of the sin φ vs radius curve and its effect on the minimum frequency ω_- as a function of radius. Fig. 1 shows the envelope of maximum and minimum frequencies as a function of radius for a 33.5 MeV proton field. Because the phase curve rises rapidly at large radii, the frequency required to drive the phase of the central ray to $-90°$ is a constant for all radii greater than a certain value characteristic of the particular phase curve. This feature renders the phase measuring procedure invalid at large radii. Such behavior is observed in all fields of the MSU cyclotron to varying degrees, and care must thus be exercised in applying the method at large radii.

Also shown on fig. 1 are the results of experimental measurements of this envelope of frequency cutoffs. Such an experimental determination of the frequency cutoff envelope was obtained for several fields and the data used to compute experimental phase curves, which are discussed in section 3.1.

A more complete comparison of phase vs energy between use of the longitudinal equation (with phase slip per turn data from equilibrium orbit calculations) and use of actual orbit integration is shown in fig. 2, for a family of rf frequencies. The extremely good agreement reflects the accuracy of the approximations under the conditions obtained in the MSU cyclotron. The larger deviation apparent in the 19.082000 mc run is probably the result of a coupling term proportional to (x/R) which enters the longitudinal equation where x is the displacement from the equilibrium orbit radius

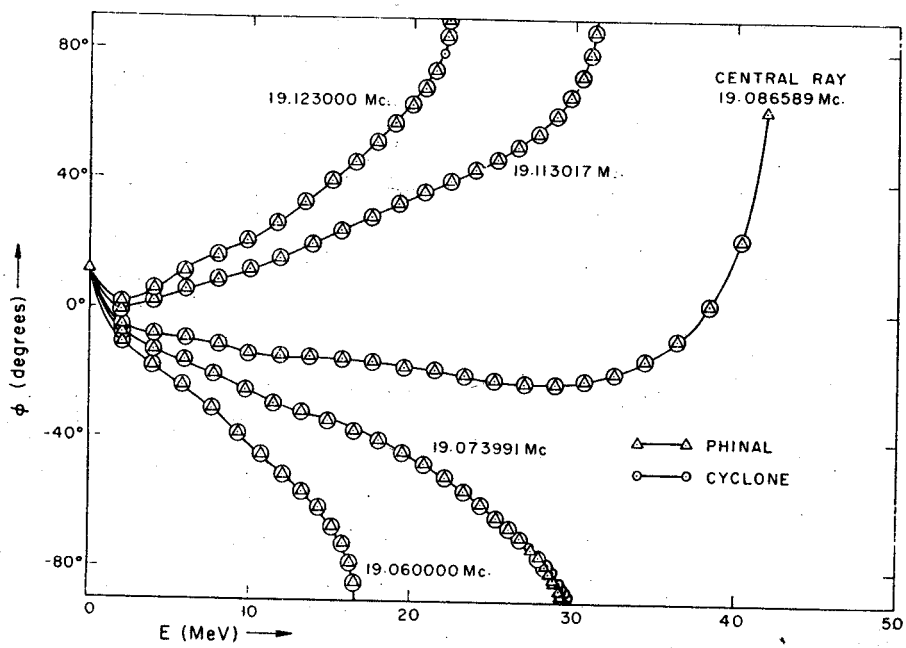

Fig. 2. Comparison of φ vs E as a function of frequency for the 42 MeV proton field using: 1. the separated longitudinal equations (PHINAL) and 2. exact integration of the median plane equations of motion (CYCLONE).

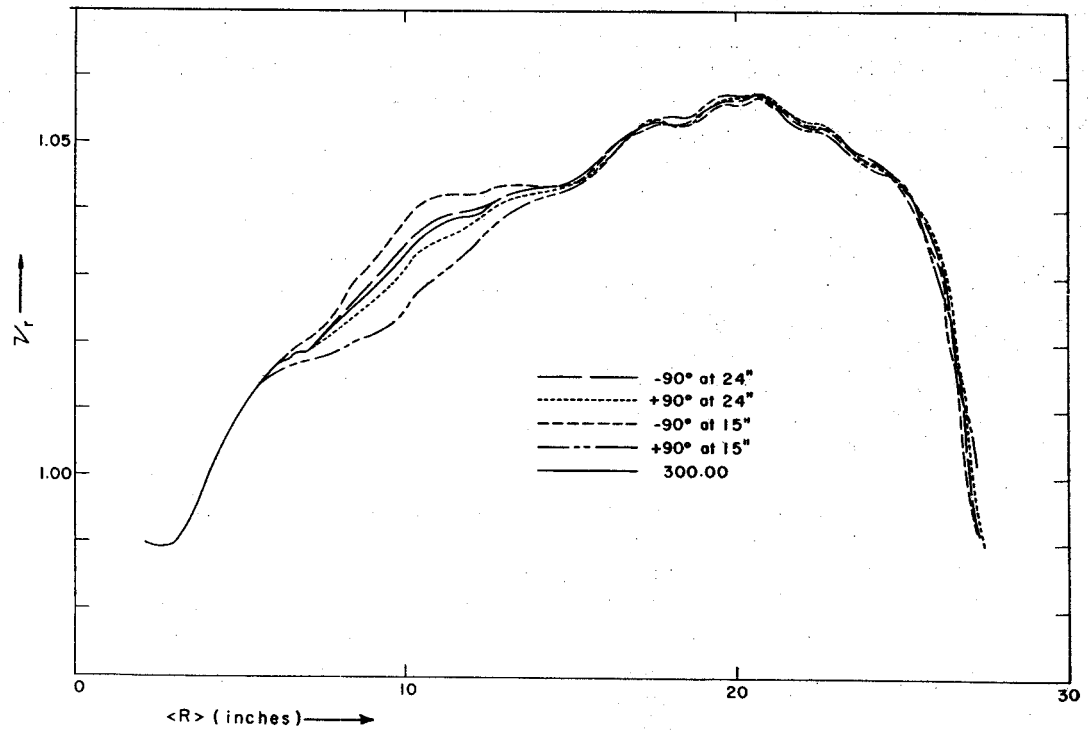

Fig. 3. Computed ν_r vs radius for the 42 MeV proton field obtained when trim coils are detuned to drive the beam intensity to half maximum (central ray phase to $\pm$ 90°) at the indicated radii.

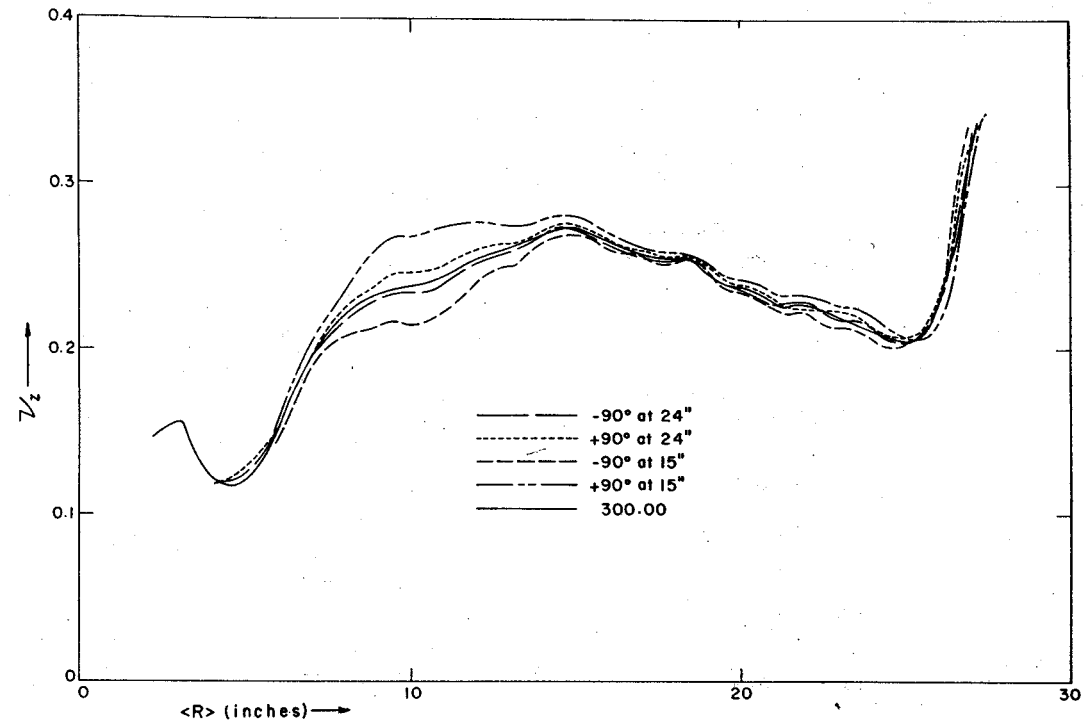

Fig. 4. Computed ν_z vs radius for the 42 MeV proton field obtained when trim coils are detuned to drive the beam intensity to half maximum (central ray phase to $\pm$ 90°) at the indicated radii.

TABLE 3
Energy vs radius as a function of trim coil current for the 42 MeV field; such data establish the uniqueness of the radius as a function of energy within limits of experimental measurement, and validate the method of trim coil detuning described.

	$\Delta I_{TC8} = -33.80$A	$\Delta I_{TC8} = -22.49$A	$\Delta I_{TC8} = 0$	$\Delta I_{TC8} = +13.63$A	$\Delta I_{TC8} = +15.24$A
E (MeV)	$\varphi \to +90°$ at 24″ R″	$\varphi \to +90°$ at 27″ R″	central ray R″	$\varphi \to -90°$ at 27″ R″	$\varphi \to -90°$ at 24″ R″
10	13.521	13.520	13.523	13.518	13.519
15	16.480	16.474	16.463	16.464	16.455
20	18.883	18.911	18.876	18.882	18.891
25	21.041	21.051	21.046	21.042	21.016
30	–	23.032	23.026	–	–

R; such terms become especially significant in the region where the phase curve approaches $-90°$ very slowly and a large number of turns results.

One feature obtained from the longitudinal equation is linearity of sin φ vs ω at a given radius. Eq. (3) can be written in the standard slope-intercept form as:

$$\sin\varphi(\omega) = A\omega + B, \tag{5}$$

where A and B are functions only of the magnetic field, dee voltage, and initial phase. This has been checked by examination of computed accelerated orbits and linearity has been established to well within the accuracy of the experimental measurements.

2.2. Field detuning

A less frequently used method for phase diagnosis employs detuning of the magnetic field by using trim coils. This method involves several additional approximations; however, careful analysis has shown the method to be essentially identical in accuracy to the frequency detuning method. In addition, trim coil detuning possesses several operational advantages for the MSU cyclotron.

Assuming that the particle orbital angular velocity to the average field by the equation:

$$\omega(R) = q\langle B(R)\rangle / m(R), \tag{6}$$

where $\langle B(R)\rangle$ is the average Fourier field component at the average radius R, and converting to a radial integral using the approximate relation:

$$E = p^2/(2m) = q^2\langle B(R)\rangle^2 R^2/(2m), \tag{7}$$

eq. (1) becomes:

$$\sin\varphi(R) = \sin\varphi_0 + (2\pi q\omega_0/E_1)\times \times \int_0^R [B_0(R) - \langle B(R)\rangle] R\,\mathrm{d}R, \tag{8}$$

where $B_0(R)$ is the isochronous average field. The derivation given above is not rigorous; however, the result is valid for small (first order) field deviations – relativistic effects actually cancel out and flutter effects can be minimized by taking R as the mean radius of the equilibrium orbit.

If the equation is written twice, where in one of these the field of a trimcoil is introduced specifically, a relation analogous to eq. (3) for the case of trim coil detuning can be obtained:

$$\sin\varphi'(R) = \sin\varphi(R) - (2\pi q\omega_0/E_1)\int_0^R (\Delta B)_{TC} R\,\mathrm{d}R, \tag{9}$$

where $\varphi'(R)$ is the phase resulting from the introduction of a change in the trim coil field $(\Delta B)_{TC}$. If a change in trim coil current ΔI reduces the beam to half amplitude knowledge of the field per unit current in the trim coil (assumed linear) allows calculation of the original beam phase as a function of radius:

$$\sin\varphi(R) = \{\Delta I_-(R) - \Delta I_+(R)\}/\{\Delta I_-(R) + \Delta I_+(R)\}, \tag{10}$$

where ΔI_+ and ΔI_- are the changes in the trim coil currents required to displace the phase of the central ray to $\pm 90°$ respectively, at the average radius R. An additional complexity enters in actual practice; in order not to disturb the path of the first turn through the central region radial slit, it is necessary to use two trim coils – a larger coil to produce the desired phase excursion to the $\pm 90°$ limits, and a second smaller coil to cancel the field perturbation at the position of the central slit. Eq. (9) then contains the difference between two trim coil field functions in the integral. However, since the trim coil fields are assumed to be linear with respect to current, the ratio of the currents in the trim coils required to produce zero net field at the position of the slit remains constant and eq. (10) remains valid, where I_+ and I_- refer to the currents in the outer trim coil.

Because it is necessary to use two coils in combination to maintain the field at a constant value at the slit

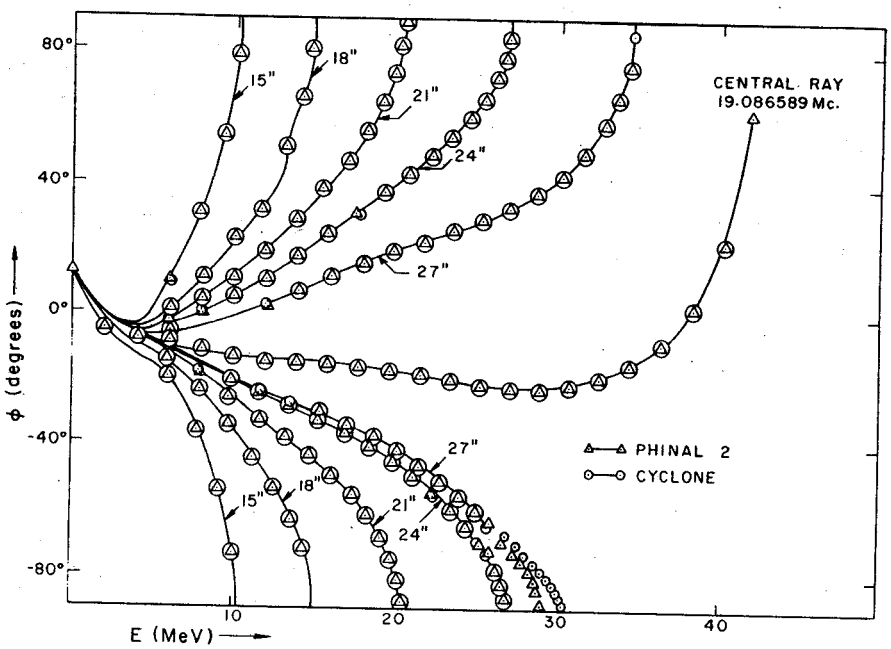

Fig. 5. Comparison of φ vs E as a function of trim coil detuning for the 42 MeV proton field using: 1. exact integration of the median plane equations of motion (CYCLONE), and 2. integration of the longitudinal equations (PHINAL) where the phase slip per turn is obtained from equilibrium orbit data. The radii at which the beam intensity falls to half maximum are indicated.

position, the possibility of introducing additional resonances must be considered. The resulting error field possesses large gradients in the edge region of the inner coil; this could lengthen the radial extent of the $\nu_r = 1$ resonance and thereby introduce large radial oscillations into an otherwise stable beam, or if the gradient is large, a region of axial instability could result.

The importance of such phenomena was investigated by calculating equilibrium orbits in various detuned fields using trim coil currents computed to drive the beam to the $\pm 90°$ phase limits at various radii. Fig. 3 shows the radial focusing frequency ν_r as a function of average radius for a widely varied set of such detuned magnetic fields, including the computed ideal field; fig. 4 shows the axial focusing frequency ν_z as a function of radius for the same fields. (The field used here is that for 42 MeV protons.) The general absence of unstable conditions indicates that resonance errors a.e unlikely.

Another source of error can arise if magnetic field changes lead to variation of energy with radius. The equilibrium orbit data show only small variations in radius versus energy for field displacements which drive the beam off resonance at about half of the extraction radius. In addition, centering errors described previously can create inaccuracies in resulting measurements. These problems were investigated by computation of accelerated orbits in CYCLONE; a table of radius versus energy for several detuned fields is given in

TABLE 4

Comparison of central ray maximum radius and corresponding phase obtained by CYCLONE using trim coils detuned to drive the phase of the central ray to $\pm 90°$ at the indicated radii. The pre-computed trim coil currents were obtained from SETOP using simple approximations as described in the text.

Pre-computed	$\varphi \to +90°$ ray			$\varphi \to -90°$ ray		
Maximum radius (inch)	$R''(\varphi = +90°)$	R''_{max}	$\varphi(R''_{max})$ (deg)	$R''(\varphi = -90°)$	R''_{max}	$\varphi(R''_{max})$ (deg)
15.00	14.964	14.976	93.1	14.950	14.965	−87.8
18.00	18.002	18.037	85.4	17.998	18.005	−89.0
21.00	21.047	21.061	91.7	20.950	20.985	−93.0
24.00	24.004	24.058	86.0	23.905	23.948	−92.7
27.00	27.096	27.097	89.2	–	–	–

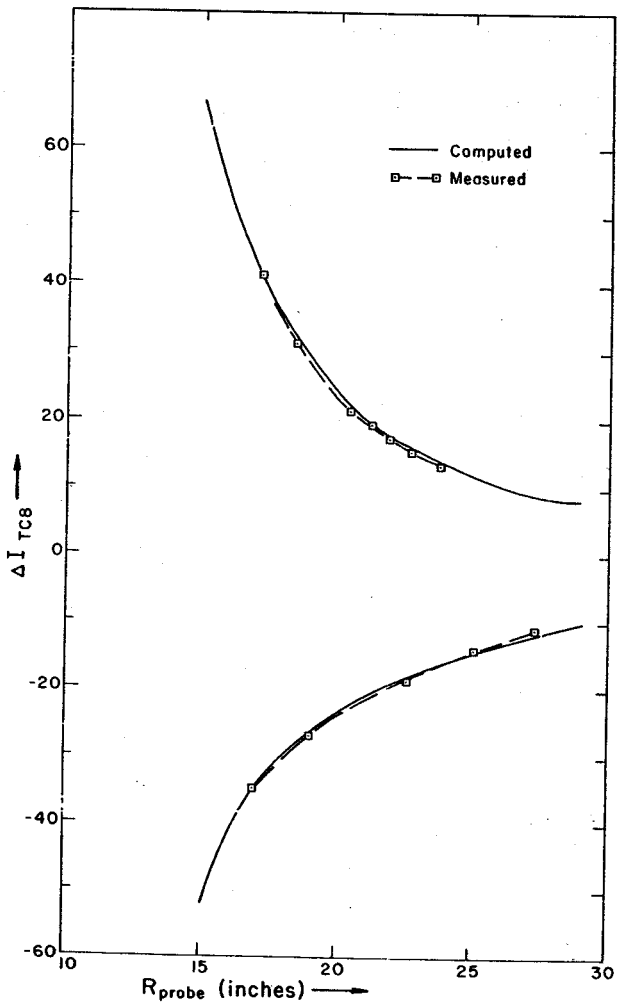

Fig. 6. Computed and measured envelopes of trim coil current versus radius required to reduce beam intensity to half maximum for the 25 MeV proton field.

table 3. Using appropriate starting conditions, the amplitude of the radial oscillation was retained at the minimal value of about one millimeter and no increase of oscillation amplitude was observed with variation of trim coil current. The uniformity of the radius versus energy function indicates that no significant errors result from the use of the method of trim coil detuning.

A result of the theory, analogous to the case of frequency adjustment, is linearity of sin φ with trim coil current. Examination of computed acclerated orbits verified this assumption to essentially the same degree as in the case of frequency variation. The linearity of sin φ with current depends only on the assumption of a first-order change in field and is independent of the other assumptions made in deriving eq. (10) since the field changes required to shift the phase to $\pm 90°$ are quite small, it is not surprising that this linear relation is accurate.

As in the case of frequency detuning, it was found to be impossible to use the trim coil adjustment method at large radii due to the rapid rise in phase at the outer radii.

Results of comparison of actual integrated orbits with data obtained from integration of the longitudinal equations are presented in fig. 5 for the 42 MeV field discussed before. The good agreement between the two procedures again verifies the adequacy of the longitudinal equation; as in the case of frequency variation shown in fig. 2, discrepancy results in the region where the phase approaches $-90°$ slowly and coupling effects become significant. Furthermore, agreement between maximum radius obtained for given trim coil displacements precomputed using eq. (9) and that obtained by orbit integration verifies the accuracy of the assumptions involved in the derivation of these relations; these data are summarized in table 4.

Further evidence of the overall accuracy of the trim coil detuning procedure lies in its use to set the main field; by adjusting the main field such that precomputed

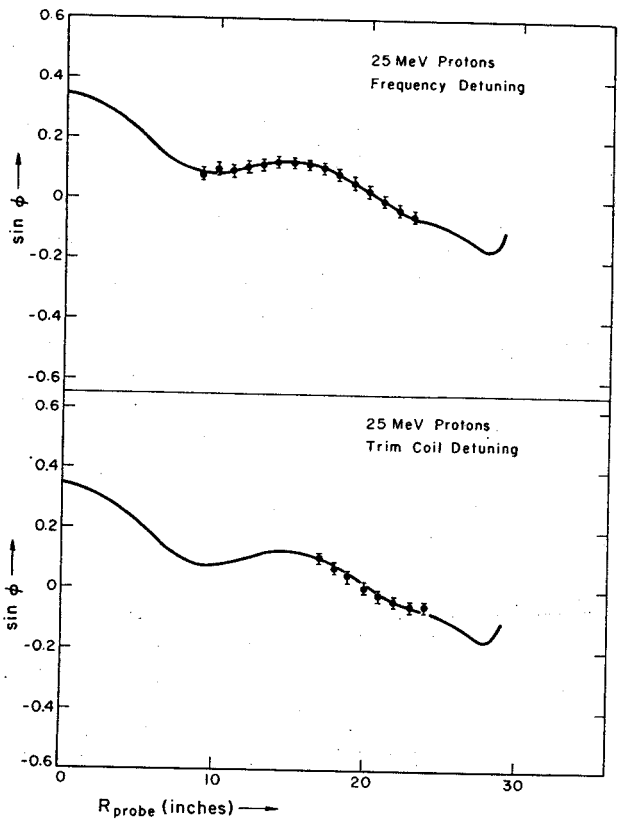

Fig. 7. Computed and measured curves of sin φ vs radius for 25 MeV proton field using both trim coil and frequency detuning.

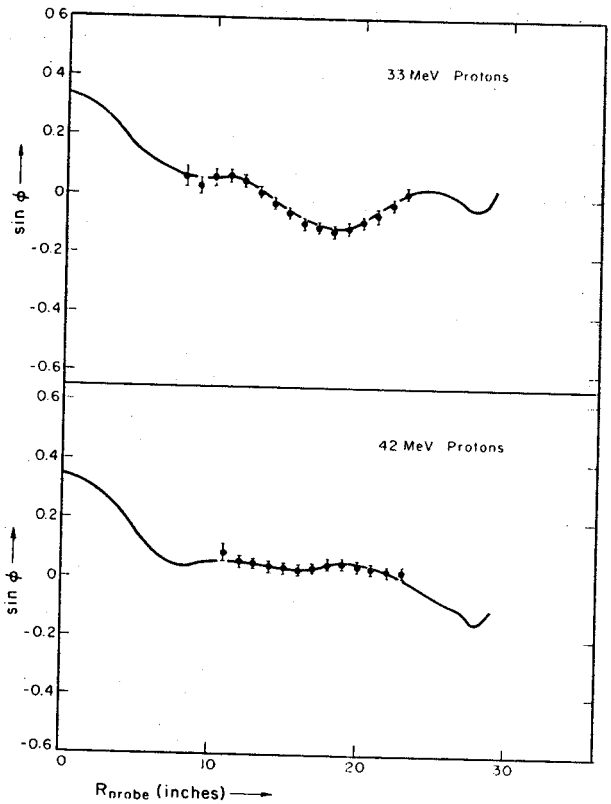

Fig. 8. Computed and measured curves of sin φ vs radius for 33 and 42 MeV proton fields using frequency detuning.

trim coil currents drive the beam to half amplitude at a fixed radius, the main field excitation can be resolved to within a few parts in 100000. If the beam is well-centered and the starting phase is accurately known, the precomputed phase history behavior is obtained to within ± 0.025 in sin φ for all energies.

Similar to the case of frequency detuning, an envelope of trim coil displacement current necessary to drive the beam to half maximum is computed for each operating point. Such an envelope is plotted in fig. 6 for a 25 MeV proton field, along with the experimentally determined curve. The trim coil displacement current envelope was used to determine the phase curve experimentally.

3. Experimental results

This section presents results of several detailed experimental measurements of beam properties in the MSU cyclotron.

Experimental results are in each case compared to theoretical predictions obtained using the equilibrium orbit program and the longitudinal equations.

3.1. Phase history

Using the trim coil current and frequency limit data shown in fig. 1 and 6, the phase of the central ray particle as a function of radius may be obtained. Such phase curves are shown in fig. 7 and 8 for 25, 33 and 42 MeV proton fields using both frequency and field detuning. Note that in the case of the 25 and 42 MeV fields all field data was obtained by direct measurement; the trim coil fields for 33 MeV protons were obtained by interpolation.

3.2. Initial phase

It is possible to extrapolate back to zero energy by comparison of the computed and measured curves to obtain the nominal starting phase φ_0. For a given source-to-puller geometry and source location, there is an rf "starting time" τ_0 at which the particles leave the ion source, corresponding to the nominal starting phase φ_0 used in the longitudinal equations of motion. Since this starting time is an essentially incalculable quantity it has been necessary to assume a reasonable value in order to perform detailed calculations of behavior of orbits in the central region[10]). Understanding of such behavior and knowledge of the central starting phase is

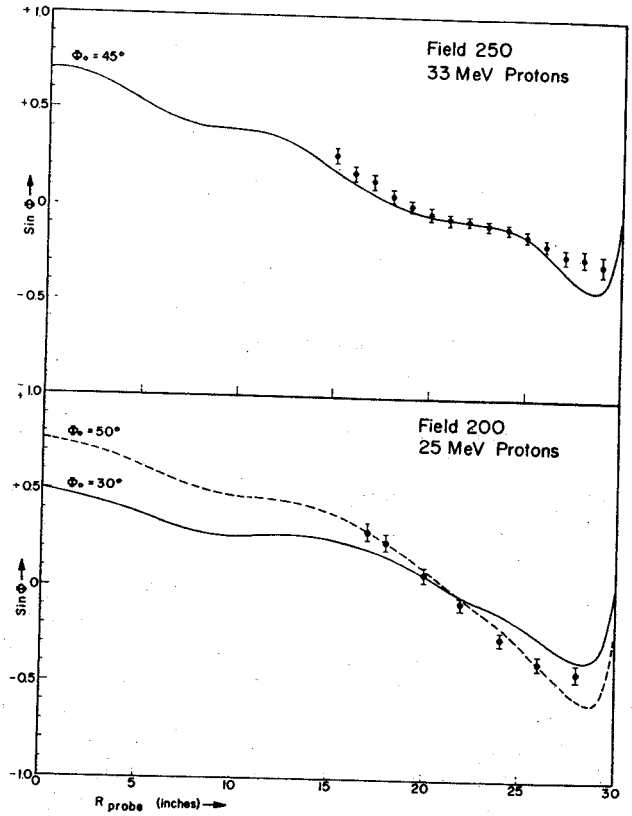

Fig. 9. Illustration of procedure for determination of central ray initial phase for two proton fields. Extrapolation of difference between computed curves and measured data inside 25" allows precise determination of initial phase.

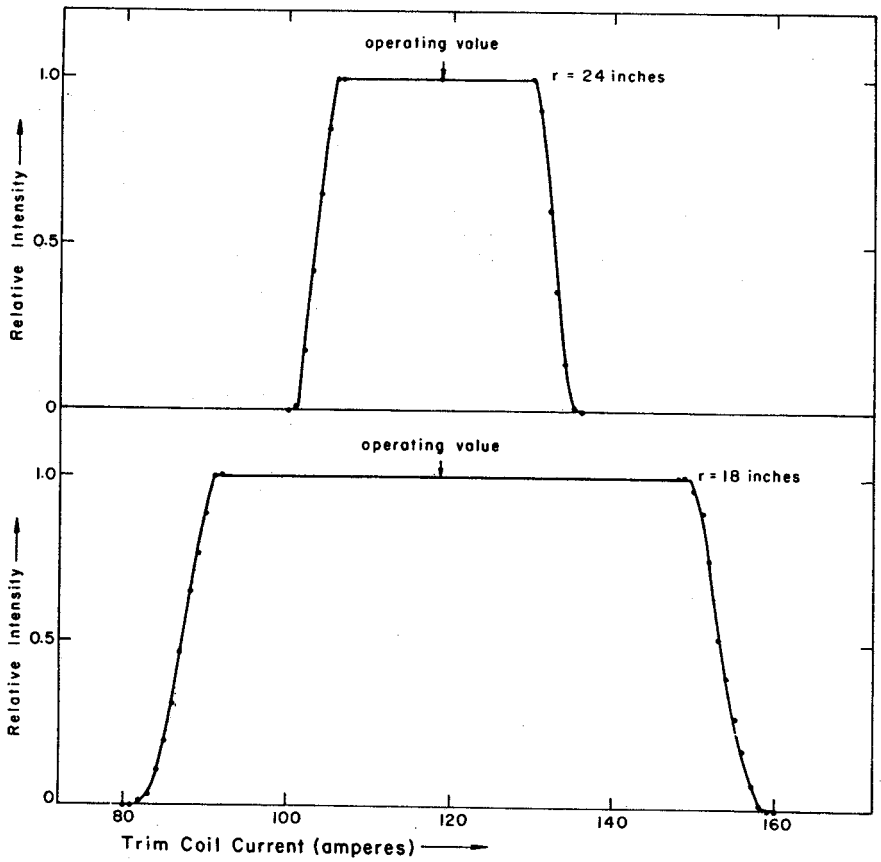

Fig. 10. Beam intensity vs trim coil current at two radii for the 25 MeV proton field; phase widths as well as central ray phase are obtained from this data.

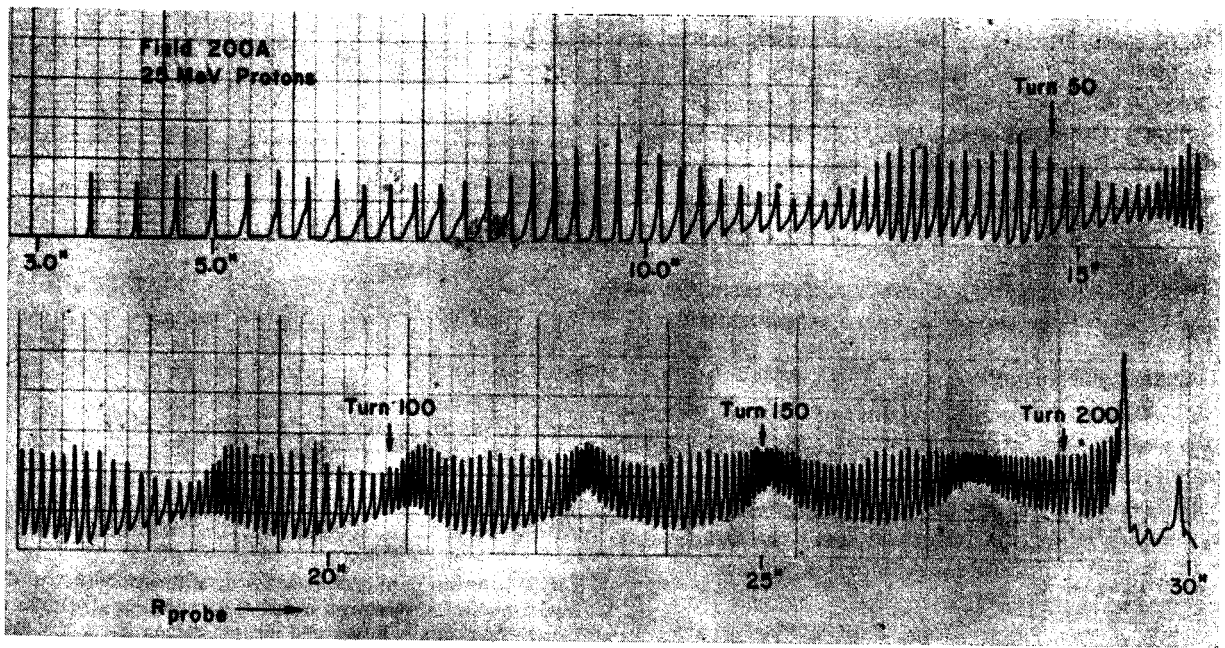

Fig. 11. Radial differential probe pattern for 25 MeV protons.

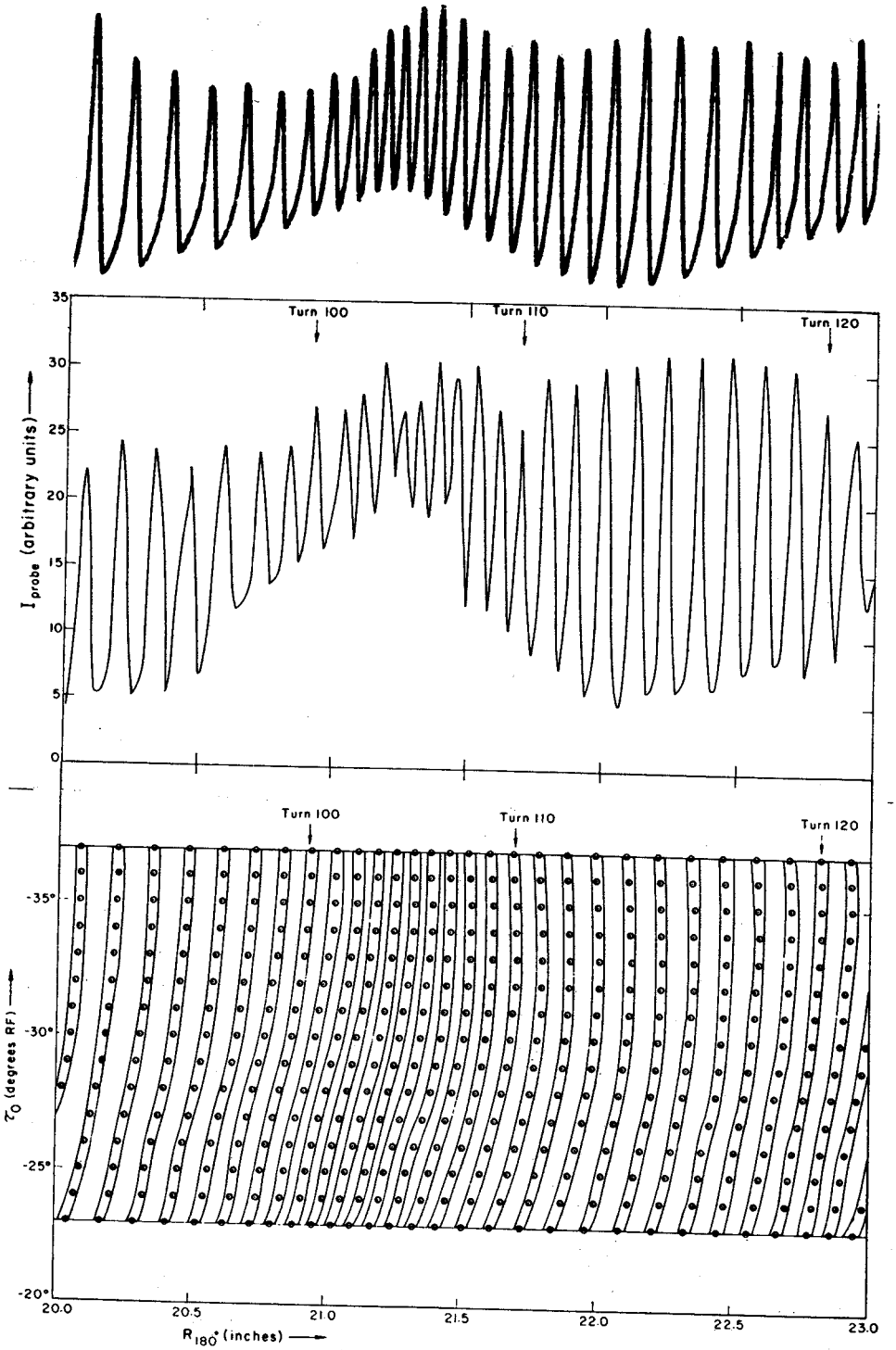

Fig. 12. Comparison of "computed" and experimental radial probe patterns for 25 MeV proton field near turn 100: a. radius vs starting phase of successive turns for particles accelerated in CYCLONE, assuming constant radial width and density as a function of starting phase to obtain "beam"; b. density of particles in (a) as a function of radius for a radial width equal to the differential probe sensitive area; c. corresponding turns in experimental turn structure pattern (fig. 11).

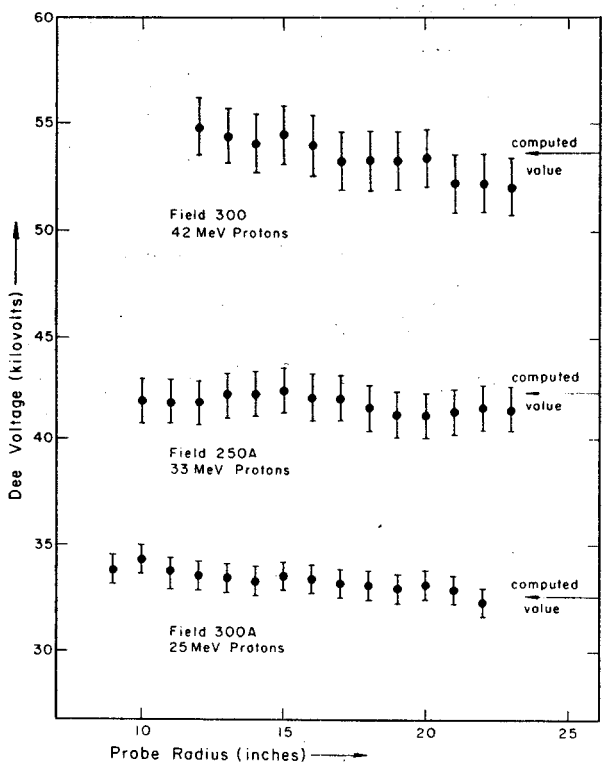

Fig. 13. Experimentally determined dee voltage as a function of radius for 25, 33 and 42 MeV proton fields. Computed values are indicated by arrows on right.

basic to the procedure of the phase selection using slits.

It is desirable therefore to determine τ_0 as accurately as possible, since small starting time errors can introduce substantial deviations into the energy-phase history curve, especially near fixed points where the $\sin\varphi$ approaches -1 asymptotically, as in the examples of figs. 2 and 5.

Fig. 9 illustrates the procedure for determination of starting phase for two proton fields. The main field has been adjusted to render the phase correct for outer radii of about 25″. By extrapolating back to zero energy the difference between the various computed curves and the experimental curves can be obtained; the initial phase assumptions are then improved until exact agreement experiment and calculation is reached, as shown in previous results of phase measurements. With such a method, the nominal starting phase was determined to be $+20° \pm 1°$.

Comparison of several computed accelerated orbits from CYCLONE with different rf starting times allowed identification of the orbit which attained the experimentally observed radius and phase history. The corresponding rf starting time is $-28° \pm 1°$ for the MSU central region geometry.

These results are consistent with orbit calculations as well as the results of experimental "foil burns" which accurately trace orbit paths in the central region[3]).

It should be noted that the phase width and the rf starting time of the central ray are independent of beam current for reasonably small beam currents. It should also be noted that the phase width is restricted by the geometry of the electrode structure in the central region.

3.3. Phase width

A useful variation of the phase measuring technique is to obtain the complete intensity vs frequency or trim coil displacement current profile, from which both the phase and the phase width of the accelerating beam as a function of radius can be determined.

Such a profile of beam intensity as a function of trim coil current has been obtained experimentally and is shown in fig. 10 for the 25 MeV proton field at two radii. From these profiles the phase width of the beam is computed to be constant in $\sin\varphi$ and approximately equal to 15° at the nominal central initial phase of $+20°$.

With the aid of CYCLONE, the measured phase widths can be compared to widths inferred from the turn structure patterns obtained with a differential radial probe. Fig. 11 shows a turn structure pattern obtained in the 25 MeV field using a $\frac{1}{32}$″ differential probe. The pattern clearly shows the turn structure out to the extraction region, where the effect of the $\nu_r = 1$ resonance is observed (turn 210). Using CYCLONE, a "beam" of fifteen particles, of one degree starting phase intervals about the central ray of initial rf starting time $\tau_0 = -28°$, equivalent to $\Phi_0 = +20°$, was accelerated and the radius at the azimuth of the probe of each particle was plotted as a function of starting phase over the region from turn 90 to turn 120 in fig. 12a. The "beam" was assumed to be of constant intensity as a function of starting time and each turn was given a radial width of one millimeter, the size of the slit in the ion source chimney. The resulting "turns" are indicated by the gray areas in fig. 12a. From this turn pattern, the densities of particles due to all turns present in radius intervals equal to the probe width were determined and the resulting current density structure is plotted in fig. 12b. Finally, in fig. 12c the section of the experimental turn structure pattern obtained with the differential probe is plotted for the same radius region.

The computed and measured turn structure patterns are similar in every respect: 1. both possess the same radial oscillation amplitude of about 0.120″; 2. the peak-to-valley ratio is essentially identical for all phases

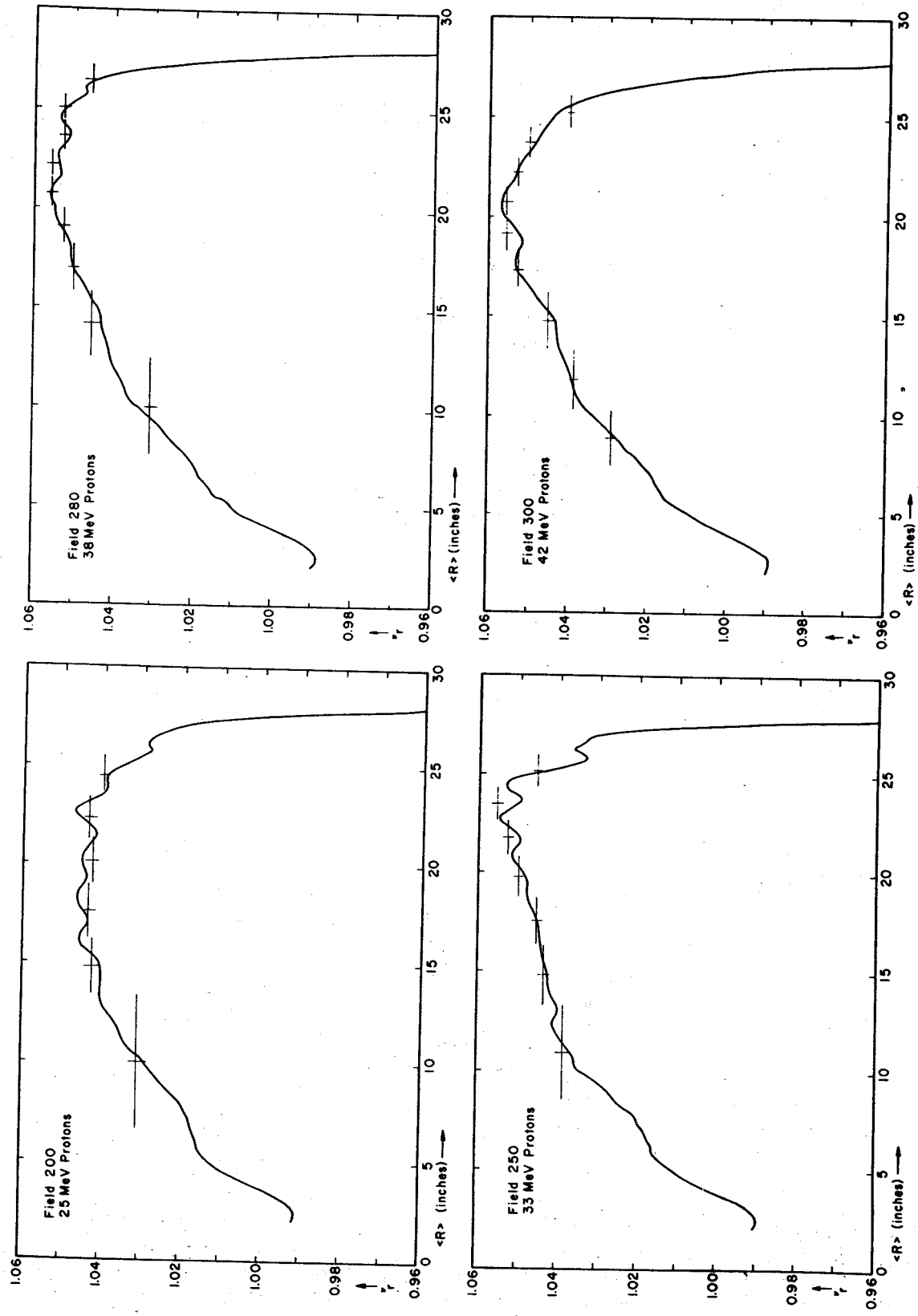

Fig. 14. Computed and measured radial focusing frequency versus average radius for 25, 33, 38 and 42 MeV proton fields. Bars indicate error in average ν_r over radius interval in which the average value was determined.

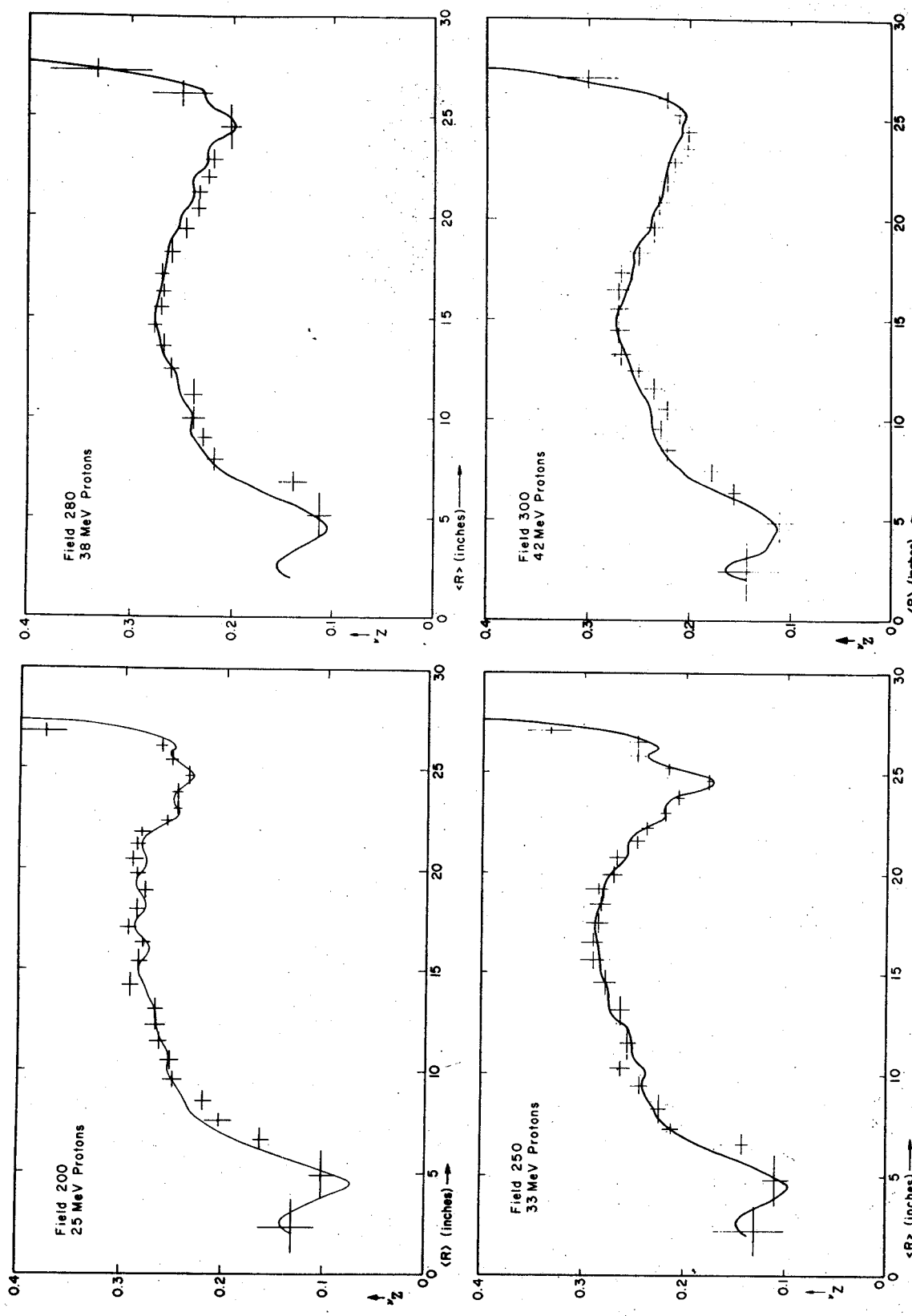

Fig. 15. Computed and measured axial focusing frequency versus average radius for 25, 33, 38 and 42 MeV proton fields. Bars indicate error in average ν_z over radius interval in which the average value was determined.

of the radial oscillation cycle; 3. the characteristic sharp edge of each turn on the high-radius side resulting from the "parabolic" radial contour of individual turns appears in both plots. Use of either: 1. substantially different starting phase widths for the computed beam or: 2. substantially different radial width for each turn, or any combination thereof, destroys the striking similarity between the computed and measured turn structure patterns. The similarity of these two density patterns is taken as further evidence to support the phase width, phase history and starting phase measurements discussed previously.

3.4. Dee voltage

Eq. (3) may be written twice and solved to obtain the maximum energy gain per turn E_1 as a function of radius, in terms of the measured cutoff frequencies ω_+ and ω_-:

$$E_1 = \{\pi(\omega_+ - \omega_-)/\omega_0\}[E + F(E)].$$

The dee voltage is a function of E_1 which depends upon the rf mode and the dee geometry.

The radial dependence of the dee voltage obtained in this manner is given in fig. 13 for the 25 MeV and 42 MeV proton fields. These data are in good agreement with results of calculations in which the dees are composed of short sections of transmission line. It should be noted that E_1 can not be obtained without reference to calculation; the energy E and the quantity $F(E)$ at each radius must be obtained by inspection of equilibrium orbit data.

3.5. Radial focusing frequency

It can be seen from fig. 11 that the turn structure pattern obtained using the differential probe possesses a periodic behavior. The radial focusing frequency is related to the number of turns in one precession cycle: $N_r = 1/(\nu_r - 1)$ where the number of turns per cycle N_r can be readily obtained from such a turn structure pattern.

Fig. 14 shows the computed ν_r vs radius curves for four magnetic fields, along with the experimentally obtained values. The horizontal bars indicate the radial interval over which the turns were counted to obtain an average value of ν_r and the vertical bars indicate the error in the average value of ν_r over that radial interval arising from inaccuracies in the number of turns counted. Note that for the 25 and 42 MeV cases both trim coil fields and main magnet fields were measured. For the 33 MeV case the trim coil fields were obtained by interpolation, while the 38 MeV field was obtained entirely by interpolation in the main magnet and trim coil fields.

3.6. Axial focusing frequency

A z-probe with a $\frac{1}{8}$ inch sq. sensitive area, movable vertically over a $\frac{3}{4}''$ range, has been used to obtain data on axial motion. For these measurements a large coherent axial oscillation was induced in the beam by placing a thin slit 0.15″ above the median plane at the position of the first quarter turn. Making successive radial scans with the probe at various z values, an effective nine-finger axial probe was obtained. Analyzing these data, it was possible to follow the coherent axial oscillation out to the edge region of the magnetic field. The number of turns in a complete cycle of axial motion is related to the axial focusing frequency: $\nu_z = 1/N_z$ where N_z is the number of turns per precession cycle for ν_z less than $\frac{1}{2}$.

The results of such measurements are shown in fig. 15 for the same proton fields illustrated in fig. 14. The radial interval over which each average value of ν_z was obtained (generally one to two vertical oscillations) is indicated by the horizontal bars; the vertical error bars arise from inaccuracy in counting the number of turns per cycle of axial motion. Computed values are indicated by the smooth curves. The effect of the central field cone can be easily seen.

No appreciable electric focusing was observed using this method beyond the third turn; the measured ν_z values agree with those obtained using only magnetic field focusing. Experiments using foil burns establish this result to the center. Lack of the expected strong first order electric focusing is attributed to the particular geometry of the MSU cyclotron central region electrodes.

References

1) H. G. Blosser, Magnet design for the MSU 50 MeV cyclotron, Proc. Intern. Conf. Sector-focused cyclotrons and Meson factories (CERN, 1963) CERN 63-19.
2) W. P. Johnson, Radio-frequency system for the MSU cyclotron; ibid.
3) H. G. Blosser, Nucl. Sci. **13** (1966) 1.
4) M. M. Gordon, Nucl. Sci. **13** (1966) 48.
5) R. E. Berg, Michigan State University Cyclotron, Project Report MSUCP-24 (Sept., 1966) Ph. D. thesis.
6) T. I. Arnette, private communication.
7) M. M. Gordon and W. Joho, private communication.
8) A. A. Garren and L. Smith, Diagnosis and correction of beam behavior in an isochronous cyclotron. Proc. ref. 1).
9) M. M. Gordon, Nucl. Instr. and Meth. **18-19** (1962) 268.
10) M. Reiser, Michigan State University Cyclotron Project Report MSUCP-15 (Febr., 1963).

1.E.1:
3.B

Nuclear Physics A104 (1967) 274—282;

CONVERSION ELECTRON MEASUREMENTS OF TRANSITIONS FOLLOWING THE BETA DECAY OF ^{131m}Te

L. M. BEYER † and W. H. KELLY
Department of Physics, Michigan State University, East Lansing, Michigan, USA ††

Received 11 July 1967

Abstract: The MSU six gap orange and $\pi\sqrt{2}$, iron-free beta-ray spectrometers have been used to study the internal conversion electron spectrum of ^{131m}Te. The multipolarities (in parentheses) of the 80.9 (M1), 102.3 (M1), 149.7 (90% M1, 10% E2), 200.7 (E1), 240.6 (E1), 334.5 (M1, E2), 452.7 (M1, E2) and 773.7 (80% E2+20% M1) keV transitions have been determined. The E1 multipolarities of the 200.7 and 240.6 keV transitions and the log *ft* values of the beta decay to the high-energy states suggest negative-parity assignments for the 1797, 1899 and 1980 keV states in ^{131}I. In addition to the data presented, a survey of the low-energy, positive-parity states of the odd-mass iodine isotopes has been performed. The energies of separation of several states have been found to have a strong quadratic dependence on the neutron number.

E | RADIOACTIVITY: ^{131}Te[from ^{130}Te(n, γ)]; measured I_{ce}, K/L. ^{131}I deduced levels, J, π, cc. Enriched target.

1. Introduction

In order to complement the recent gamma-ray coincidence studies [1]) of ^{131m}Te, the conversion electron spectrum of this decay has been investigated. Such measurements are of particular interest for this isotope since the low-energy, more highly converted transitions occur between high-energy states in the decay scheme. Hence, additional information on the higher-energy states may be obtained. During the course of this experiment, Devare, Singru and Devare reported [2]) similar measurements. This study confirms a large part of their work, and the more extensive use of Ge(Li) detectors facilitates more accurate determinations of the internal conversion coefficients.

2. Source preparation

The sources of ^{131m}Te were produced by the irradiation for one week periods of 20 mg samples of tellurium metal (enriched to 99.5% ^{130}Te) in the Oak Ridge Research Reactor. The thermal neutron fluxes were approximately 2×10^{14} n cm^{-2} sec^{-1}. Several sources were used during the course of the experiment. All of the sources were chemically purified to remove the ^{131}I contaminant by distilling the ^{131}I from an aqua

† NDEA Fellow. Now at the Department of Physics, Murray State University, Murray, Kentucky, USA.

†† Work supported in part by the National Science Foundation.

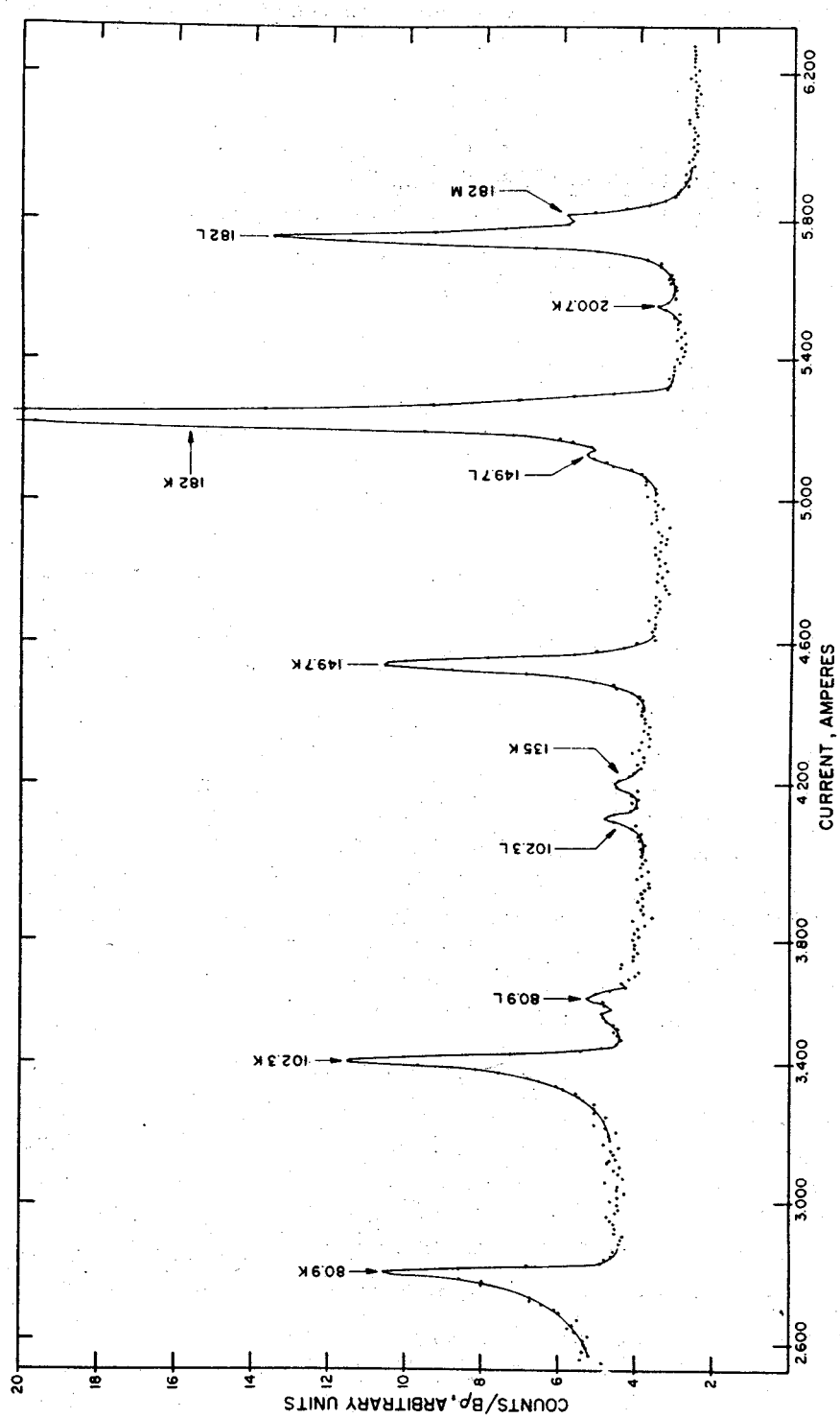

Fig. 1. The ^{131m}Te internal conversion electron spectrum measured from 45 to 240 keV. It was recorded with the orange spectrometer.

regia solution. The tellurium metal was then precipitated from an HCl solution by the addition of SO_2 gas and hydroxylamine hydrochloride. The spectrometer sources were prepared by vacuum sublimation of the precipitate onto a 0.7 mg/cm^2 aluminium backing. Such procedure does not remove the trace amounts of ^{110}Ag present in the source; however, no noticeable interference was produced by this contaminant.

The sources for the orange spectrometer, which is similar to the instrument described by Bisgård [3]), were 2 mm in diam. The sources for the Moussa-Bellicard type $\pi\sqrt{2}$, iron-free double-focussing spectrometer [4]) were 1 mm × 15 mm. The resolutions of both spectrometers were limited by source thickness effects.

3. The internal conversion electron spectrum

The internal conversion electron spectrum covering the energy range of 45-240 keV, recorded with the orange spectrometer, is shown in fig. 1. The K-conversion line

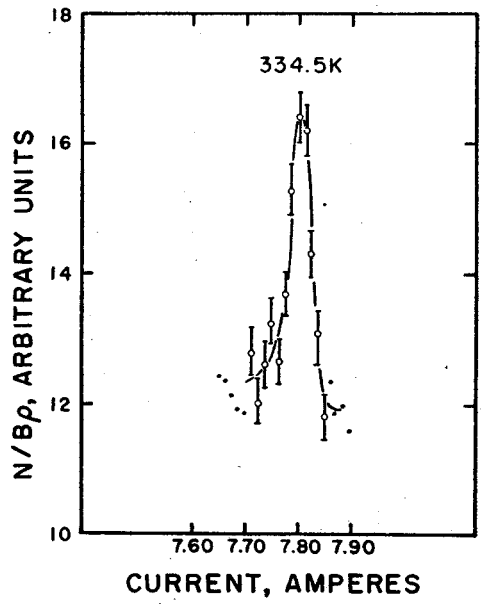

Fig. 2. The K-conversion line of the 334.5 keV transition recorded with the orange spectrometer.

of the 334.5 keV transition recorded with the same instrument is shown in fig. 2. The K- and L-internal conversion lines of the 149.7 keV ground-state transition recorded with the $\pi\sqrt{2}$ spectrometer are shown in fig. 3. Additional lines corresponding to the K-conversion lines of the 452.6 and 773.7 keV transitions have also been observed with both instruments but are not shown here. The relative conversion electron intensities thus obtained, coupled with the relative gamma-ray intensities reported in ref. [1]), can be used to determine the internal conversion coefficients if the coefficient is

known for one of the transitions. The number has been obtained by assuming that a correct value for α_K of the 149.7 keV transition can be derived from the experimental K/L ratio, i.e.

$$\frac{A_1}{A_2} = \frac{(K/L)\alpha_L(E2) - \alpha_K(E2)}{\alpha_K(M1) - (K/L)\alpha_L(M1)},$$

where K/L is measured, the α are from the tables [5]), and A_1 and A_2 are the fractions of M1 and E2 multipole mixtures in the transition. The A_1/A_2 ratio is then used to determine the 149.7 keV α_K.

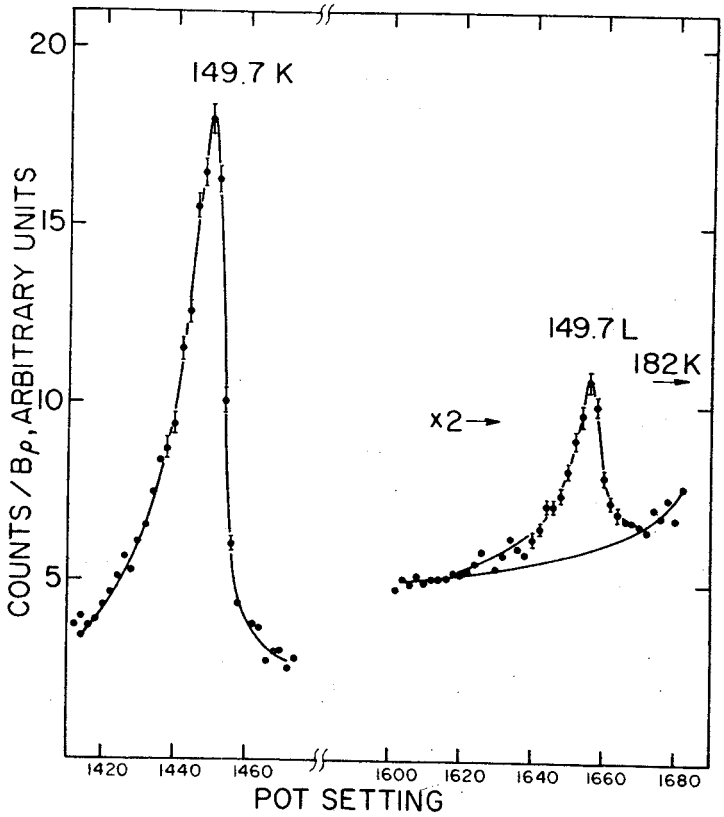

Fig. 3. The K- and L-conversion lines of the 149.7 keV transition in the decay of ^{131m}Te. This was recorded with the iron-free $\pi\sqrt{2}$ spectrometer.

The results of the data analysis are summarized in table 1 with the theoretical values of the conversion coefficients for the various multipolarity possibilities. The data are in agreement with the results of Devare *et al.* [2]). The most important aspect of these data is that they confirm the E1 assignment for the 201 and 241 keV transitions [2]), indicating the presence of negative-parity states in ^{131}I. The results do not indicate

TABLE 1

The results of conversion electron measurements of ^{131m}Te

E_γ (keV)	Electron intensity (K 149.7 ≡ 100)	I_γ (I 149.7 ≡ 100)	α_K [a] (exp) [c]	α_K (theoretical) [b]			K/L (exp)	K/L (theoretical) [b]				Multipole
								Rose		Sliv		
				E1	E2	M1		M1	E2	M1	E2	
80.9	K 103 ±10 L 11 ± 4	17	1.25±0.1(0)	3.2(0)	2.3(0)	1.2(0)	9 ±3	8.4	2.0	7.6	1.8	M1
102.3	K 108 ±10 L 12 ± 4	38	5.8±0.5(−1)	1.7(−1)	1.1(0)	6.2(−1)	9 ±3	8.4	2.8	7.6	2.7	M1
149.7	K 100 L 12.6±0.6	100	2.1±0.1(−1)	5.6(−2)	3.3(−1)	2.1(−1)	7.9±0.4	8.4	4.1	7.6	2.9	M1, 10 % E2
200.7	K 3.8±0.5	28	2.6±0.4(−2)	2.6(−2)	1.2(−1)	9.6(−2)						E1
240.6	K 3.0±1.0	32	1.8±0.6(−3)	1.5(−2)	6.7(−2)	5.8(−2)						E1
334.5	K 4.5±0.5	36	2.6±0.3(−2)	6.6(−3)	2.3(−2)	2.4(−2)						M1, E2
452.7	K 1.4±0.5	21	1.4±0.5(−2)	3.1(−3)	9.7(−3)	1.1(−2)						M1, E2
773.7	K 1.2±0.6	135	1.8±0.9(−3)	9.4(−4)	2.4(−3)	3.1(−3)						E2, 20 % M1

[a]) The numbers in parentheses are the appropriate powers of 10, i.e. 1.25±0.1(0) means (1.25±0.1)×10°.
[b]) Ref. [5]).
[c]) The conversion coefficients are in good agreement with the results of Devare *et al.* [3]).

which of the levels have negative parity. A measurement of the multipolarity of the 822 keV transition, which we were not able to obtain, should suffice to allow the assignment of parities to the levels at 1556, 1596, 1797, 1899 and 1980 keV, when coupled with the information already obtained. However, log *ft* values indicate that the latter three levels are probably the negative-parity states.

4. Discussion of the decay scheme

The decay scheme of ^{131m}Te is shown in fig. 4. The positions of the states, the ordering of the transitions and the log *ft* values are taken from ref. [1]). The new information

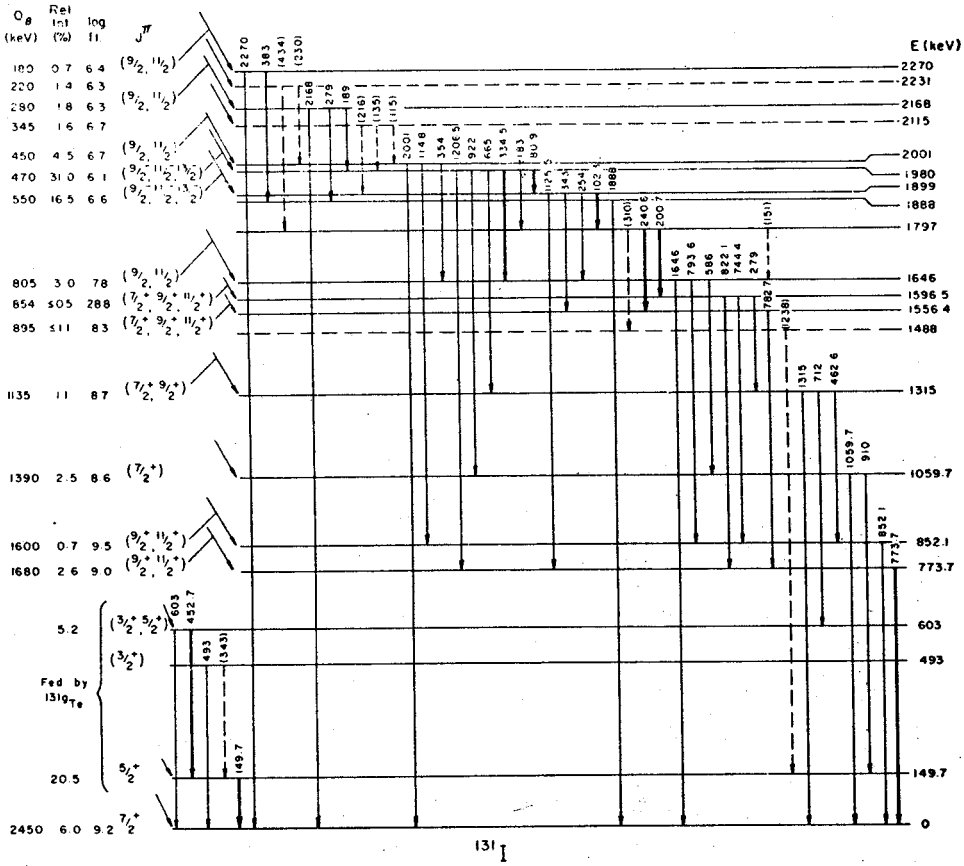

Fig. 4. The proposed energy level scheme of ^{131m}I populated by the decay of 30.5 h ^{131m}Te. The log *ft* of the beta decay to the 1596.5 keV state should be $\geqq 8.8$.

in the decay scheme is that derived from the determination of the multipolarities of the low-energy transitions from internal conversion coefficient measurements.

The M1 characters of the 81 and 102 keV transitions and the E1 characters of the 201 and 241 keV transitions define a parity difference in the higher excited states. The

1556 and 1596 keV levels have one parity, while the 1797, 1899 and 1980 keV levels have the opposite. The relatively low log *ft* values of the β-transitions to the upper two levels, coupled with the high log *ft* values to the 1556 and 1596 keV levels, indicate that the latter probably are the positive parity levels.

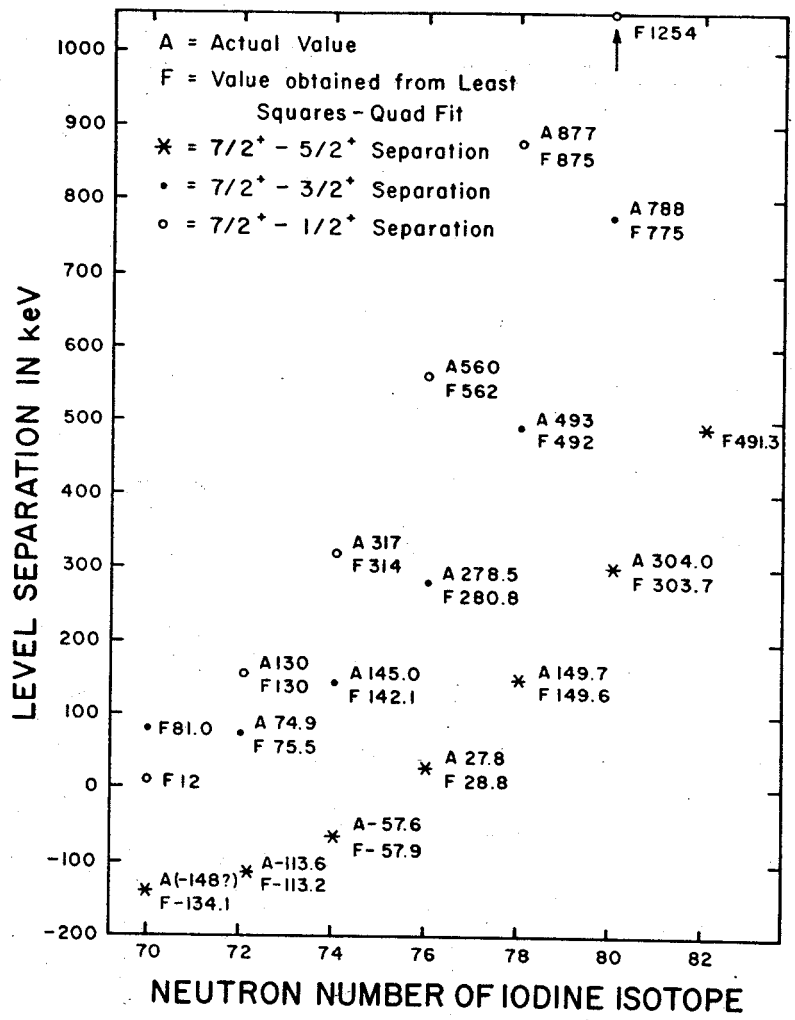

Fig. 5. A comparison of the systematic energies of separation of the low-lying levels of odd-mass iodine isotopes with the values obtained from a least-squares quadratic fit of the data points. All values marked A (except the $\frac{5}{2}$-$\frac{7}{2}$ value for ^{133}I and the $\frac{3}{2}$-$\frac{7}{2}$ value for ^{133}I) have been included in the least-squares fit. The values marked F are those obtained from the fitted equation.

The positive-parity assignments to the 1556 and 1596 keV states are plausible relative to expectations based on a core-coupling model with these energies corresponding approximately to the expected energy of the second phonon excitation. Absence

of crossover transitions and high log *ft* values may be additional indications of this type of state.

The character of the high-energy, negative-parity states is, as yet, unknown. Singru and Devare have measured the *g*-factor of the 1797 keV level with the results possibly suggesting ($g_{\frac{7}{2}}p$, $d_{\frac{3}{2}}n$, $h_{\frac{11}{2}}n$) or ($d_{\frac{3}{2}}p$, $d_{\frac{3}{2}}n$, $h_{\frac{11}{2}}n$) three-quasi-particle configurations [6]). Another possibility is an octupole excitation of the core coupled to a single-quasi-particle state. However, the energies of the states in question are considerably lower than the 2700 keV 3^- state in the neighbouring ^{130}Te doubly even isotope.

5. Systematics of odd-mass iodine isotopes

There are now sufficient data available on the low-energy states of the odd-mass iodine isotopes in the range ^{125}I-^{133}I to allow quantitative study of the systematic energy level trends. In particular, the studies by the Chalk River group [7]) on ^{125}I and ^{127}I and the studies by the M.I.T. and M.S.U. groups [1, 8–11]) of ^{127}I, ^{129}I, ^{131}I and ^{133}I provide accurate energy measurements of the low-lying states of these isotopes.

Perhaps the most interesting phenomenon observed in this study of systematic trends is shown in fig. 5. The energy level separation of the $\frac{1}{2}^+$, $\frac{3}{2}^+$ and $\frac{5}{2}^+$ states with respect to the $\frac{7}{2}^+$ states have been plotted as a function of neutron number for the iodine isotopes. A least-squares quadratic fit has been performed on each curve for the known experimental points. As can be noted from the figure, the fit is exceptional. It should be noted that the 560 keV state in ^{129}I has been included as a $\frac{1}{2}^+$ state. The published spin assignment identifies this state as $\frac{3}{2}^+$ or $\frac{5}{2}^+$ on the basis of a very weak transition to the $\frac{7}{2}^+$ ground state[9]). If $\frac{3}{2}^+$ or $\frac{5}{2}^+$ assignment is the case, it seems plausible that a very weakly excited $\frac{1}{2}^+$ state also exists with comparable energy in ^{129}I because of the accuracy of the least-squares fit for the other spin states. The curves have been extrapolated to both ^{123}I and ^{135}I, with the hope that experimental data will become available to check the range of validity of this quadratic behaviour.

Kisslinger and Sorensen have used a short-range pairing force and a long-range quadrupole force to calculate the low-energy properties of a wide range of nuclei [12]). Their results for some of the states of ^{125}I, ^{127}I, ^{129}I and ^{131}I are in qualitative agreement with the above trends. Hamamoto has made a related study in which she considers the effect of the neutron-proton interaction [13]). Again, the general trends are in qualitative agreement.

The authors wish to thank Mr. W. Johnston and Dr. S. K. Haynes for assistance with the operation of the $\pi\sqrt{2}$ spectrometer and Dr. G. Berzins for assistance with the data analysis and interpretation.

References

1) L. M. Beyer, G. Berzins and W. H. Kelly, Nuclear Physics **A93** (1967) 436
2) S. H. Devare, R. M. Singru and H. G. Devare, Phys. Rev. **140** (1965) B536
3) K. M. Bisgård, Nucl. Instr. **22** (1963) 221

4) A. Moussa and J. B. Bellicard, J. Phys. Rad. **15** (1954) 85;
Q. Baird, J. C. Nall, S. K. Haynes and J. H. Hamilton, Nucl. Instr. **16** (1962) 275;
L. J. Velinski, thesis, Michigan State University (1965) (unpublished)
5) M. E. Rose, Internal conversion coefficients (Interscience Publishers, New York, 1958);
L. A. Sliv and I. M. Band, in α-, β- and γ-ray spectroscopy, ed. by K. Siegbahn (North-Holland Publ. Co., Amsterdam, 1965)
6) R. M. Singru and H. G. Devare, to be published
7) J. S. Geiger and R. L. Graham, Nuclear Physics **89** (1966) 81 and references cited therein
8) R. L. Auble and W. H. Kelly, Nuclear Physics **73** (1965) 25
9) G. Berzins *et al.*, Nuclear Physics **A93** (1967) 456
10) W. B. Walters, C. E. Bemis and G. E. Gordon, Phys. Rev. **140** (1965) B268
11) W. B. Walters, private communication (1966)
12) L. S. Kisslinger and R. A. Sorenson, Revs. Mod. Phys. **35** (1963) 853
13) I. Hamamoto, Nuclear Physics **86** (1966) 208

ARKIV FÖR FYSIK Band 36 nr 63

3.66 11 21 Communicated 14 September 1966 by E. RUDBERG and K. SIEGBAHN

Nuclides far off the stability line · Proc. of the Lysekil Symposium, 1966 · Session X, No. 1

A new kind of radiation analyzer

By T. H. CLOSE, D. V. HIRST, J. V. KANE, C. Y. KAO, J. KATELEY, W. A. SHUNK and M. E. WILLIAMS

ABSTRACT

A computer radiation analyzer system is under construction at the Michigan State University Cyclotron Laboratory. The system is based upon the Scientific Data Systems Sigma 7 Computer which is a real-time time-sharing stored program computer. A general purpose interface will be used to aid in the transfer of information between the computer and the laboratory. This interface, which is itself a computer, has the following properties:

(*a*) It is designed to cover a large class of laboratory problems rather than a few special problems.
(*b*) It is programmable using a removable panel of cables.
(*c*) It is capable of performing many different and unrelated operations in parallel.
(*d*) It is designed to receive signals from and to send signals to a large number of different devices.
(*e*) It is capable of processing both analog and digital pulses and levels.

It is our intention to use this system to record data fom counters, to display information on cathode-ray oscilloscopes, to establish experimental conditions and to control the cyclotron. The design permits us to do all of these things simultaneously. One of the principal uses of this device will be the study of unstable nuclei, using nuclear reactions which emit more than two particles.

Introduction

Recognizing that nuclear physics experimentation often requires mastery of a large number of different kinds of devices, we have attempted to build a radiation analyzer which is capable of servicing or being serviced by a very broad class of devices. In the past radiation analyzers have been built primarily to receive data from radiation detectors and to provide a facility for display and print-out of such information [1]. More recently the introduction of radiation analyzers based upon stored-program computers has led to the use of these machines to process or simulate nuclear detector information [2]. However, when one views all of the operations which are required for the successful completion of almost any physics experiment, it is clear that the above devices are helpful for certain aspects of these experiments, but not for other aspects. If the radiation analyzer instrument could be made in a general fashion rather than a special fashion, it seems reasonable to believe that by using current technology it could handle any aspect of any given experiment, thereby making possible automated physics experimentation. In this paper we will describe

a radiation analyzer which is capable of processing or producing a very large set of electrical signals, a subset of which includes those functions normally associated with radiation analyzers. While it is not yet a completely general purpose instrument, it is at least an order of magnitude more general than any other electrical device.

The instrument which we will describe in this paper is actually not a radiation analyzer *per se*. It is rather a kind of process control instrument. The words "process control" are generally understood in the computer industry to mean the art of measuring and controlling a manufacturing process. This approach to experimental science is perhaps worth some consideration. Many laboratories have particle accelerating machines. These machines manufacture the projectiles needed for experimental investigations. Further, when an experiment is under way the radiations being measured may be thought of as the product of a manufacturing process. The comparison of measured information with theory is a kind of quality control process. When data is being obtained, it may be desirable to adjust the manufacturing apparatus on the basis of the data being measured at the time so as to improve the data.

It is the purpose of this paper to describe an instrument which is based upon the concepts outlined above. The instrument to be described is capable of controlling an accelerator and various pieces of ancillary apparatus in addition to being able to do pulse height analyzer-type measurements. It is the product of an attempt to design a more general research instrument than has existed previously.

There are many arguments which indicate the desirability of a general purpose research instrument as opposed to the special purpose instruments in common use at the present time. Two of these arguments are: (*a*) The cost of construction of a plethora of special-purpose instruments is a serious burden upon most research projects. A general purpose instrument can eliminate the need for these special purpose devices. (*b*) Measurements of physical effects are often structured by the instruments available at the time when the measurement is performed. Often the measuring instrument so limits the experimental accuracy that a unique interpretation of the experimental results is not possible. A general purpose instrument, on the other hand, can allow the researcher to measure those things in which he is interested in a way more appropriate to the interpretation process which will be needed if a logical deduction is to be performed upon the results of the measurement [3].

The design of the radiation analyzer

Digital input–output under program control

The basic means of communication between the Sigma 7 Central Processor Unit (CPU) and the General Purpose Interface are the Read Direct (RD) and Write Direct Instructions (WD). These instructions have the following format [4].

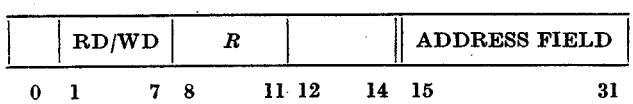

When WD is executed the contents of the register given in the *R* field (bit positions 8 through 11) and the contents of the address field (bit positions 16 through 31) are transmitted to the input/output connectors on the computer. Simultaneously the computer reads the logical status of two input lines on the same connector into

special condition code flip-flops CC3 and CC4. On RD the address field is again transmitted and the condition codes are again read into CC3 and CC4, but in this case, the computer reads the connectors into a register specified by the contents of the *R* field.

The designer's intention in this system is as follows: Information is transmitted (WD) or received (RD) by the register specified by the *R* field. The source (RD) or destination (WD) of the information is determined by the address field bits. A programmable check on external conditions can be had via two instructions, Branch on Condition Set (BCS) or Branch on Conditions Reset (BCR) which can be used to test the status of CC3 and CC4. A non-programmable check on the success or failure of RD or WD is also provided when a special signal Function Strobe Acknowledge (FSA) signal is received. It is the duty of any external device to return an FSA signal if it finds its own address present on the address field lines. This system is employed both to synchronize data transmission through cables of variable length and to provide a diagnostic test for faulty input/output operations, including the non-existence or unavailability of the addressed external device. If the computer executes RD or WD and an FSA signal is not received within a few microseconds a special interrupt will occur to transfer the control of program to an error subroutine. This procedure cannot usually be avoided or modified by a user unless he has complete access to the system monitor program; hence, as described above, this special interrupt procedure is considered to be non-programmable. Users do not normally have such access because the Sigma 7 Computer can operate in two modes—Master and Slave. The former mode is reserved for the Monitor program and certain subroutines and has access to all machine instructions. In the Slave mode most instructions are available to users, but attempted execution of certain instructions (the privileged instructions) will cause an unconditional transfer (trap) to the Monitor program. The user normally gets a controlled access to these instructions via Monitor Subroutines. Thus (assuming an error-free monitor program) accidental or intentional violations of the system logic caused by execution of faulty instructions by users can be found and diagnosed by the system program before they have caused any non-recoverable damage. Attempted improper use of external devices can be avoided and corrected. Also, a user who attempts to access memory outside the region assigned to him by the monitor program will be trapped by a memory protection system before he can do any damage.

A second way to do input/output is available on the Sigma 7 via the input/output processor (IOP). This device is a special-purpose stored-program computer designed for a memory copy-in and copy-out operations. A special adaptor (SDS 7929) is available which provides electrical RD or WD signals from either the CPU or the IOP. These signals are applied to the General Purpose Interface. If these signals are supplied by the IOP, the CPU is available at least 90 % of the time for other work. IOP signals are, however, not as flexible to program as compared with the CPU signals because the IOP has a smaller instruction set than the CPU does. It, therefore, seems that some operations are best done using the IOP and others are best done using the CPU. Figure 1*a* shows a block diagram of the wiring path described above.

At this point it is interesting to illustrate several ways of connecting a computer to nuclear physics experiments. Method A is shown in Figure 1*b*. Here a standard wired multiparameter analyzer is connected to a stored program computer. This method has the disadvantage that it involves duplication of electronic hardware; on the other hand, it leaves the computer free to do other kinds of processing while the

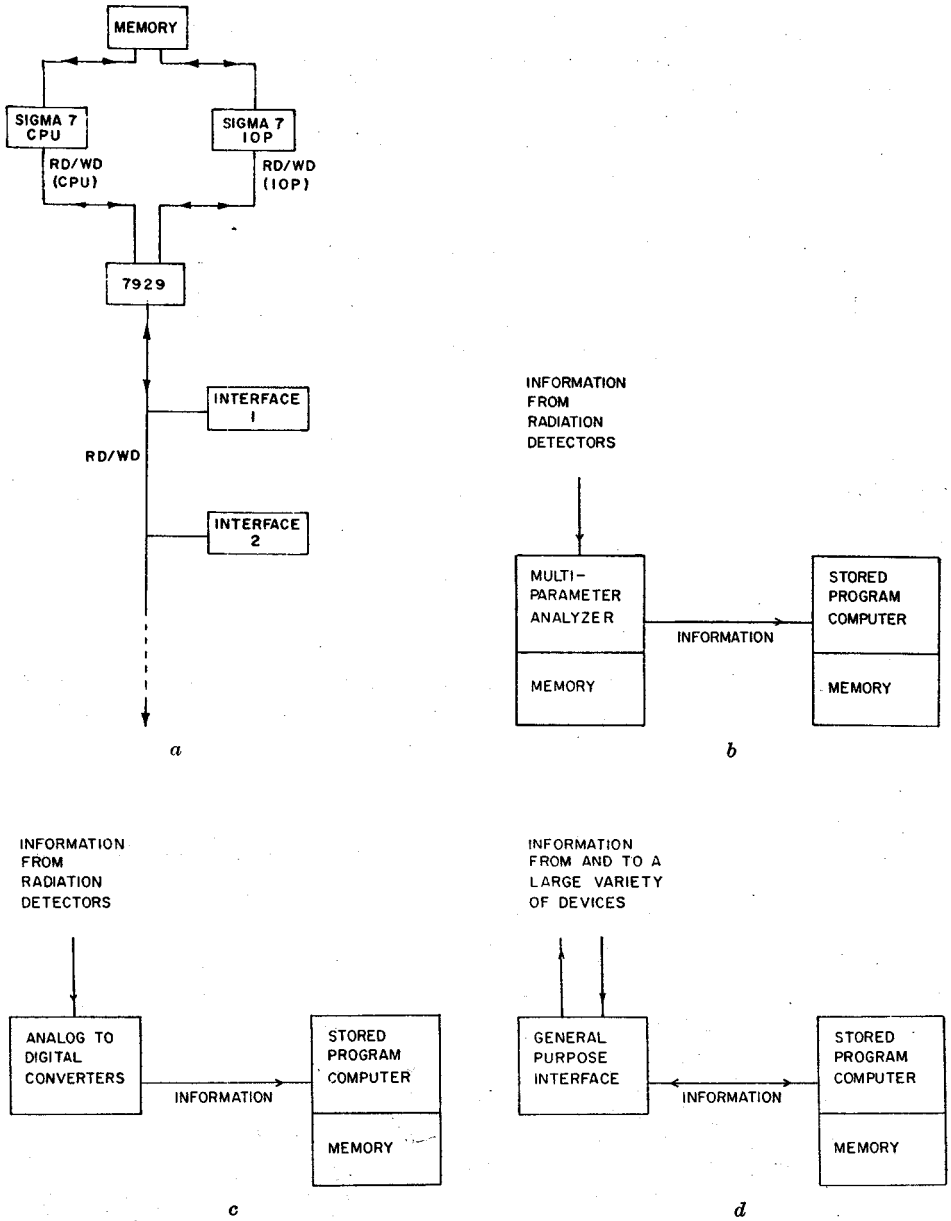

Fig. 1. (*a*) A block diagram of the major components of the system. A special version of the 7929 is used to combine the CPU and IOP signals. This unit is not announced at the present time. (*b*) A block diagram of a computer system using Method A (see text). (*c*) A block diagram of a computer system using Method B (see text). (*d*) A block diagram of a computer system using Method C (see text).

analyzer is recording data. Method B is shown in Figure 1*c*. This system stores data from detectors directly in the computer memory. While this method does tie up the computer it has the advantage of simplicity and it encourages users to use the computer to process data while the data is being recorded. Method C is shown in Figure 1*d* and is like method B except that the input device is now bi-directional and is also generalized so that it can process a broader class of signals. The analyzer described in this paper is a method C analyzer.

The general purpose interface

The general purpose interface receives and sends RD and WD signals as described above. Table 1 lists the function which it provides and Fig. 2 shows a drawing of the coaxial patch panel which provides users a programmable control over the interface logic.

The register logic

The Registers are built from SDS T series logic modules [5]. There are 4 registers, each 32 bits wide. Fig. 3 shows the schematic for the first 8 bits of register number 0 and the read-out logic gates for the first 8 bits of all four registers. The logic shown consists of two BT 10 cards and one ZT 15 plug card which provides the wired coaxial cable connection to the patch panel.

A typical flip-flop is illustrated in Fig. 4. Flip-flop registers can be set by the computer Write Direct or read by the computer Read Direct. They may also be set and read from the patch panel. The register bits are set by providing a signal on the clock input (GIrii) while the set input (SIrii) is true. The flip-flops are reset by providing a signal transition from true to false on the clock input while the set input is false.

The patch panel input to a register is inhibited by NWRrb if the computer is attempting to write into the same register.

The clock signal for writing from the patch panel is GIrii and is provided via the

Table 1

Item	Description	Services provided
4 registers	These registers can be written into by WD and read from by RD. They can also be written into or read from the patch panel. Each register is 32 bits long	SET RESET CC3·WRITE[a] CC4·WRITE CC3·READ CC4·READ FS·READ (Most significant 16 bits) FS·READ (Least significant 16 bits) FS·WRITE (Most significant 16 bits) FS·WRITE (Least significant 16 bits)

Table 1 (*continued*)

Item	Description	Services provided
32 test lamps	When a "True" logic signal is applied to the lamp input, the lamp lights	
8 interrupts	When a "True" logic signal is applied to the interrupt input II, an interrupt flip-flop in the CPU will be set	Interrupt flip-flop return line (IR). This provides a way to check whether the interrupt is set or not
one shots	Each time the input lines go true, the output will go true for the specified time. (See Fig. 2)	Durations of 0.1, 1.0, 10.0 and 100.0 uses are provided. Some units have both true and false output signals simultaneously available
4 clocks	50 nanosecond strobe pulses are available at 100 MC, 1 MC, 100 KC and 10 KC rates	
2 decoders	Provide conversion from binary to one out of 16 lines	
64 ANDS	Gives $A \cdot B = C$	The complement of C is also provided
64 ORS	Gives $A + B = C$	The complement of C is also provided
32 relays	Provides an SPDT contact closure when a true signal is applied	Relay grounds are isolated. Can be used for programmed rewiring of either analog or digital signals
Multiplexer MUX 1 unit of 8 inputs 1 unit of 16 inputs	When a gate line is held true an analog voltage transfer is provided between the selected input and the output	The analog and digital grounds are separated
12 digital to analog converters	Each converter is 15 bits including sign bit. Range is -10 volts to $+10$ volts	The analog and digital grounds are separated
6 current to voltage operational amplifiers	Output voltage range ± 10 volts for ± 4 Ma input current	
6 Sample/Hold amplifiers	Range ± 10 volts	Will sample any voltage in this range
24 Schmitt triggers	Hysteresis -1 Mv	Used to decide whether an analog voltage is greater than or less than zero
16 pulse stretchers	Input range $0 \rightarrow +10$ volts	When gate line is true stretcher will convert an analog pulse to an analog level. A clamp circuit is included to reset the pulse stretcher

[a] The Notation CC3 · WRITE indicates the logical AND of the signal CC3 and the signal WRITE.

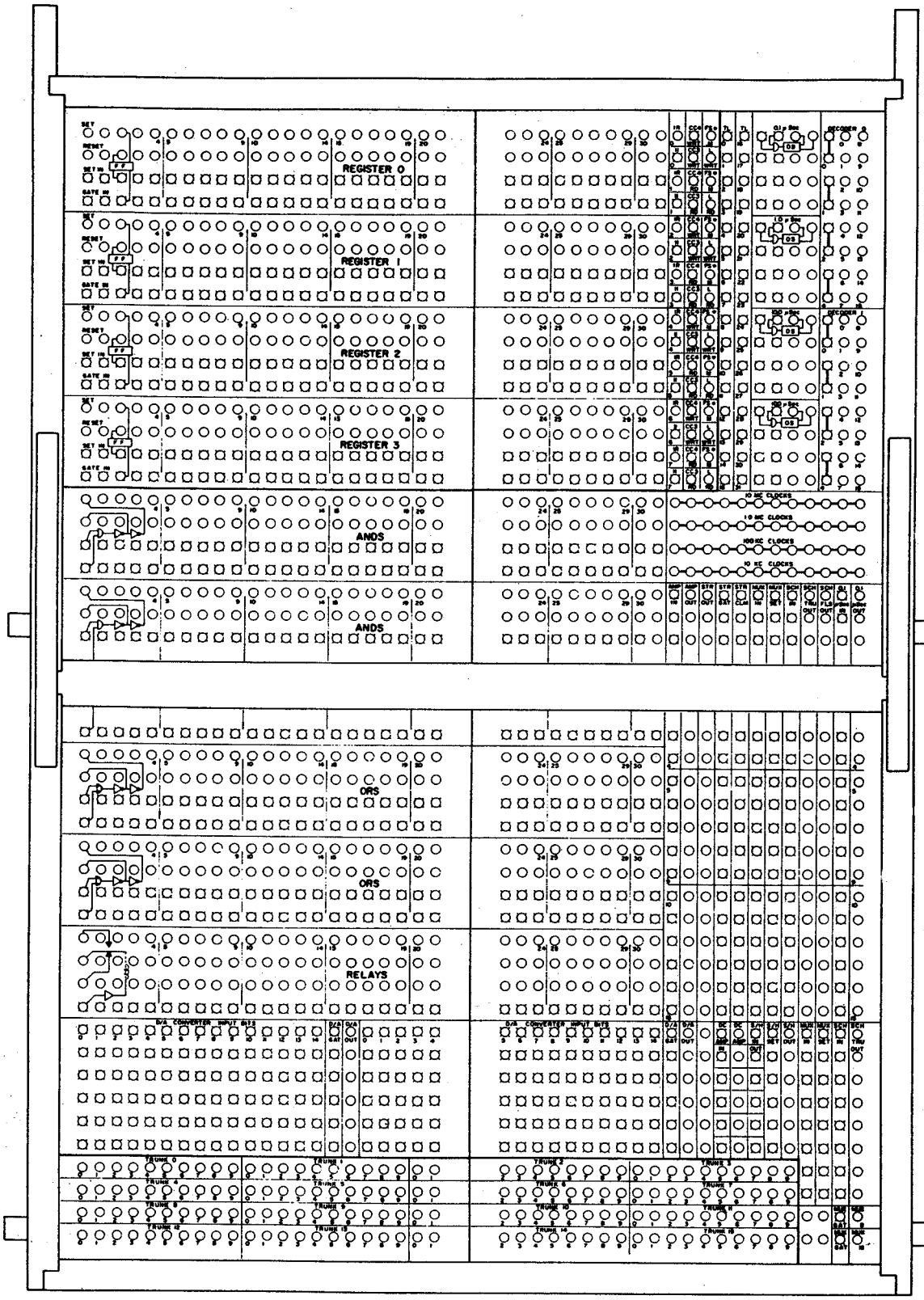

Fig. 2. This figure shows the legend for the removable coaxial cable patch panel. The panel shown is an AMP 2024 and is available from American Pamoor Inc., Harrisburg, Pa., U.S.A.

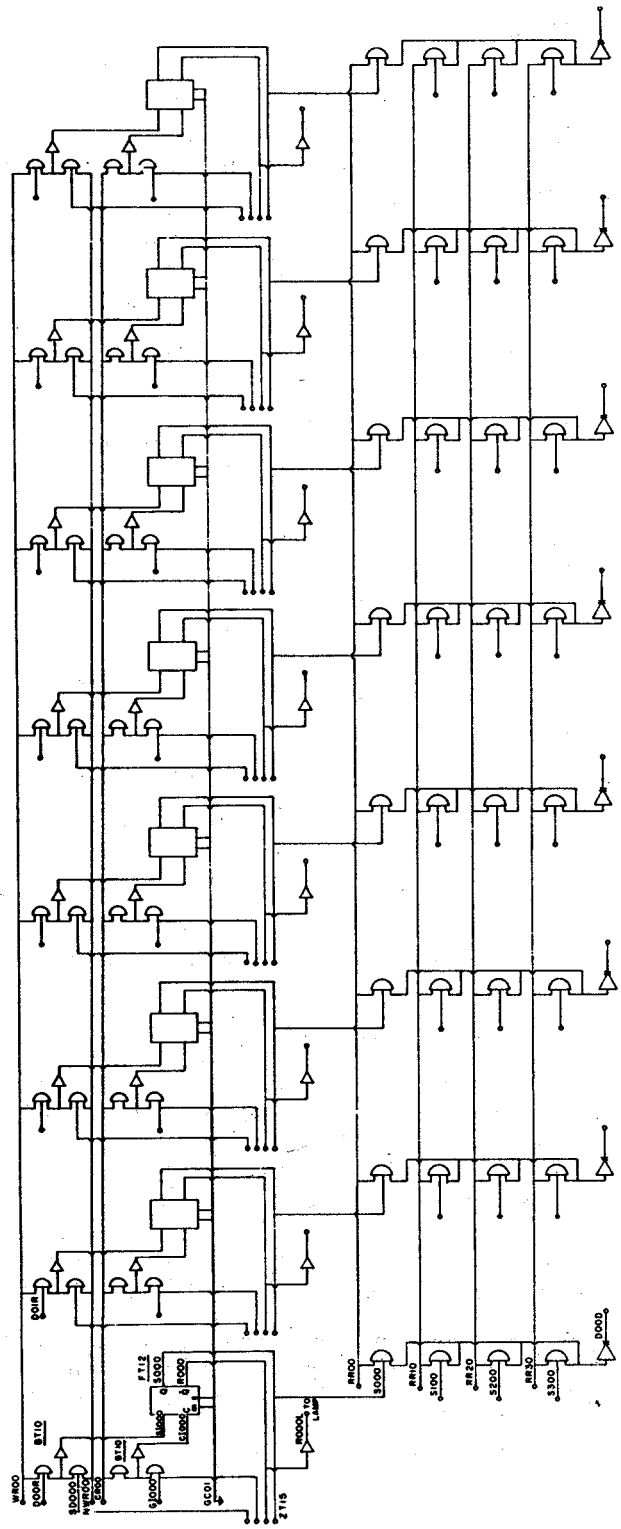

Fig. 3. A schematic of the first 8 bits of the interface registers. There are four registers and the read out gates for all four registers are shown. The symbols used are explained in ref. 5.

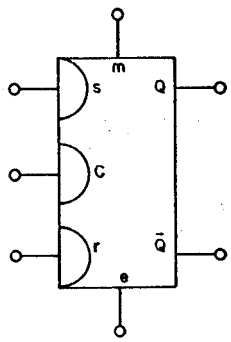

a

TRUTH TABLE

PERIOD n		n+1
s	r	Q
0	0	Q^n
0	1	0
1	0	1
1	1	1

b

Fig. 4. The truth table for the FT12 flip-flop. Terminal designations are as follows: *m*, mark input or unclocked D.C. set; *e*, erase input or unclocked D.C. reset; *s*, set input, must be clocked; *r*, reset input, must be clocked; *c*, clock input, works on trailing edge; *Q*, set output; $\bar{Q}$, reset output.

patch panel from external logic. The clock signal for a computer Write (CRrb) is generated (as shown in Fig. 6) from

$$\mathrm{CRrb} = \mathrm{UA}\cdot\mathrm{WD}\cdot\mathrm{FS}\cdot\mathrm{r}\cdot\mathrm{b},$$

where

r = register number,
b = byte number,
FS = is the Write Direct Function Strobe,
WD = is the signal indicating that a Write Direct function is in progress.

and

UA = is a term denoting that the Registers are the units being addressed by the Write Direct command.

The signal WRrb is used to gate the computer output data line to the correct register and is given by

$$\mathrm{WRrb} = \mathrm{UA}\cdot\mathrm{WD}\cdot\mathrm{r}\cdot\mathrm{b}.$$

The term "b", indicating a group of 8 bits, is included in the logic only because the loading of the driver for CRrb, WRrb, NWRrb and RRrb had to be split up. Generation of these control signals is shown in Fig. 6.

The output of a register is gated onto the computer input data lines by RRrb. RRrb is similar to WRrb except that it denotes that a Read Direct operation is in progress.

The rationale behind the logic shown in Fig. 3 is that it provides users with a very flexible bit logic system at the patch panel except for those times when the computer is executing a write operation.

Some useful elementary patch panel connection configurations are shown in Fig. 5.

At this point a major aspect of the general purpose interface becomes evident. The general purpose interface can perform many logical operations *in parallel*. The con-

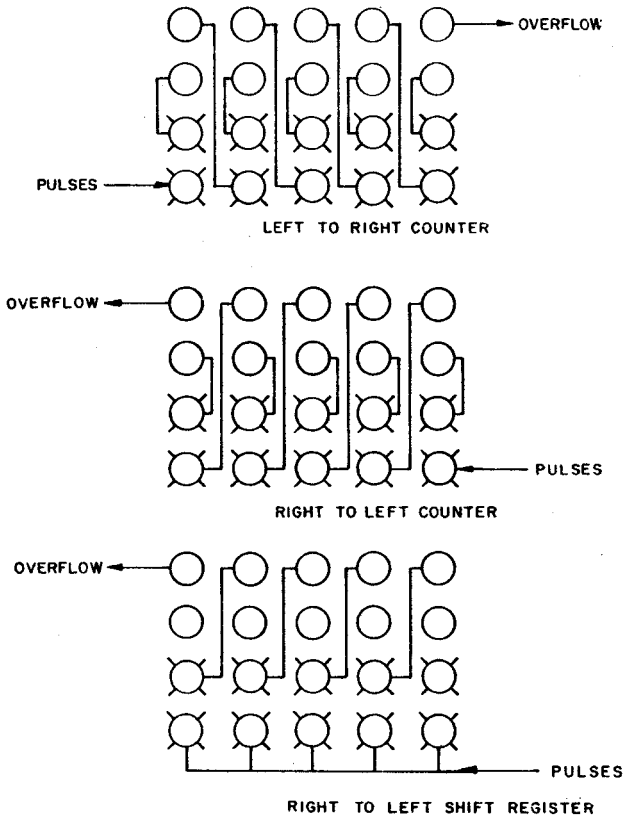

Fig. 5. Some useful elementary patch panel connections. The circles shown represent the cable plug holes on the panel. Inputs are distinguished from outputs by the short diagonal lines which are supposed to remind the user of the tails of arrows.

trast with the CPU is extreme. The CPU is organized to execute a certain small *set of* instructions *one after the other*. The general purpose interface in a kind of computer[1] with an *extremely large instruction set* which can do many instructions *at the same time*. It therefore provides a tool which has a valuable complementarity with respect to the CPU.

The register addressing logic

Fig. 6 gives a drawing of the logic which determines the data path between the RD/WD lines [6] of the Sigma 7 and the register bits of the GPI. This figure shows how the general purpose interface interprets the address field of the RD and WD instructions. The address field includes bits 16 through 31 of the instructions field which we designate as bits 0 through 15 of the address field. Interpretation is accomplished as shown below.

[1] The word "computer" is used here not in the sense of a stored-program computer (von Neumann machine) but rather in the sense of a very flexible rewireable electronic logic system.

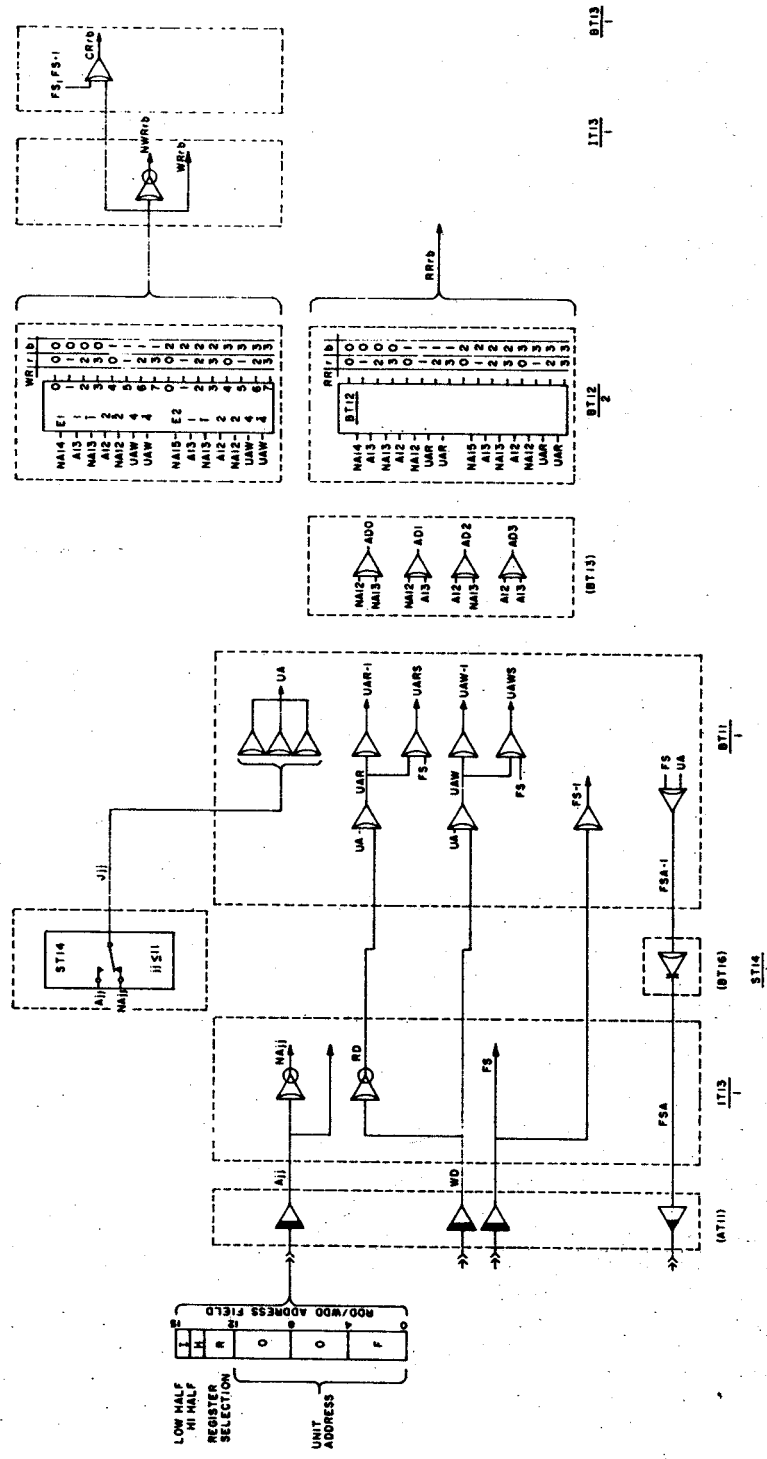

Fig. 6. This figure shows how the logic which interprets the RD/WD instruction address field is implemented.

$X(F)$	Interface #	N	N	L
0 3	4 11	12 13	14	15

Bits 0 through 3 have the value "*F*" in hexadecimal notation, i.e., in binary bits 0 through 3 must have the value 1111. This is an SDS system convention. All other values of these four bits are reserved for use with computer apparatus manufactured by SDS.

Bits 4 through 11 designate which interface is being addressed. For the first interface these bits have the value 00000000 in binary. The interface number of a given interface is established by toggle switch settings on an ST 14 card (see Fig. 6).

Bits 12 and 13 designate in binary which of the four registers is being addressed.

Bits 14 and 15 are complemented logical masks on the first 16 bits of each register (Most Significant Half or MSH) and on the second 16 bits of each register (Least Significant Half or LSH).

The computer will access the registers in the following way according to the following settings of bits 14 and 15.

Bit 14	*Bit 15*	*Result*
0	0	MSH plus LSH
0	1	MSH only
1	0	LSH only
1	1	Neither MSH nor LSH

This system is consistent with SDS standard practice. It assumes that most accesses to the registers will be 32 bit data transfers and the convenience is that, in this case, the programmer need not remember to put ones in these bits.

The condition code and function strobe logic is also shown in Fig. 6.

System organization

Only two parts of the system described above have a direct connection with the Sigma 7 Computer system; these are the Interrupt lines and the registers. All other components are free-standing. The computer can affect them only via signals patched to them from the registers and vice versa.

These remaining components comprise four major classes of devices. These are: (*a*) Wholly digital logic, e.g., the AND gates, the OR gates, etc. (*b*) Partially digital and partially analog logic, e.g., the DAC's. (*c*) Wholly analog logic, e.g., the operational amplifiers. (*d*) External system connections, e.g., the trunk lines.

In the schematic circuits in this paper, these conventions are observed. If a module name is shown in parentheses, e.g., (ZT15), then that module is shared and has been counted elsewhere.

A cable type is indicated by a letter, A through D, in a hexagon.

The length in feet is shown near this symbol for type C cables.

Open unconnected logic inputs will always be true.

The system uses SDS T series Modules and SDS C, H and L series Modules (older types). The T series modules are integrated circuit designs, a true digital signal is +4 volts and a false signal is 0 volts. The older series have true equal to +8 volts and false equal to 0 volts (except for the flip-flops in the DAC circuits which have true equal to +4 volts [7, 8, 9].

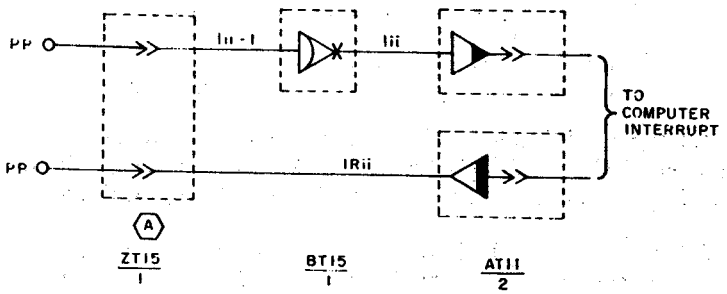

Fig. 7. This figure shows how the Sigma 7 interrupt system is wired to the patch panel. See ref. 5.

The interrupt logic

Fig. 7 shows how the interrupt system is wired between the Sigma Computer and the patch panel.

The computer interrupts are laid out with 14 interrupt lines on one cable and 14 interrupt return (acknowledge) lines on a second cable. The only logic required in the interface is a BT 15 to provide one unit load to the patch panel input and to drive the 7 unit loads of the cable drive.

A true signal on the patch panel input generates an interrupt. Receipt of the interrupt is indicated by a true signal on the acknowledge line. If the patch panel input is left open (no connection), it is *true*.

This method provides an immediate wired check for setting (IR true) of an interrupt and for completion (IR false) of an interrupt. Experience has shown that a convenient wired diagnostic for interrupt flip-flop condition can be much more useful in tracking down interrupt signals problems than a program.

The register system and the interrupt system are the only Interface components which have a direct access to the remainder of the Sigma System. The parts to be described in the next sections rely upon the registers, the interrupts or external sources for their information.

The AND circuits and the OR circuits

The AND Circuits are implemented as shown in Fig. 8*a*. The OR Circuits are implemented as shwon in Fig. 8*b*.

The action of these circuits is explained in reference 5. The choice of these circuits was based upon a desire to provide a maximum of user convenience. This has been done by adhering to a policy of providing most digital signals in direct and in complemented form.

The relay logic

The relay logic is shown in Fig. 9*a*. A true signal on the patch panel input KDi causes the relay to close contacts KCi and KPi. A false signal on KDi closes contacts KOi and KPi. Like the AND and OR Circuits, the relays can provide a programmed way to rewire or change the function of a circuit system. The relays, however, can do this for signals on coaxial cables and they provide isolation of the ground or

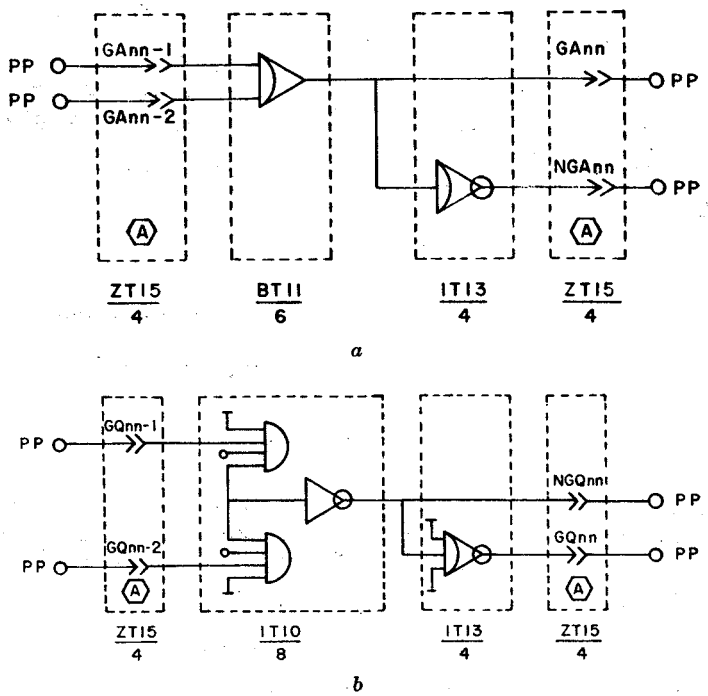

Fig. 8. (*a*) The AND circuits. (*b*) The OR circuits.

shield. The relays can be used to provide for interconnection of high or low level analog signals as well as digital signals. The relays can also be used to run small motors and by connecting a condenser to the movable pole they can be used to convert a high precision voltage level into a high precision pulse. Fig. 9*b* shows two of the many uses for the relays.

The one-shots

The one-shot logic schematic is shown in Fig. 10. For the 16 one-shots set at 0.1 microseconds and designated M16 through M31, only the true output (Mi) and the set input (SMi) are provided.

The sample and hold amplifiers

The Sample and Hold logic is shown in Fig. 11*a*. With the patch panel hold input (HLDi) false, the amplifier will track the analog input (SHIi). The transition of HLDi from false to true will trigger a 4 microsecond OT12 one-shot HLDSi. The output of this one-shot is connected to the transformer coupled input of a flip-flop with the output labeled FSHi (SX39 card). The flip-flop will be set which will cause the HX34/42 amplifier to go into the hold state. In this state the value of signal present on the line labeled SHIi at the time of transition from sample to hold is now held on the patch panel line labeled SHOi. The transition of HLDi to the false state

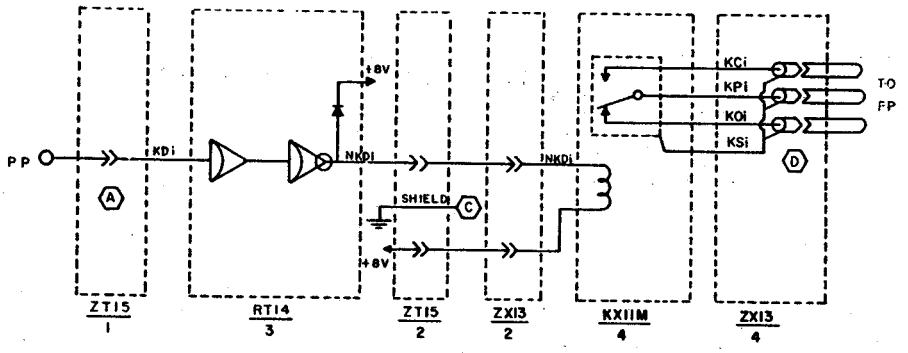

a

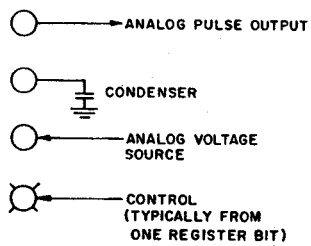

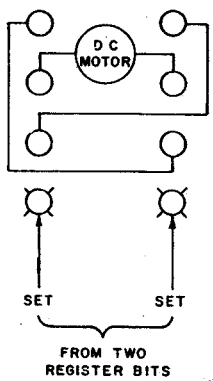

b

Fig. 9 (*a*) The relay circuits. Note that this wiring uses both T series modules and standard series modules. Standard series modules have been employed only because some T series components were not yet available when this system was being designed. (*b*) Two simple uses for the relays. The upper shows a program controlled pulse generator such as one might use to check out a nuclear amplifier system. The lower shows a D.C. motor control. D.C. voltage must be applied to the upper two terminals in the motor control.

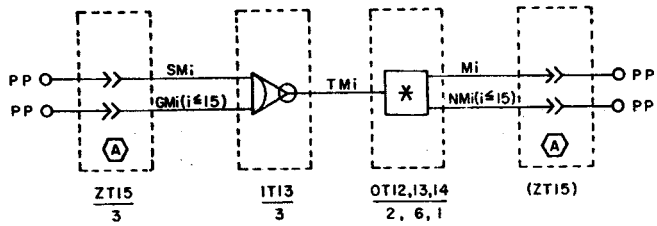

*

TIME(μs)	0.1	1.0	10	100
CKT TYPE	OT13	OT13	OT12	OT14
QUANTITY	20	4	4	4

Fig. 10. The one-shot circuits.

will trigger another OT12 one-shot, SAMi. The transformer coupled pulse will reset FSHi, and the amplifier will return to the tracking state.

Somewhat more detail of the analog section is shown in Fig. 11*b*.

The Schmitt triggers

The Schmitt Trigger logic is shown in Fig. 12. When the analog input signal STSi passes through the threshold level of the AT22 Schmitt Trigger, the digital output of the AT22 will change state. The state change will trigger one of the two OT12 one-shots. The pulse produced by the one-shots are transformer coupled to set or reset an FT12 flip-flop. The set and the reset both occur on the pulse leading edge. The net result is that if the output of AT22 is true, then the output of the FT12 will be true and vice versa.

The multiplexer

The multiplexer is a high speed analog switch which is used to selectively connect one of a number of analog input signals to a single output. The multiplexer provides a way to avoid the need for a large number of analog to digital converters. In order

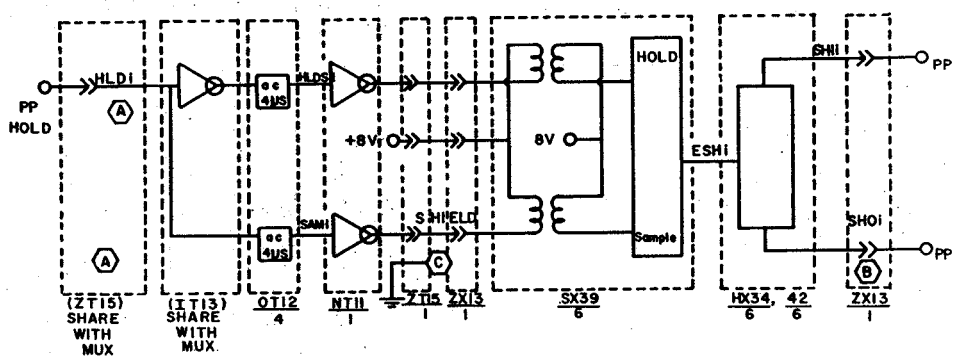

Fig. 11*a*

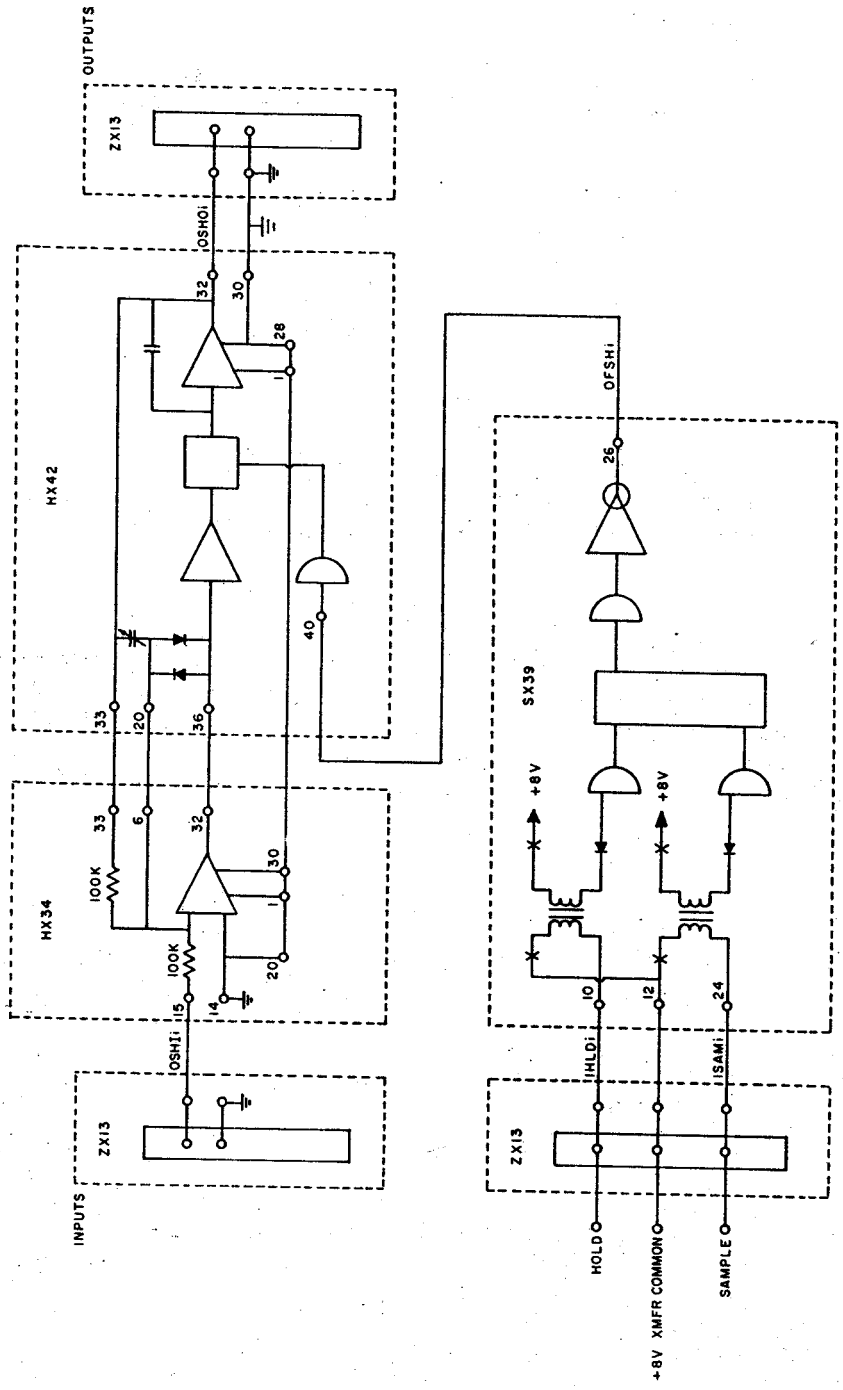

Fig. 11 *b*

Fig. 11. (*a*) The Sample and Hold amplifier logic. (*b*) The Sample and Hold amplifier itself.

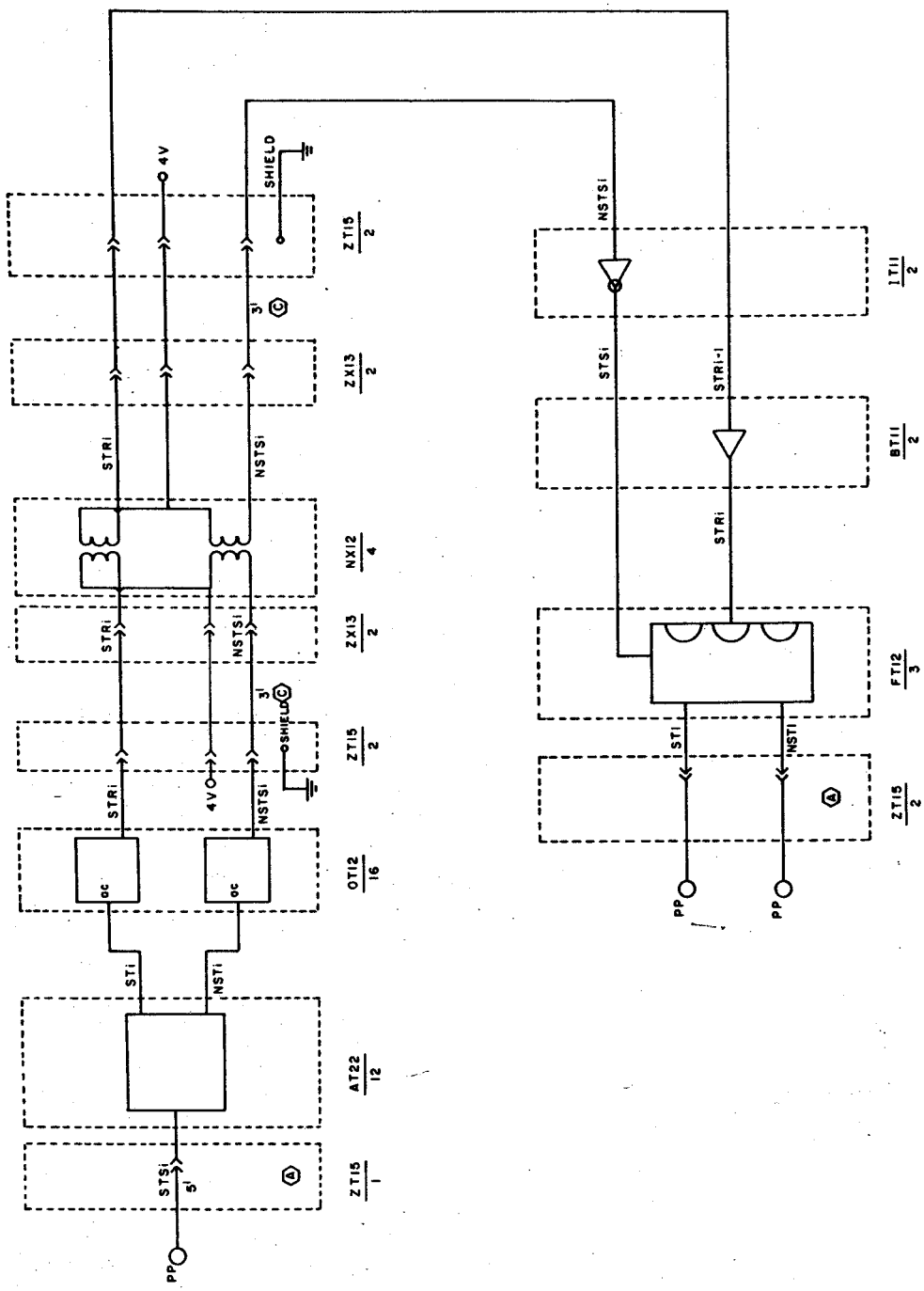

Fig. 12. The Schmitt trigger logic.

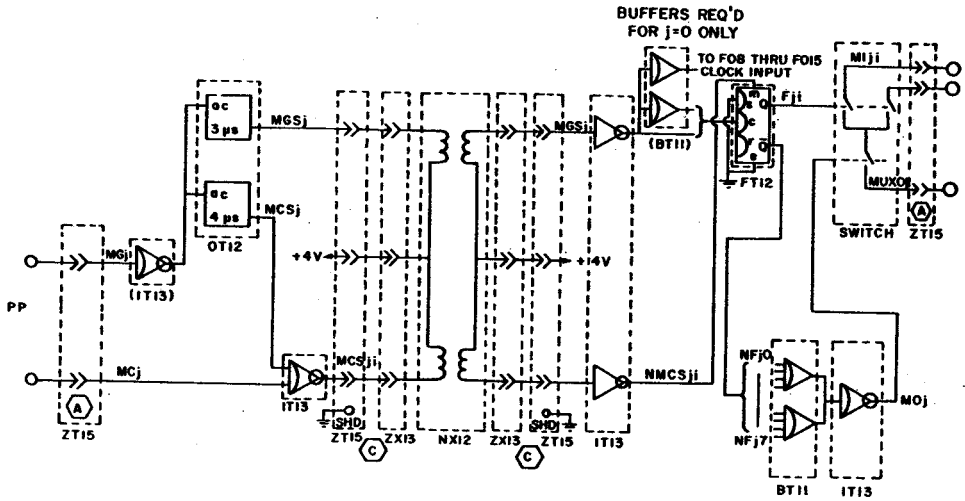

Fig. 13. The multiplexer logic.

to maintain separation of digital and analog system grounds, a transformer isolation system is used to separate the digital and analog system grounds. Fig. 13 shows how this is done.

There are two multiplexers, one for 8 input channels and one for 16 input channels. The first 8 channels of both multiplexers are illustrated in Fig. 13.

The rise of the multiplexer select gate signal, MGj, triggers two one-shots—MGSj and MCSj. The one-shots provide pulses to allow transformer coupling. MGSj transmits a 3 microsecond pulse that will reset all channel select flip-flops (Fji) of multiplexer j. After transformer coupling and inversion to provide a positive going pulse, the MGSj pulse is fed to the clock input of the FT12. The channel select signal MCi is anded with MCSj to provide a 4 microsecond pulse. This pulse is fed to the DC-set of the FT12 flip-flop; thus, the selected channel flip-flop will be set. To allow for uncertainties in pulse transmission timing, the MCS pulse is longer than the MGS pulse.

If any of a group of 8 channels is selected, the term

$$\mathrm{MOj} = \mathrm{Fj0} + \mathrm{Fj1} + \mathrm{Fj2} + \ldots + \mathrm{Fj7}$$

will be true. This term selects (closes) a multiplexer output switch for a group of 8 multiplexer input switches. The true flip-flop selects the individual channel input switch.

(Note: Since the switch module design is not yet complete, it is not included in the design.)

The digital to analog converters

Twelve digital to analog converter units are included, each of 15 bits. This is sufficient to provide two independent Bi-Directional Self Calibrating Analog to Digital Converter systems [12]. Transformer isolation of the analog and digital supply voltages and grounds is provided as is shown in Fig. 14*b*. There are two one shots

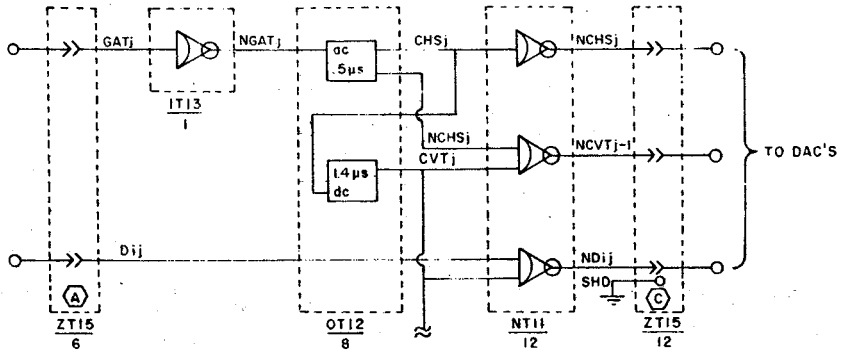

Fig. 14*a*

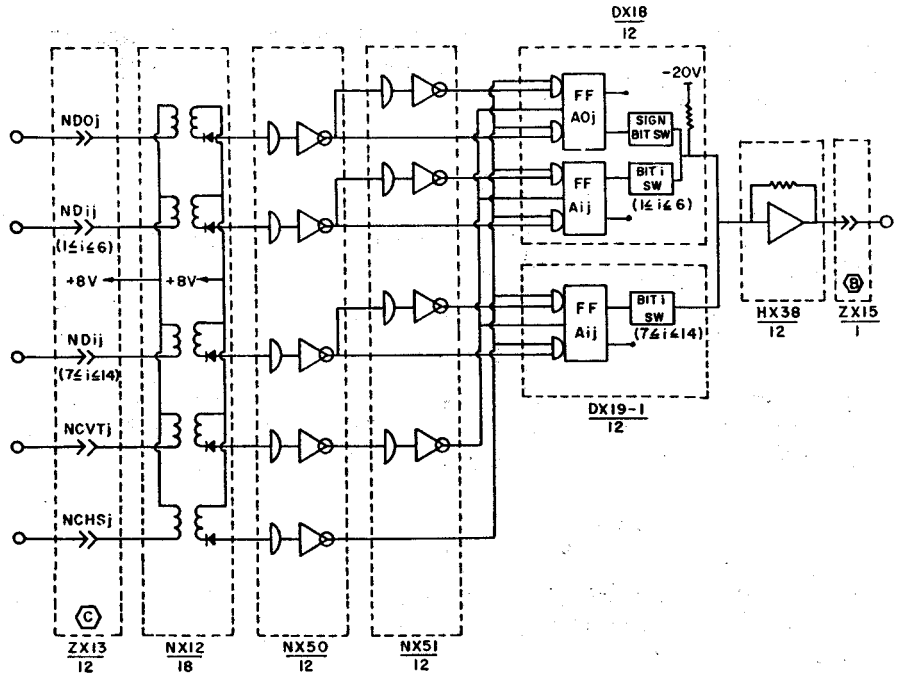

Fig. 14*b*

(Figure 14*a*) associated with each DAC. The first one-shot (CHSj) is triggered on the rise of the channel convert control-signal (GATj). The second oneshot (CVTj) is triggered on the rise of the first one shot. From these one-shots, three timing pulses are generated to facilitate transformer coupling of channel data and the convert control signal. These timing pulses are illustrated in Fig. 14*c*. The three timing pulses are used as follows. The signal CVTj (Fig. 14*a*) is anded with each data signal to provide transformer pulses on those lines for which there is a true data bit. The

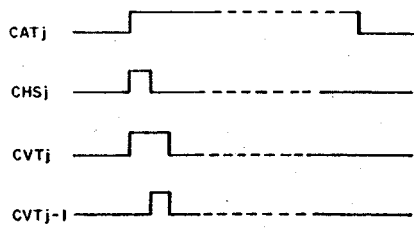

Fig. 14 c

Fig. 14 (*a*) Timing circuits used to transformer couple digital data in pulse form to the holding flip-flops in the DAC's. (*b*) The DAC's. The flip-flops shown are double ranked. Data in the first rank is transferred to the second rank when the central wire to each flip is made true. See ref. [8]. (*c*) The timing used for data transfer to the DAC's.

signal CHSj gates the data bits into the first rank register of the DAC register (Fig. 14*b*). The signal CVTj-1 causes the data to be transferred from the first to the second rank register and thus to be converted.

The decoder logic

The decoders are provided to give a fast wired conversion from binary to one out of 16 lines. The logical implementation is shown in Fig. 15.

The test lights

32 Test lamps are provided to enable users to get a rapid wired diagnostic via the patch panel of the condition of any signal. These lights are in addition to the 128 Test lamps which are permanently wired to each register bit (see Fig. 16).

The operational amplifiers

Six operational amplifiers are included to provide current summing nodes for analog to digital conversion operations. These amplifiers have a wired in gain of 0.4 Ma per volt. (See Fig. 17.)

The cables

Four RDD/WDD cables and two interrupt cables are required [6]. These are standard Sigma Computer Cables. All other cables are special cables and have been classified as types A through D.

Type A cables (Fig. 18*a*) are used to connect patch panel coaxial terminals to SDS T series modules via ZT15 plug card. Fifty Ohm RG-174/U coaxial cable is used.

Type B cables are used to connect patch panel coaxial terminals to SDS standard series modules. The cable construction is similar to type A cable construction except that ZX13 plug cards are used.

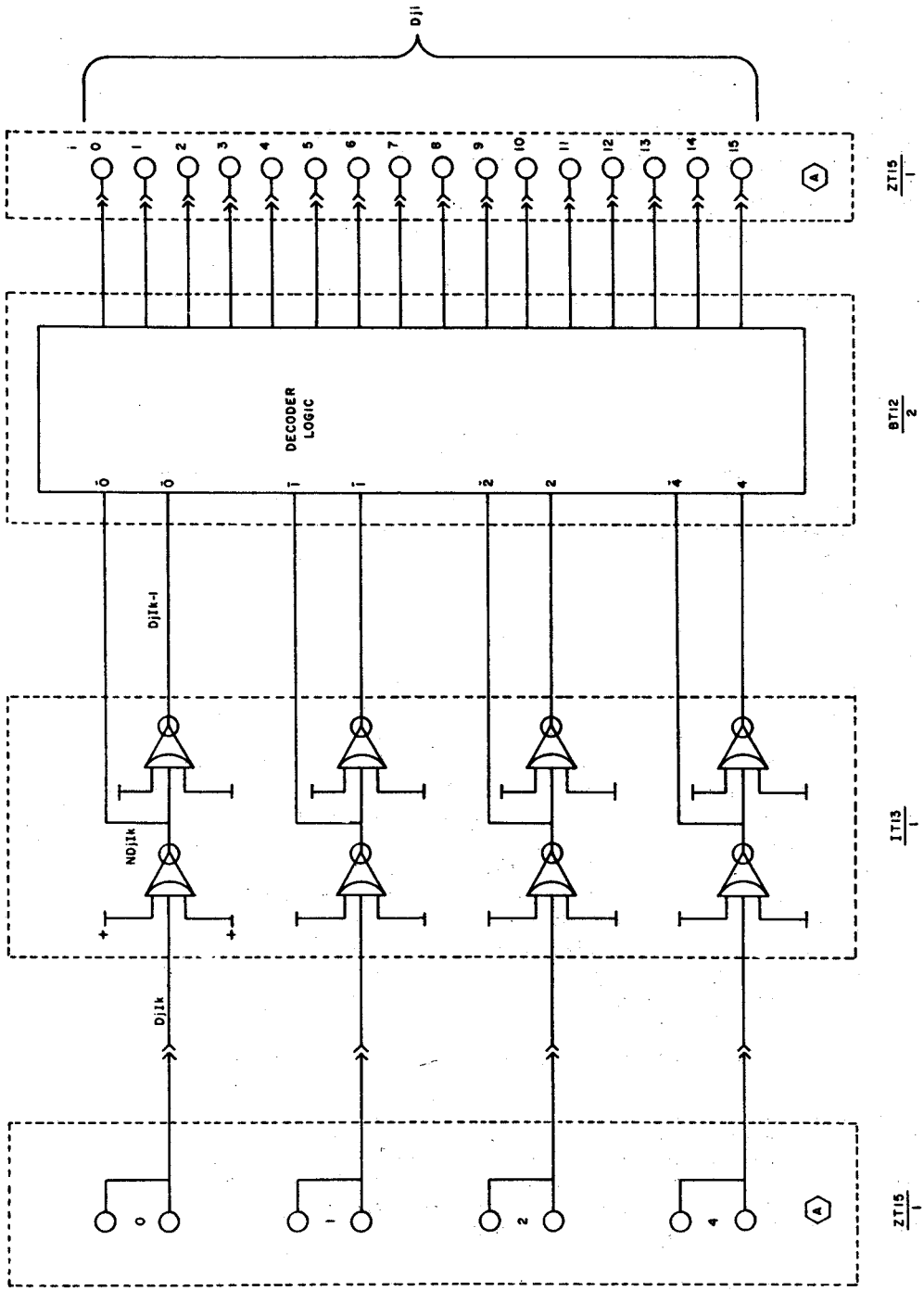

Fig. 15. The decoder logic.

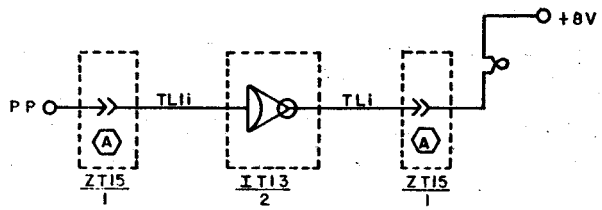

Fig. 16. The test lamp wiring.

Type C cables are used to interconnect SDS standard series modules and SDS T series modules (Fig. 18*b*).

Type D cables are used to connect the relay contact terminals to the patch panel (see Fig. 18*c*).

Special pulse handling circuits

There are two kinds of circuits wired into the patch panel which are specially designed for pulse distribution analysis. These are prototypes of an *N* detector nuclear pulse interface. The circuits are a set of 16 amplifiers and 16 pulse strectcher. The purpose of the amplifiers is pulse shaping, the parameters of this shaping have not yet been established.

The Pulse Stretcher logic is presently under development. Fig. 19*a* shows the logic of the pulse stretchers which are a gated double integrater type.

This particular type of stretcher is interesting because it gives a proper D.C. stretched output for any pulse which crosses through zero volts one or more times. Thus it works on a double delay line clipped pulse and it also works on an exponentially decaying sine wave. This property is shown graphically in Fig. 19*b*. A second property of this circuit is that it provides a shot noise supression effect. This is because shot noise goes as 1/T where T is the measurement (unclamp) time. The contrast between this type of pulse stretcher and the more common peak rectifier design is noteworthy. A peak rectifier circuit is forced to sample the height of a signal in a time small compared with the duration of the signal—thus it typically samples in about 0.1 microsecond a signal with a duration of several microseconds. The integration type samples over the whole duration of the signal. At long sampling times resolution is worsened by 1/f noise in the amplifier system. With a peak integrator system, a variation of one parameter (the gate duration) can be used to find the minimum noise sample time between shot and 1/f noise contributions. We are currently testing

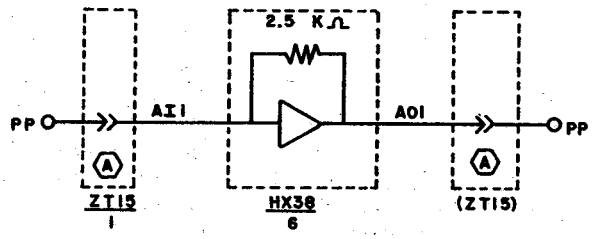

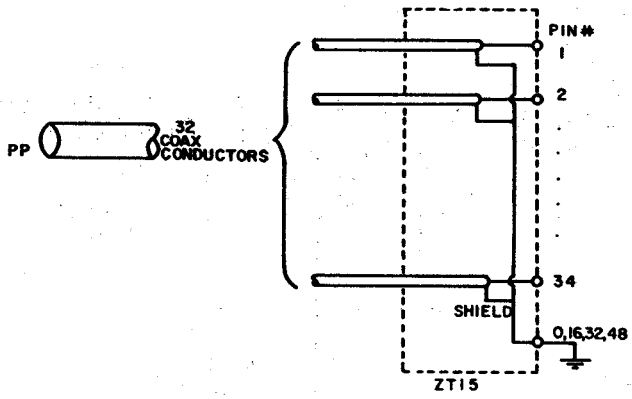

a

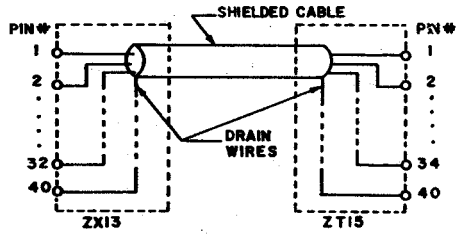

b

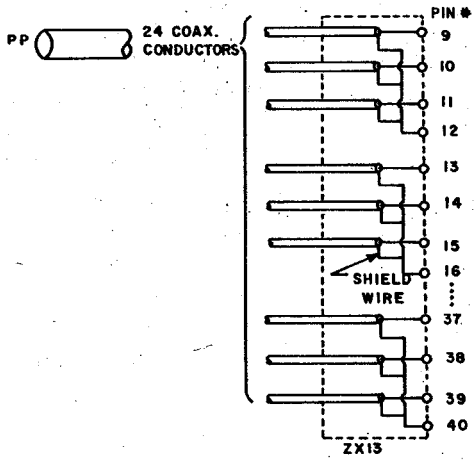

c

Fig. 18 *a*, *b*, *c*. The interconnection cables.

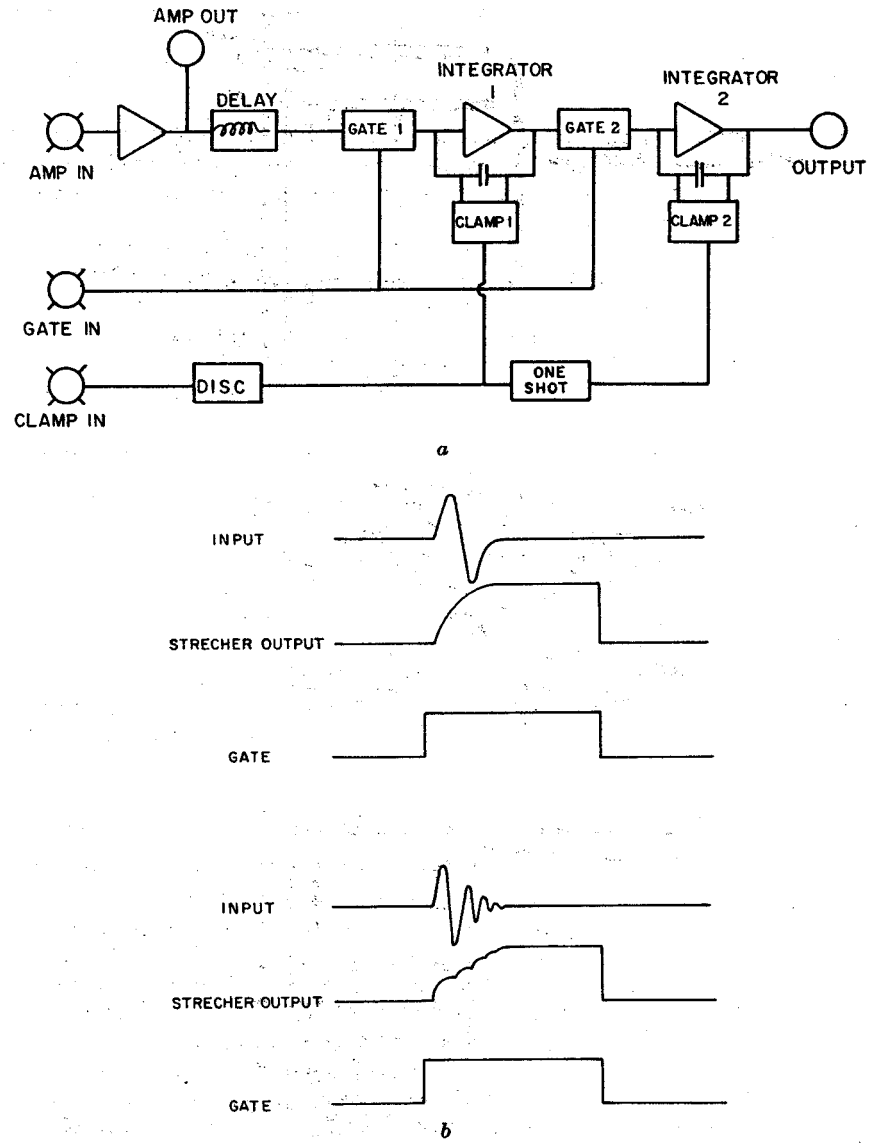

Fig. 19. (*a*) The double integrator pulse stretchers. (*b*) Response of the pulse stretchers to typical signals.

noise performance on this type of pulse stretcher and hope to report results soon. Heuristic arguments indicate that the integrator type pulse stretcher may exceed the performance of peak rectifier type pulse stretchers, but a logical proof is difficult because the peak rectifier systems do not lend themselves to analytic description and hence comparison of algebraic noise expressions.

A pulse stretcher—amplifier interface

Having established the principle of the general purpose interface, we now must meet the need for more specialized types of functions. The General Purpose Interface is conceived for the purpose of satisfying the general needs of a laboratory. Situations occur where the need for a large number of more specialized devices is the only way to accomplish a given objective. When the number of these functions become large (and only then) a design for a more specialized type of interface becomes a desirable approach. It seems, however, that a good policy is to attempt to connect the specialized interface to a general purpose interface rather than to a computer directly. The arguments for specialization are usually based upon attempts to reduce expenditures, but in nuclear physics reduced expenditures via specialization usually result only when a large number of identical devices are involved.

The essential point in the General Purpose Approach (which is the main burden of this paper) is that it is better to proceed from the general to the particular instead of vice versa.

Fig. 20 gives a logical diagram for a multiple nuclear detector Interface which interfaces itself to a General Purpose Interface.

Two arguments for this approach run in a parallel vein. Because the General Purpose Interface is available, the more specialized interface is cheaper (i.e. fewer parts) and relatively simple (i.e. more understandable). These arguments are identical to the argument which says that because the computer is present, the general purpose interface is cheaper and relatively simple.

Fig. 20 gives a diagram of an N detector interface which will transfer data to a General Purpose Interface. This interface can detect and process results from N-fold coincidence events and is self calibrating. Its estimated cost is about $1000 per detector.

One particular use for the new type of radiation analyzer

The authors' main intent behind the system design given here is to provide a facility capable of quickly analyzing events generated by multi-particle emitting nuclear reactions. Arguments for these reactions have been presented previously [10] but some special arguments arise in connection with the purpose of investigations concerned with nuclei which are far off the line of stability although it is to be expected that a general purpose instrumental approach should have a strong validity for nearly any kind of research.

The principle facts are:

(1) Nuclei off the line of stability have extra-ordinary values of isotopic spin.

(2) Isotopic spin is conserved in nuclear reactions; hence, one way to achieve extraordinary isospin is to cause a reaction which emits a large number of particles. Each emitted particle can "bump" the isospin of the residual nucleus up by 1/2.

Experimentally it is difficult when using existing apparatus to detect accurately the emission of a large number (N) of particles but, correspondingly, such emissions have a very distinct characteristic since the space available for the particles is 4N dimensional; such emissions may have a very great freedom from background because the measurement volume available for all events is P^{3N} where P is the inverse of the average precision of any given measurement and P = 100 is not unusual. It seems

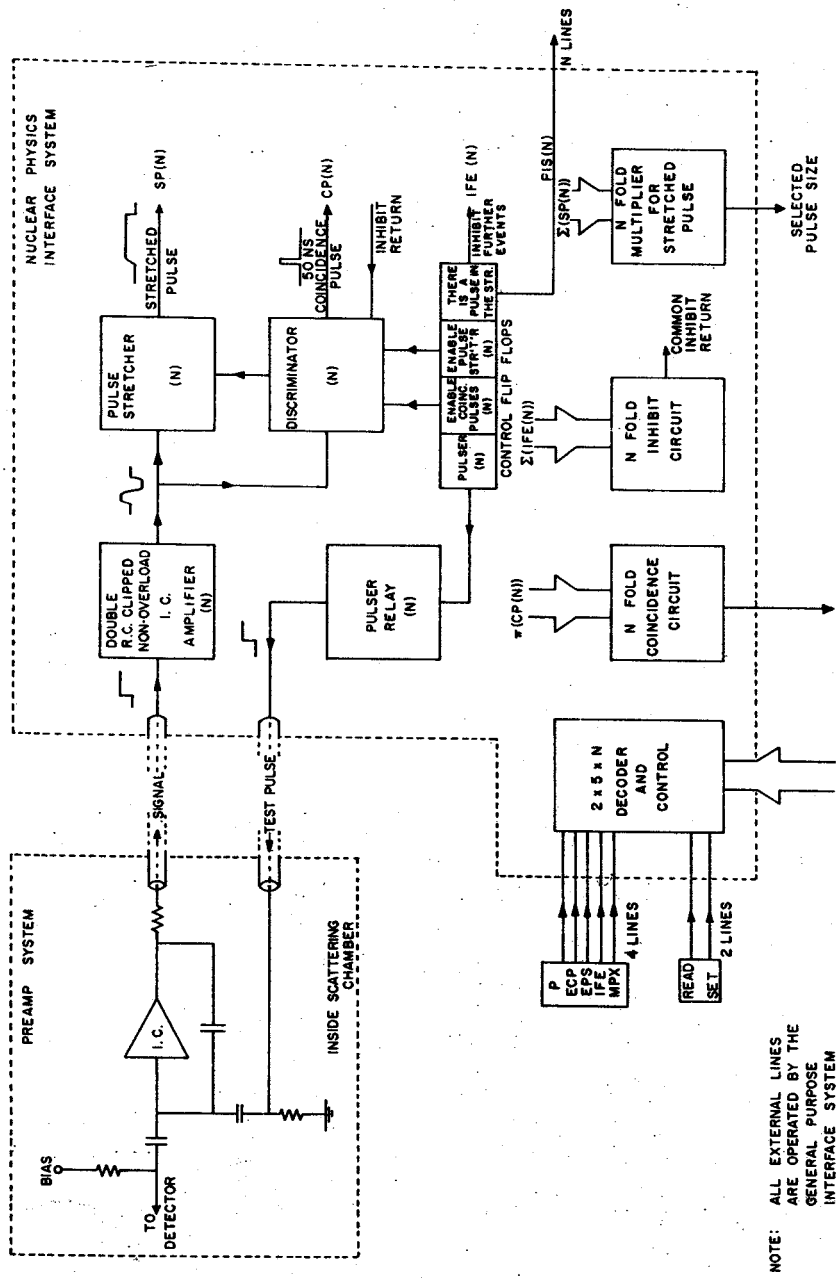

Fig. 20. A typical multiple detector interface.

to be a rule that most nuclear matrix elements yield particles which are "peaked" into small and frequently well separated regions of this space. With typical detector counting rates such a space is nearly empty except where specific nuclear matrix elements contribute and hence, the "local" background is low.

Nuclear far off the line of stability are clearly "extraordinary" nuclei. When they are to be manufactured from "ordinary" nuclei it seems likely that a great number of unwanted "ordinary" nuclei will also be produced. It seems reasonable that the background problems in this effort can be expected to be extraordinary also. The multi-particle reaction approach to the study of these nuclei may be successful because it reduces the "local" background even though the "total" background may be high.

ACKNOWLEDGEMENTS

We are most highly indebted to R. W. Hamming, the mathematician, of Bell Telephone Laboratories. Hamming's contribution to this paper is his emphasis on relationships. The system, which this paper describes in part, is designed by principles which maximumize its ability to investigate relationships rather than specific quantities. With particular reference to the Lysekil symposium, however, we believe that the analyzer described here provides an approach to research which will be valid no matter how good or how poor any particular idea of how much research should be done may turn out to be. Regardless of whether "isospin bumping" turns out to be the key to measurements of nuclei off the line of stability, we can anticipate that nearly any approach will be subject to considerable problems associated with the background. Devices of great perspicuity will be needed and the device described here is specifically designed to be such a tool in order to help us to find things which we don't yet know how to find.

We are also indebted to the National Science Foundation for the support of this research through a special computer grant and to Professor Charles Gruhn of Michigan State University who has begun the development of multiple element semiconductor radiation detectors [11], without which our end goal would not be achieved.

Cyclotron Laboratory, Michigan State University, East Lansing, Michigan, U.S.A.

REFERENCES

1. Proceedings of the Conference on Utilization of Multiparameter Analysers in Nuclear Physics, Grossingers, New York, November, 1966; Nucl. Instr. Meth. *25*, 141 (1963).
2. MOLLENAUER, J. F., Data simulation with an on-line computer as a diagnostic and analytical tool. Proceedings of the 9th Scintillation and Semiconductor Counter Symposium, Washington, D.C., February, 1964.
3. KANE, J. V., Physics Today *19*, No. 7, 59 (1966).
4. Sigma 7 Computer/Reference Manual, p. 76. (Available from Scientific Data Systems, Santa Monica, California.)
5. SDS T Series: Integrated Circuit Logic Modules/Description and Specifications. (Available from Scientific Data Systems, Santa Monica, California.)
6. Sigma Series Computers, Input/Output Structure. (Available from Scientific Data Systems, Santa Monica, California.)
7. SDS Logic Modules; C, H and L Series/Reference Manual. (Available from Scientific Data Systems, Santa Monica, California.)
8. Digital-to-Analog Converter, DA30-15. (Available from Scientific Data Systems, Santa Monica, California.)
9. SDS Silicon Logic Circuit Modules. (Available from Scientific Data Systems, Santa Monica, California.)
10. Rev. Mod. Phys. 37, 327–536 (1965) (especially articles by Kane, J. V.; Donovan, P. F.; Zupancic, C.; Kim, Y. E.); PARKER, P. F., *et al.*, Phys. Rev. Lett. *14*, 15 (1965).
11. KANE, J. V., GRUHN, C. R., and KELLY, W. H., Bull. Am. Phys. Soc. *11*, 477 (1966).
12. KANE, J. V., Rev. Sci. Instr. *30*, 1062 (1965).

Tryckt den 24 oktober 1967

Uppsala 1967. Almqvist & Wiksells Boktryckeri AB

2.G

Nuclear Physics A99 (1967) 540—546; © *North-Holland Publishing Co., Amsterdam*

THE ^{14}N(p, d)^{13}N REACTION AT 30 MeV

R. L. KOZUB, L. A. KULL and E. KASHY

Cyclotron Laboratory, Michigan State University, East Lansing, Michigan, USA †

Received 10 April 1967

Abstract: Energy spectra and angular distributions of deuterons from the ^{14}N(p, d)^{13}N reaction have been measured at an incident proton energy of 30.3 MeV. The data indicate that the ^{13}N levels at 0.0, 3.51, 7.38, 8.93 and 11.80 MeV correspond to the levels calculated by Cohen and Kurath at excitation energies of 0.0, 3.7, 7.4, 8.7, and 10.6 MeV with J^π of $\frac{1}{2}^-$, $\frac{3}{2}^-$, $\frac{5}{2}^-$, $\frac{1}{2}^-$ and $\frac{3}{2}^-$, respectively. Spectroscopic factors obtained from DWBA analysis of the angular distributions are compared with theoretical predictions of intermediate coupling calculations. In addition, the excitation of positive parity states in this reaction indicates configuration admixtures of 2s–1d shell in the ground state of ^{14}N.

E NUCLEAR REACTIONS ^{14}N(p, d), E_p = 30.3 MeV; measured $\sigma(E_d, \theta)$. ^{13}N levels deduced J, π. Natural target.

1. Introduction

The properties of nuclear levels of ^{13}N have been studied to a considerable extent in nuclear reactions involving principally compound nuclear formation [1]), for example, results from the scattering of protons by ^{12}C give the widths, excitation energies, angular momentum and parity of excited levels of ^{13}N. Because of the strong binding of ^{12}C, all ^{13}N excited levels are accessible through this reaction [2]). More recently, with the availability of higher energy, direct reactions such as the ^{14}N(p, d)^{13}N [refs. [3,4])] and ^{15}N(p, t)^{13}N [refs. [5])] reactions have been studied and the present investigation falls in that class. To the extent that one can trust distorted-wave Born approximation calculations, the (p, d) reaction provides a direct measure of the overlap of the initial target wave function with the wave functions of excited states of the residual nucleus, i.e. the coefficients of fractional parentage are directly measurable quantities. The intermediate coupling calculations of Kurath [6,7]) predict the values of these coefficients of fractional parentage. Thus, this reaction represents a good test of the intermediate coupling model for nitrogen. In addition, the presence of configuration admixtures from higher shells is easily detected through the excitation of positive-parity states in a direct process.

2. Experimental method

The protons were accelerated to an energy of 30.3 MeV by the Michigan State University, sector-focussing cyclotron. The target was ^{14}N gas maintained at a

† Work supported in part by the U.S. National Science Foundation.

pressure of 25 cm of Hg in a gas cell with 25 μm kapton windows. The detection system consisted of a $dE/dX-E$ counter telescope, and the thickness of the detectors was such that deuterons corresponding to excitation energies up to 14 MeV in ^{13}N could be observed. Data were obtained at lab angles from 10 to 160° with an overall instrumental energy resolution in the deuteron spectra of 130 keV. The uncertainty in the measured cross sections is estimated to be about $\pm 7\%$, not including the statistical error which is indicated at each of the data points.

3. Results

Fig. 1 shows a deuteron spectrum obtained at a lab angle of 30°. The prominent peaks are clearly identified as the five negative parity states, which one would expect to be strongly excited by the direct pick-up of a 1p nucleon from ^{14}N. Since ^{14}N

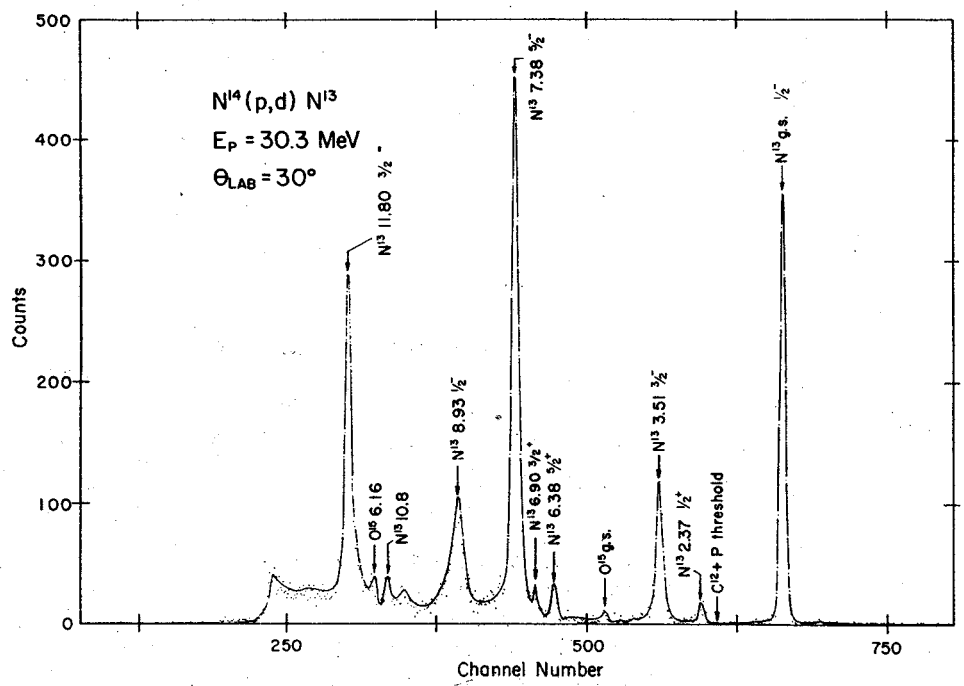

Fig. 1. Typical deuteron spectrum from the ^{14}N(p, d)^{13}N reaction.

has spin 1^+, the removal of a $p_{\frac{1}{2}}$ nucleon would lead to a $\frac{1}{2}^-$ and a $\frac{3}{2}^-$ level of ^{13}N, while removal of a $p_{\frac{3}{2}}$ nucleon would yield levels of ^{13}N with spins of $\frac{1}{2}^-$, $\frac{3}{2}^-$ and $\frac{5}{2}^-$. Angular distributions of deuterons leaving ^{13}N in the strongly excited levels at 0, 3.51, 7.38, 8.93 and 11.80 MeV are shown in fig. 2, where the spins of the ground, 3.51 and 8.93 MeV levels are previously determined as $\frac{1}{2}^-$, $\frac{3}{2}^-$ and $\frac{1}{2}^-$, respectively. All the angular distributions are identified as resulting principally from the pick-up

of a neutron from the 1p shell. A sizable dependence upon the Q of the reaction is seen as a flattening of the cross section versus angle for the higher excited levels. The 7.38 MeV level of ^{13}N was known to have possible spin and parity assignments

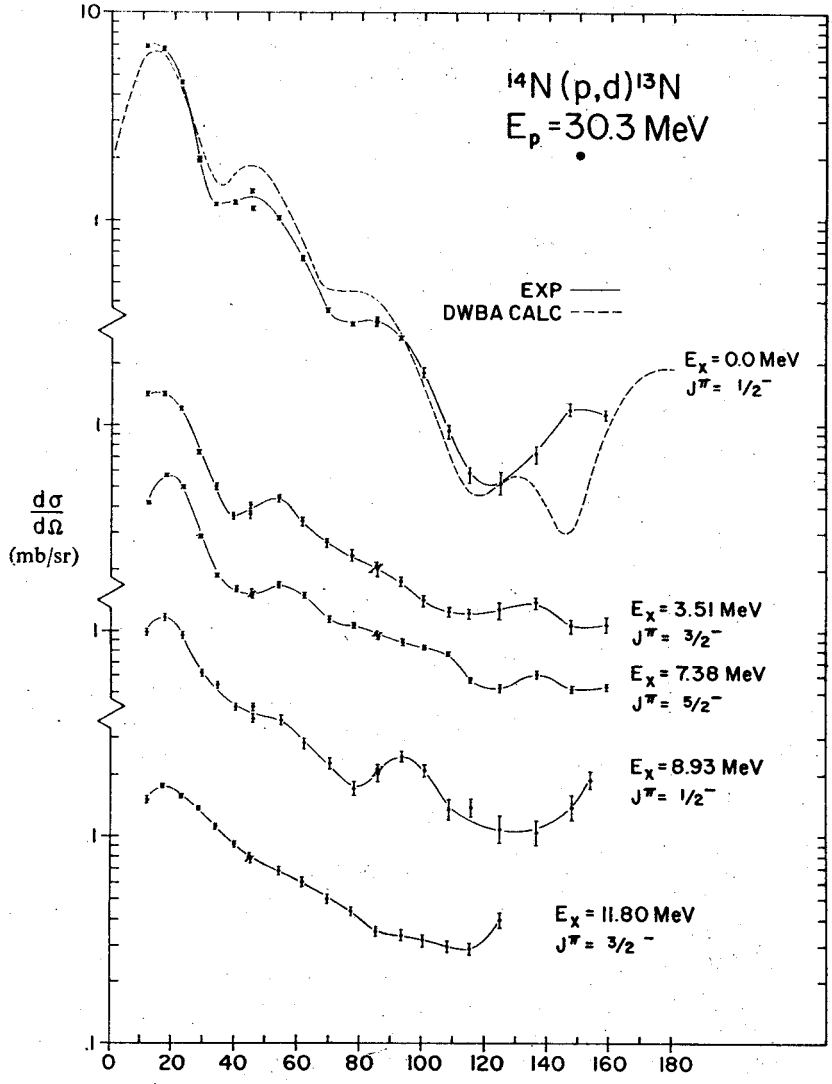

Fig. 2. Angular distributions of deuterons for the ground, 3.51, 7.38, 8.93 and 11.80 MeV levels of ^{13}N from the ^{14}N(p, d)^{13}N reaction.

of $\frac{5}{2}^+$, $\frac{5}{2}^-$ or $\frac{7}{2}^-$ previous to work with pick-up reactions [1, 8]). This experiment agrees with previous (p, d) results [3]) and a recently reported result from the ^{15}N(p, t)^{13}N reaction [5]) in selecting the $\frac{5}{2}^-$ assignment.

The parity of the ^{13}N level at 11.8 MeV is negative since we have an $l_n = 1$ pick-up. In addition, its spin is determined since, as was mentioned earlier, only five levels are expected to be excited strongly in this reaction, four of which have known spins and parity. Thus, the only remaining possibility for the 11.80 MeV level is an assignment of $J^\pi = \frac{3}{2}^-$. This is in agreement with work at 156 MeV by Bachelier *et al.* [9]). It is also clear that this $\frac{3}{2}^-$ level at 11.80 MeV corresponds to that predicted by Cohen and Kurath [7]) at an excitation energy of 10.6 MeV.

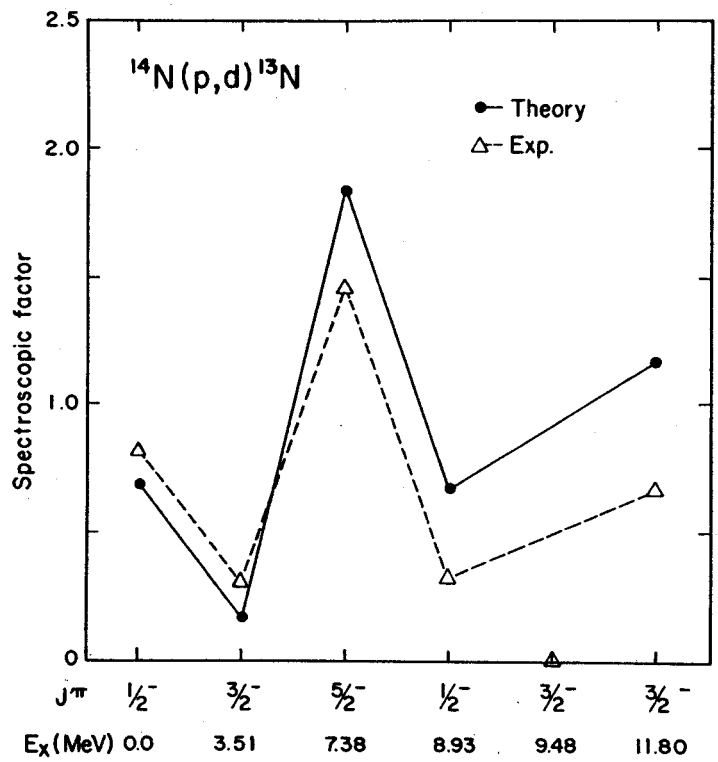

Fig. 3. Comparison of experimentally extracted spectroscopic factors for negative parity levels of ^{13}N to the calculations of Kurath. The error for the experimental values is estimated to be ±20 %.

DWBA calculations were carried out with the Macefield code using deuteron optical parameters of Testoni *et al.* [10]) and the proton optical parameters of Barrett [11])†. The calculated angular distributions were found to be in fair agreement with the data. The comparison for the ground state distribution is shown in fig. 2. Fig. 3 shows the comparison of the experimentally extracted spectroscopic factors to the

† The actual parameters used are the following:
for the protons, $V = 32.53$ MeV, $W = 6.05$ MeV, $r_0 = r' = r_c = 1.25$ fm, $a = a' = 0.65$ fm;
for the deuterons, $V = 53.10$ MeV, $W = 9.90$ MeV, $r_0 = 1.57$, $r' = 1.63$, $r_c = 1.30$, $a = a' = 0.30$ fm;
for the neutron, $r_0 = 1.25$, $a = 0.65$ fm.

calculations of Kurath [6]). The qualitative agreement between experiment and theory is very good, although a sizable difference between the two is seen, especially at the higher excited levels. The results do not agree with the theory as well as the results at 156 MeV, where normalized experimental spectroscopic factors are reported to agree within approximately 20 % for each of the levels [9]). This may reflect in part the

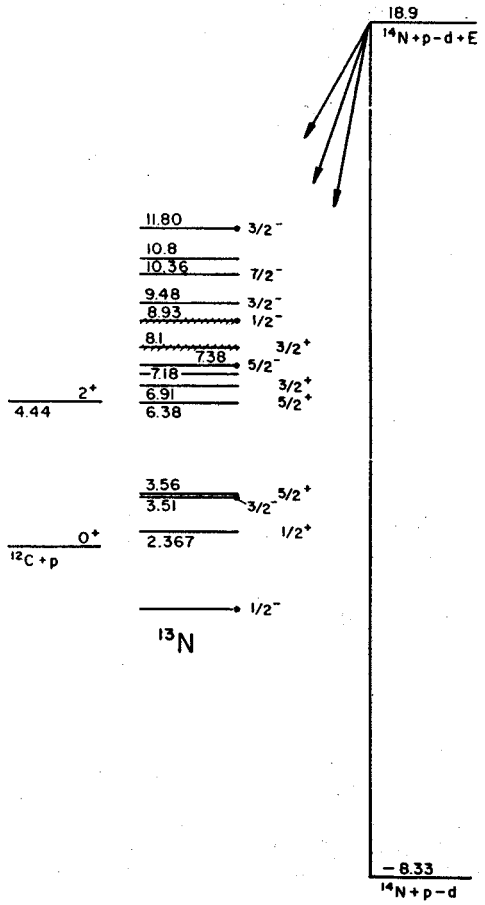

Fig. 4. Energy level diagram of ^{13}N. The heavy dots indicate the strong transitions for the ^{14}N(p, d) reaction.

uncertainty in the extraction of spectroscopic factors, especially for the levels where the Q-values of the reactions are strongly negative, and the bombarding energy is not very high. Fig. 3 also indicates the fact that the 9.48 MeV $\frac{3}{2}^-$ level of ^{13}N, which was previously thought to be the level predicted by the intermediate coupling calculations at 10.6 MeV, is not excited to any significant degree in the (p, d) reaction. A level scheme for ^{13}N showing the states that are strongly excited in this reaction is presented in fig. 4.

As can be seen in the spectrum shown in fig. 1, a number of positive parity levels in ^{13}N are also excited. In particular, the level at 2.37 MeV is the well-known, single-particle, $\frac{1}{2}^+$ state of ^{13}N. From comparison of its angular distribution to a calculation for the pick-up of an $l = 0$ neutron one obtains a total $s_{\frac{1}{2}}$ strength of ≈ 0.02 for the ground state of ^{14}N. If the entire yield of the 2.37 MeV level arises from the pick-up of a $2s_{\frac{1}{2}}$ neutron, the observed strength is considerably greater than that predicted by True [12]). However, if there is some $l = 2$ admixture in the angular

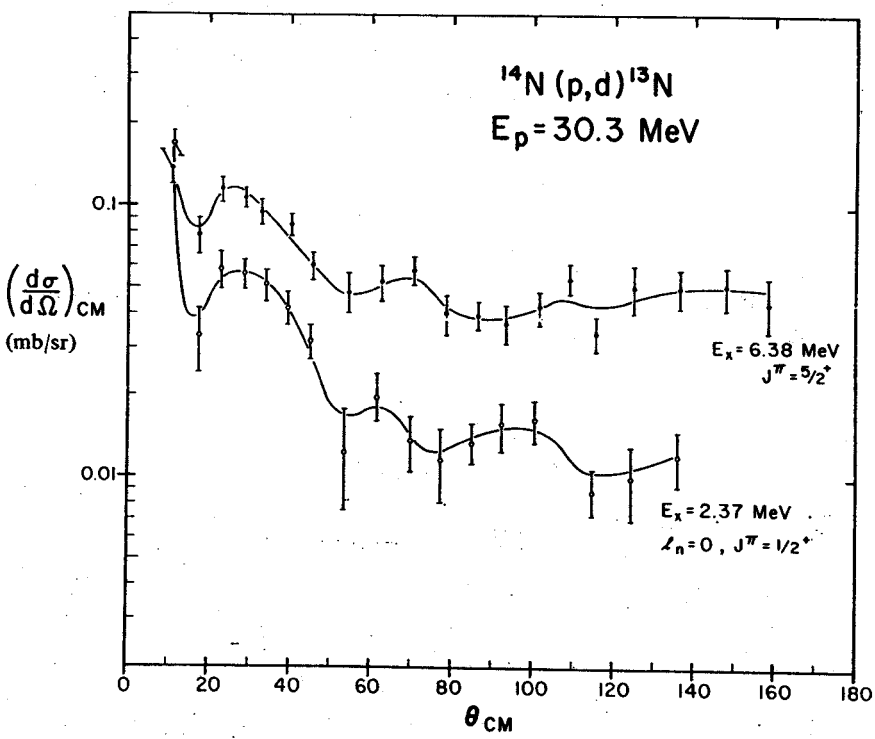

Fig. 5. Angular distributions of deuterons for the 2.37 and 6.38 MeV levels of ^{13}N from the ^{14}N(p, d)^{13}N reaction.

distribution for this state due to a $1d_{\frac{5}{2}}$ pick-up, the experimental result is in better agreement with the calculated ^{14}N wave function.

The 6.38 and 6.90 MeV levels of ^{13}N have been interpreted as belonging principally to a configuration of the ^{12}C(2^+) core plus a $2s_{\frac{1}{2}}$ nucleon [2]). Assuming that the principal contribution to the yield of the 6.38 MeV level ($J^\pi = \frac{5}{2}^+$) arises from a direct process, as the angular distribution shown in fig. 5 indicates, there also appears to be some $d_{\frac{5}{2}}$ admixture in the ground state wave function of ^{14}N. Unfortunately, the single-particle $d_{\frac{3}{2}}$ level of ^{13}N is not resolved in the spectra obtained in this experiment. Its excitation energy is 3.56 MeV and its width has been measured [2]) in a previous experiment as 61 keV; the 3.51 MeV $\frac{3}{2}^-$ level of ^{13}N has a comparable

width ($\Gamma \approx 55$ keV). Thus one is unable to determine to what degree the 3.56 MeV level ($J^\pi = \frac{5}{2}^+$) contributes to the yield of the 3.51 MeV $\frac{3}{2}^-$ level. This means of course that the spectroscopic factor calculated for the 3.51 MeV level and shown in fig. 3 should be reduced.

A recently reported investigation of the angular correlation between the alpha particles from ^{14}N(^{3}He, ^{4}He)^{13}N and the protons from the decay of the 3.51 MeV excitation region in ^{13}N to ^{12}C+p shows a strong interference pattern indicating that a significant fraction of the yield belongs to the 3.56 MeV $d_{\frac{5}{2}}$ level [13]). This result is not surprising since in the present experiment the 6.38 MeV $\frac{5}{2}^+$ level is seen, and therefore one would expect the 3.56 MeV level to have a considerably greater cross section in the (p, d) reaction. Because of the high degree of interest in determining configuration admixtures in the ^{14}N ground state, we are planning to measure, in an experiment similar to that of Detenbeck and Bathia [13]), the d-p correlation in the decay of the 3.51 MeV state, to better assess the relative yield of p- and d-waves in that group.

We wish to thank Mr. D. A. Johnson for his help with computer calculations and Professor A. Galonsky for a number of helpful discussions.

References

1) F. Azjenberg-Selove and T. Lauritsen, Nuclear data tables (National Academy of Sciences-National Research Council, Washington, D.C., 1962) p. 174
2) C. W. Reich, G. C. Phillips and J. L. Russell, Jr., Phys. Rev. **104** (1956) 143
3) S. K. Mark, K. G. Standing and Y. I. Wu, Bull. Am. Phys. Soc. **11** (1966) 471
4) E. Kashy, R. L. Kozub and L. A. Kull, Bull. Am. Phys. Soc. **12** (1967) 52
5) D. G. Fleming, F. Cerny and C. C. Maples, Bull. Am. Phys. Soc. **11** (1966) 904
6) D. Kurath, private communication
7) S. Cohen and D. Kurath, Nuclear Physics **73** (1965) 1
8) F. C. Barker, G. D. Symons, N. W. Tanner and P. B. Treacy, Nuclear Physics **45** (1963) 449
9) D. Bachelier *et al.*, Nuclear Physics **88** (1966) 307
10) J. Testoni, S. Mayo and P. E. Hodgson, Nuclear Physics **50** (1964) 479
11) R. C. Barrett, A. D. Hill and P. E. Hodgson, Nuclear Physics **62** (1965) 133
12) W. W. True, Phys. Rev. **130** (1963) 1530
13) R. W. Detenbeck and T. S. Bathia, Bull. Am. Phys. Soc. **12** (1967) 52

Reprinted from THE PHYSICAL REVIEW, Vol. 163, No. 4, 1066–1073, 20 November 1967
Printed in U. S. A.

(p,d) Reactions with ^{6}Li, ^{7}Li, and ^{9}Be†

L. A. KULL
Cyclotron Laboratory, Michigan State University, East Lansing, Michigan
(Received 27 March 1967; revised manuscript received 22 May 1967)

Excited states of ^{5}Li, ^{6}Li, and ^{8}Be were studied by means of the (p,d) reaction, using 33.6-MeV incident protons. Deuteron groups were observed corresponding to strongly excited levels in ^{5}Li at 0.0 and 16.6 MeV; in ^{6}Li at 0.0, 2.15, 3.57, and 5.38 MeV; and in ^{8}Be at 0.0, 3.1, 11.4, 16.95, 17.62, 18.18, and 19.21 MeV. Small deuteron yields were observed for excited levels of ^{8}Be at 16.6 and 19.15 MeV. Angular distributions were taken for the strongly excited states, and the results were compared with a distorted-wave Born-approximation (DWBA) calculation. Angular distributions for the elastic scattering of 33.6-MeV protons from targets of ^{6}Li, ^{7}Li, and ^{9}Be were measured and fitted with an optical-model calculation to obtain the proton optical parameters used in the DWBA analysis. With a few exceptions, which are discussed, the (p,d) angular distributions are characteristic of a direct pickup of a $1p$-shell neutron. Spectroscopic factors were extracted from the experimental data and were compared with those obtained from theoretical intermediate-coupling calculations in the $1p$ shell. The results are discussed for the high excited states of ^{8}Be, where isotopic-spin mixing is indicated.

INTRODUCTION

THIS paper discribes the results of (p,d) reactions on ^{6}Li, ^{7}Li, and ^{9}Be with 34-MeV protons.[1] Previous studies of the (p,d) reaction on these nuclei have been made at Princeton University with an incident proton energy of approximately 18 MeV in which only the lower excited states of the residual nuclei could be observed.[2–4] The same reactions were also studied at the University of Minnesota using 40-MeV protons,[5,6] where a magnetic spectrometer was used to measure angular distributions out to 40° for most of the lower excited states of the residual nuclei. Many other studies of these reactions have been done at even lower proton energies, most of which examined the properties of the ground state and lower excited states of ^{5}Li, ^{6}Li, and ^{8}Be.[7] The (p,d) reactions on these nuclei have also been investigated with incident proton energies of 95 MeV and above.[8–10] The range of observable excitation energy in the residual nuclei included all the known strongly excited levels; however, the energy resolution did not permit the separation of closely spaced levels.

The purpose of this work was to use an incident proton beam with sufficient energy to allow observation of all the strongly excited levels in ^{5}Li, ^{6}Li, and ^{8}Be, and yet with a low enough energy to enable the use of solid-state detectors with their desirable resolution capabilities. An incident proton energy of about 34 MeV fulfilled both requirements. The data were analyzed to extract spectroscopic factors using a method successfully applied to (p,d) reactions with medium weight nuclei.[11,12] The experimental results were then compared to the theoretical intermediate coupling calculations in the $1p$ shell of Kurath[13] and of Barker.[14]

EXPERIMENTAL DETAILS

General

Negative hydrogen ions were accelerated by the Michigan State University sector-focused isochronous cyclotron to an energy of 33.6 MeV, and a proton beam was extracted by means of a 700-μg/cm^2 aluminum stripping foil.[15] Single turn extraction was obtained with a beam spread of $\sim$0.1%; over-all energy resolution in the deuteron spectra of 100 to 130 keV can then be achieved as is seen in the sample ^{12}C$(p,d)^{11}$C spectrum in Fig. 1. The proton beam energy was determined by the kinematic crossover method[16] and by an independent range-energy calibration. Results from both methods agree to within an experimental uncertainty of 200 keV.

The extracted proton beam was focused on a collimator at the entrance of a 36-in. scattering chamber by means of two quadrupole magnets and a 20° bending magnet. The dimensions of the beam on the target were approximately 0.25-in. high and 0.12-in. wide. A beam which passed through the target was collected at the rear of the scattering chamber in a Faraday cup, and the collected charge was integrated and measured by a current integrator which was calibrated and

* Work supported in part by the National Science Foundation.
[1] L. A. Kull, Bull. Am. Phys. Soc. 12, 17 (1967).
[2] J. G. Likely, Phys. Rev. 98, 1538A (1955).
[3] J. B. Reynolds and K. G. Standing, Phys. Rev. 101, 158 (1956).
[4] E. F. Bennett and D. R. Maxson, Phys. Rev. 116, 131 (1959).
[5] T. H. Short and N. M. Hintz, Bull. Am. Phys. Soc. 9, 391 (1964).
[6] University of Minnesota Linac Laboratory Progress Report, No. 61, 1964 (unpublished).
[7] T. Lauritsen and F. Ajzenburg-Selove, Nucl. Phys. 78, 1 (1966).
[8] W. Selove, Phys. Rev. 101, 231 (1956).
[9] D. Bachelier *et al.*, J. Phys. (Paris) Colloq. 1, 70 (1966).
[10] D. Bachelier *et al.*, International Conference on Nuclear Physics, Gatlinburg, 1966 (unpublished).
[11] E. Kashy and T. W. Conlon, Phys. Rev. 135, B389 (1964).
[12] R. Sherr *et al.*, Phys. Rev. 139, B1272 (1965).
[13] D. Kurath (private communication).
[14] F. C. Barker, Nucl. Phys. 83, 418 (1966).
[15] M. E. Rickey and R. Smythe, Nucl. Instr. Methods 18, 19, 66 (1962).
[16] B. M. Bardin and M. E. Rickey, Rev. Sci. Instr. 35, 902 (1964).

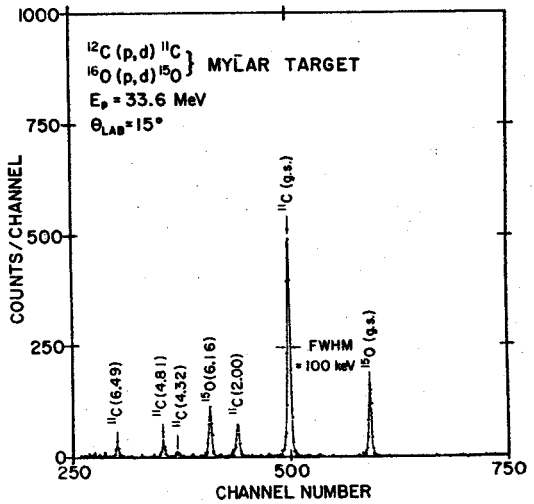

FIG. 1. ^{12}C(p,d)^{11}C deuteron spectrum at 15°. The target was a 1.03-mg/cm² Mylar foil; this thickness represents ~45-keV energy loss to 19-MeV deuterons. Over-all energy resolution in the neighborhood of 100 keV is indicative of single turn extraction as the individual turns are separated by ~80 keV.

checked to be accurate to better than 1%. The beam current was varied from 1–60 nA, depending on the angle at which the counters were placed relative to the beam.

The counters were mounted on an arm which could be remotely positioned to an angular accuracy of ±0.4°; the target angle was determined to within ±2°. Counters were mounted in a $\Delta E-E$ counter telescope configuration. The ΔE counter was a silicon surface barrier detector whose selected thickness varied between 150 and 770 μ, depending on the particular target in use and on the counter arm angle; the E counter was a lithium-drifted silicon detector with a nominal thickness of 3 mm. With this system, deuterons with energies from 7 to 35 MeV could be detected and identified. The angle subtended by the counter in the scattering plane was 1° or less.

Pulses from the E and ΔE detectors were amplified and routed to a Goulding particle identification system.[17] The resulting deuteron spectra were stored in a 4096-channel analyzer. For the particular case of ^{7}Li(p,d)^{6}Li, the energy resolution for the entire system was 125 keV, the major portions of which were electronic noise (~70 keV) and target thickness (~75 keV).

The experimental apparatus used for the measurement of elastically scattered protons was similar to that described above for (p,d) reactions with the following exceptions. A cylindrically shaped cesium iodide crystal, 0.5-in. long and 0.25 in. in diameter, mounted on a photomultiplier tube was used as the proton detector. The over-all energy resolution obtained for these measurements was approximately 500 keV.

[17] F. S. Goulding, D. A. Landis, J. Cerny, and R. H. Pehl, Nucl. Instr. Methods 31, 1 (1964).

Targets

The ^{6}Li targets were made by rolling isotopically enriched lithium (99.32% ^{6}Li) to a thickness of approximately 1.8 to 1.9 mg/cm². Except for brief periods of exposure to air, the targets were kept in a vacuum or in an argon atmosphere to avoid oxygen and nitrogen contamination. The ^{7}Li targets were similarly fabricated from isotopically enriched lithium (99.993% ^{7}Li) with thicknesses of about 2.3 mg/cm². The ^{9}Be target was commercially purchased 2.06-mg/cm² foil of natural beryllium (100% ^{9}Be). These thicknesses represent an energy loss of 60–75 keV for 30-MeV deuterons.

EXPERIMENTAL RESULTS

^{6}Li(p,d)^{5}Li

Figure 2 is a deuteron energy spectrum taken at $\theta_{lab}=15°$ showing deuteron groups corresponding to the ground state ($J^\pi=\frac{3}{2}^-$) and 16.65-MeV state ($J^\pi=\frac{3}{2}^+$) of ^{5}Li. The location of the broad ground state of ^{5}Li ($\Gamma=1.3$–1.4 MeV) just above the $\alpha+p$ separation energy (Fig. 3) is an inducement to use a simple cluster model[18] description of the state, consisting of an α particle coupled to a proton with orbital angular momentum $l=1$. Possible spin and parity assignments for this configuration are $\frac{3}{2}^-$ and $\frac{1}{2}^-$. A very broad $\frac{1}{2}^-$ level ($\Gamma=3$–5 MeV) has been reported at an excitation energy of 5 to 10 MeV.[7] A deuteron group corresponding to this level has not been identified in the energy spectra, but because of its large width, it may be impossible to isolate it from the background due to three-body breakup. It is also possible that a significant fraction of the yield of this $\frac{1}{2}^-$ level lies below 5-MeV excitation energy, and that the deuterons corresponding

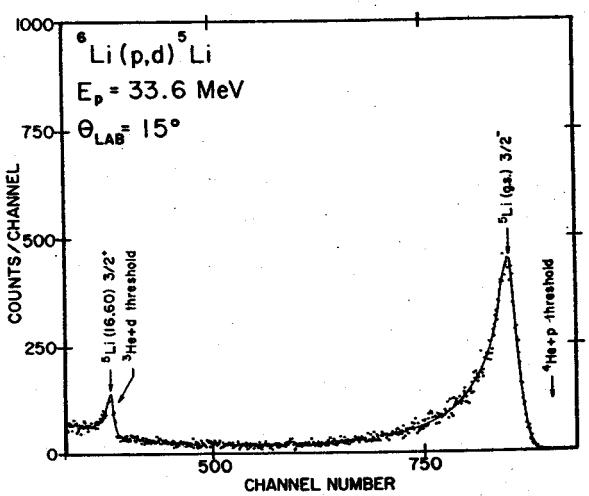

FIG. 2. ^{6}Li(p,d)^{5}Li deuteron spectrum at 15°. The long tail on the ground-state peak may include a contribution from a previously reported $J^\pi=\frac{1}{2}^-$ state.

[18] K. Wildermuth and Th. Kanellopoulos, Nucl. Phys. 1, 150 (1958).

to this state have been included in the tail of the ground-state peak.

No other levels have been reported[4] below the relatively narrow ($\Gamma=360$ keV) 16.6-MeV state which lies just above the ^{3}He+d separation energy as shown in Fig. 3. There, in a situation analogous to that of the ground state, a simple cluster-model description consisting of a ^{3}He nucleus coupled to a deuteron with $l=0$ seems appropriate for this state. The above configuration allows J^π values of $\frac{3}{2}^+$ and $\frac{1}{2}^+$.

The 16.6-MeV level of ^{5}Li($J^\pi=\frac{3}{2}^+$) was strongly excited in this reaction and a search was made in the vicinity of this peak in order to detect the presence

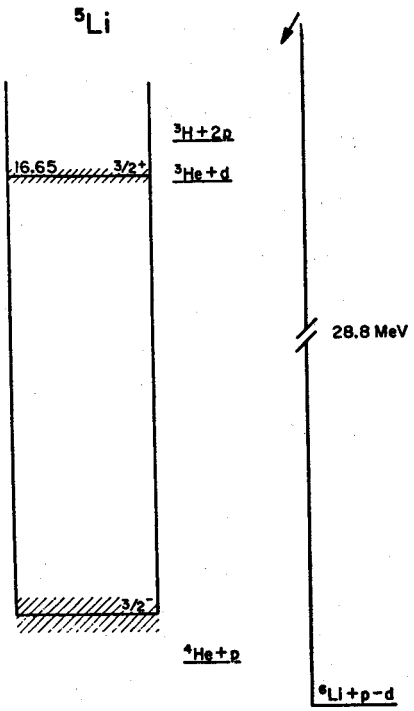

FIG. 3. Energy-level diagram of ^{5}Li. Only the states observed in the ^{6}Li(p,d)^{5}Li reaction are shown and the excitation energies listed are those given in Ref. 7.

of the $\frac{1}{2}^+$ member of the doublet. Various incident proton energies were tried between 30 and 40 MeV, as this was the experimentally obtainable range of energies where the available phase space for competing three-body breakup was calculated to be smallest.[19] No evidence was found that would locate the excitation energy of the $\frac{1}{2}^+$ level. There was also no indication that a $(\frac{3}{2},\frac{5}{2})^+$ state previously reported at 20-MeV excitation is excited in this reaction.[20]

Figure 4 shows a comparison of the angular distributions for the reaction ^{6}Li(p,d)^{5}Li (g.s.) calculated using

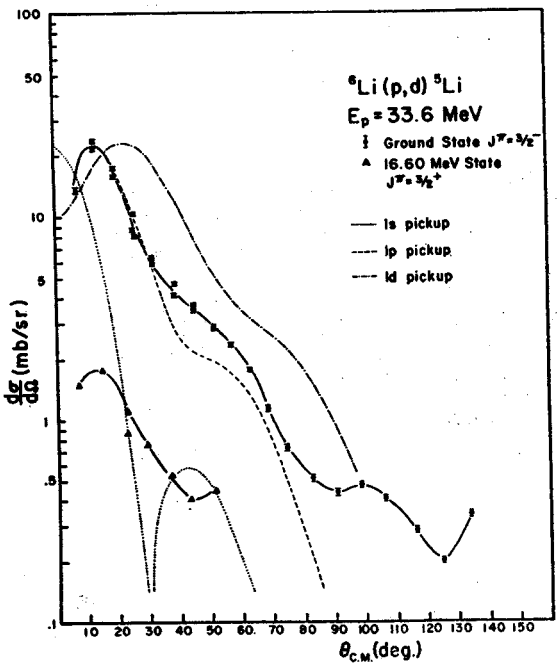

FIG. 4. ^{6}Li(p,d)^{5}Li angular distributions. The error bars shown only represent the uncertainty due to statistics and the solid lines are drawn to guide the eye. Results from DWBA calculations for the ground state differential cross section are shown assuming the neutron was picked up from the 1s, 1p, and 1d shells.

the distorted wave Born approximation assuming the neutron was picked up from the 1s, 1p, and 1d shells (orbital angular momenta $l_n=0$, 1, and 2, respectively). In the same figure it can be seen that the experimental angular distribution for the ground state of ^{5}Li shows a characteristic shape for transfer of a neutron from the 1p shell ($l_n=1$) by a direct reaction mechanism (Fig. 4). The angular distribution for the 16.6-MeV state could not be obtained for lab angles greater than

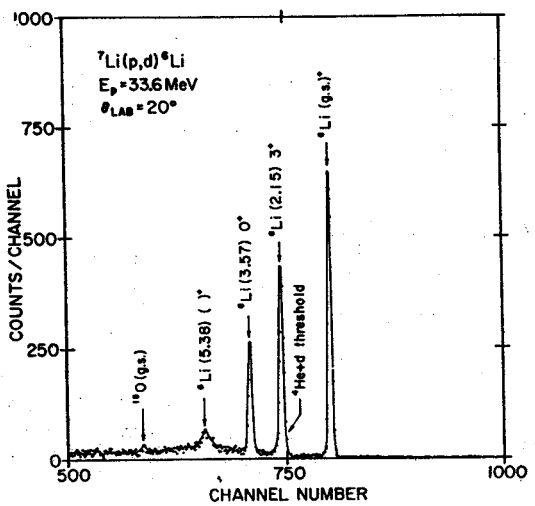

FIG. 5. ^{7}Li(p,d)^{6}Li deuteron spectrum at 20°. A small peak due to ~1.5% oxygen contamination can be seen.

[19] I. L. Rozental, Zh. Eksperim. i Teor. Fiz. 28, 118 (1955) [English transl.: Soviet Phys.—JETP 1, 166 (1955)].
[20] T. A. Tombrello, A. D. Bacher, and R. J. Spiger, Bull. Am. Phys. Soc. 10, 423 (1965).

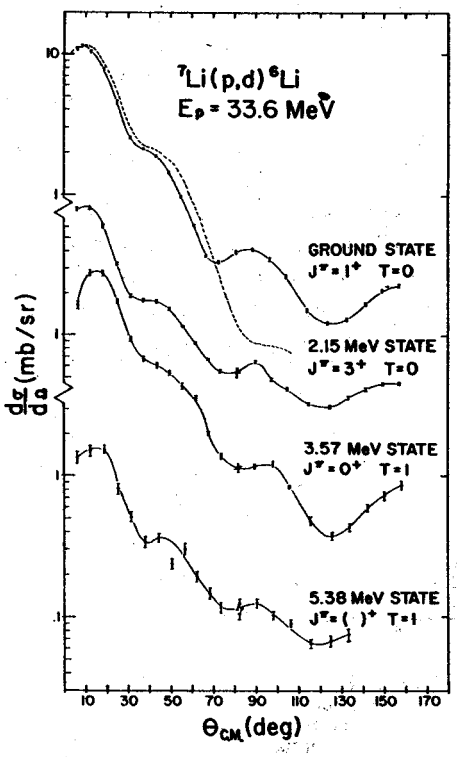

FIG. 6. ^{7}Li$(p,d)^6$Li angular distributions. The DWBA fit to the ground-state differential cross section is shown by a dashed line.

35° because the deuteron peak could not be distinguished from a strong background due to three-body breakup. This state is excited by the pickup of a 1s neutron from ^{6}Li but, because of the small amount of data, little can be said concerning the shape of the angular distribution.

^{7}Li$(p,d)^6$Li

Four deuteron groups were observed in the energy spectra from the ^{7}Li$(p,d)^6$Li reaction corresponding to states of ^{6}Li at 0.0-, 2.15-, 3.57-, and 5.38-MeV excitation energy (Fig. 5). A small peak corresponding to the ground state of ^{15}O indicates the presence of a small amount of oxygen contamination on the target (less than 1.5%). No evidence for any other strongly excited states was found up to 18 MeV of excitation energy for ^{6}Li. Deuteron groups corresponding to the positive parity states of ^{6}Li at 4.57 and 6.0 MeV were not observed; however, these states are broad and if weakly excited the peaks would be difficult to extract from the background. The shapes of the angular distributions for the 0.0-, 2.15-, 3.57-, and 5.38-MeV states are characteristic of $l_n=1$ pickup (Fig. 6). This fixes the relative parity between the initial and final states[21]; in particular, this assigns a positive parity to the 5.38-MeV level. A positive parity fits in with the tentative $T=1$ isospin assignment[7] for this state and places it in the isospin multiplet of which 1.80-MeV state of ^{6}He $[J^\pi=(2)^+]$ is a member.

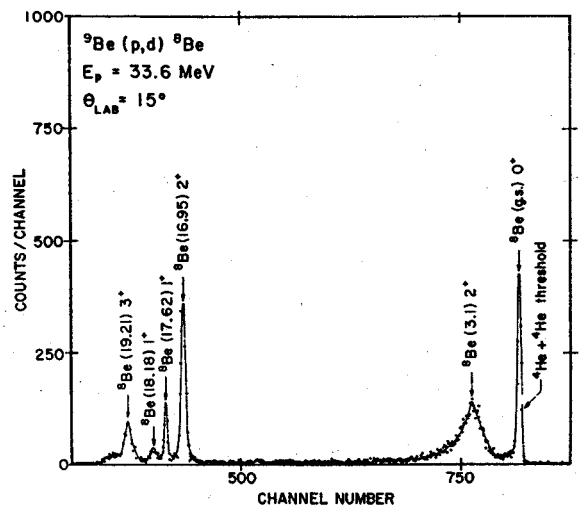

FIG. 7. ^{9}Be$(p,d)^8$Be deuteron spectrum at 15°.

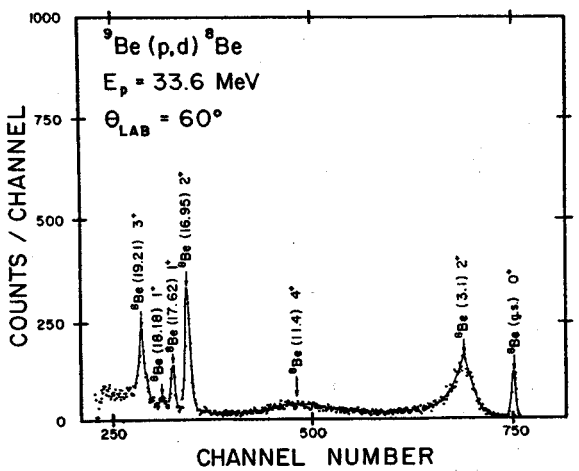

FIG. 8. ^{9}Be$(p,d)^8$Be deuteron spectrum at 60°. The broad peak corresponding to the 11.4-MeV level of ^{8}Be can be clearly seen at back angles where its yield is comparable to that of the narrower levels.

It is interesting to note that the slopes of the first peak of the angular distributions for the $T=0$ states at 0.0 and 2.15 MeV are much steeper than those of the lowest $T=1$ states at 3.57 and 5.38 MeV. This may have some implication concerning the isotopic-spin dependence of the reaction mechanism.

^{9}Be$(p,d)^8$Be

The energy spectra from the reaction ^{9}Be$(p,d)^8$Be (Figs. 7 and 8) show deuteron groups corresponding to strongly excited levels of ^{8}Be at 0.0, 3.1, 11.4, 16.95, 17.62, 18.18, and 19.21 MeV. A very small yield was observed for excited states of ^{8}Be at 16.6 and 19.15 MeV. The first three levels of ^{8}Be can be understood, at least qualitatively, by a cluster model of two α

[21] S. T. Butler, Phys. Rev. 106, 272 (1957).

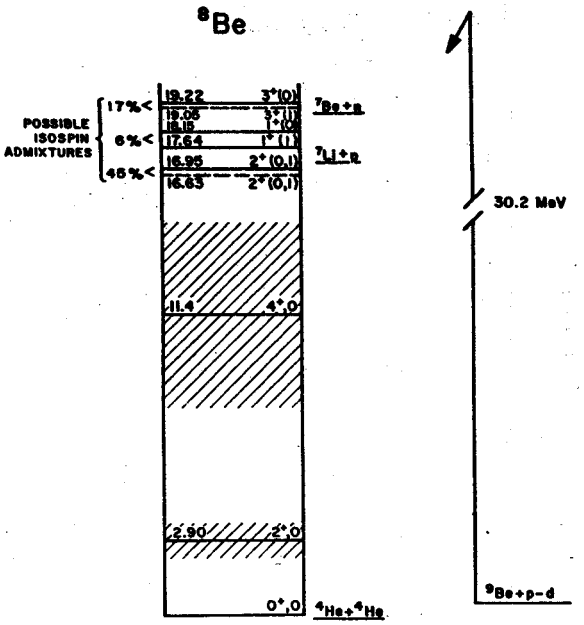

FIG. 9. Energy-level diagram of ^{8}Be. The levels drawn in with dashed lines are those weakly excited in the ^{9}Be$(p,d)^8$Be reaction while those drawn in with the solid lines correspond to strongly excited levels. Also shown are the isospin admixtures which have been calculated for $J^\pi=2^+$, 1^+, and 3^+ doublets (Ref. 14).

particles excited into the rotational sequence 0^+, 2^+, and 4^+ (Fig. 9).[22] Measurements of the differential cross section for the 11.4-MeV state ($J^\pi=4^+$) were made from 40° to 140° in the lab with a large uncertainty due to the width of the state ($\Gamma\sim7$ MeV)[7] and a high background. The data show little structure in this range, the average value of the cross section falling between 0.02 and 0.05 mb/sr MeV at the resonance. The angular distribution does not exhibit the forward peaking characteristic of a direct reaction, since the peak could not be seen at angles less than 35°. This leads to the conlcusion that this state is excited principally by a compound nucleus mechanism and not by a direct process in which some $1f$ admixture in the ground state of ^{9}Be contributes to the cross section.[10]

The next set of known levels of ^{8}Be appear in the region of the ^{7}Li+p and ^{7}Be+n separation energies (Fig. 9). Previous experimental evidence has established the fact that isospin mixing is present within each of the three doublets ($J^\pi=2^+$, 1^+, and 3^+) in this region of excitation energy.[22–27] Wave functions for these doublet states have been calculated by mixing intermediate-coupling shell-model wave functions of pure isospin with a charge-dependent interaction.[12] The

TABLE I. Experimental cross section ratios and isospin admixtures calculated by Barker[a] for the $J=1^+$, 2^+, and 3^+ doublets.

Doublet	Ratio of cross sections (34 MeV)	Ratio of cross sections (41 MeV)[b]	Isospin admixtures[c] (amplitude squared) as calculated by Paul[a]
(16.6)/(16.9)	<1/20	1/25	45%
(17.6)/(18.2)	2.6	3.5	6%
(19.1)/(19.2)	<1/20		17%

[a] Reference 14.
[b] Reference 28.
[c] 50% admixture represents a doublet with maximal isospin mixing and 0% a doublet with states of pure isospin.

mixing coefficients were obtained by fitting existing experimental data and are given in Table I. The ratio of spectroscopic factors $S(16.6)/S(16.95)$ calculated using this model is 1/45,[14] whereas the ratio obtained experimentally is less than 1/20.

Some indication of the amount of isospin mixing within the doublets can be obtained if the single-particle cluster model is used to describe the states.[28] In this case, the (p,d) reaction will excite only one

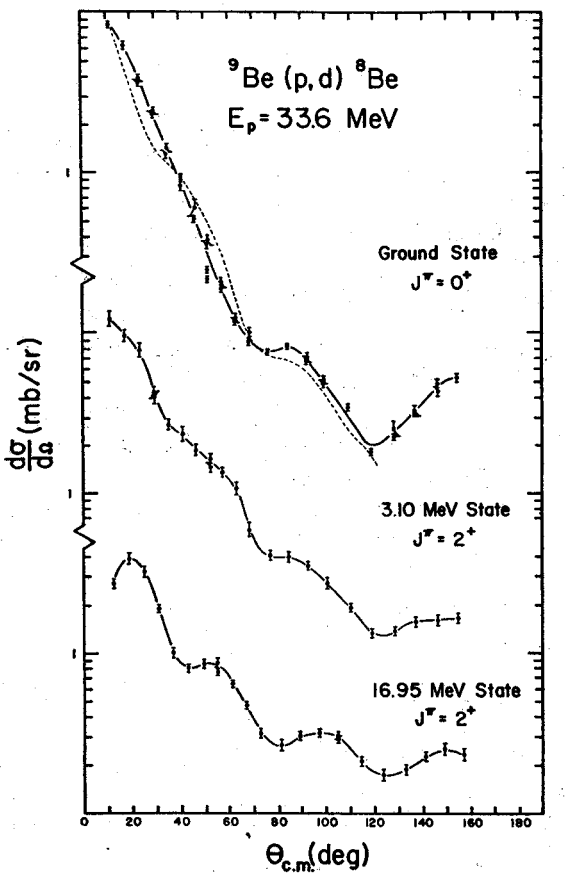

FIG. 10. ^{9}Be$(p,d)^8$Be angular distributions for the 0.0, 3.1, and 16.95-MeV states of ^{8}Be. The DWBA fit to the ground-state differential cross section is shown with a dashed line.

[22] K. Wildermuth, Nucl. Phys. 31, 478 (1962).
[23] J. B. Marion, Phys. Letters 14, 315 (1965).
[24] C. P. Browne and J. R. Erskine, Phys. Rev. 143, 683 (1966).
[25] P. Paul, Z. Naturforsch. 21, 914 (1966).
[26] P. Paul, D. Kohler, and K. A. Snover, Bull. Am. Phys. Soc. 11, 26 (1966).
[27] G. T. Garvey, J. Cerny, and H. Pugh, Bull. Am. Phys. Soc. 11, 26 (1966).

member of the doublet if the pair is maximally mixed in isospin (50%). Conversely, if the members of the doublet are states of pure isospin ($T=0$ or 1), both states should be observed by the (p,d) reaction with the same yield. Table I shows the data to be in general agreement with this simple model. The experimentally measured widths for the 16.95- and 19.21-MeV deuteron groups of 103±15 and 208±30 keV, respectively, are in agreement with the previously obtained values[7] of 83±10 and 190 keV, insuring that only one of the states in these doublets is strongly exctied. The experimentally obtained cross-section ratios for these doublets are in agreement with those obtained at $E_p=40$ MeV.[28]

The angular distributions for all strongly excited states of ^{8}Be (except for the above-mentioned 4^+ state) exhibit the characteristic shape for $l_n=1$ pickup (Figs. 10 and 11). The differential cross section measurements for these states are in reasonable agreement with those obtained for $E_p=36$ MeV.[29] The relative flattening of the differential cross sections as the excitation energy of the state increases is a Q-value effect and was reproduced in the distorted-wave Born-approximation (DWBA) calculations.

DWBA ANALYSIS

Angular distributions for the elastically scattered protons from targets of ^{6}Li, ^{7}Li, and ^{9}Be were measured from 12° to 130° in the lab with an incident proton energy of 33.6 MeV. In the case of ^{7}Li, the proton groups corresponding to the ground state and the 0.48-MeV state of ^{7}Li could not be resolved. Angular distributions for both states had been measured at $E_p=25$ MeV[30] and the same relative yields were assumed in computing the differential cross section for the ground state of ^{7}Li at $E_p=33.6$ MeV. This amounted to an average correction of 2% at forward angles and between 15% and 25% at backward angles.

The ABACUS computer code,[31] which employs a least-squares criterion, was used to fit the experimental distributions with an optical potential of the form

$$U_c - Vf(r,R,a_R) - i4a_I W\frac{d}{dr}f(r,R,a_I) - \left(\frac{1}{mc}\right)^2 V_{so}\frac{d}{r\,dr}f(r,R,a_R).$$

Here

$$f(r,R,a)=1/e^x+1;\quad x=r-RA^{1/3}/a,$$

and U_c is the Coulomb potential from a uniformly charged sphere of radius $RA^{1/3}$ F. A compilation of the optical parameters obtained for proton scattering is given in Table II.

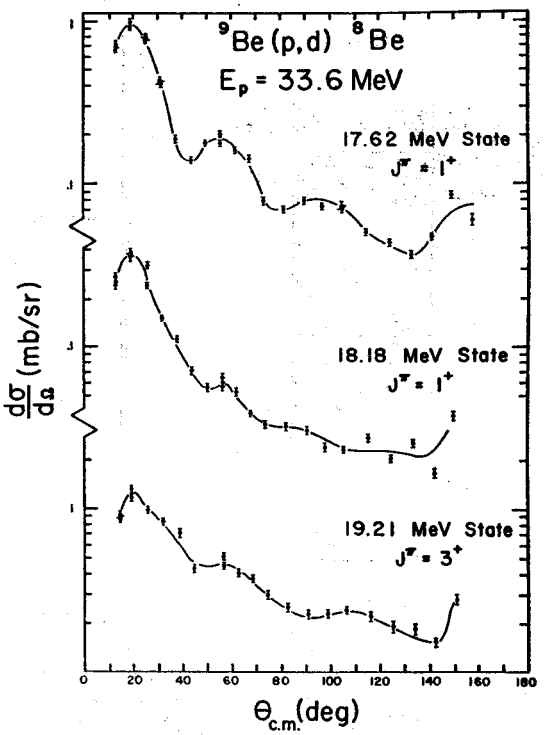

FIG. 11. ^{9}Be$(p,d)^8$Be angular distributions for the 17.62-, 18.18-, and 19.21-MeV states of ^{8}Be.

Data for the elastic scattering of deuterons from ^{9}Be at $E_d=27.7$ MeV[32] and from ^{7}Li at $E_d=28$ MeV[33] were also fitted by an optical potential using the ABACUS code; the parameters obtained are given in Table III. No spin-orbit term was included in the optical potential and the imaginary diffuseness (a_I) was set equal to the real diffuseness (a_R).

The DWBA analysis was carried out using the Masefield computer code. Geometry parameters for the picked-up neutron were $a_n=0.65$ F and $R_n=1.25A^{1/3}$ F. No spin-orbit term was included in the neutron potential.

The DWBA calculations led to an interesting result, in that it was impossible to get a reasonable fit to the (p,d) angular-distribution data using the optical parameters in Tables II and III. However, if the imaginary

TABLE II. Proton optical parameters.

Target	V (MeV)	W (MeV)	V_{SO} (MeV)	R(F)	a_R(F)	a_I(F)
^{6}Li	44.56	6.92	7.38	1.124	0.578	0.685
^{7}Li	46.45	6.34	7.18	1.187	0.478	0.727
^{9}Be	48.92	6.44	6.30	1.139	0.613	0.616

[28] J. B. Marion and C. A. Ludemann, Bull. Am. Phys. Soc. 11, 26 (1966).
[29] I. Slaus (private communication).
[30] G. Grawley and S. Austin, International Conference on Nuclear Physics, Gatlinburg, 1966 (unpublished).
[31] E. H. Auerbach, Brookhaven National Laboratory Report No. BNL6562, ABACUS-2, 1962 (unpublished).
[32] R. J. Slobodrian, Phys. Rev. 125, 1003 (1962).
[33] R. J. Slobodrian, Nucl. Phys. 32, 684 (1962).

TABLE III. Deuteron optical parameters.

Target	V(MeV)	W(MeV)	R(F)	a_R(F)
^{7}Li[a]	79.45	11.23	1.094	0.769
^{9}Be	74.03	11.67	1.239	0.736

[a] Data renormalized by 0.85.

well of the deuteron optical potential (W_d) is increased by a factor of three in the case of ^{9}Be$(p,d)^8$Be and a factor of 4 in the cases of ^{7}Li$(p,d)^6$Li and ^{6}Li$(p,d)^5$Li, reasonable fits are obtained in all cases (Figs. 4, 6, 10). A 20% variation of any of the other parameters would not produce similar results. The same situation was encountered in applying a DWBA analysis to the data from ^{4}He$(p,d)^3$He with $E_p=31$ MeV.[34]

This anomalously large value of W_d may be a consequence of using the optical-model potential to describe the interaction of the scattered deuteron with a relatively small number of nucleons which comprise the scattering nucleus. It may also be due to the fact that in the optical model, the deuteron is treated as a point particle, whereas the weak coupling within the deuteron itself is likely to be sensitive to deformations caused by interactions with the target nucleus. No similar effect was noted, however, when optical parameters obtained from elastic scattering were used in DWBA calculations of the (p,d) reaction with heavier nuclei.[11] Thus it appears that the first possibility may be the more relevant of the two.

SPECTROSCOPIC FACTORS

The experimental spectroscopic factor $S_{A\to B}$ for the transition $A(p,d)B$, which proceeds by a direct pickup of $1p_{3/2}$ and $1p_{1/2}$ neutrons, was calculated from the expression

$$S_{A\to B}=\sigma_{\mathrm{EXP}}/1.6\sigma^M{}_{\mathrm{DWBA}},$$

σ^M is the magnitude of the differential cross section at the angle for which it has its characteristic $l_n=1$ maximum. The DWBA result, which uses the zero-range approximation, is multiplied by a factor of 1.6 to make it approximately equivalent to a calculation using the effective-range theory.[35,36]

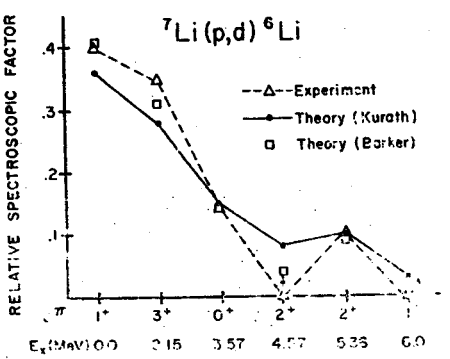

FIG. 12. Comparison of theoretical and experimental relative spectroscopic factors for ^{7}Li$(p,d)^6$Li. The arrows above the levels at 4.57- and 6.0-MeV excitation energy are used to indicate that small deuteron yields from these levels may not have been observed because of the width of these states and a high background.

The theoretical spectroscopic factors were obtained for the transition $A(p,d)B$ from the coefficients of fractional parentage, β_{lj}, calculated by Kurath using the intermediate-coupling model for $1p$ shell nuclei.[21] The theoretical spectroscopic factor $S_{A\to B}$ is given by

$$S_{A\to B}(l_n=1;j_n=\tfrac{3}{2},\tfrac{1}{2})=n(T'\tfrac{1}{2}M_T'\tfrac{1}{2}|TM_T)^2\sum_{j=\frac{1}{2},\frac{3}{2};l=1}\beta_{lj}{}^2,$$

n is the number of nucleons in the $1p$ shell of A and $(|)$ is a Clebsch-Gordan coefficient with T', M_T' and T, M_T; the isotopic spin and its projection for the final state and initial state, respectively. As calculated above, the spectroscopic factors relate to states with pure isospin. Another set of spectroscopic factors for the reaction ^{7}Li$(p,d)^6$Li was obtained from the shell-model calculations of Barker.[14]

Theoretical and experimental relative spectroscopic factors were obtained by normalizing the sum of the spectroscopic factors for each reaction to 1. Considering the difficulty in extracting meaningful absolute spectroscopic factors from the DWBA comparison to the data, the relative spectroscopic factor was calculated to provide a better look at the relative amount of overlap between the target nucleus's ground-state wave function and the wave functions of the residual nucleus's different excited states plus a $1p$-shell neutron. The comparisons of experimental results to theoretical calculations are shown for ^{7}Li$(p,d)^6$Li and ^{9}Be$(p,d)^8$Be in Figs. 12 and 13(a).

The agreement between theory and experiment for ^{7}Li$(p,d)^6$Li is good. The experimental spectroscopic factors of zero for the 4.57- and 6.0-MeV states could be due to the difficulty in extracting the small deuteron yields, corresponding to these broad states, from the background.

Figure 13(a) shows the large discrepancy between theory and experimental spectroscopic factors for the ^{8}Be $J^\pi=2^+$ doublet at 16.6 and 16.9 MeV and also for the $J^\pi=3^+$ doublet at 19.1 and 19.2 MeV. This disagreement could result from the fact that the experimental spectroscopic factors have been extracted using a DWBA calculation with deuteron potential parameters obtained from the elastic scattering of deuterons from the ground state of ^{9}Be, whereas the nucleus is actually left in a state 17 to 19 MeV in excitation above the ground state of ^{8}Be. The effect of this approximation on the extraction of the spectroscopic factor is not known, but it should be noted that the same large discrepancies are not present in the results for the

[34] S. M. Bunch, H. H. Foster, and C. C. Kim, Nucl. Phys. 53, 241 (1964).

[35] R. Satchler (private communication).

[36] N. Austern, in *Fast Neutron Physics*, edited by J. B. Marion and J. L. Fowler (Interscience Publishers Inc., New York, 1961), Vol. II.

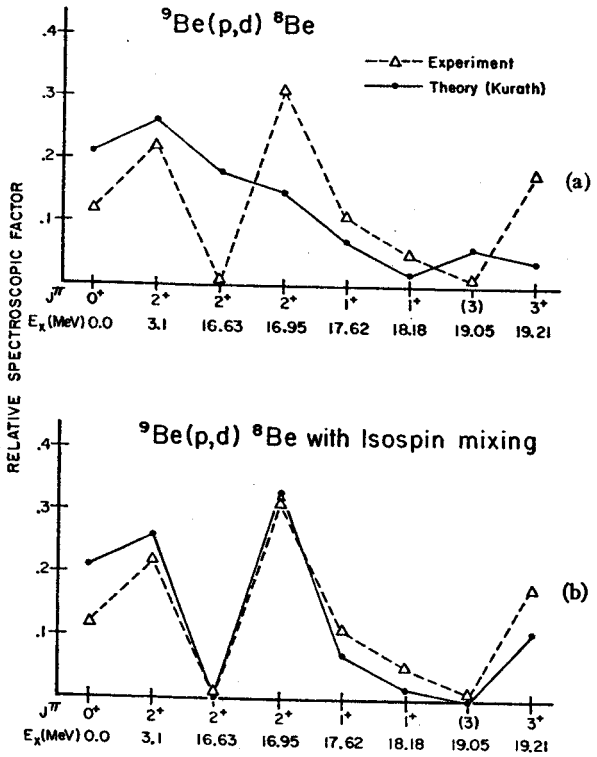

FIG. 13. Comparison of theoretical and experimental relative spectroscopic factors for ^{9}Be$(p,d)^8$Be. Good agreement is obtained except for the $J^\pi=2^+$ and 3^+ doublets. If the sum of the theoretical spectroscopic factors within these doublets in (a) is fixed, but the ratio of strengths is adjusted to best fit the experimental data, (b) is obtained. This is equivalent to mixing states with definite isospin within the doublets.

$J^\pi=1^+$ doublet at 18 MeV excitation. This last observation fits in with another possible explanation for the observed disagreement. The theoretical calculations assume the states to be pure in isotopic spin, whereas previous experiments have shown considerable isospin mixing to be present within the $J^\pi=2^+$ and 3^+ doublets. If two states of pure isospin are mixed to produce two new final states of indefinite isospin, the ratio of spectroscopic factors for the isospin mixed pair will be different, in general, from that originally found for the pair with pure isospin. However, the sum of the spectroscopic factors for each pair is the same for both cases. Assuming, therefore, that the experimental results only represent a mixing of the theoretical isospin pure states, there should be agreement between theoretical and experimental sums of spectroscopic factors for each doublet. The sum of the experimental spectroscopic factors for the $J^\pi=2^+$ and 3^+ doublets is 0.32 and 0.19, respectively, whereas the sum of the theoretical spectroscopic factors for the same $J^\pi=2^+$ and 3^+ doublets is 0.33 and 0.11, respectively. This same approach was also used in obtaining Fig. 13(b) where the ratio of spectroscopic factors within the $J^\pi=2^+$ and 3^+ doublets has been adjusted to give better agreement with experiment, while the sum of spectroscopic factors within the doublets is the same as that in Fig. 13(a). Thus, good agreement with theory can be obtained, assuming that the isospin mixing with the $J^\pi=2^+$ and 3^+ doublets is the cause of the major differences observed.

SUMMARY

In general, there is relatively good agreement between experimentally obtained relative spectroscopic factors and the calculations of Kurath[13] and of Barker.[14] The inclusion of isotopic-spin mixing within the $J^\pi=2^+$ and 3^+ doublets of ^{8}Be resolves the large difference between experiment and theory for these cases. In fact, considering the good agreement obtained between theory and experiment in the case of ^{7}Li$(p,d)^6$Li, the discrepancies noted in the ^{9}Be$(p,d)^8$Be reaction illustrate in a very concise manner that the wave functions of the ^{8}Be 2^+ and 3^+ states contain admixtures of $T=0$ and $T=1$. With this modification, the intermediate-coupling model appears to give a satisfactory picture of lower $1p$-shell nuclei with regard to spectroscopic factors obtained by (p,d) reactions.

No evidence was found for any $2s-1d$ shell admixtures in the ground-state wave functions of ^{6}Li, ^{7}Li, and ^{9}Be, and the strongly excited 16.6-MeV state of ^{5}Li is the only case where neutron pickup from the $1s$ shell was observed with any appreciable yield. The 11.4-MeV state of ^{8}Be$(J^\pi=4^+)$ appears to be excited by a compound nucleus mechanism and not because of any $1f$ admixture in the ^{9}Be ground-state wave function.[10] From this study, therefore, the ground states of ^{6}Li, ^{7}Li, and ^{9}Be appear to consist of tightly bound $1s$ cores, the remaining nucleons residing in the $1p$ shell with no sizable admixtures from other shells.

ACKNOWLEDGMENTS

The author is indebted to Professor E. Kashy for suggesting this work and for helpful discussions of the results. Many thanks go to R. L. Kozub and P. Plauger for assistance in taking data.

Reprinted from THE PHYSICAL REVIEW, Vol. 162, No. 4, 957–962, 20 October 1967
Printed in U. S. A.

Excitation Energy of the First Excited State of C^{12}, and Observation of a Coherent Doppler Effect*

J. J. KOLATA,† R. AUBLE,‡ AND A. GALONSKY
Department of Physics, Michigan State University, East Lansing, Michigan
(Received 19 October 1966; revised manuscript received 17 April 1967)

The excitation energy of the first 2^+ state in C^{12} has been determined to be 4440.0 ± 0.5 keV by means of the $(p,p'\gamma)$ reaction at 23 MeV incident proton energy. γ rays were detected by a Ge(Li) detector in coincidence with inelastically scattered protons to reduce Doppler broadening. An anomaly in which a symmetrical doublet appeared in the γ-ray singles spectrum observed at 90° to the beam direction is explained on the basis of a coherent Doppler effect involving selective population of the magnetic sublevels of the 2^+ state in the inelastic scattering process.

I. INTRODUCTION

THE general utility of the levels of C^{12} as calibration standards for magnetic spectrometers makes desirable a high-precision determination of their excitation energies. The high-resolution capability of Ge(Li) detectors makes such a measurement possible for the strongly excited first 2^+ level. The present measurement was carried out by detecting de-excitation gamma rays following the $C^{12}(p,p')C^{12*}$ reaction. Doppler broadening effects were removed by detecting inelastically-scattered protons in coincidence with the γ radiation. The measurements were made with the γ detector at 0°, 90°, and 180° relative to the C^{12} recoil direction. This choice of angles minimizes the sensitivity of the measurement to errors in recoil velocity (90°) and detection angle (0° and 180°).

An anomaly was observed in the γ-ray singles spectra taken at 90° to the incident beam direction. A symmetric double peak appeared at this angle, with the valley between the two peaks centered on the expected location of the double-escape peak corresponding to the first excited state of C^{12}. The double peak became asymmetric when the detector was moved to other angles, and finally one peak disappeared completely at 40° and 140° to the beam direction. The explanation of these observations is given in Sec. IIIB.

II. EXPERIMENTAL METHOD

A. Beam Line

The experimental arrangement is shown in Fig. 1. A beam of 23-MeV protons from the Michigan State University Isochronous Cyclotron was collimated by a pair of remotely adjustable slits, focused by a quadrupole doublet, and directed by a steering magnet through a 4-cm-high by 1.2-cm-wide aluminum collimator. A small target chamber containing an 0.2-mm-thick

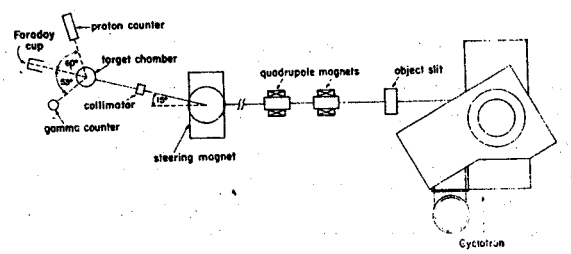

FIG. 1. The experimental arrangement (not to scale), with the proton and γ counters shown set up for a "0°" measurement.

* Work supported in part by the National Science Foundation.
† National Science Foundation Co-operative Graduate Fellow.
‡ Present address: Oak Ridge National Laboratory, Oak Ridge, Tennessee.

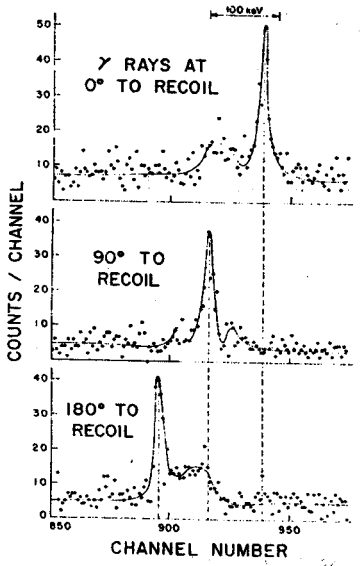

FIG. 2. γ-ray spectra taken in coincidence with protons scattered inelastically, exciting the 4.44-MeV level in C^{12}. $\theta_p = 60°$; $\theta_{recoil} = 53°$. The background illustrated is the sum of an almost flat true Compton distribution and an appropriately scaled singles spectrum, as discussed in Sec. IIIA. Energy dispersion = 3.41 keV/channel.

polystyrene target was located at a distance of 2 m from this collimator. The polystyrene was in the form of a narrow strip, 5 cm long and 5 mm wide. This enabled us to attain the required angular definition of the beam without inserting a collimator near the target area, thus keeping to a minimum the flux of background γ radiation reaching the Ge(Li) detector. The target chamber was electrically insulated from the beam transport system so that the fraction of the beam current striking its walls could be monitored. This varied from 0.1 to 0.3% of the beam current collected in a 5-cm-diameter Faraday cup which was placed 2 m beyond the target chamber. All experimental data were obtained with beam currents of from 1 to 5 nA.

The beam energy was determined from the energy spectrum of a NaI(Tl) monitor counter detecting protons scattered from C^{12}. We were able to measure the beam energy to ±0.25 MeV from kinematics, after making appropriate corrections for proton energy loss in the target, in the 0.03-mm-thick Mylar window of the target chamber, and in the 0.0125-mm-thick Havar window of the monitor counter itself.

B. Detectors and Electronics

Scattered protons were detected by a NaI(Tl) scintillation counter preceded by a 3.25-cm-high by 0.65-cm-wide collimator. This collimator was placed from 7.5 to 10 cm from the target, at an angle of 60° relative to the incident beam. The ratio of 2^+ inelastic scattering to elastic scattering has a maximum at this angle. At the corresponding recoil angle of 53°, the energy of the C^{12} recoil is 1.71 MeV for an incident proton energy of 23 MeV, so that the maximum Doppler shift is ±78 keV.

The γ-ray detector was a gallium-doped, lithium-drifted germanium wafer which was operated at liquid-nitrogen temperature with a 400-V bias. Under these conditions, the best energy resolution obtained (with a Co^{56} calibration source) was 6 keV full width at half-maximum (FWHM). Orientation of the wafer, whose dimensions were 0.8 cm×1.7 cm×2.2 cm, was always that which gave the smallest angular acceptance. This was particularly important in the 90° coincidence runs in which the gamma-ray energy has the greatest variation with angle. Target-to-detector distance varied from 9 to 14 cm.

Conventional circuitry was used to determine $p'-\gamma$ coincidences. Protons scattered inelastically from C^{12}, exciting the first 2^+ level, were selected by a single-channel analyzer and coincidence was required with a γ event appearing in the double-escape peak at 3.42 MeV. The resultant logic pulse was used to open the linear gate of a 1024-channel analyzer. The resolving time (2τ) of the coincidence circuitry was 50 nsec (FWHM).

C. Calibration

The spectrum of Co^{56} was used as a standard to obtain an absolute γ-energy calibration. Peaks appearing at 3254.5 and 3451.1 keV in this spectrum bracket the region in which the double-escape peak from C^{12} occurs. All of the peaks used in the calibration have been measured to ±0.5 keV or better.[1-3] In this experiment the centroids of the calibration peaks were determined and a quadratic calibration curve of energy versus pulse height was fitted to the resultant points. Then the energies of the standard were calculated from the calibration curve, to test the validity of the quadratic

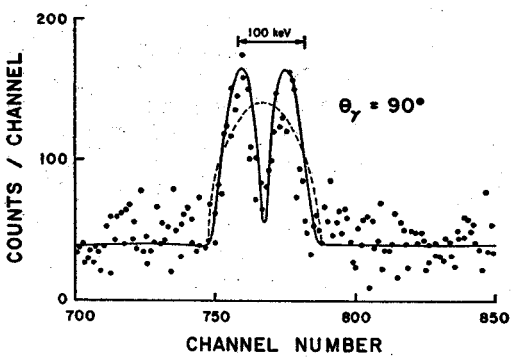

FIG. 3. γ-ray singles spectrum taken at 90° to the beam direction. The solid and dashed lines represent theoretical fits to the data, as discussed in Sec. IIIB. Energy dispersion = 4.40 keV/channel.

[1] H. Petterson, O. Bergman, and C. Bergman, Arkiv Fysik 29 423 (1965).
[2] K. W. Dolan, D. K. McDaniels, and D. O. Wells, Phys. Rev. 148, 1151 (1966).
[3] R. L. Auble, W. C. McHarris, and W. H. Kelly, Nucl. Phys. A91, 225 (1967).

TABLE I. Individual measurements and their estimated errors. All values are in keV.[a] For a discussion of the singles measurement, see Sec. IIIB.

Type of measurement	Measured energy ±total error	Statistical uncertainty	Calibration uncertainty	Error due to recoil-velocity uncertainty	Error due to angular-positioning uncertainty
0°	4440.3±0.8	±0.44	±0.22	±0.7	±0.01
180°	4440.6±0.9	±0.52	±0.36	±0.7	±0.01
90°	4437.9±1.3	±0.50	±0.61	±0.04	±1.0
90°	4438.3±2.0	±1.03	±0.85	±0.1	±1.5
90°	4442.8±2.0	±1.00	±0.85	±0.05	±2.0
90°	4438.9±1.2	±0.62	±0.34	±0.05	±1.0
Singles (90°)	4440.9±1.5	±1.15	±0.24	±0.24	±1.0

[a] Weighted average 4440.0±0.5.

fit. Twelve calibration peaks were used in each run, and their rms deviation from the calibration curve in all cases was 0.3 keV or less.

A calibration run was made immediately following each C^{12} run. To check against a possible change in pulse height due to drifts in the electronics, standard pulses, equivalent in amplitude to about 3.5 MeV, were fed into the γ-ray preamplifier during both the Co^{56} and C^{12} runs. Approximately 10^{-3} of these standard pulses were in accidental coincidence with proton pulses, and these generated a reference peak whose shape and location enabled us to determine if there had been any change in amplifier gain or base line during the course of the 4-hour coincidence runs. It was not feasible to calibrate by counting a Co^{56} source in accidental coincidence because the most useful peaks, those in the vicinity of 3.42 MeV, were too weak.

III. ANALYSIS AND RESULTS

A. γ Coincidence Spectra

γ-ray coincidence spectra taken at 0°, 90°, and 180° to the recoil direction are presented in Fig. 2. The corresponding γ-ray angles relative to the beam direction are 53°, 90°, and 127°, respectively. The observed background is the superposition of accidental coincidences upon an almost flat distribution of true coincidences in which the γ ray was detected by a Compton-scattering event in the Ge(Li) detector. The shape of the accidental-coincidence spectrum for each of the three types of runs is the same as the singles spectrum observed at the appropriate angle relative to the beam direction. γ-singles spectra taken at various angles relative to the beam direction are presented in Figs. 3 and 4.

Table I lists the excitation energy measured in several different runs, after appropriate corrections have been made for the relativistic Doppler shift and the nuclear recoil after γ decay. The C^{12*} recoil energy was calculated from the measured incident beam energy, and corrected by 3% for energy loss in the target[4] before γ decay on the basis of the known half life of the state.[5] The corresponding mean velocity was used to calculate the Doppler correction, which was −76.2 keV for the 0° measurement, +74.8 keV for the 180° measurement, and +0.7 keV for the 90° runs. The correction for nuclear recoil after γ decay amounted to 0.9 keV.

Estimated errors of each measurement due to various uncertainties are also listed in Table I. The Doppler correction is given to first order by $E_0\beta\cos\theta$, where E_0 is the true γ-ray energy, β is the recoil velocity (units of the speed of light), and θ is the angle between the recoil direction and the direction of the γ ray. It can be seen that the correction is most sensitive to angular positioning errors at $\theta=90°$, where $\cos\theta$ is a rapidly varying function of angle. The sensitivity is 1.3 keV per degree. In contrast, for the 0° and 180° runs, an error of 1 degree in the positioning of the γ-ray detector produces only a 0.01 keV error in the Doppler correction, since $\cos\theta$ is a much more slowly varying function near these angles. The estimated errors due to angular positioning uncertainties shown in Table I were computed on the basis of these results.

Error can be introduced into the measured value of the recoil velocity β (1.7×10^{-2}) by uncertainties in the beam energy or in the positioning of the proton detector. An error in the measured beam energy of ±0.25 MeV will produce a corresponding error of ±20 keV in the energy of the recoiling C^{12} nucleus, which will in turn introduce an error of ±0.4 keV into the Doppler correction for the 0° and 180° runs. In addition, the sensitivity to the positioning of the proton detector is 1.2 keV per degree for these two runs. At $\theta=90°$, the error introduced by uncertainties in recoil velocity is small, since $\cos\theta=0$ here. The recoil velocity enters only in second-order terms of the form β^2 (second-order Doppler shift) and $\beta\Delta\theta$ (due to possible errors $\Delta\theta$ in the measurement of the angle θ). The estimated errors due to recoil-velocity uncertainties shown in Table I were computed according to these results.

It is interesting to compare the results for the 0° and 180° runs as listed in Table I. To obtain these values, we applied first-order corrections of ∓75.5 keV to the measured γ-ray energies. The second-order Doppler correction was −0.7 keV in both cases. The results from these two independent runs agree to within

[4] L. C. Northcliffe, Ann. Rev. Nucl. Sci. 13, 67 (1963).

[5] F. Ajzenberg-Selove and T. Lauritsen, National Academy of Sciences—National Research Council Report No. NRC-61, 5, 6, 1962 (unpublished).

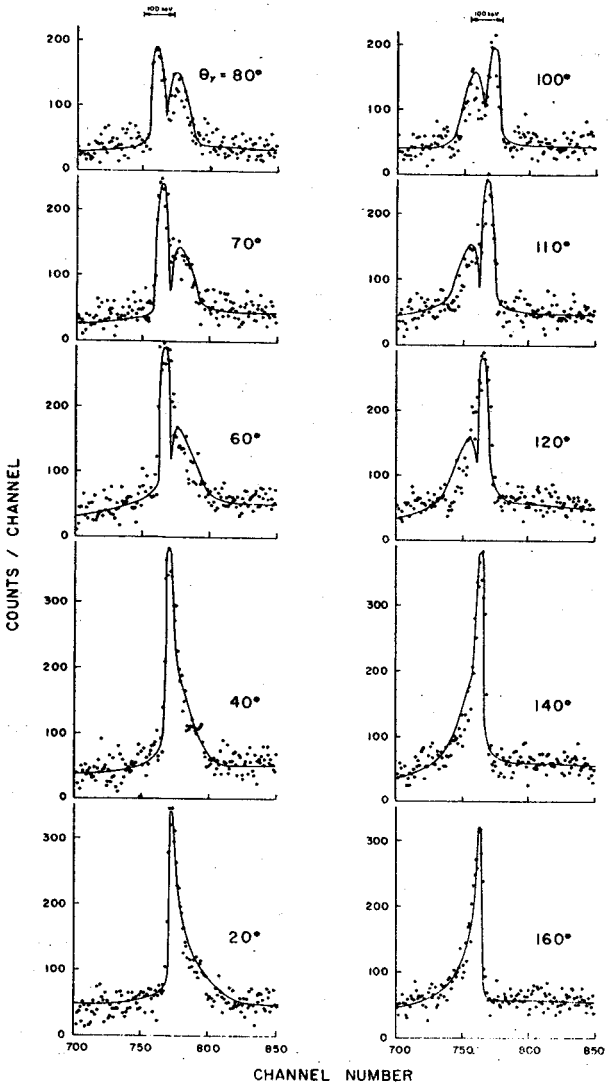

FIG. 4. γ-ray singles spectra showing the behavior of the line shape with angle of observation relative to the beam direction. The solid curves again represent theoretical fits to the data, with the same parameters as those used at 90° in the solid curve of Fig. 3. Energy dispersion = 4.40 keV/channel.

0.3 keV. This constitutes a sensitive test of the accuracy to which we were able to compute the Doppler correction. In any event, since the first-order correction at 0° and 180° is given by $\mp E_0\beta$, the average result of these two runs is independent of the Doppler correction to first order.

One of the energy measurements listed in Table I is a γ-ray singles run. A discussion of this particular run is included in Sec. IIIB.

A systematic error in our data could have occurred because we observed a double-escape peak from C^{12}, while most of the calibration points used were from full-energy peaks in Co^{56}. In the former case the electron-positron pairs are produced in the detector with a maximum energy of 3.4 MeV to be shared by the pair. In the latter case the peak observed is a result of multiple Compton scatterings followed by photoelectric absorption. The electron spectrum extends to 3.2 MeV. A correction should be made in both cases for incomplete absorption of electrons produced near the surface of the crystal.[6] However, the correction is presumably different in the two cases because of the difference in the electron energy spectra. It should be noted that the agreement between magnetic spectrometer results[1] and data taken using Ge(Li) detectors[2,3] indicates that any such correction must be of the order of 0.2 keV or less. We were unable to observe any significant effect in this experiment. Therefore, we have introduced neither a correction nor a corresponding error into the final results.

Taking a weighted average of the individual measurements, and adding their estimated errors in quadrature, we conclude that the excitation energy of the first excited state of C^{12} is 4440.0±0.5 keV. This should be compared to the value of 4439.79±0.31 keV obtained by Chasman *et al.*[7] for the level energy after correction for the recoil. The best result previous to these two measurements, a weighted mean of experimental data available to 1961, was 4433±5 keV.[5]

B. Anomaly in the γ-Ray Singles Spectrum: The Coherent Doppler Effect

When the γ-ray singles spectrum was observed at 90° to the beam axis, a symmetric double peak appeared as shown in Fig. 3. This effect has been seen with several Ge(Li) detectors and at several different incident proton energies. The spectrum is symmetric about its centroid, which will be shown to correspond to the true γ-ray energy. Since the valley between the two peaks was only about 30 keV wide at 23-MeV incident proton energy, it was possible to determine its centroid accurately, yielding an energy measurement for the γ ray with precision comparable to that obtained from the coincidence measurements, as shown in Table I. The explanation for this interesting doubling phenomenon lies in the coherence between the Doppler shift and the selective population of magnetic sublevels of the 2^+ state in the inelastic-scattering process.

The geometry of the 90° γ-singles measurement is illustrated in Fig. 5. In the particular case of C^{12} nuclei excited to the 4.44-MeV level by inelastic scattering of 23-MeV protons, kinematics restricts the laboratory recoil angle θ_R to be 63° or less. Also, the incident protons are unpolarized so that the scattering process has cylindrical symmetry about the beam direction. That is, recoil nuclei having a particular θ_R are evenly distributed over the surface of a cone. One such cone is shown in Fig. 5.

Consider the effect of the Doppler shift on de-excita-

[6] Toshimitsu Yamazaki and Jack M. Hollander, Phys. Rev. 140, B630 (1965).
[7] C. Chasman, K. W. Jones, R. A. Ristinen, and D. E. Alburger, Phys. Rev. 159, 830 (1967).

tion γ rays from nuclei on this cone. Neglecting small second-order effects, we have

$$E \equiv E_\gamma - E_0 = E_0\beta(\theta_R)\sin\theta_R \sin\phi_R, \quad (1)$$

where E_γ is the measured γ-ray energy and E_0 is the excitation energy of the state. Letting $\sigma(\theta)$ be the number of recoils per unit solid angle at θ, we find that the number of γ rays striking the detector from recoils in a small solid angle with coordinates (θ,ϕ) is

$$d^2N_\gamma(\theta,\phi) = \sigma(\theta)\sin\theta d\theta\, \omega(\phi)d\phi, \quad (2)$$

where $\omega(\phi)$ is the angular distribution function for the gamma radiation. Taking $\hat{n}$, the normal to the scattering plane, to be the axis of quantization we have[8]

$$\omega(\phi) = \sum_m P(m)F_2^m(\phi), \quad (3)$$

where the functions $F_2^m(\phi)$ are[9]

$$F_2^m(\phi) = \tfrac{1}{2}\{1-[m(m+1)/6]\}\,|\,Y_2^{m+1}(\phi,\xi)\,|^2 + \tfrac{1}{2}\{1-[m(m-1)/6]\}\,|\,Y_2^{m-1}(\phi,\xi)\,|^2 + (m^2/6)\,|\,Y_2^m(\phi,\xi)\,|^2. \quad (4)$$

$Y_2^m(\phi,\xi)$ is the spherical harmonic of order 2 and $P(m)$ is the population of the magnetic sublevel m of the 2^+ state.

Combining (1) and (2), we obtain an expression for the distribution at the detector of γ radiation coming from recoils on a single cone:

$$\frac{d^2N_\gamma}{dE}(\theta,\phi) = \frac{\sigma(\theta)\omega(\phi)d\theta}{E_0\beta(\theta)\cos\phi}. \quad (5)$$

The spectrum can be obtained as a function of E by inverting (1) and substituting for ϕ, defining $\Omega(\theta,E) = \omega(\phi[\theta,E])$, to obtain

$$\frac{d^2N_\gamma}{dE}(\theta,E) = \frac{\sigma(\theta)\Omega(\theta,E)\sin\theta d\theta}{\{[E_0\beta(\theta)\sin\theta]^2 - E^2\}^{1/2}}, \quad (6)$$

which is the spectrum due to the cone at angle θ. The function $\Omega(\theta,E)$ contains the coherence between the Doppler effect and the selective population of magnetic sublevels.

At this point, a qualitative explanation of the observed line shape can be given. From (1) and (4) it is apparent that $\Omega(\theta,E)$ is an even function of E. Therefore, the spectrum (6) must be symmetric about $E=0$, so that its centroid corresponds to the unshifted γ-ray energy. In addition, recoils which produce γ rays having $E=0$ must have $\phi=0°$; that is, they must be moving in the x-z plane. Only $F_2^{\pm1}$ can contribute to $\omega(0°)$ since no other modes have components along the normal to the scattering plane.[10] But it has been shown by Schmidt *et al.*[10] that the $m=\pm1$ magnetic sublevels can only be populated by "spin-flip" processes, in which the projection of the spin of the incident proton onto the normal to the scattering plane changes sign. This conclusion follows from a theorem by A. Bohr,[11] and is independent of the particular reaction mechanism assumed. Therefore, the number of γ rays observed with $E=0$ depends upon the "spin-flip" cross section. If this is small, one expects to see few of these γ rays, and the result is a valley between two peaks as observed.

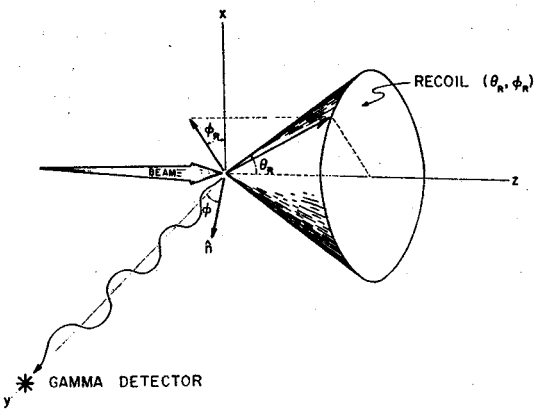

FIG. 5. The geometry of the 90° singles measurement. The vector $\hat{n}$ represents the normal to the scattering plane defined by the beam direction and the recoil (θ_R,ϕ_R). Note that $\phi=\phi_R$.

To obtain a more quantitative description of the expected γ ray spectrum it is necessary to integrate (6) over all cone angles up to the maximum angle $\theta_{max}=63°$. For any value of E, there are some cone angles which make no contribution to the integral. Therefore, it is convenient to multiply (6) by a function $S(\theta,E)$ which selects only those cone angles which can contribute. Setting $\sin\phi=1$ in (1), we arrive at an appropriate form for S:

$$S(\theta,E) = 1 \quad \text{if } E_0\beta(\theta)\sin\theta \geq E$$
$$= 0 \quad \text{if } E_0\beta(\theta)\sin\theta < E. \quad (7)$$

Noting that the kinematics of the center-of-mass to lab transformation makes β a double-valued function of θ, we find

$$\frac{dN_\gamma}{dE}(E) = \sum\left[\int_0^{\theta_{max}} \frac{\sigma(\theta)S(\theta,E)\Omega(\theta,E)\sin\theta d\theta}{\{[E_0\beta(\theta)\sin\theta]^2 - E^2\}^{1/2}}\right], \quad (8)$$

where the summation sign indicates that the integration is to be performed for both branches of β. This form of the spectrum clearly indicates the possibility for anomalous, i.e., non-Gaussian shapes.

We have written a FORTRAN program for the MSU Sigma 7 computer which numerically integrates (8).

[8] H. Frauenfelder and R. M. Steffen, in *Alpha-, Beta- and Gamma-Ray Spectroscopy*, edited by K. Siegbahn (North-Holland Publishing Company, Amsterdam, 1965), p. 1003.

[9] J. M. Blatt and V. F. Weisskopf, *Theoretical Nuclear Physics* (John Wiley & Sons, Inc., New York, 1963), p. 594.

[10] F. H. Schmidt, Ronald E. Brown, J. B. Gerhart, and Wojciech A. Kolasinski, Nucl. Phys. 52, 356 (1964).

[11] A. Bohr, Nucl. Phys. 10, 486 (1959).

Input to the program consists of the measured angular distributions for inelastic scattering and spin-flip scattering[12] from the 4.44-MeV level. The spin-flip data give a direct measure of the population of the $m=\pm1$ magnetic sublevels. No information was available regarding the relative populations of the $m=0$ and the $m=\pm2$ magnetic sublevels. Provision was made to input the population ratio of these sublevels, which was varied to obtain a good fit to the experimental data. Although the population ratio is in general a function of the proton scattering angle, we assumed no angular dependence in an effort to reduce the number of degrees of freedom in the problem to a practical level.

Output from the program consists of a theoretical peak shape which is then normalized to the experimental data. After a number of trials, the solid curve shown in Fig. 3 was obtained by assuming that the $m=\pm2$ sublevels were not populated in the reaction. In order to determine whether or not kinematic effects alone could produce a double peak, in the absence of selective population of the magnetic sublevels, the calculation was repeated with the assumption that all five sublevels were equally populated. The dashed curve shown in Fig. 3 represents the theoretical peak shape obtained, normalized to the same total number of counts under the peak. The double-peaking effect was not reproduced.

Figure 4 illustrates the behavior of the observed line shape as the detector is moved away from 90°. The double peak becomes asymmetric, and its centroid shifts. Finally, at 40° and 140° to the beam direction one of the peaks becomes unobservable. In all cases, the spectra exhibit mirror symmetry about 90°.

Doppler shifting of the centroid of the line, in addition to the expected broadening, is readily explained by the fact that the C^{12} nuclei are restricted to recoil within a forward cone having a half-angle of 63°. γ rays observed at forward angles come from nuclei which always have a component of velocity toward the observer and are therefore shifted upward in energy. Similarly, γ rays observed at backward angles are shifted downward in energy. Finally, the antisymmetry of the first-order Doppler shift about the 90° observation angle, and the fact that the angular distribution function $\omega(\phi)$ satisfies

$$\omega(\phi)=\omega(\phi+\pi), \quad (9)$$

lead to the requirement that singles spectra taken at supplementary angles be mirror images of each other.

Theoretical line shapes were calculated for detector angles between 20° and 160°. When the detector angle is not 90°, the expression for the first-order Doppler shift is somewhat more complicated. The correct expression for the shift E, which replaces (1), is

$$E=E_0\beta(\theta_R)[\cos\theta_R\cos\theta_D+\sin\theta_R\sin\phi_R\sin\theta_D], \quad (10)$$

where θ_D is the detector angle relative to the beam axis. Otherwise, the calculation proceeds as before. The results are shown in Fig. 4, normalized to the experimental data. The magnetic sublevel populations used in these calculations were the same as those used for the 90° spectrum.

Anomalous line shapes should be observable in more complicated transitions than the $0^+\rightarrow2^+\rightarrow0^+$ sequence considered here. However, the theoretical interpretation of the observed shapes can be much more difficult. In particular, if the ground state is not 0^+ one needs to consider the possibility of competing multipolarities in the γ transition, and it is also necessary to know the relative probability for a γ transition to each of the m sublevels of the ground state.

The detailed structure resulting from the coherent Doppler effect can only be observed if the maximum Doppler shift is much greater than the resolution of the γ detector. This requirement means that the recoil nucleus must be given a sufficiently large energy, and that the lifetime of the state must be much less than the stopping time of the recoil in the target. For incident protons of energy less than 50 MeV, one is restricted to relatively light nuclei ($A\lesssim40$). If a solid target is used, the lifetime of the state in question should be of the order of 10^{-13} sec or less.

The coherent Doppler effect is not limited to inelastic proton reactions. The Bohr theorem, applied to the general two body reaction, will yield selection rules leading to unequal populations of the magnetic sublevels of a given state. We conclude that a Doppler-broadened γ-ray line will in general reveal "anomalous" structure if viewed with a sufficiently high resolution detector, as long as a beam axis exists to define a preferred direction in space.

ACKNOWLEDGMENTS

We wish to express our thanks to Dr. R. E. Berg for allowing us the use of his Ge(Li) detector, and to G. Berzins for developing the computer code used to determine the calibration curve. Finally, we wish to thank E. H. Pierson for his assistance in setting up the apparatus and collecting the data.

[12] J. J. Kolata and A. Galonsky, Bull. Am. Phys. Soc. 12, 500 (1967).

NUCLEAR INSTRUMENTS AND METHODS 52 (1967) 153–154; © NORTH-HOLLAND PUBLISHING CO.

LETTERS TO THE EDITOR

ENERGY REPRODUCIBILITY IN BEAM ANALYZING MAGNETS*

J. L. SNELGROVE† and E. KASHY

Cyclotron Laboratory, Michigan State University, East Lansing, Michigan, U.S.A.

Received 23 March 1967

Measurements of magnetic field reproducibility made with one of the Michigan State University cyclotron beam analyzing magnets indicate that an energy setting can be reproduced to better than 1 part in 15000.

An important consideration in the use of a beam analyzing system is the accuracy with which a given beam energy can be reproduced. Measurements made with one of the 45° analyzing magnets constructed for use in the beam handling system of the Michigan State University cyclotron facility are used to determine the effect the magnet turn-on procedure has on the beam energy and the reproducibility of a given energy if the same turn-on procedure is used.

The method used to set an analyzing magnet is the following. The excitation of the magnet is set by bringing the magnet to a given field, B_0, measured at a fixed point in the central region of the magnet using a nuclear magnetic resonance probe. Since the iron undergoes hysteresis, B_0 will in general be reached for different values of current in the coils. It is possible to establish a definite hysteresis loop by following a set procedure for reaching the desired field. In this investigation a loop was established by raising the current from zero to 0.99 I_{max}, waiting 10 min, lowering the current to zero, waiting 10 min, and repeating the cycle. The value of B_0 for $I = 0.99\ I_{max}$ was 13.1 kG. Measurements were made at a field of 10.132 kG, corresponding to a proton energy of 42 MeV. Two procedures were used to reach this value once the hysteresis loop was established. In procedure I the current was increased from zero until the field was reached. In procedure II the current was decreased from 0.99 I_{max}.

The field was monitored by a nuclear magnetic resonance probe positioned 9.5″ from the center of the pole piece at an angle of 45° from the beam entrance line (fig. 1). A radial field map was made along the beam entrance line. The interior region from 0.0″ to 10.0″ was mapped in 1.0″ steps using the nuclear

* Research supported by National Science Foundation.

† National Aeronautics and Space Administration Graduate Fellow.

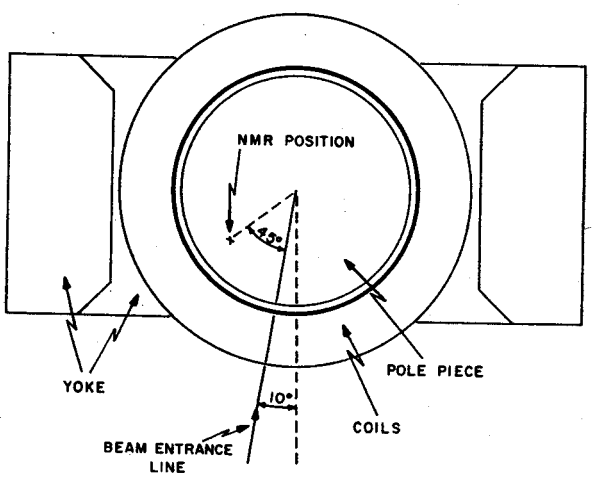

Fig. 1. Diagram of the magnet used in this investigation.

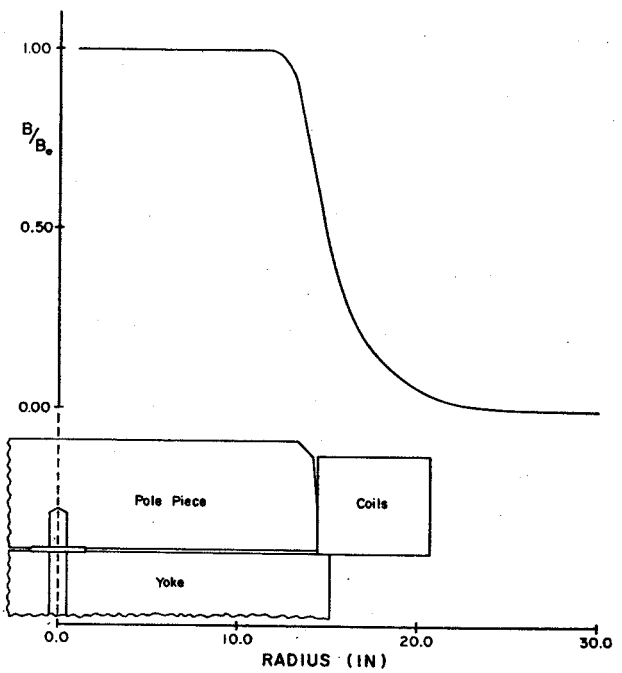

Fig. 2. Plot of B/B_0 along the beam entrance line as a function of distance from the center, showing the physical elements of the magnet. The gap width is 2.50″.

magnetic resonance probe. The region from 9.0″ to 30.8″ was mapped in 0.2″ steps using a Rawson rotating coil fluxmeter mounted on an automated milling table. The signal from the fluxmeter was passed through a voltage-to-frequency converter, and the one-second-averaged value of the voltage was punched automatically on computer cards. Five passes were taken to minimize the fluctuations in the rotating coil readings, and the average value was used at each point. These readings were then normalized to the nuclear magnetic resonance probe readings between 9.0″ and 10.0″. A plot of the field vs radius, matched to a diagram of the pole piece, is shown in fig. 2.

TABLE 1

Values of the field integrals obtained with procedure I(a) and procedure II(b), for various ranges of integration.

Range (in.) / Run	0–10.0	0–12.0	0–14.0	0–30.8
1	9.9949	11.9917	13.8025	15.4796
2	9.9948	11.9915	13.8021	15.4777
3	9.9948	11.9917	13.8025	15.4807
4	9.9950	11.9917	13.8026	15.4806
5	9.9950	11.9919	13.8029	15.4823
6	9.9949	11.9916	13.8023	15.4790
Ave	9.9949	11.9917	13.8025	15.4800

(a)

Range (in.) / Run	0–10.0	0–12.0	0–14.0	0–30.8
1	9.9939	11.9909	13.8019	15.4862
2	9.9939	11.9909	13.8023	15.4846
3	9.9939	11.9909	13.8018	15.4858
4	9.9938	11.9909	13.8021	15.4859
5	9.9938	11.9911	13.8028	15.4883
6	9.9938	11.9907	13.8020	15.4846
Ave	9.9939	11.9909	13.8021	15.4859

(b)

Since

$$p \propto \int B\,ds,$$

values of

$$\int_0^R (B/B_0)\,dr$$

were computed using Simpson's rule for numerical integration. Six sets of data were gathered for each procedure. The values of the integrals are shown in table 1. For procedure I the mean value of the integral was 15.4800″ with a standard deviation of 0.0016″. For procedure II it was 15.4859″ with a standard deviation of 0.0013″. The difference between the two values is 0.0059 ± 0.0009″, representing a difference in the resulting beam energy of 8 parts in 10^4 if procedure II is used rather than procedure I. The smallness of this difference undoubtedly reflects the careful shaping of the pole piece edges as described by Braams[1]). Reference to table 1 shows that the major contribution to the difference of the two integrals occurs in the fringe field from 14.0″ on. This result is to be expected since the setting procedure forces the magnetic field to be the same in the probe region. Careful consideration of the sources of error shows that at least 70% of the error quoted in the field integrals is due to random fluctuations in the measuring apparatus. Thus, if the same turn-on procedure is carefully followed each time, these measurements indicate that one can expect the energy setting to be reproduced to better than 1 part in 15000. Most nuclear spectroscopy laboratories use similar turn-on procedures for their analyzing magnets because of the problems involving differential saturation[2]). Thus, this work represents, by the direct measurement of magnetic fields, a quantitative assessment of the effect.

The authors would like to thank Professor M. M. Gordon for helpful discussions. We also thank D. R. Gilbert for his help with the measurements.

References

[1]) C. M. Braams, Nucl. Instr. and Meth. **26** (1964) 83.
[2]) H. A. Enge, Nucl. Instr. and Meth. **28** (1964) 119 and references therein.

1.E.1:
3.A

Nuclear Physics A104 (1967) 241—262; © *North-Holland Publishing Co., Amsterdam*

Ge(Li)-NaI(Tl) STUDIES OF THE DECAY OF ^{117}Te

G. BERZINS † and W. H. KELLY
Department of Physics, Michigan State University, East Lansing, Michigan, USA ††

G. GRAEFFE ††† and W. B. WALTERS
Department of Chemistry and Laboratory for Nuclear Science Massachusetts Institute of Technology, Cambridge, Massachusetts, USA ‡

Received 3 July 1967

Abstract: Results of independent investigations performed at MSU and MIT on the decay of 1.1 h ^{117}Te suggest an energy level scheme for ^{117}Sb. Sources were produced at MIT via the ^{114}Sn(α, n) ^{117}Te reaction, while the MSU group bombarded natural antimony metal with 52 MeV protons. Ge(Li)–NaI(Tl) coincidence experiments, γ-ray energy and relative intensity measurements, and positon end-point measurements were performed at both laboratories and produced results which were in excellent agreement. On the basis of these results, excited states in ^{117}Sb are placed at 719.7, 923.9, 1354.5, 1454.5, 1716.4, 1810.5, 2213, 2284.8 and 2300.0 keV. Additional levels, accommodating only very weak ground state transitions, may be present at 1596, 2380 and 2885 keV. No conclusive evidence for the existence of a possible ^{117m}Te was obtained.

E

RADIOACTIVITY: ^{117}Te [from ^{121}Sb (p, 5n) and ^{114}Sn(α, n)]; measured E_γ, I_γ, γγ-coin, βγ-coin. ^{117}Sb deduced levels. Natural Sb and enriched Sn targets. Ge(Li), Si(Li) and scintillation detectors.

1. Introduction

Recent high resolution and scintillation studies [1–5]) of energy levels in odd-mass antimony isotopes ($A = 119$–125), populated in the beta decay of Te and Sn isomers, have indicated systematic trends of several low-lying states. Where comparisons can be made, the results of these studies are in reasonable agreement with results of (^{3}He, d) and Coulomb excitation experiments [6–8]). It is the purpose of this paper to report an extension of such studies to levels in ^{117}Sb as populated by the beta decay of ^{117}Te.

Past studies of the decay of ^{117}Te have yielded a substantial amount of information [9–12]) but have been hampered by the inherently poor resolution of scintillation detectors. The difficulty is compounded by the complexity of the decay scheme and by the short half-life. Some previously reported evidence [11]) for the existence of 1.9 h

† Present address: Los Alamos Scientific Laboratory, Los Alamos, New Mexico.
†† This work was supported in part by the U.S. National Science Foundation.
††† Permanent address: Laboratory of Physics, Institute of Technology, Otaniemi, Finland.
‡ This work was supported in part by the U. S. Atomic Energy Commission under contract No. AT(30-1)-905.

^{117m}Te and 1.1 h ^{117g}Te isomers is in agreement with the extrapolation from systematic trends. However, other groups [9,10,12]) have failed to observe any transitions which can be attributed to ^{117m}Te. In particular, a positon end-point of approximately 1.8 MeV has been reported, but disagreement exists over the origin of this transition (refs. [9-12])).

In this investigation, several previously unreported gamma rays were observed. Coincidence data, obtained with various Ge(Li)-NaI(Tl) detector combinations, coupled with energy sums and relative intensity considerations, suggest a decay scheme for ^{117}Te which differs considerably from those previously proposed [9,12]). Positon-gamma coincidence data indicate a lower limit for the disintegration energy of ^{117}Te.

Little evidence was found for the existence of a possible ^{117m}Te. Although one γ-ray was observed that might be attributed to an isomer, neither its yield nor other γ-rays that would follow the decay of such an isomer suggested the presence of ^{117m}Te.

2. Source preparation and apparatus

The ^{117}Te activity was produced by proton bombardments of natural $SbCl_3$ in the Michigan State University Cyclotron. Bombardments were carried out for approximately 5 μa min at 48 or 52 MeV. The higher energy was desirable because of increased yield of ^{117}Te relative to that of ^{119}Te. No other significant differences were observed in spectra obtained from the 52 MeV as opposed to the 48 MeV bombardments.

The target was dissolved in 3N HCl and the Te activities were precipitated with SO_2 gas after traces of $TeCl_4$ and hydroxylamine hydrochloride had been added. The total time lapse between the end of bombardment and initial counting was approximately 15-20 min. Sources produced at 52 MeV could be counted for three half-lives before the presences of ^{119}Te became significant. Although the spectra of ^{119g}Te and ^{119m}Te are known [4,5]), the large number of gamma rays present in $^{119m+g}$Te serves only to complicate the spectrum and mask lines in ^{117}Te. Hence fresh sources were prepared before the intensity of the 644 keV gamma in ^{119g}Te became comparable to that of the 720 keV line in ^{117}Te.

The experimental arrangement at MSU was very similar to that described previously [4]). However, a Ge(Li) counter with somewhat better resolution than before was employed for some of the singles counting.

The ^{117}Te was produced at MIT by irradiating $^{114}SnO_2$, enriched to 60 % in ^{114}Sn, with ^{4}He ions in the MIT cyclotron. In experiments where only the ^{114}Sn(α, n) ^{117}Te reaction was sought, the ^{4}He ions were degraded to $\approx$22 MeV with Al foil. At this energy only a small amount of ^{116}Te was produced. Using higher energies gave higher yields of ^{117}Te but also resulted in the production of a great deal of ^{116}Te. As the ^{116}Sn fraction of the target was 10 %, some ^{119}Te was produced, but it did not interfere with the study of ^{117}Te decay until 4 to 5 h after irradiation.

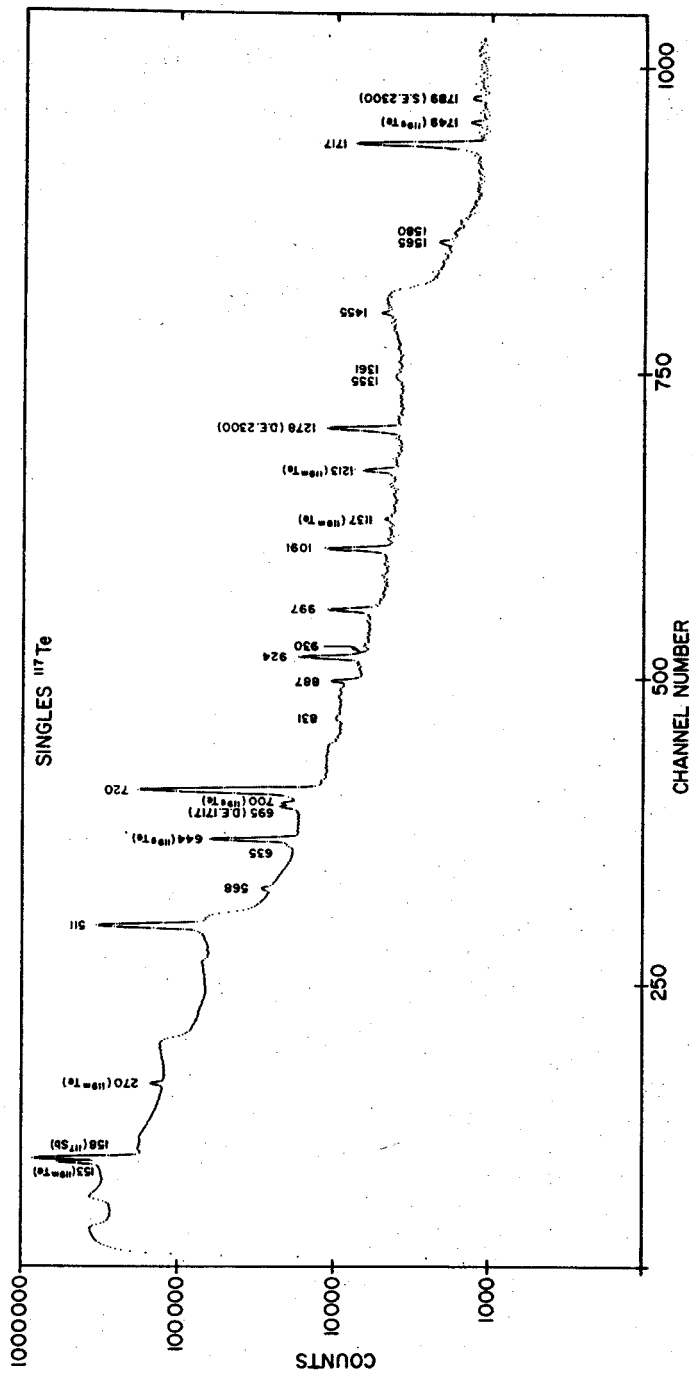

Fig. 1. Singles spectrum of ^{117}Te below approximately 1800 keV, recorded at MSU with a 3 cm^3 Ge(Li) detector.

3. Gamma-ray singles spectrum

Gamma-ray singles spectra were recorded at MSU with several Ge(Li) detectors. Below 1800 keV a 3.0 cm^3 counter with $\approx$ 3.0 keV FWHM resolution for the 662 keV gamma of ^{137}Cs was used. The efficiency for detection of weak, high-energy transitions was increased with a 7 cm^3 counter whose resolution was $\approx$ 4.5 keV

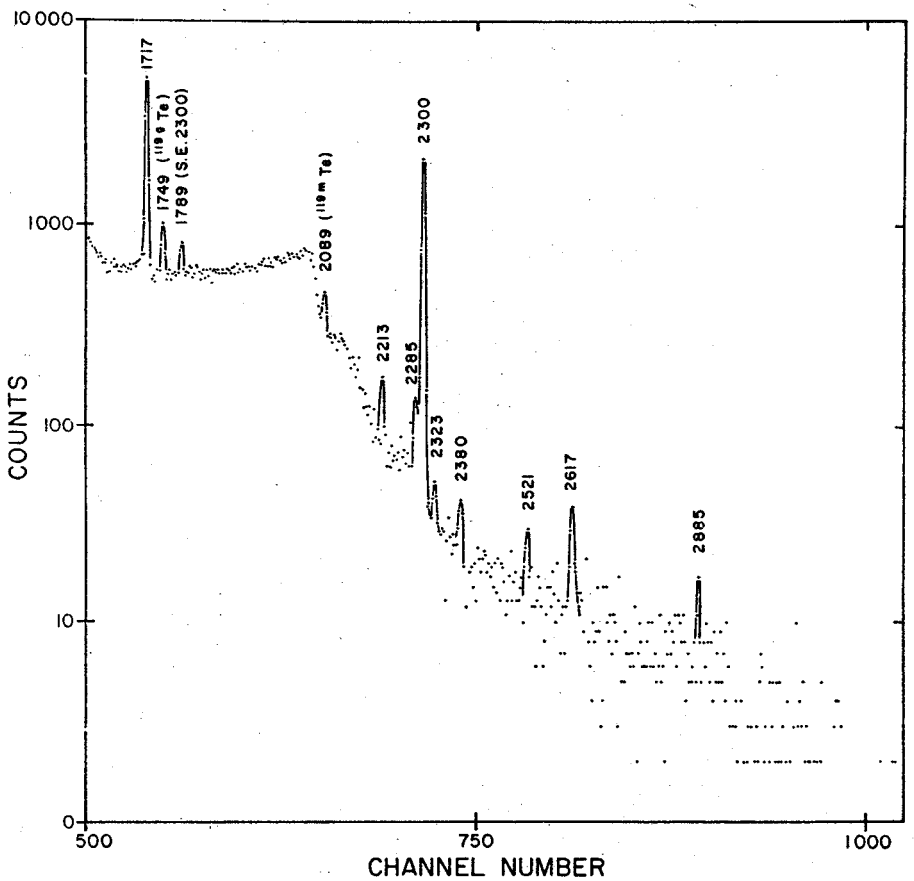

Fig. 2. High-energy portion of a singles spectrum of ^{117}Te, recorded at MSU with a 7 cm^3 Ge(Li) detector. This spectrum was recorded after approximately one half-life of ^{117}Te to allow traces of ^{34}Cl contaminant to decay out. Several spectra were recorded from sources of comparable age, and were summed to give the above spectrum. Lines at 2323, 2521 and 2617 keV are of unknown origin but decay with a half-life longer than that of ^{117}Te.

FWHM. Portions of typical singles spectra are shown in figs. 1 and 2. A list of transitions and their relative intensities is given in table 1.

Half-life measurements were performed on the 720, 1091, 1278 (D.E. of 2300), 1717 and 2300 keV lines. Two series of 8 min runs were taken – the first set spanning about 80 % of a half-life, the second about 1.5 half-lives. Corrections were made for

deadtime and source decay. The mean value obtained was 1.14 h with an average deviation of 0.08 h from the mean. The value of 1.14 h is in agreement with values of 61 ± 2 min, 1.1 ± 0.1 h and 65 ± 5 min reported by refs. [9,10,12]), respectively.

The gamma-ray energies were measured a number of times with both internal and external calibrations, and second-order, least-squares calibration equations were

TABLE 1

Energies and relative intensities of γ-rays present in the decay of ^{117}Te

MSU			MIT		Adopted	
Energy (keV)	Uncertainty (keV)	Rel. intensity [a,b])	Energy [c]) (keV)	Rel. intensity [a,b])	Energy [c]) (keV)	Rel. intensity [a,b])
			473 [d])	≈0.5		
568.8	0.5	1.3	568.8	0.8	568.8	1.0
634.6	0.5	0.8	634.3	0.5	634.5	0.7
719.8	0.4	100	719.5	100	719.7	100
830.8	0.5	0.9	831.3	0.6	831.0	0.8
886.8	0.5	2.4	886.5	2.2	886.7	2.3
923.9	0.4	9.4	923.8	9.8	923.9	9.6
930	1.0	≈0.5	930.4	0.3	930.2	0.3
996.7	0.4	6.1	996.7	6.1	996.7	6.1
1090.8	0.4	10.5	1090.5	10.6	1090.7	10.6
1354.6	0.7	0.6	1354.3	0.9	1354.5	0.8
1361.0	0.7	0.6	1359.8	0.7	1360.5	0.7
1454.8	0.4	1.2	1454.3	1.4	1454.5	1.3
1565.2	0.6	1.3	1565.0	1.7	1565.1	1.5
1579.9	1.5	0.8	1581.0	0.3	1580.5	0.3
1596 [e,f])	2.0	0.5	1595.3 [d])	0.3	1595.3 [e])	0.3
1716.5	0.4	23	1716.2	26.0	1716.4	24.5
2213	1.0	0.6	2213	0.5	2213	0.5
2285	1.0	0.7	2284.5	0.4	2284.8	0.6
2300.0	0.5	16	2300.1	18.0	2300.0	17.3
2380 [d])	1.5	0.2	2379.5 [e])	≈0.2	2379.3 [e])	0.2
2885 [d])	2.0	0.1	2885 [e])	≈0.1	2885 [e])	0.1

[a]) Uncertainties in relative intensity are estimated as ±10 % for the strong transitions.
[b]) Gamma intensity only.
[c]) Uncertainties in energy values are 0.7 keV for those whose relative intensities are greater than 2, and 1.5 keV for others.
[d]) Seen only in coincidence spectra.
[e]) Assignment to ^{117g}Te tentative.
[f]) Possibly double escape peak of a contaminant 2617 keV transition.

constructed. The data were treated essentially as described previously [4,13]). The relative intensities were measured with the 7 cm^3 Ge(Li) counter. Corrections for relative photopeak efficiencies were made from a curve obtained from ^{129}Te and ^{119}Te sources whose gamma-ray relative intensities had been previously measured (refs. [4,14])). The energy and relative intensity values given in table 1 are mean values taken from a number of runs. The errors in the energies are rms deviations from the

mean, while the errors in relative intensities are estimated as ±10 %, except for the very weak lines.

Gamma rays were detected at MIT with a Ge(Li) detector whose volume was 1.2 cm^3. The spectra were recorded with a 4096-channel, multi-parameter, pulse-height analyser system that included a 4096-channel ADC, two 1024-channel ADC, a 4096-channel memory, a buffer memory and control unit, a magnetic tape unit and an eight-channel digital gate. Singles spectra were recorded using the 4096-channel ADC and memory. Energies were determined by calibrating the gain of the system with γ-rays whose

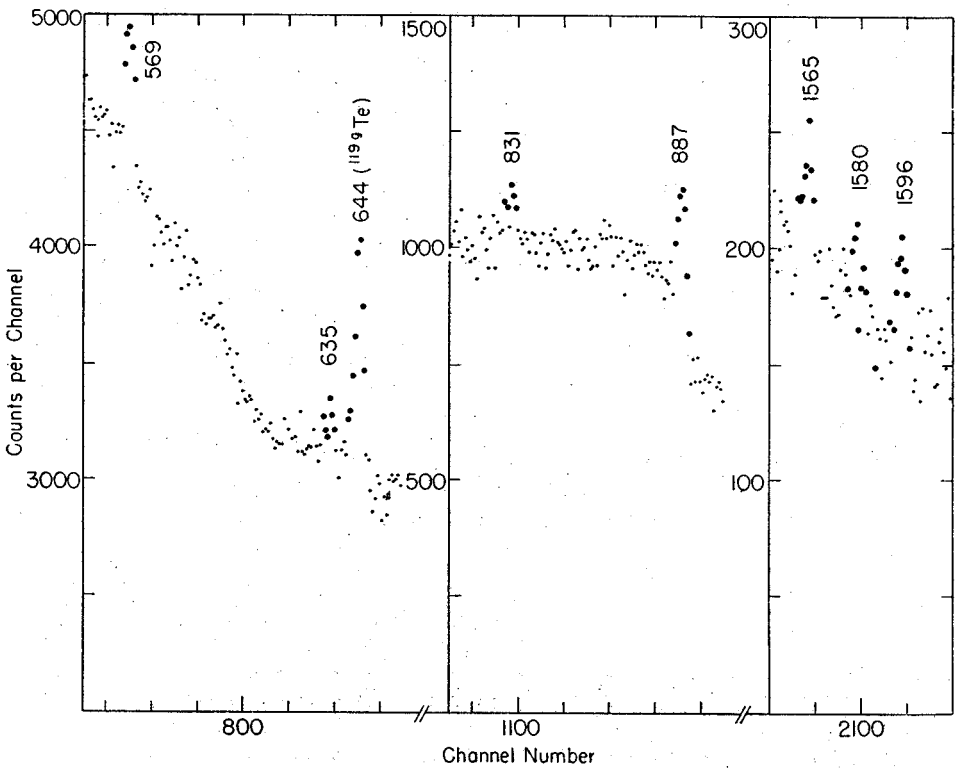

Fig. 3a. Portions of 4096-channel spectra taken at MIT.

energies were well known and using a linear interpolation between the peaks of known energy. The relative intensities were calculated by correcting the photopeak areas using a curve constructed by counting a number of radioactive sources whose γ-ray intensities are well known. The results are also summarized in table 1. A half-life of 62 ± 3 min was determined by following the decay of the 720 keV peak. This was done by recording the spectrum on magnetic tape every 15 min over a period of 3 h. The intensities of the other γ-ray peaks, relative to the 720 keV γ-ray peak, were also determined over longer counting periods. The relative intensities were also observed at different ^{4}He ion bombarding energies. Only those γ-rays whose relative intensities

remained constant within the limits of our error were assigned definitely to ^{117}Te. We have shown in fig. 3 selected portions of 4096-channel spectra where several low intensity peaks of interest are observed.

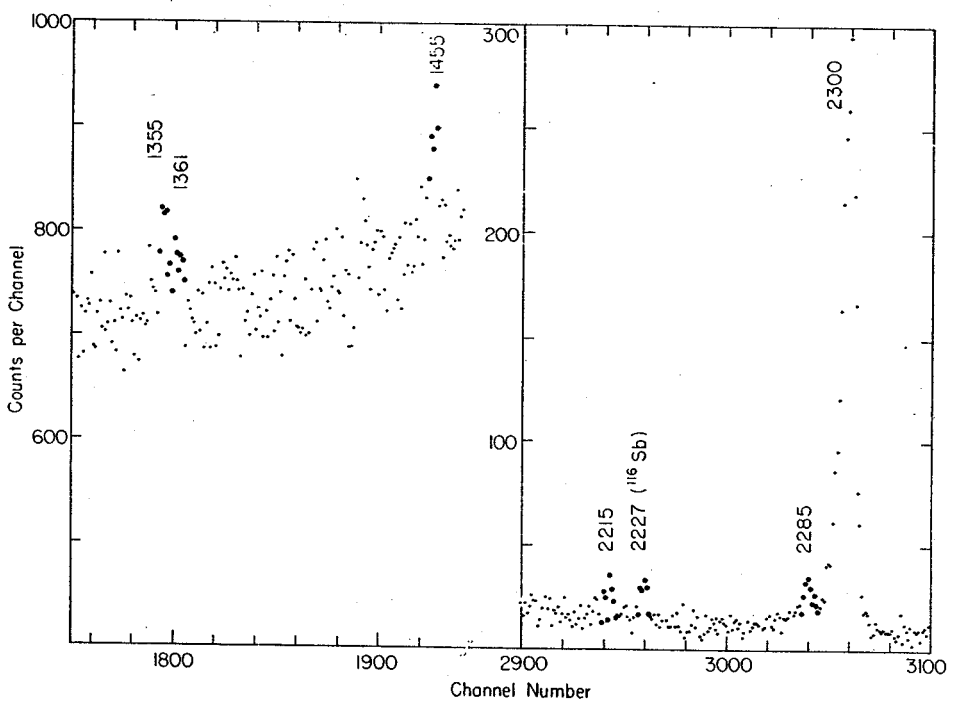

Fig. 3b. (See caption fig. 3a.)

4. Gamma-gamma coincidence results

Coincidence experiments were limited by the 1.1 h half-life. Besides conventional Ge(Li)-NaI(Tl) coincidence experiments, three other types of coincidence counting were performed at MSU. First an "any-coincidence" spectrum, employing an integral NaI(Tl) gate above the 511 keV photopeak, was recorded. In this manner, due to lower Compton backgrounds from positon-fed ground state transitions and due to increased efficiency in the gate, transitions in coincidence with gamma rays of energy higher than 550 keV were enhanced. A second type of experiment, complementary to the "any-coincidence", was to count only those pulses from the Ge(Li) counter which were not in coincidence with a signal from the NaI(Tl) crystal. This and the "any-coincidence" experiments were performed with a 20.3 cm × 20.3 cm NaI(Tl) split annulus [15]). The "anti-coincidence" spectrum served to indicate any transitions which are primarily electron capture fed and proceed directly to ground. In this spectrum Compton scattered photons from the Ge(Li) counter were generally detected by the NaI(Tl) annulus, reducing underlying Compton backgrounds in the

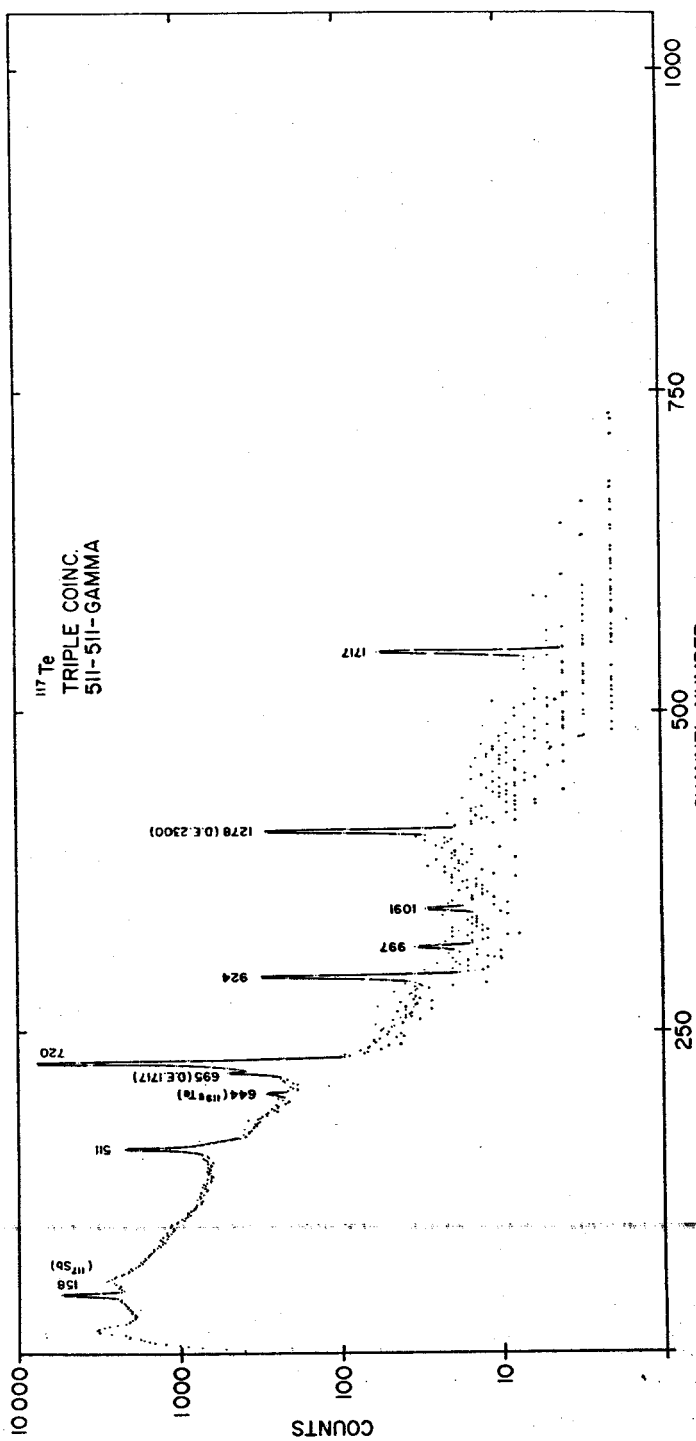

Fig. 4. Results of a triple coincidence experiment recorded with a 20.3 cm × 20.3 cm NaI(Tl) split annulus and a 7 cm³ Ge(Li) detector. Each half of the annulus was gated on the 511 keV photopeak, while the resulting coincident Ge(Li) spectrum was recorded in the analyser.

Ge(Li) spectrum. However, this same scattering resulted in enhanced Compton tails of high-energy lines in the "any-coincidence" spectrum.

A third type of coincidence experiment performed with the split annulus was to simultaneously gate on 511 keV photons in each half and count the resulting coinci-

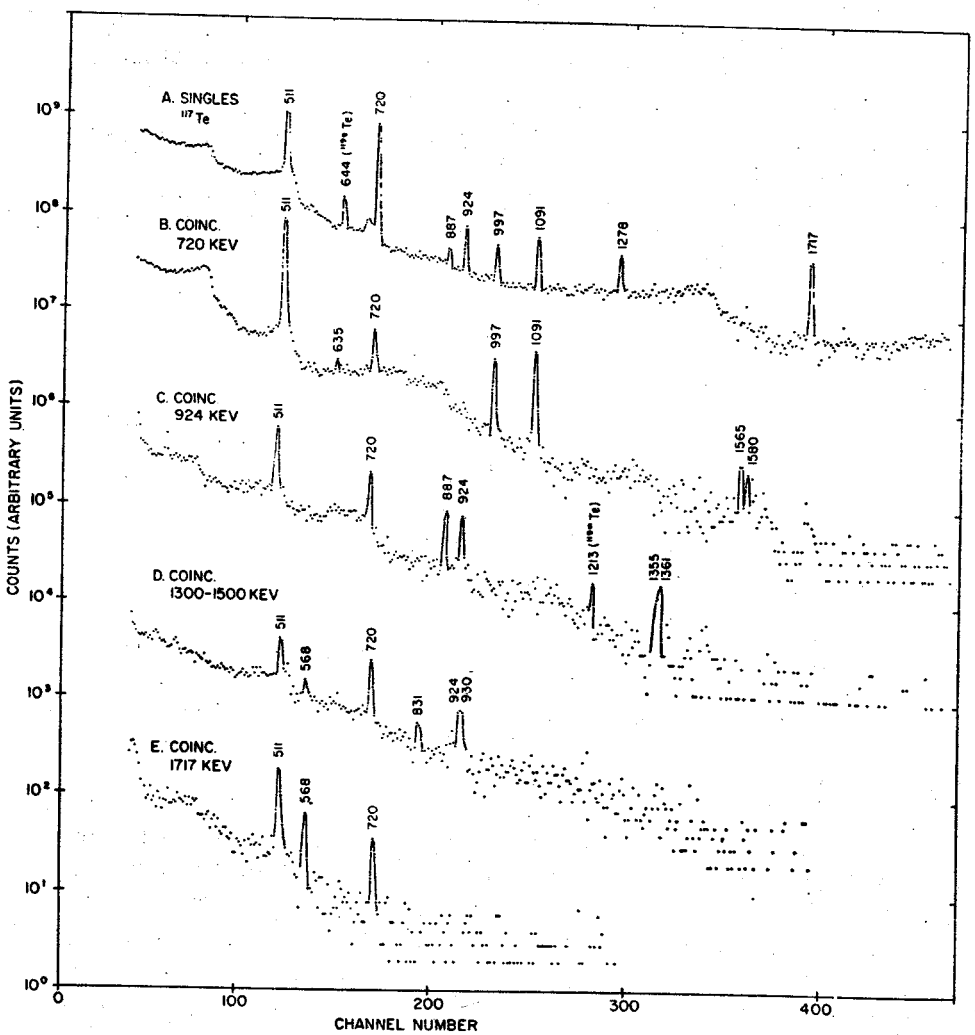

Fig. 5. Coincidence spectra obtained with a 7 cm³ Ge(Li) counter and a 7.6×7.6 cm NaI(Tl) crystal.

dent Ge(Li) spectrum. This established any positon-fed levels and indicated double escape peaks of high-energy gamma rays. The spectrum is shown in fig. 4.

Other coincidence spectra were recorded with the NaI(Tl) detector scanning essentially all of the spectrum above 600 keV. To compensate for the short half-life, strong sources were used at the start of all coincidence counting, leading to a large

number of chance events. Hence, interpretations of the coincidence spectra must be based not necessarily on the presence of a given line but by its enhancement from singles relative to other lines.

Because counting could be done for only relatively short periods at a time, most coincidence spectra exhibit regions with large statistical fluctuations. In order to ascertain whether a number of possible peaks were more than background fluctuations, most of the coincidence runs were repeated with different sources. Coincidence evidences were obtained for all lines of less than 1800 keV energy which could be observed in singles spectra. In addition, several other possible gamma rays were suggested by some coincidence experiments, but these did not reproduce well enough to warrant their placement in the decay scheme.

The results of the coincidence studies are summarized in table 2. Several typical spectra are shown in fig. 5.

TABLE 2

^{117}Te gamma-gamma coincidence relationships observed at MSU

Fig.	Gamma in NaI(Tl) gate (keV)	Coincident gammas in Ge(Li) spectrum (keV)
4	511-511 [a])	720, 924, 997, 1091, 1717
5B	720	635, 997, 1091, 1565, 1580
5C	887	924
5C	924	887, 1361
5C	930	1355
5D	1355	930
5D	1361	924
5D	1455	831
5E.	1717	569
	>1850 [b])	none observed

[a]) Triple coincidence experiment.
[b]) Spectrum not shown.

Coincidence data were recorded at MIT using the buffer memory and magnetic tape unit to store addresses of coincident pulses from the 1024-channel ADC units. In such experiments, a 7.6 cm × 7.6 cm NaI(Tl) detector was used in conjunction with the Ge(Li) detector. The coincidence circuitry consisted of two amplifiers that were operated in a double delay line mode whose pulses were fed into two single-channel analysers operated in the zero-crossing mode. The outputs from the single-channel analysers were fed into a coincidence unit whose resolving time (2τ) was set at 40 nsec. The two detectors were at $\approx 120°$ with a 0.6 cm lead shield to eliminate Compton scattering coincidences.

The results of the coincidence experiments at MIT are listed in table 3. They may oe seen to correspond closely with those obtained at MSU although, in general, the statistics at MIT were not as good as those at MSU as a smaller Ge(Li) detector was used. By using the buffer system, however, it was possible to observe coincidences

with smaller gates in the NaI(Tl) spectrum and to observe many coincidences from both directions.

TABLE 3

^{117}Te gamma-gamma coincidence relationships observed at MIT [a])

Gate area (keV)	Gamma rays in NaI(Tl) gate (keV)	Coincident gamma rays in Ge(Li) spectrum (keV)
690- 750	720	635, 997, 1091, 1360, 1565
800- 850	831	1455
850- 910	887	924
910- 960	924, 930	887, 1355, 1360, 1292 [b])
960-1040	997	569, 720
1050-1140	1091	473, 720
1300-1400	1355, 1361	924, 930
1400-1500	1455	831
1550-1635	1465, 1580, 1596	720
1680-1760	1717	569

[a]) Spectra not shown. [b]) ^{116}Te.

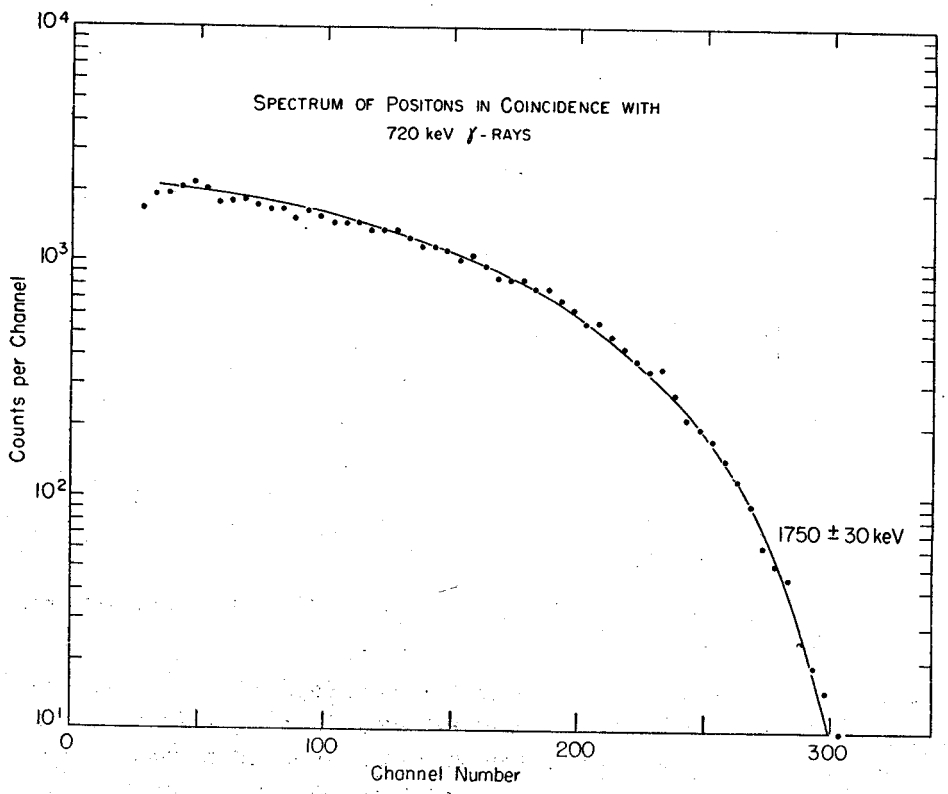

Fig. 6. Positon spectrum in coincidence with 720 keV γ-rays taken with a Si(Li) detector. Each point represents the sum of five channels.

5. Positon-gamma coincidence results

Positon-gamma coincidence spectra were recorded at MSU with an 8.8 cm × 0.5 cm plastic scintillator and a 7.6 cm × 7.6 cm NaI(Tl) detector. Gating regions in the NaI(Tl) spectrum were selected at 511, 720, 924 and 1717 keV. The resulting coincident positon spectra confirmed that there is no significant positon decay to the

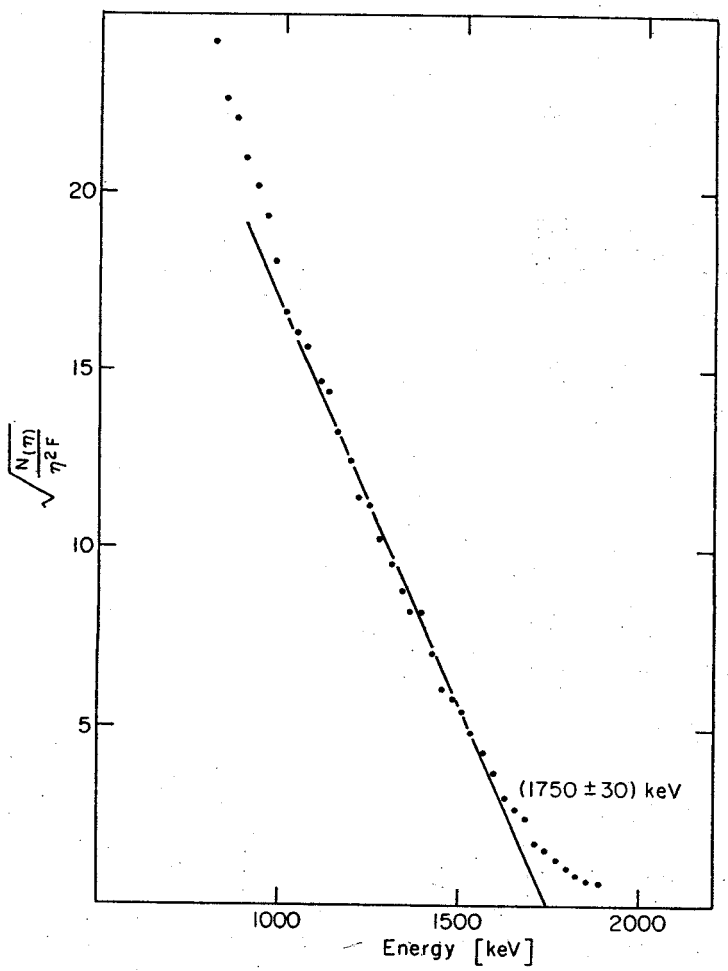

Fig. 7. A Fermi-Kurie plot of positons in coincidence with 720 keV γ-rays.

ground state of ^{117}Sb. All positon end-points indicated the beta disintegration energy to be 3550 ± 100 keV.

At MIT positon coincidences with γ-rays were also observed by using a 3 mm deep Si(Li) detector whose full width at half maximum for ^{137}Cs conversion electrons was ≈ 20 keV. Counting was accomplished by placing the source inside of the vac-

uum chamber housing the detector, evacuating the chamber and cooling the detector to near liquid N_2 temperature. Both the singles spectrum and the spectrum in coincidence with 720 keV γ-rays (fig. 6), showed the same end-point of $\approx$ 1750 keV. The Fermi plot in fig. 7 indicated an end-point of 1750 ± 30 keV. The Q_{EC} would thus be 3492 ± 30 keV.

6. The proposed decay scheme of ^{117}Te

The proposed decay scheme of ^{117}Te, shown in fig. 8, is supported by coincidence results, energy sums and relative intensity considerations. It accommodates all of the γ-rays that we have definitely attributed to the decay of ^{117}Te but does not show several low-intensity γ-rays that have been observed by both groups. These low intensity γ-rays are not definitely attributed to the decay of some other nucleide and are not definitely assigned a half-life unequal to 1.1 h. The weaker γ-rays which we do place in the decay scheme (those whose relative intensities are $\leqq 2$) are clearly observed by both groups and have half-lives which are not noticeably different from 1.1 h. Although the agreement on relative intensities is not too good on the very weak transitions, the uncertainties in these values are large enough to accommodate both numbers. The agreement is poorest on those γ-rays whose presence or absence from the decay scheme does not affect the level scheme, i.e. the 634, 1580 and 2285 keV γ-rays, each of which is placed as decaying from a level that is well established by other transitions. The inclusion of weak γ-rays in the decay scheme is strengthened by their observance by both groups. In only the rarest of instances would it be possible for contaminant γ-rays to be in approximately the same relative intensity to ^{117}Te γ-rays in sources produced by the two different methods of source preparation.

Three levels that are heavily fed by positons are indicated at 720, 924 and 1717 keV by the 511-511 keV gamma coincidence spectrum (fig. 4). The lines at 695 and 1278 keV are assigned as double escape peaks of the 1717 and 2300 keV gamma rays, respectively. The non-existence of cascades among the 720, 924 and 1717 keV transitions can be seen from spectra taken in coincidence with these regions. In each case the presence of the other two lines can be accounted for by chance coincidences and underlying Compton scattering events in the gate.

Strong coincidences between the 720 keV region and the 997, 1091 and 1565 keV gamma rays and between the 924 keV region and the 887, 1355 and 1361 keV lines confirm the 1717 keV level and suggest additional levels at 1811 and 2285 keV. Further evidence for the level at 2285 keV is provided by a 2285 keV transition, by the suggested presence of 924-1361 and 930-1355 keV cascades, and by the presence of the 831 keV line in coincidence with the 1455 keV region. The intermediate levels of the latter two of the above cascades are placed at 1355 and 1455 keV from relative intensity considerations.

The 1355 keV level may also depopulate to the 720 keV state as is suggested by the trace of the 635 keV line in coincidence with the 720 keV region. The 1455 keV level has not been found to involve any transitions other than the 831-1455 keV cascade.

Additional coincidence data show the 569 keV transition to take place from the 2285 keV state to the 1717 keV level and a possible 473 keV transition from the 2285 keV state to the 1811 keV level. The absence of the strong 2300 keV line from the "any-coincidence" spectrum indicates a state at 2300 keV. The 2300 keV state also

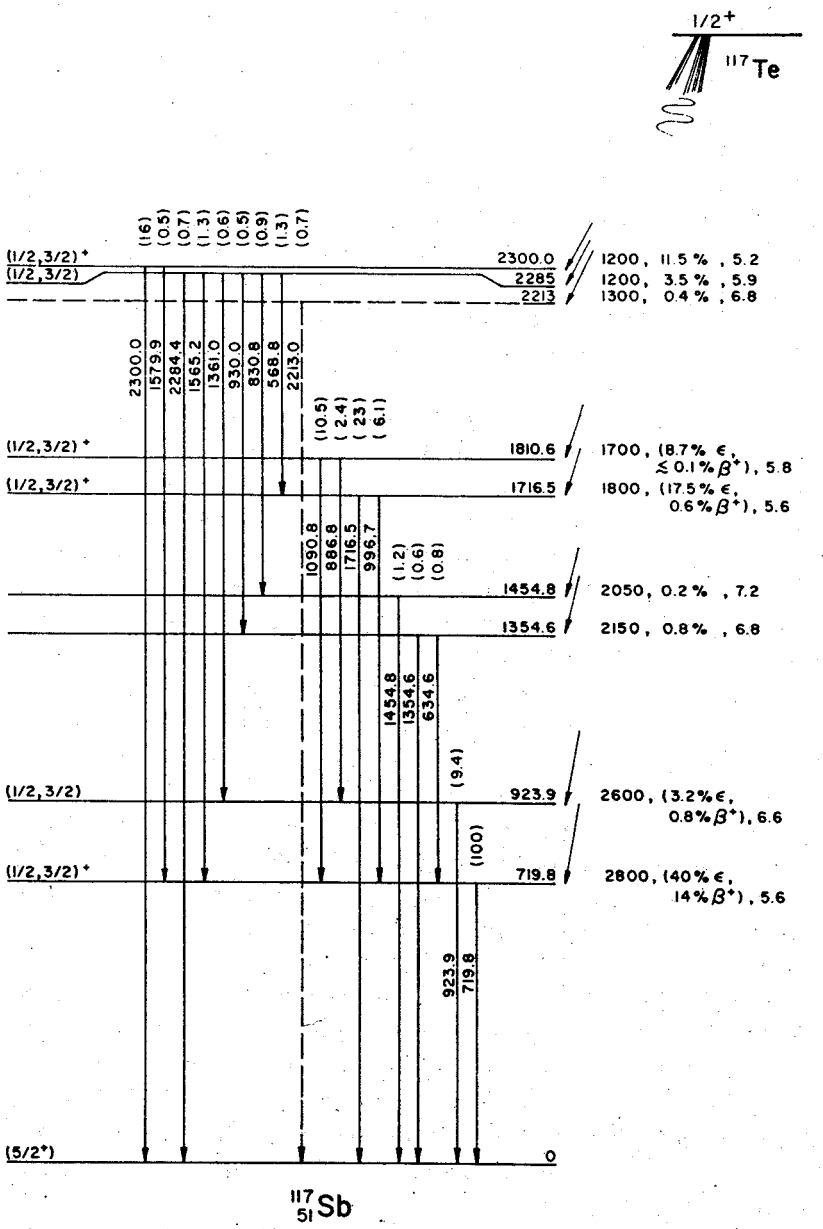

Fig. 8. The proposed decay scheme of ^{117}Te. Weak transitions of 1596, 2380 and 2885 keV, which could not be definitely assigned to the decay of ^{117}Te, have been omitted.

depopulates to the 720 keV state as is evidenced by the trace of the weak 1580 keV line in coincidence with the 720 keV region.

No coincidence experiments involving the high-energy transitions are feasible at this time. Estimates from singles and coincidence counting rates indicate that at least a 24 h counting time would be necessary with fresh sources produced at frequent intervals to obtain conclusive coincidence data for any of the lines above 2300 keV.

The very weak γ-rays that are observed by both groups at 1596, 2380 and 2885 keV have not been placed in the level scheme. As these γ-rays do not fit between any existing states and are not seen in any coincidence spectra, their inclusion could be accomplished only by placing levels at these energies. As the presence or absence of levels at these energies does not significantly alter the interpretation of the level scheme or its comparison with other nuclei or theoretical calculations, we have not included them in the level scheme.

The very striking similarity with respect to level structure and beta feeding ratios between this decay scheme and that of ^{119g}Te suggests this to be the decay of a low-spin ^{117}Te parent. The ground state spin of ^{117}Te is known to be $\frac{1}{2}^+$ from atomic beam measurements [17]). If this is indeed the decay of the ground state, then tentative spin and parity assignments can be made for some of the levels on the basis of log ft values. States at 720, 1717, 1811 and 2300 keV all have $4.0 \leqq \log ft \leqq 5.8$, indicating allowed beta decay [18]). Hence, these states should all have positive parity and $J = \frac{1}{2}$ or $\frac{3}{2}$. Slightly higher log ft values for the remainder of the levels indicate allowed or first forbidden beta transitions, implying $J = \frac{1}{2}, \frac{3}{2}$.

The assignments for the 720 and 924 keV states are consistent with other data and systematics in this region (see discussion in sects. 7 and 8).

7. The search for ^{117m}Te

7.1. SYSTEMATICS OF ODD-MASS TELLURIUM AND ANTIMONY STATES

As shown in fig. 9, excited states of $J = \frac{3}{2}^+$ and $\frac{11}{2}^-$ can be seen to migrate upward in energy with decreasing neutron number in ^{125}Te, ^{123}Te and ^{121}Te relative to the $\frac{1}{2}^+$ state. Isomeric transitions, originating at the $\frac{11}{2}^-$ states, are known to occur in all three isotopes [19]). However, while ^{119m}Te is known to exist, no isomeric transition has been observed [4,5,20,21]).

Two plausible explanations for this phenomenon can be obtained if one relies on the shell-model systematics in this region. As can be seen in fig. 9, the separation of the $\frac{11}{2}^-$ and $\frac{3}{2}^+$ levels decreases to less than 100 keV as one approaches ^{119}Te from the right. The Weisskopf estimate for single-particle M4 transition probabilities of less than 100 keV in energy, indicates a half-life of a few years, which is much too long to compete with 4.7 d beta decay. In the case of ^{117}Te, the $\frac{3}{2}^+$ level may be even closer to or possibly higher than the $\frac{11}{2}^-$ state.

Systematics of antimony levels [1–8]), (fig. 10), suggest a $\frac{7}{2}^+$ state at approximately 530 keV in ^{117}Sb. A state at this energy, tentatively identified as having spin $\frac{7}{2}$, has

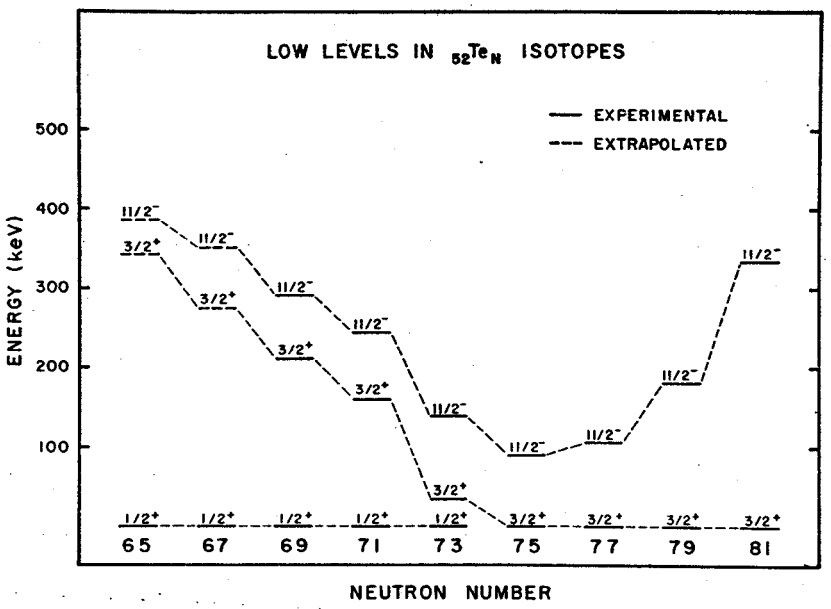

Fig. 9. Low-lying levels in $_{52}Te_N$ isotopes [19]). The $\frac{3}{2}^+$ and $\frac{11}{2}^-$ levels for ^{117}Te and ^{119}Te are extrapolated from the neighbouring isotopes.

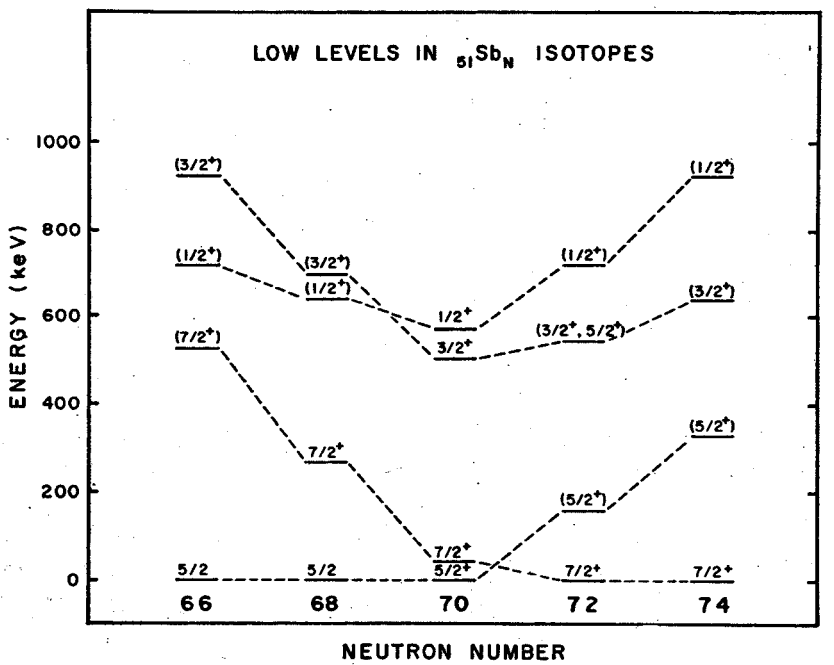

Fig. 10. Low-lying states in $_{51}Sb_N$ isotopes. The information has been obtained from published decay schemes [3–5, 29]), (^{3}He, d) data [6–8]) and private communications [30]).

been observed via (^{3}He, d) reactions [6-8]). Analogous to the decay of ^{121m}Te and ^{119m}Te, ^{117m}Te should decay via a first-forbidden, unique beta branch to the 530 keV $\frac{7}{2}^+$ state in ^{117}Sb with a partial half-life of several days. However, this may be much too slow to compete with allowed or other first-forbidden beta groups which are expected to be present from systematics and the large decay energy. Especially if, as in ^{119}Sb, high-spin negative-parity states are present [5,21,22]), the beta decay process could be very rapid.

An alternative explanation for the absence of an identifiable ^{117m}Te activity can be sought from the case of ^{115}Te. A 275 keV M3 transition in ^{115}Te has been reported to have a half-life of approximately 0.1 sec, suggesting a $\frac{7}{2}^+$ excited state [23,24]). Hence it is possible that a $\frac{7}{2}^+$ level may exist below the $\frac{11}{2}^-$ state in ^{117}Te, making de-excitation of the $\frac{11}{2}^-$ state comparatively rapid. Such a situation is also known to exist in ^{115}Sn which has the same number of neutrons ($N = 65$) as ^{117}Te. In that nucleus, the $\frac{7}{2}^+$ level is found 107 keV below the $\frac{11}{2}^-$ level and the $\frac{11}{2}^-$ level has a half-life [25]) of 159 μs.

7.2. EXPERIMENTAL RESULTS

A number of attempts were made to identify an isomeric activity ^{117m}Te and were primarily based on a search for a 530 keV gamma ray depopulating a spin $\frac{7}{2}^+$ state of this energy as predicted from systematics and observed via (^{3}He, d) reactions [6-8]). Neither at MIT nor MSU was any evidence observed for any gamma-ray activity from a possible ^{117m}Te having a half-life longer than about 2 min but shorter than 1 h.

In one type of experiment a thin target of antimony metal was bombarded at MSU to produce the highest available ratio of ^{117}Te to ^{119}Te. The chemically extracted activities were followed for several days. A very weak, but unquestionable, peak at 530 keV became evident as the 16 h ^{119g}Te activity decayed away. Since this line was present in a spectrum recorded immediately after subsequent specific tellurium chemistry, it must be associated with the decay of some tellurium parent.

Next, a search was made at MSU for the 2.5 h daughter of ^{117}Te. The antimony daughters of ^{118}Te and ^{119}Te were periodically extracted from the source which emitted the 530 keV gamma ray, among others, but the prominent 160 keV transition in the decay of ^{117}Sb could not be identified in the samples. However, the amount of activity expected was extremely small, and could have been masked by the presence of small amounts of ^{119}Te impurity.

Furthermore, assuming that any ^{117m}Te would be produced in approximately the same ratio to ^{117g}Te as ^{117m}Te is produced to ^{119m}Te, a far greater amount of the 530 keV gamma activity should have been present if this transition does indeed originate from ^{117m}Te. This is especially true in the ^{114}Sn(α, n)^{117}Te reaction used at MIT to produce the ^{117}Te. It can be noted from fig. 1 that the ^{119g}Te that gives rise to the 644 keV γ-ray is the major interfering isomer at MSU. At MIT, where a target containing 60 % ^{114}Sn and 10 % ^{116}Sn was used, the γ-rays at 270 and 1213 keV, which follow the decay of the $\frac{11}{2}^-$ ^{119m}Te isomer, were found in nearly as much abundance

as the 644 keV γ-ray from ^{119g}Te. If an $\frac{11}{2}^-$ isomer of ^{117}Te were present, it should have been six times as abundant as the ^{119m}Te that we observed, if the two had comparable half-lives. Failure to observe any evidence of a 530 keV γ-ray could be accounted for only by a half-life for ^{117m}Te of no less than 1 y. Also, because of the large beta disintegration energy, a far richer gamma-ray spectrum can be anticipated. On the basis of systematics in this region it is very unlikely that most of the beta decay of ^{117m}Te would go directly to the ground state of ^{117}Sb (third-order forbidden transition).

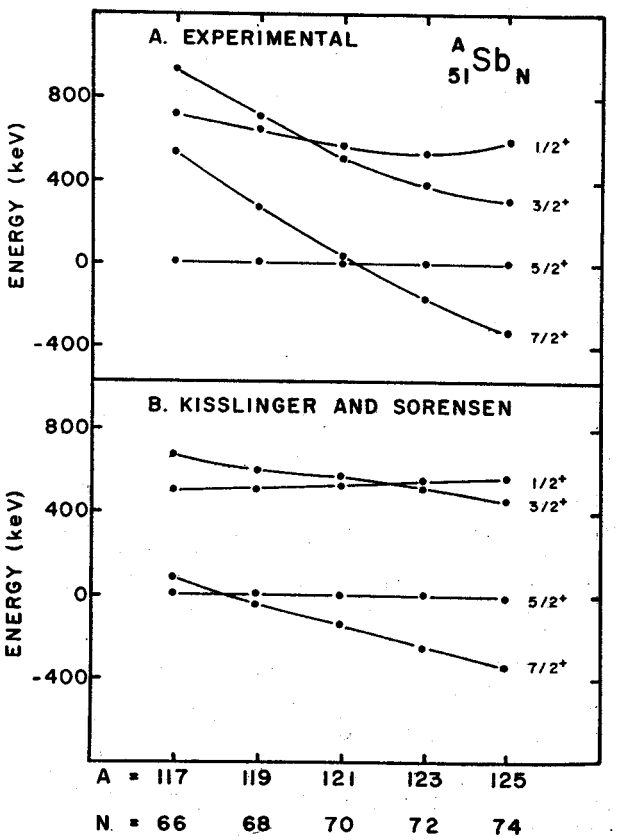

Fig. 11. A comparison of the trends of low-lying states in odd-mass antimony isotopes with the trends calculated by Kisslinger and Sorensen [25]). The states have been shifted to allow the $\frac{5}{2}^+$ state to be used as a reference level.

Hence, while the existence of an isomeric state ^{117m}Te with an appreciable half-life cannot be definitely excluded, it is suggested to be very unlikely. The fact that the 530 keV gamma ray is associated with a tellurium parent or with an activity which survives specific tellurium chemistry, remains, at present, a mystery. The resolution of this problem is complicated by the very low intensity of this gamma ray relative to the gamma rays of ^{119m}Te.

8. Discussion of results

Although no definite spins can be assigned from our experiments, comparisons with (^{3}He, d) data [6-8]) and recent (p, n) experiments [26]) suggest the probable assignments for the low-lying states of adjacent 51-proton, odd-mass nuclei to be as shown in fig. 10. These levels have been redrawn in fig. 11 A with the $\frac{5}{2}^+$ state as the reference level. A very smooth variation can be seen with respect to neutron number.

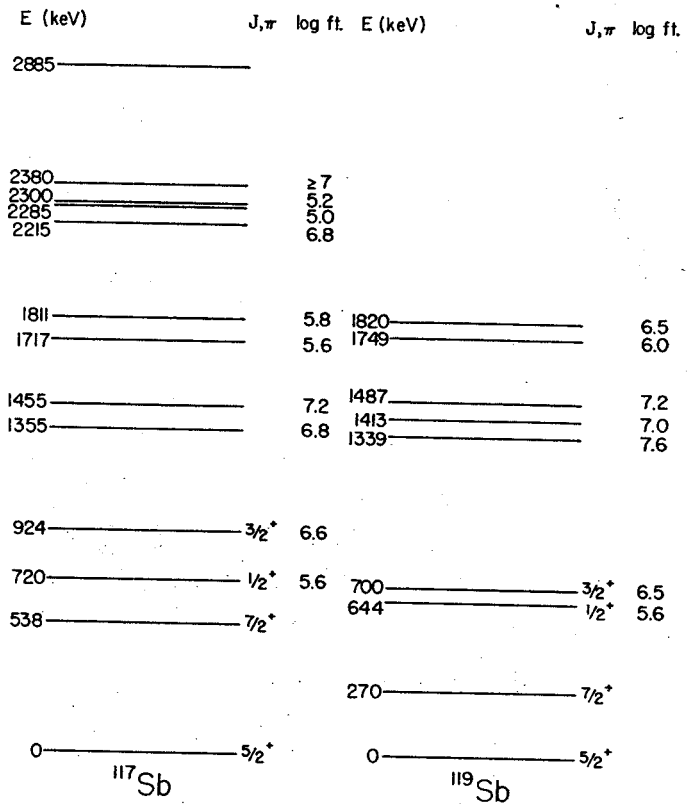

Fig. 12. Low-spin levels of ^{119}Sb compared to the levels of ^{117}Sb.

It is of interest to compare the low-lying levels with the calculation of Kisslinger and Sorensen [27]), in which a pairing plus quadrupole interaction is assumed. The results of this calculation are shown in fig. 11 B. While quantitative discrepancies in energy exist, there is very impressive agreement in the order of the levels and in their relative positions. However, the crossing of the $\frac{1}{2}^+$ and $\frac{3}{2}^+$ and of the $\frac{5}{2}^+$ and $\frac{7}{2}^+$ states occurs slightly later and earlier, respectively, in the calculated than in the experimental set of states.

We show in fig. 12 a comparison of the low-spin levels observed in ^{119}Sb with those observed in ^{117}Sb. The two groups of levels are quite similar except that the higher

Q in ^{117}Te decay permits higher energy ^{117}Sb levels to be observed. The log ft values are seen to range over ≈ 2 units in each case with some transitions that are likely allowed having log ft values > 7. It may be observed that, in spite of an approximately 260 keV increase in the difference between the $g_{\frac{7}{2}}$ level and the $d_{\frac{5}{2}}$ ground state, the levels around 1400 keV and around 1800 keV remained almost unchanged (except

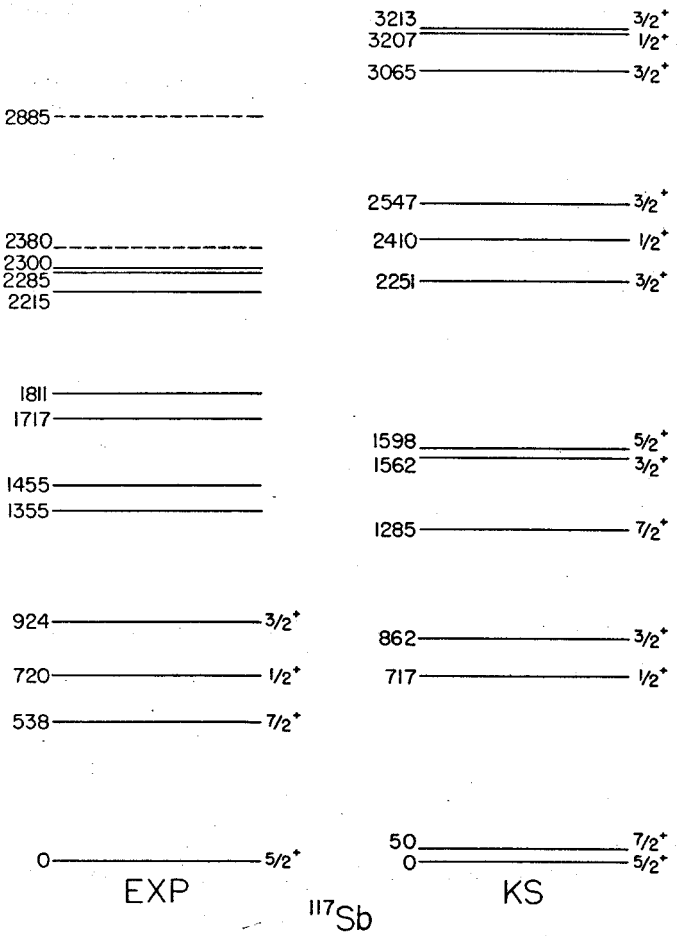

Fig. 13. Low-spin levels from Kisslinger and Sorensen calculations compared to the levels of ^{117}Sb.

for our failure to observe a level in ^{117}Sb similar to the 1437 keV level in ^{119}Sb). This is in contrast to the rise in the positions of the lowest $\frac{1}{2}^+$ and $\frac{3}{2}^+$ levels that were discussed earlier and may indicate that the main configuration of these levels is that of a core excitation coupled to the $d_{\frac{5}{2}}$ proton in its ground state. As the first excited states of ^{116}Sn and ^{118}Sn are 1294 and 1230 keV, respectively [28]), such levels would be expected at similar positions in the two schemes.

It is also of interest to compare the high-energy levels that we have observed in ^{117}Sb with those whose spins are $\frac{1}{2}^+$ and $\frac{3}{2}^+$ as calculated by KS. They are shown in fig. 13 where we have also shown the calculated positions of the lowest $\frac{5}{2}^+$ and $\frac{7}{2}^+$ phonon levels as well. The calculated levels at 717, 862 and 1562 keV are primarily made up of one phonon-core vibration coupled to the single-particle $\frac{5}{2}^+$ or $\frac{7}{2}^+$ levels. The higher levels are primarily made up of two phonon-core vibrations coupled to the single-particle levels. The general pattern of calculated levels appears to compare well with the observed levels below 2 MeV, although the observed levels are, in general, lower in energy.

To the best of our knowledge, at this time, there exist for the case of ^{117}Sb no calculations based on the core-coupling model, in which vibrations of a doubly even core are assumed to couple with single-particle states of extra-core nucleons. The model shows some qualitative agreement with experimental states in ^{119}Sb. Hence, it would be of interest to locate the corresponding high-spin states in ^{117}Sb. However, other means of excitation would be necessary since it appears that an isomeric state does not exist in ^{117}Te. Estimates from a comparison with the set of states populated by beta decay of ^{119m}Te and ^{119g}Te, suggest that a large number of high-spin levels should exist in the ^{117}Sb nucleus.

The authors at MSU wish to thank Dr. W. P. Johnson for his assistance with the cyclotron operation during bombardments. They are grateful to Dr. R. E. Berg for the use of one of his detectors for some of the measurements. A special note of thanks goes to Dr. L. M. Beyer for many helpful discussions and suggestions. The authors at MIT wish to thank Mr. Earl White and the crew of the MIT Cyclotron for their assistance with the irradiations and Mr. John Wild for helping prepare the samples for counting. They also wish to express appreciation to Professor L. S. Kisslinger for supplying detailed calculations for the levels of ^{117}Sb as well as to Dr. V. Orphan and Mrs. B. Hites for assistance with the Ge(Li) detectors.

References

1) R. L. Auble and W. H. Kelly, Nuclear Physics **79** (1966) 577
2) R. L. Auble and W. H. Kelly, Nuclear Physics **81** (1966) 442
3) R. L. Auble, W. H. Kelly and H. H. Bolotin, Nuclear Physics **58** (1964) 337
4) G. Berzins and W. H. Kelly, Nuclear Physics **A92** (1967) 65
5) G. Graeffe *et al.*, Phys. Rev. **158** (1967) 1183
6) G. Bassani *et al.*, Phys. Lett. **22** (1966) 189
7) T. Ishimatsu *et al.*, Bull. Int. Conf. on nuclear physics (Sept. 1966) p. 16
8) P. D. Barnes *et al.*, Phys. Lett. **23** (1966) 226
9) R. W. Fink, G. Andersson and J. Kantele, Ark. Fys. **19** (1961) 323
10) N. A. Vartanov *et al.*, JETP (Sov. Phys.) **14** (1962) 215
11) F. D. S. Butement and S. M. Quaim, J. Inorg. Nucl. Chem. **27** (1965) 1729
12) D. E. Khulelidze *et al.*, Izv. Akad. Nauk. SSSR **26** (1962) 1026
13) L. M. Beyer, G. Berzins and W. H. Kelly, Nuclear Physics **A93** (1967) 436
14) G. Berzins *et al.*, Nuclear Physics **A93** (1967) 456

15) R. L. Auble *et al.*, Nucl. Instr. **51** (1967) 61
16) D. B. Beery and W. H. Kelly, to be published
17) S. Axensten, G. Liljegren and I. Lindgren, Ark. Fys. **20** (1961) 473
18) K. Way *et al.*, Nucl. Data **1** (1966) B1-1-VII
19) Nuclear Data Sheets (National Research Council, Washington, D.C.)
20) J. Kantele and R. W. Fink, Nuclear Physics **43** (1963) 187
21) R. M. Singru, S. H. Devare and H. G. Devare, preprint
22) J. Svedberg and G. Andersson, Nuclear Physics **48** (1963) 313
23) D. E. Khulelidze *et al.*, ZhETF (USSR) **47** (1964) 1167
24) A. G. Demin *et al.*, ZhETF (USSR) **45** (1963) 1344
25) E. Ivanow *et al.*, Nuclear Physics **54** (1964) 177
26) R. L. Kernell *et al.*, Bull. Am. Phys. Soc. **12** (1967) 545
27) L. S. Kisslinger and R. A. Sorensen, Revs. Mod. Phys. **35** (1963) 853
28) G. Berzins, W. B. Chaffee and D. B. Beery, unpublished data (1966)
29) S. H. Devare and H. G. Devare, Phys. Rev. **133** (1964) B568
30) R. L. Auble, private communication

NUCLEAR INSTRUMENTS AND METHODS 54 (1967) 268–276; © NORTH-HOLLAND PUBLISHING CO.

A SINGLE CRYSTAL Ge(Li) COMPTON SPECTROMETER*

C. R. GRUHN, J. V. KANE, W. H. KELLY, T. KUO and G. BERZINS

Department of Physics, Michigan State University, East Lansing, Michigan, U.S.A.

Received 12 May 1967

A single crystal Ge(Li) Compton spectrometer has been tested showing considerable promise as a device for detecting γ-rays in the presence of strong Compton and neutron backgrounds

With the advent of high resolution lithium-drifted germanium, γ-ray spectroscopy has been completely revolutionized. The chief advantage of these detectors is in their ability to make precise (typically a few parts in 10^4) energy measurements. A major disadvantage of these devices is that the gamma ray of interest, in many instances, is submerged in a rather large number of background events. These background events are primarily due to the Compton-scattering of gamma rays out of the detector. Several methods have been previously reported which reduce the effects of Compton-scattered γ-rays as a source of background. For example, one method employs a NaI(Tl) annulus detector which detects the scattered γ-ray and vetoes this event as detected in the Ge(Li) detector[1]); a second method employs a NaI(Tl) split annulus which detects two 511 keV γ-rays in triple coincidence with events detected in the Ge(Li) detector, thus emphasizing pair produced events with a double escape[2]). The first method has the advantage of reducing the background under the peak by about a factor of ten or so and the

* This work was supported in part by NSF Contract ≈GP-6760.

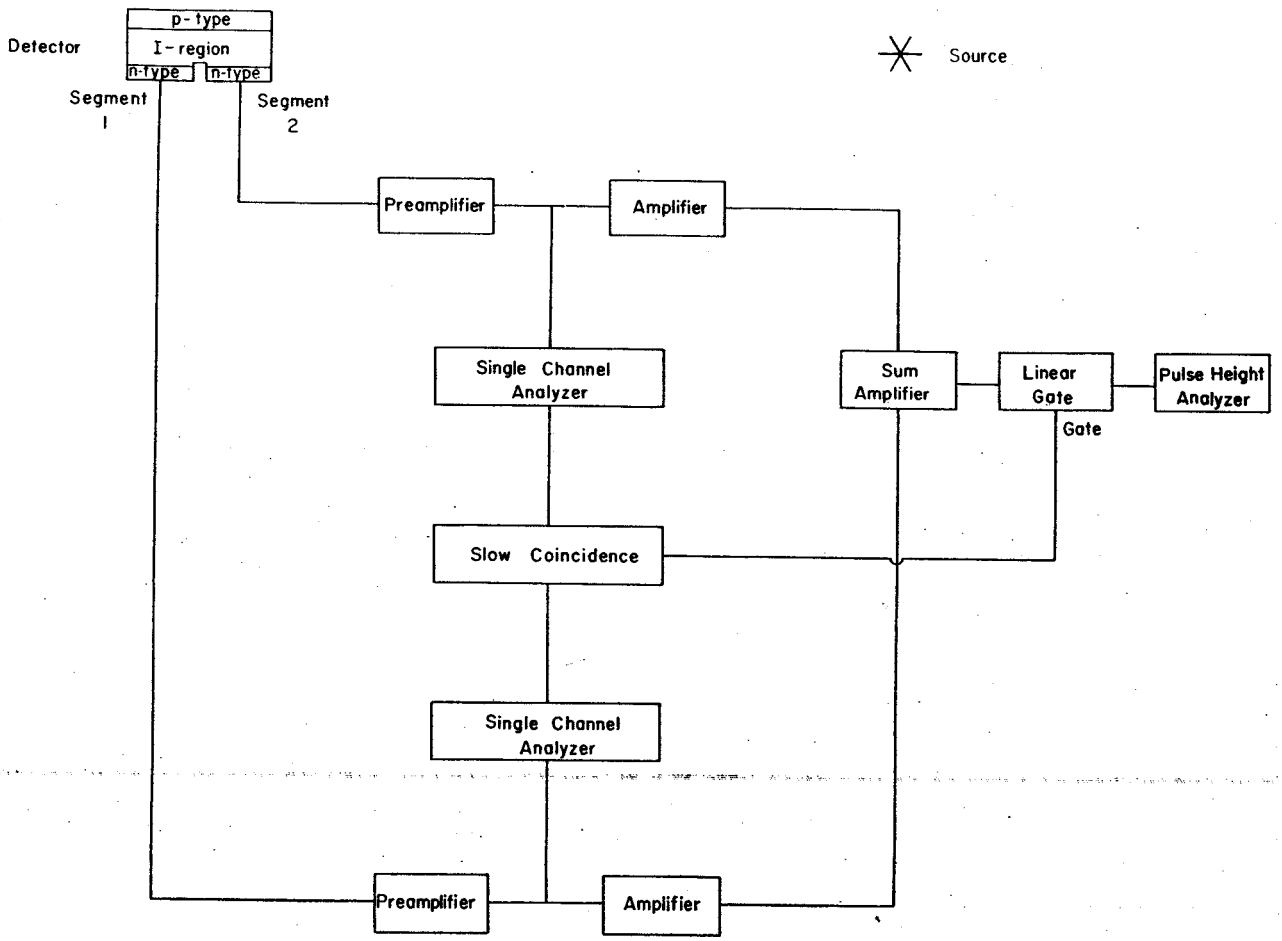

Fig. 1. The experimental arrangement of a Compton-spectrometer and block diagram of electronics.

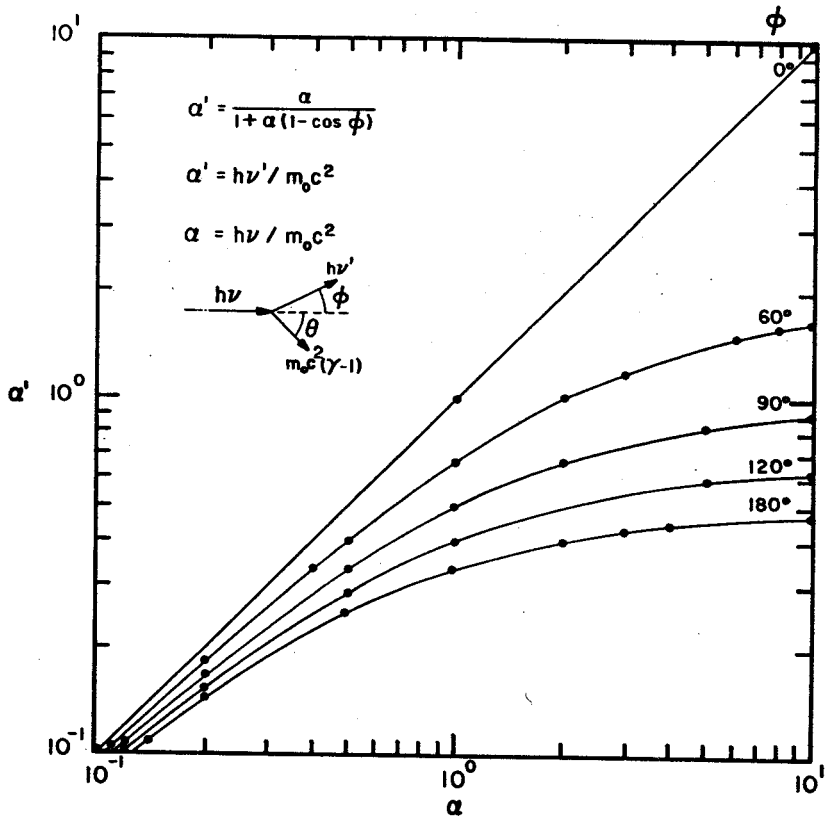

Fig. 2. A plot of the Compton-scattered γ-ray energy, α' (in units of m_0c^2), vs the incident γ-ray energy, α, for several scattering angles.

disadvantages of suppressing coincident γ-rays unless one resorts to elaborate precautions of using collimators. The second method can be used only for the detection of γ-rays having energies greater than 1022 keV.

The purpose of this paper is to explore the feasibility of using a single Ge(Li) crystal as a Compton spectrometer and thereby reducing the background due to the Compton-scattering of γ-rays out of the detector. Such a detector has been fabricated and tested at this laboratory and is observed to have the following properties: The background events, relative to the full energy events, are reduced by a factor that ranges between 10 and 30; the efficiency for detecting a full energy event is strongly dependent upon the direction of incidence of the γ-ray relative to the orientation of the detector; and the detector has a high efficiency for rejecting neutron events.

We show in fig. 1 the experimental arrangement of a Compton-spectrometer. Compton events are emphasized by demanding a coincidence between the two germanium segments. By summing pulses due to the charge collected in each of the two segments, we can obtain a measure of the energy of the incident γ-rays. Whenever we have detected simultaneously a recoil Compton electron in one segment and a photo electron of the Compton-scattered γ-ray in the other segment, the resulting (summed) pulse corresponds to the full energy of the incident gamma ray.

By use of a differential discriminator on the pulses coming from the segment, we can emphasize back-scattered Compton events, thus strongly enhancing the directional sensitivities of the detector. This can be easily understood by considering fig. 2 where we show a plot of the Compton-scattered γ-ray energy, α' (in units of m_0c^2), vs the incident γ-ray energy, α for several scattering angles. Notice, for example, that by requiring $\alpha' \leqq 0.5$ we restrict $\phi \geqq 90°$ for all $\alpha \geqq 1.0$; a requirement of $0.60 \leqq \alpha' \leqq 0.66$, yields $60° \leqq \phi \leqq 100°$ for $1.0 \leqq \alpha \leqq 2.0$ and $90° \leqq \phi \leqq 120°$ for all $\alpha \geqq 2.0$. Invariably, one must compromise between directional sensitivity and overall efficiency.

A #6 ingot of approximately 11 ohm·cm horizontally grown, gallium-doped germanium* with an etch-

* Sylvania Electronic Products, Chemical and Met. Div., Tawanda, Pennsylvania.

Fig. 3. A comparison between an ungated ^{23}Na spectrum (the upper spectrum) and the gated sum spectrum of the same source (lower spectrum).

Fig. 4. A comparison between an ungated ^{56}Co spectrum and the gated sum spectrum of the same source.

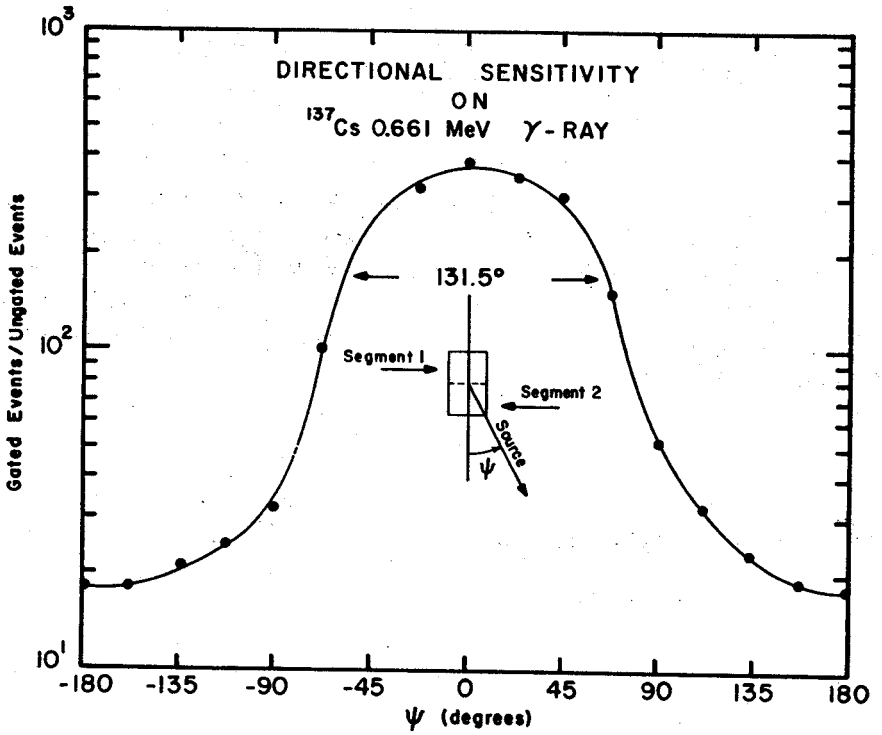

Fig. 5. The directional sensitivity of the Compton spectrometer to 611 keV γ-rays with a 150 to 250 keV gate.

pit density of 700/cm^2 and a carrier lifetime of 400 μsec was the starting material. A 0.7 cm length of the ingot was cut with a diamond saw and lapped on all sides. Lithium was evaporated and diffused on one cross-sectional face of the ingot. The diffusion and drift techniques were the same as has been reported elsewhere. The lithium was drifted into a depth of 0.5 cm. After the drift, a 0.076 cm wide saw cut was made bisecting the n-type lithium diffused surface. This cut was made such that it just penetrated into the compensated region. We have found that the electronic cross-talk between the two segments of the crystal divided by such a cut is extremely small. In fact, we find essentially no deterioration of the resolution in one segment of the crystal as an adjacent segment is allowed to avalanche break down. The idea of making such cuts is not new and is discussed elsewhere[4]). Hayashi et al.[5]) find that the region of confusion at such a cut is approximately 0.1 mm wide. By region of confusion, we mean that region in which a fraction of the ion pairs is collected by each set of electrodes. The crystal was mounted in a cryostat similar in design to one reported by Chasman[6]). The cryostat mount was designed such that it could be used in the tunnel of a NaI(Tl) annulus detector.

A block diagram of a typical electronics arrangement is shown in fig. 1. The gain of the electronics associated with each segment was matched to less than 0.2% using a ^{137}Cs source. The resolution of each segment was 6 keV (fwhm) and the sum had a resolution of 9 keV (fwhm) for the 661 keV ^{137}Cs γ-ray.

Fig. 3 shows a comparison between an ungated ^{22}Na spectrum (the upper spectrum) and the gated sum spectrum of the same source (the lower spectrum) with the electronic gate set between 60 and 250 keV. The region of Compton-background events between the 511 and 1274 keV peaks is reduced by a factor of ~ 10 relative to the number of events in the full energy peaks. By comparing these spectra it is found that the efficiency of detection of the 1274 keV gamma-ray in the full energy peak by the Compton spectrometer is one tenth of that for detecting it when the system operates as a normal detector.

Fig. 4 shows, in the same way, a comparison between an ungated ^{56}Co spectrum (the upper spectrum) and the gated sum spectrum of the same source (the lower spectrum).

Table 1 gives the Ge(Li) Compton spectrometer enhancement of the ratios of the peak areas to the underlying backgrounds for the ^{56}Co gamma-rays. The relative efficiency is approximately constant as a function of energy; however, it is strongly dependent upon the energy width of the back-scattered γ-ray gate (150–250 keV).

Fig. 6. Singles spectrum and gated sum spectrum showing rejection of neutron associated events.

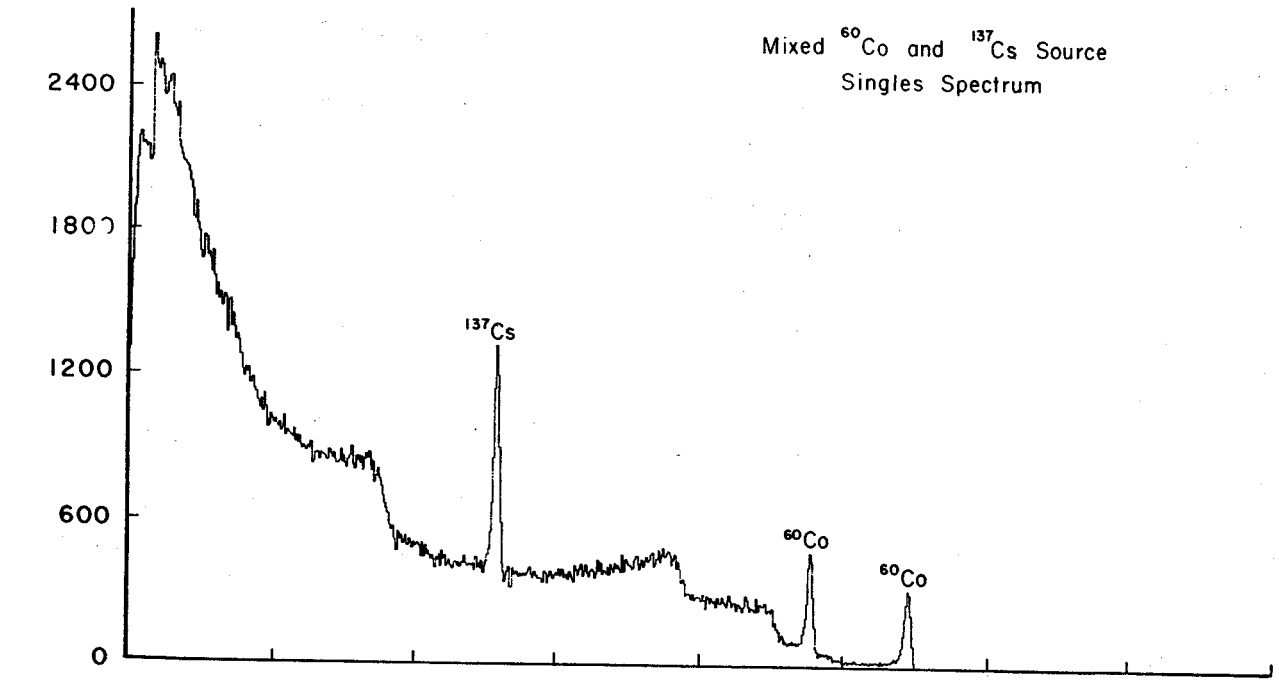
Mixed ^{60}Co and ^{137}Cs Source
Singles Spectrum
2400
1800
1200
600
0
^{137}Cs
^{60}Co
^{60}Co

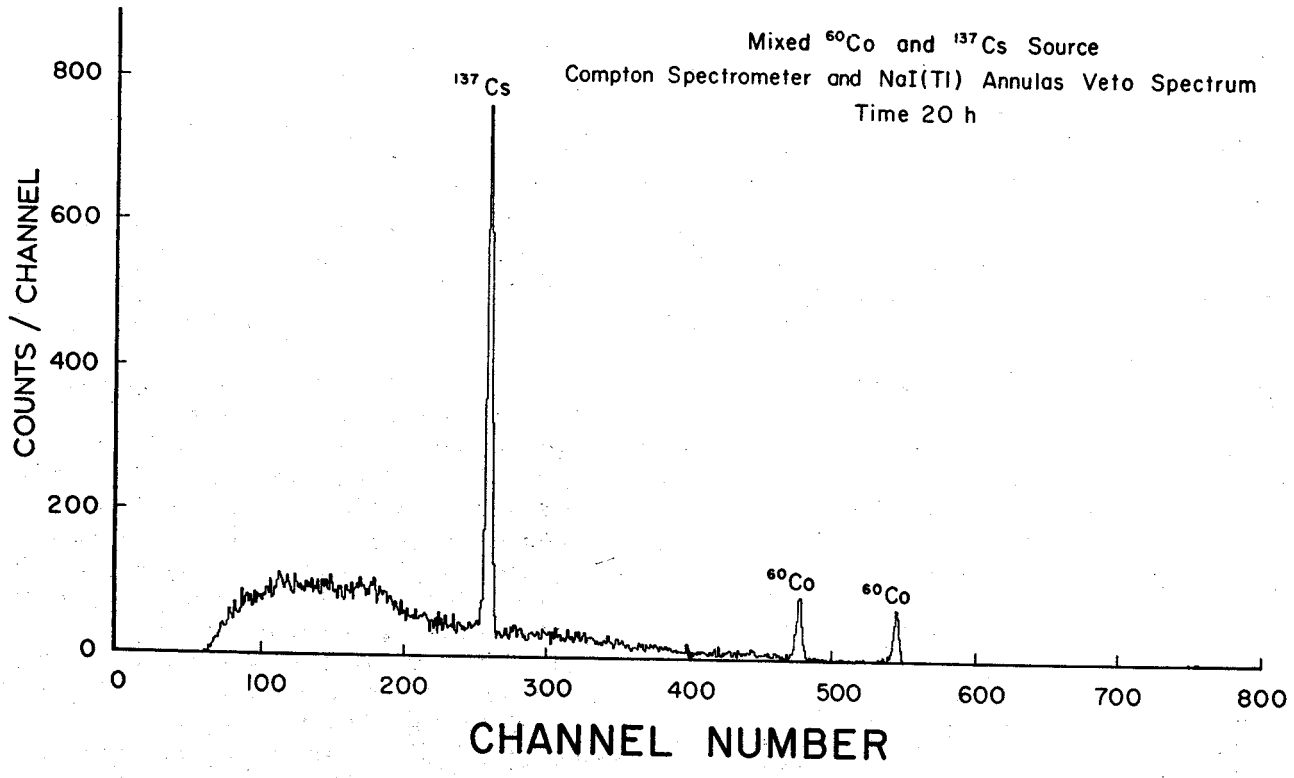
Mixed ^{60}Co and ^{137}Cs Source
Compton Spectrometer and NaI(Tl) Annulas Veto Spectrum
Time 20 h
^{137}Cs
^{60}Co
^{60}Co
COUNTS / CHANNEL
800
600
400
200
0
0
100
200
300
400
500
600
700
800
CHANNEL NUMBER

(Fig. 7)

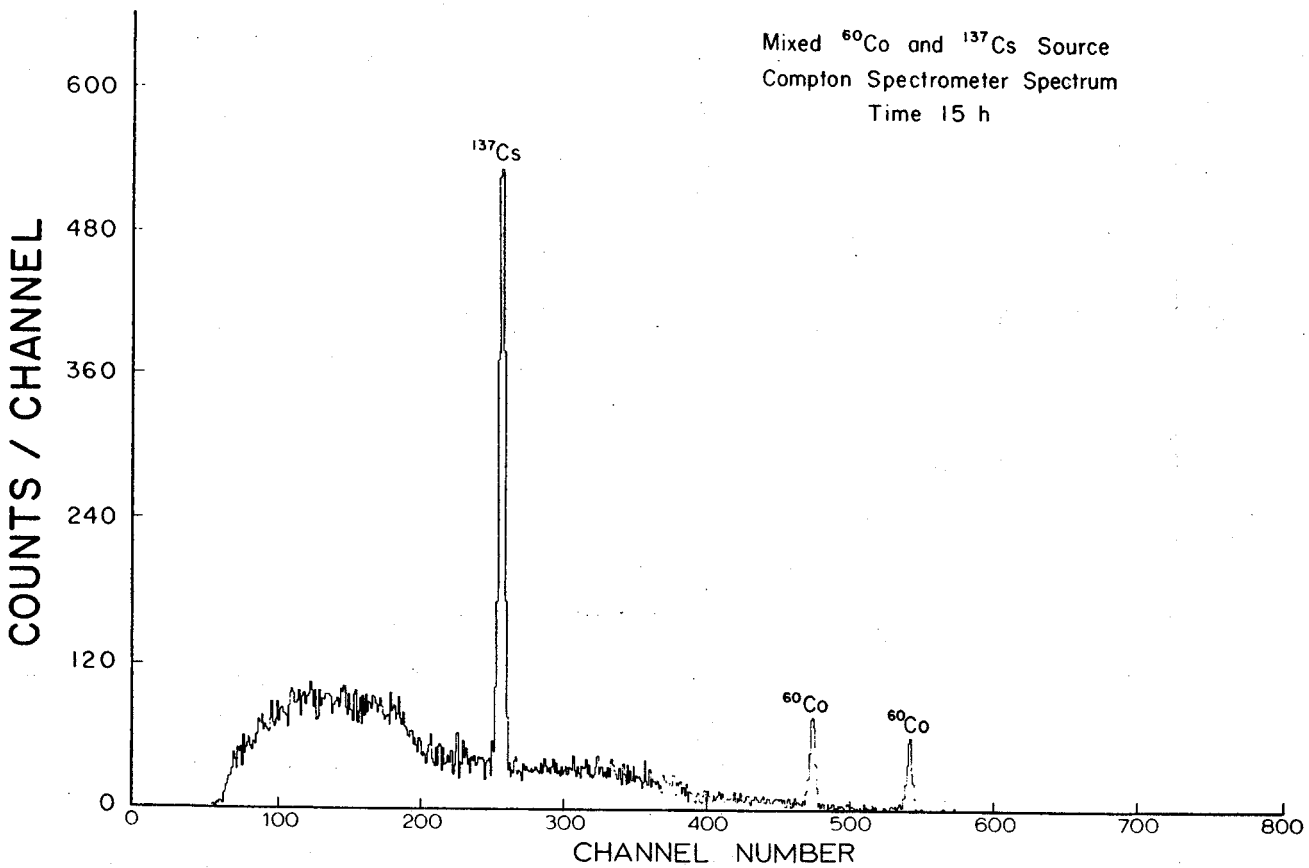

Fig. 7. Spectra of a mixed ^{137}Cs and ^{60}Co source showing improved rejection of background events using Compton spectrometer vetoed by a NaI(Tl) annulus detector.

The directional sensitivity of the Compton spectrometer to a 661 keV γ-ray with a 150 to 250 keV gate is shown in fig. 5. The directional sensitivity has a width of 131.5° (fwhm). This is consistent with the angular selectivity of the backscattered γ-ray gate (fig. 2). In order to minimize geometric corrections the data were normalized to the *ungated* counts in the full energy peak. The angle is measured between the plane of orientation of the detector and source direction.

TABLE 1
Ge(Li) Compton spectrometer enhancement of ratios of peak areas to the underlying background for ^{56}Co gamma rays.

E (keV)	(Peak area background) coinc. / (Peak area background) singles	
511	2.4	
847	2.6	
1039	15	← (Weak peak on Compton edge of 1238-keV gamma ray.)
1238	2.6	
1359	3.2	
1771	5.2	

In order to assess the performance of the Compton spectrometer in the presence of a high neutron flux, the spectrometer was placed adjacent to a thick Be target which was bombarded with 37 MeV protons from the Michigan State University cyclotron. Fig. 6 shows both a singles spectrum and a gated sum spectrum. Note the large asymmetric peak at 0.690 MeV in the singles spectrum. This peak has been identified as being due to internally converted electrons associated with an E0 transition in ^{72}Ge and could only be produced here as a result of the neutron interaction in the germanium detector. This peak is missing in the coincidence spectrum as one expects it should be.

As a further test of the Compton spectrometer, a segmented detector, similar to the one above, was placed in an annulus[2]) of NaI(Tl). The NaI(Tl) detector served as a veto of Compton-Compton events. Fig. 7

shows spectra of a mixed ^{137}Cs and ^{60}Co source. The 661 keV peak to background event ratio is 17 to 1 for the Compton spectrometer with NaI(Tl) annulus detector veto. The improvement with the annulus detector veto could be made substantially better with a more effective source – annulus – Ge(Li) detectors geometry. The arrangement used here was far from optimum.

In conclusion, the Compton spectrometer reported in this paper shows considerable promise as a device for detecting γ-rays in the presence of strong Compton and neutron backgrounds and as a directional gamma ray detector. It should prove to be especially useful over the γ-ray energy range of 0.250 and 2.0 MeV.

References

[1] Y. Sever and J. Lippert, Nucl. Instr. and Meth. **33** (1965) 347; J. Kantele and P. Suominen, Nucl. Instr. and Meth. **41** (1966) 41.

[2] R. L. Auble, D. B. Beery, G. Berzins, L. M. Beyer, R. C. Etherton, W. H. Kelly and Wm. C. McHarris, Nucl. Instr. and Meth. **51** (1967) 61.

[3] A. J. Tavandale, IEEE Trans. Nucl. Sci. NS-**11**, no. 3 (1964) 191.

[4] W. K. Hofker, D. P. Oosthoek, A. M. E. Hoeberechts, R. van Dantzig, K. Mulder, J. E. J. Oberski, L. A. Ch. Koerts, J. H. Dieperink, E. Kok and R. F. Rumphorst, IEEE Trans. Nucl. Sci. NS-**13**, no. 2 (1966) 208.

[5] I. Hayashi, H. E. Kern, J. W. Ridgers and G. H. Wheatley, IEEE Trans. Nucl. Sci. NS-**13**, no. 2 (1966) 214.

[6] C. Chasman and R. A. Ristinen, Nucl. Instr. and Meth. **34** (1965) 250.

1.E.1:
3.A

Nuclear Physics A104 (1967) 263—273; © *North-Holland Publishing Co., Amsterdam*

Ge(Li)-NaI(Tl) ANGULAR CORRELATION STUDIES OF GAMMA CASCADES IN THE DECAY OF ^{119m}Te

G. BERZINS † and W. H. KELLY

Department of Physics, Michigan State University, East Lansing, Michigan, USA ††

Received 29 June 1967

Abstract: Angular correlation measurements have been performed with a Ge(Li)-NaI(Tl) detector combination on several gamma-ray cascades present in the decay of 4.7 d ^{119m}Te. Results obtained for the 153–1213, 942–270, 1095–270, 976–979, 976–979–270, 2089–270, 1137–270 and 912–153–1213 keV cascades are in substantial agreement with previous spin assignments which were based primarily on conversion electron studies. Possible multipolarity mixing ratios are suggested for the 153, 270, 912, 942 and 1213 keV transitions.

E

RADIOACTIVITY: ^{119}Te [from ^{121,123}Sb(p, xn)]; measured $\gamma\gamma(\theta)$. ^{119}Sb levels deduced J, δ. Natural targets, Ge(Li) detector.

1. Introduction

Recent gamma-ray studies with high-resolution singles and coincidence systems [1,2]) have shown the decay schemes of ^{119g}Te and ^{119m}Te to be considerably more complex than could previously be deduced from studies with electron spectrometers and scintillation counters alone [3,4]). Earlier, results from conversion electron studies [2,3,5]) have been used in conjunction with results of some angular correlation experiments that were performed with scintillation detectors [2,5,6]) to assign spin values to a few of the states.

As has been shown by Ge(Li)-NaI(Tl) coincidence studies [1,2]), the decay scheme (fig. 1) and the gamma-ray spectrum, (fig. 2) of ^{119m}Te are far too complex to allow reliable interpretations to be made from coincidence data which have been obtained from scintillation detectors alone. It was the purpose of this investigation to perform angular correlation measurements for ^{119m}Te using a Ge(Li)-NaI(Tl) coincidence spectrometer.

The results obtained in this study are in substantial agreement with most of the previous assignments [2,3,6]). Since the previous conclusions were based primarily on conversion electron data, the present results provide an independent confirmation of most of the previous spin assignments.

† Present address: Los Alamos Scientific Laboratory, Los Alamos, New Mexico.

†† This work was supported in part by the U.S. National Science Foundation.

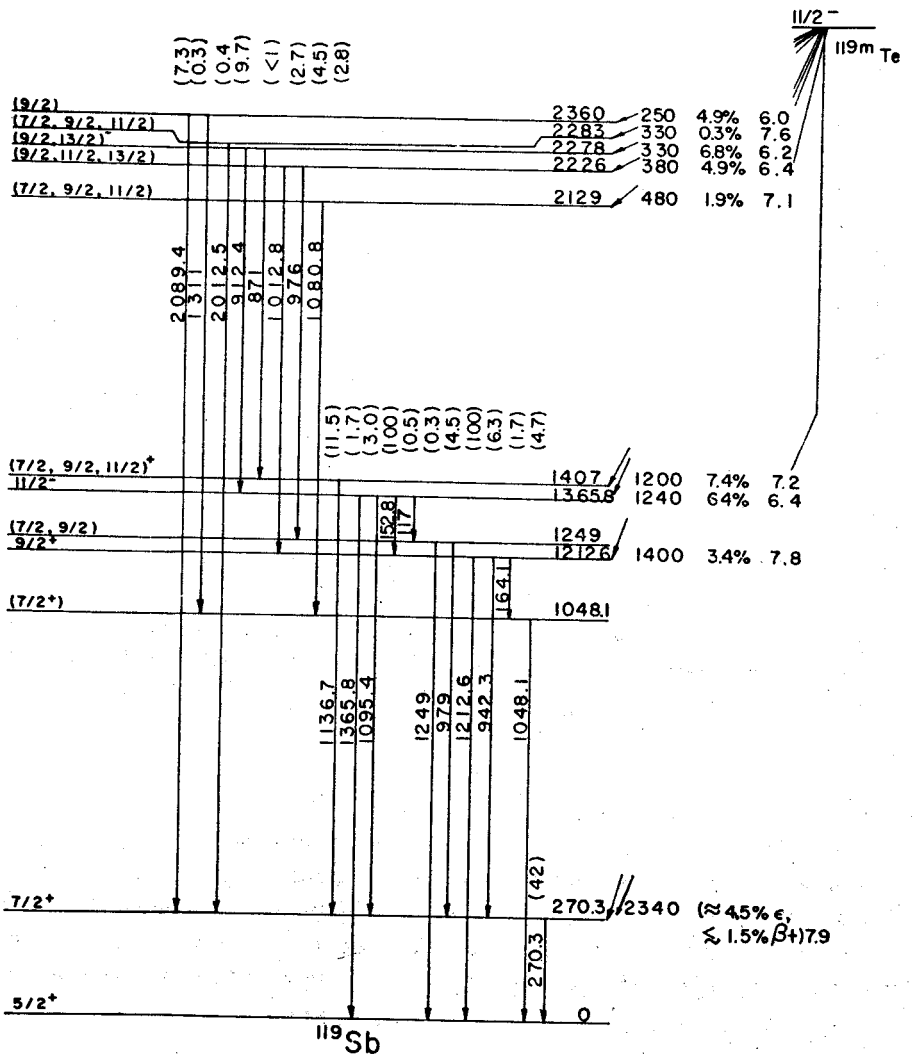

Fig. 1. Decay scheme of 4.7 d ^{119m}Te from ref. [1]). Except for minor discrepancies in relative intensities of some gamma rays, this decay scheme is identical to that proposed by Graeffe *et al.* [2]). The spin values assigned are based on the combined results of this investigation, the conversion coefficients of the 153 keV transition [3,4,5]) and log *ft* values [1,2]).

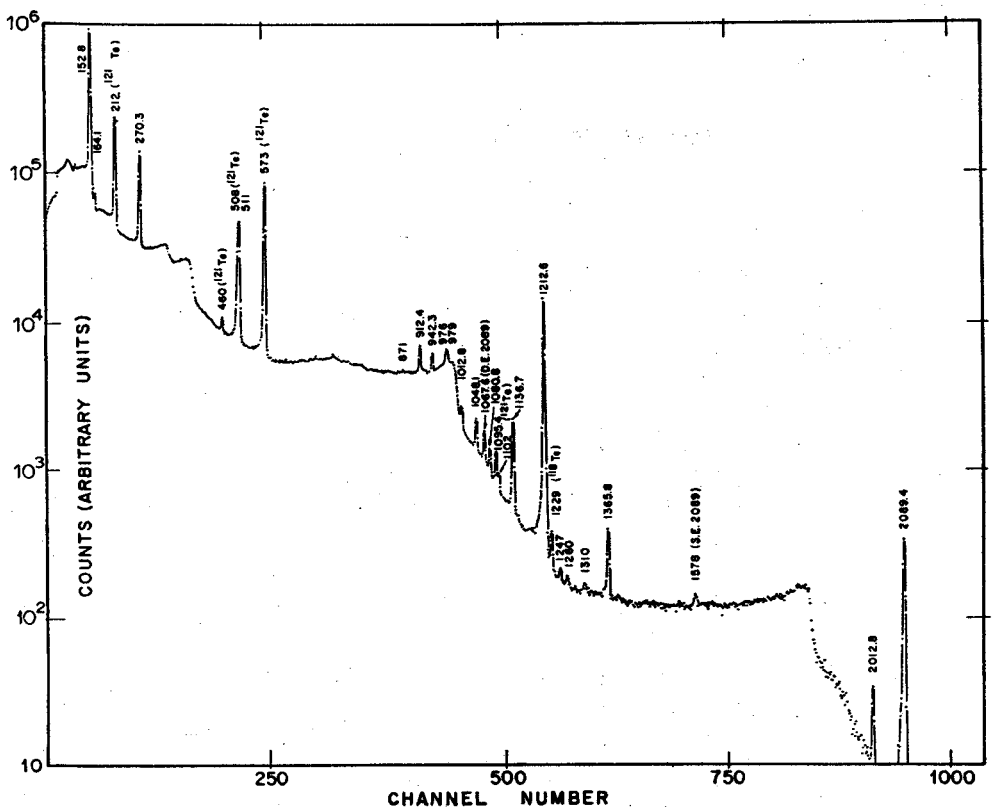

Fig. 2. A singles spectrum of ^{119m}Te recorded after the 16 h ^{119g}Te had decayed away. The spectrum, from ref. [1]), was recorded with a 3 cm^3 Ge(Li) detector. The spectrum shown is from a source which was considerably older than most of the sources used for the correlation measurements. Hence the ^{121}Te lines are more prominent here.

2. Source preparation

The ^{119m}Te activity was produced by 34 MeV proton bombardments of natural antimony metal in the Michigan State University cyclotron. Tellurium activities were chemically removed from the target material by precipitation with SO_2 gas [7]). The counting was usually performed from one to three weeks after bombardment. After one week, the 16 h ^{119g}Te activity had decayed away, and the presence of ^{121}Te did not become bothersome for two to three more weeks.

3. Apparatus

The NaI(Tl) detector was mounted on a movable arm which enabled the detector to be rotated from 90° to 270° with respect to a line defined by the center of the fixed Ge(Li) crystal and the source. The NaI(Tl) crystals employed were of two sizes,

7.6 cm × 7.6 cm and 5.08 × 5.08 cm. During the course of the experiment, two different Ge(Li) detectors were also used. Both of these were of the five sided wrap-around type and had active volumes of approximately 20 cm^3 and 30 cm^3. Under the best conditions, the 30 cm^3 detector had a resolution of $\approx$ 4.5 keV FWHM for the 662 keV line in ^{137}Cs. However, because of pulse shaping, which was necessary to satisfy the timing requirements of the coincidence circuitry and the analyser, and because a different preamplifier had to be used, the resolution was typically 8 to 9 keV FWHM during the actual experiments. The larger of these counters was mounted with the axis of the p-type core in a vertical position, while the core of the smaller was in a horizontal position with the open face farthest from the source. Each of the detectors was mounted in an elbow-type cryostat with a liquid air reservoir placed above the cold-finger.

Both Ge(Li) detectors were fabricated at the Michigan State University Cyclotron Laboratory.

To minimize gain drifts in the electronics, the temperature surrounding most of the apparatus was kept constant to within ± 0.5 C°. In order to compensate for any small drifts which might occur, spectra were recorded at each angle for short periods (typically 40 min) only. The final spectrum for each angle was a summation over a number of such individual spectra and included spectra recorded at 360° minus that angle. In this manner first-order corrections were also made for small misalignments in the source position and for source decay.

A multiple coincidence unit with a variable resolving time was employed and spectra were simultaneously recorded in the two halves of a 1024-channel analyser. Typical resolving times were $\leq$ 80 nsec.

Source strengths were of the order of a few μCi. Typically 10^3 pulses/sec from the NaI(Tl) detector satisfied the gate requirements. Approximately 0.5 % of these were in coincidence with pulses from the Ge(Li) detector.

4. Data analysis

The correlation coefficients obtained were approximately corrected for effects of the finite solid angles subtended by the detectors. The correction for the NaI(Tl) detector was obtained from calculated tables [8]). Because of the irregular geometry, calculations become very difficult for the Ge(Li) detector. It was assumed that an approximate correction could be made from tables for NaI(Tl) detectors of comparable size. That this assumption was not grossly in error was demonstrated by performing the angular correlation measurements on well-known cascades [9]) present in the decay of ^{60}Co and ^{152}Eu. Results of experiments on the well-known correlations in these two isotopes suggest that the correction in A_2 for the Ge(Li) counter is approximately 5 % for gamma-ray energies in the 1 MeV region and increases to about 10 % near 100 keV. All measurements were performed with the same source to Ge(Li) detector distance of 5.5 cm, corresponding to a solid angle of approximately 0.025 sr.

Peak areas were determined after subtraction of a background which was obtained by least-squares fitting a third-order curve to regions of the spectrum near the peak(s) of interest. The computations were performed on the MSU CDC-3600 and the MSU SDS Sigma-7 computers. A portion of a spectrum in coincidence with the 270 keV transition in ^{119m}Te is shown in fig. 3. The solid lines under the peaks are backgrounds determined by the computer.

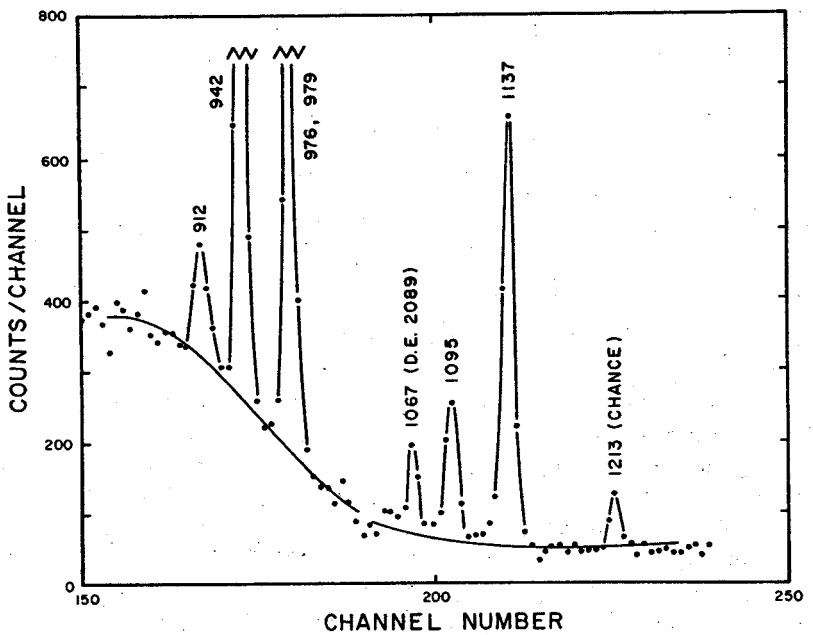

Fig. 3. A portion of the ^{119m}Te spectrum in coincidence with the 270 keV transition. This spectrum was recorded with a 20 cm^3 Ge(Li) detector oriented at 180° with respect to the source and to a 7.6×7.6 cm NaI(Tl) detector. A Compton coincidence spectrum has been subtracted. The anisotropies are of a large enough magnitude such that at a 90° orientation the heights of the 942 keV gamma ray and the 976–979 keV doublet are less than the height of the 1137 keV line. The 1213 keV line arises from purely random events, and provides an index for chance corrections. The solid lines below the peaks are computer fitted backgrounds.

First-order corrections for coincidences with Compton events in the gate were made from spectra recorded in coincidence with regions adjacent to the peak. Wherever possible, gates were simultaneously set on the photo-peak and on regions on both sides of the peak. The two Compton gates were of approximately equal width, which in turn was approximately one-half the width of the photopeak gate. The outputs of the two Compton coincidence circuits were combined through an OR circuit and the resulting Compton coincident spectrum was recorded in that half of the analyser memory which was not used to store counts in coincidence with the photopeak region.

Corrections for random events were made in one of two ways. First, a chance coincidence spectrum was recorded by delaying the signal from either detector by a time greater than twice the resolving time of the coincidence unit. After any counting time and/or decay corrections, the appropriate number of counts could be subtracted from the true plus random coincidence spectra. A second method was sometimes used if a given line in the spectrum was definitely known to be not in true coincidence with any events in the gate. Normalization of a singles spectrum to this line then yielded an appropriate correction.

That the random coincidence rate was relatively low can be seen from fig. 3. The peak at 1213 keV is the only transition not in true coincidence with the 270 keV gamma ray in the gate. Since a Compton coincidence spectrum has already been subtracted, the presence of the 1213 keV line must be due purely to random events. Because in a singles spectrum the 1213 keV gamma ray is approximately nine times as intense as the neighbouring 1137 keV transition, it is evident that the chance correction in this case is very small.

Except for most of the measurements involving the 270 keV transition, the gate was usually set on the higher-energy member of a given cascade. The advantages in this case are three-fold. First, the greater efficiency of NaI(Tl) relative to Ge(Li) for high-energy gamma rays increases the coincidence count rate. Second, in the higher-energy regions of the spectrum there are fewer gamma rays whose Compton distributions will fall in the gate. Hence, Compton corrections will usually be smaller, and, in some cases, can be eliminated. Third, because of a decrease in the total number of counts (photo plus underlying Compton) in the gate, the chance counting rate will also be reduced.

The errors assigned in the correlation measurements are based primarily on the reproducibility of the correlation function over several measurements and on the uncertainty in the solid angle corrections. It was found that the A_2 values typically reproduced to within approximately ± 10 to 15 % of an average value. The primary difficulty was due to poor statistics resulting from the low count rates. This, combined with an estimated to 5 to 10 % uncertainty in solid angle corrections, implies the results for A_2 values to be good to approximately ± 20 %, with a much larger error in the A_4 values.

To check the results, some experiments were performed with scintillation counters only. The measured individual anisotropies for several gamma rays which are not resolved in NaI(Tl) spectra, were combined and compared with results for the composite peak in a scintillation experiment. For example, the four gamma rays in the 900 keV range and the two gamma rays and one weak double escape peak in the 1100 keV range (fig. 3) appear as two separate peaks in corresponding NaI(Tl) spectra. The composite anisotropies in the Ge(Li) spectra were generally in good agreement with the anisotropies in the NaI(Tl) spectra recorded in this laboratory and elsewhere [5]).

5. Results and interpretation of the level scheme

Correlation functions obtained in this investigation for most of the cascades are shown in figs. 4 and 5. The numerical results are summarized in table 1 where a comparison is also made with values obtained by other investigators [2, 5, 6]). A summary of the multipolarities and mixing ratios which are suggested by these results and internal conversion coefficient measurements [2, 3, 5]) is given in table 2. Also listed in the same table are multipolarities assigned in previous investigations.

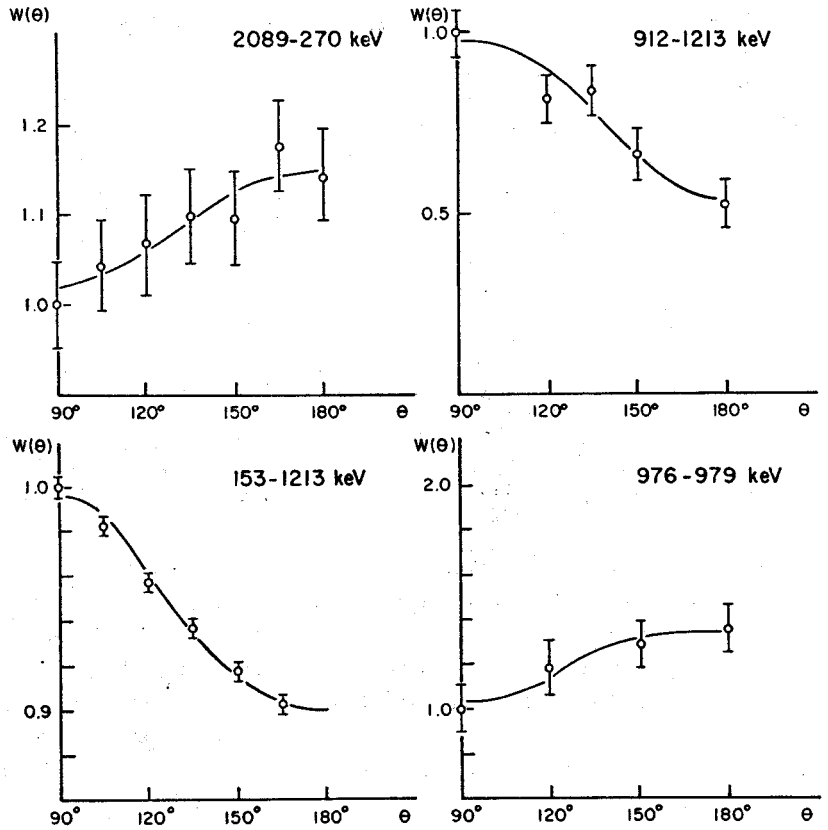

Fig. 4. Experimental correlation functions for four gamma-ray cascades. The errors associated with individual points are assigned primarily on the basis of statistics. The solid line is a least-squares Legendre polynomial fit to the data points.

Because of the large uncertainties in the A_4 values, all of the interpretation of the correlation data were based on the A_2 values only. In all cases, however, the corresponding experimental and theoretical A_4 coefficients agreed to within the experimental uncertainties. Although in general, any one experimental correlation function is consistent with more than one set of spin assignments, combining the results for several cascades involving common levels has strongly suggested unique

assignments for some of the states. The spin values assigned from this study are those in the decay scheme shown in fig. 1. A summary of the interpretation is given below.

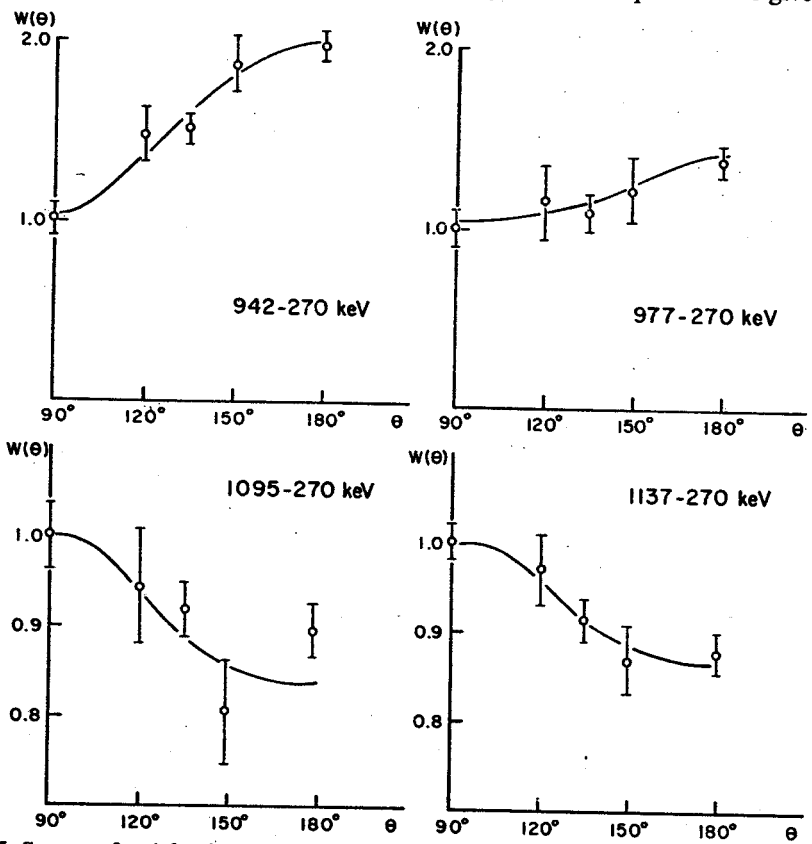

Fig. 5. Same as fig. 4 for four additional cascades. The differences in the magnitudes of the error bars for points in a given set arise from the fact that the results from several runs with different angular increments have been combined.

5.1. THE 1366, 1213, 270 AND 0 keV STATES

The only two spin sequences for the 1366, 1213, 270 and 0 keV levels which are consistent with log *ft* values [1,2]), an E1 multipolarity assignment to the 153 keV transition from conversion electron studies [2,3,5]), and previous angular correlation measurements [2,5,6]) are $\frac{11}{2}^-$, $\frac{9}{2}^+$, $\frac{7}{2}^+$, $\frac{5}{2}^+$ and $\frac{9}{2}^-$, $\frac{7}{2}^+$, $\frac{7}{2}^+$, $\frac{5}{2}^+$, respectively. Of the cascades involving these four states, only that involving the 153 and 942 keV transitions, which depopulate the 1366 and 1213 keV levels, respectively yielded a correlation function which is consistent with only the first spin sequence. However, the 942–270 keV cascade produced an experimental A_2 value which requires a most liberal allowance for experimental error in order to be consistent with the latter sequence, whereas, this A_2 value is in agreement with theoretical values obtained from the first spin sequence.

TABLE 1

Summary of ^{119}Sb gamma-gamma angular correlation data

Cascade energies (keV)	Correlation coefficients A_2	A_4	Assigned spin sequence [a]	Mixing parameters [a] δ_1	δ_2
153–1213	−0.071±0.007 −0.069±0.005 [b] −0.062±0.004 [c] −0.065±0.006 [d]	0.001±0.01 0.002±0.005 [b] −0.002±0.005 [c] 0.0006±0.006 [d]	$\frac{11}{2}(1,2)\frac{7}{2}(2,3)\frac{5}{2}$	$-0.04 \leqq \delta_{153} \leqq 0.04$	$-0.08 \leqq \delta_{1213} \leqq -0.03$
942–270	0.56 ±0.1 0.273±0.011 [c,e]	−0.10 ±0.1 0.013±0.015 [c,e]	$\frac{9}{2}(1,2)\frac{7}{2}(1,2)\frac{5}{2}$	$-3.2 \leqq \delta_{270} \leqq -0.1$	$0.2 \leqq \delta_{942} \leqq 6.0$ [f]
153–942	0.39 ±0.15	0.16 ±0.2	$\frac{11}{2}(1,2)\frac{9}{2}(1,2)\frac{7}{2}$	$-1.2 \leqq \delta_{942} \leqq -0.6$ [f]	$0.03 \leqq \delta_{153} \leqq 0.04$
1095–270	−0.16 ±0.003 −0.041±0.004 [c,g]	0.09 ±0.1 0.05 ±0.007 [c,g]	$\frac{11}{2}(2,3)\frac{7}{2}(1,2)\frac{5}{2}$	$-0.3 \leqq \delta_{1095} \leqq 0.1$ or $-2.5 \leqq \delta_{1095} \leqq -1.3$	$-5.0 \leqq \delta_{270} \leqq 0.1$
1137–270	−0.12 ±0.02	0.04 ±0.1	[h]		
2089–270	0.079±0.02 0.083±0.015 [b] 0.124±0.015 [c]	−0.02 ±0.1 0.012±0.015 [b] 0.058±0.23 [c]	$\frac{9}{2}(1,2)\frac{7}{2}(1,2)\frac{5}{2}$		
977–270	0.25 ±0.05	0.09 ±0.1	[h]		
912–1213	−0.40 ±0.08	0.07 ±0.1	[h]		
1013–1213	−0.26 ±0.1	−0.16 ±0.2	[h]		
976–979	0.23 ±0.05	−0.09 ±0.1	[h]		
912–153	0.53 ±0.2	−0.10 ±0.2	[h]		

[a]) Mixing parameters and spin sequences determined from the present correlation data. The internal conversion coefficient of the 153 keV transition has been used to restrict the choices of the spin sequences and mixing parameters.

[b]) Ref. [6]).

[c]) Ref. [5]).

[d]) Ref. [2]).

[e]) These correlation coefficients were determined in ref. [5]) ignoring data points near the 180° angle because of the presence of positons in a contaminant. This position emitting contaminant was not present in the data recorded in this investigation.

[f]) Sign change because of the change in order of emission of the 942 keV gamma in these two cascades [10]).

[g]) The 1095 keV peak was not considered to be a doublet in these data [5]).

[h]) Unique spin assignment not possible from this study.

TABLE 2
Comparison of multipolarities assigned by various investigators

Transition (keV)	Svedberg *et al.* [b])	Proposed multipolarity: Graeffe *et al.* [c])	Singru *et al.* [d])	Present work
153	E1	E1	E1	E1, ($\leqq$ 0.1 % M2)
164	M1	M1, E2		
270	M1	M1, E2	M1, 40 % E2	M1, ($\leqq$20 % or 80 to 90 % E2)
912			M1, E2	M1, (20 to 70 % E2)
942	M1	M1, E2		M1, (26 to 60 % E2)
976	M1			[e])
979				[e])
1013		M1, E2		[e])
1048	M1	M1, E2		
1081		E1		
1096	M2	M2		M2
1137	M1	E1		M1, E2
1213	E2	M1, E2	M1, E2	E2, ($\lessapprox$ 0.1 % M3)
1366	E3	E3		E3
2089				E1 or M1, E2

[a]) Energy values from ref. [1]).
[b]) Ref. [3]).
[c]) Ref. [5]).
[d]) Ref. [6]).
[e]) Results inconclusive.

Although the results of these angular correlation measurements, coupled with the internal conversion and log *ft* data, strongly suggest the spin sequence of $\frac{11}{2}^-$, $\frac{9}{2}^+$, $\frac{7}{2}^+$ and $\frac{5}{2}^+$ for the 1366, 1213, 270 and 0 keV levels, respectively, some additional remarks should be made. In order to produce an A_2 value which is as large as the measured value, even with a liberal error, the 153 keV E1 transition must have approximately a 0.1 % M2 admixture. Because of this M2 admixture in the 153 keV transition, there must be an M3 admixture of comparable magnitude in the predominately E2 1213 keV transition.

As can be seen in table 1, the mixing parameter for the 942 keV transition changes sign in the 942–270 keV as opposed to the 153–942 keV correlation. This is consistent with a well-known triple cascade theorem [10]).

5.2. OTHER LEVELS

Except for the case of the four levels discussed above, at least two possibilities still remain in the spin assignments to the other states. It should be noted that, with possibly one exception, the correlation measurements are consistent with the most recent conversion electron study assignments [2]). The possible discrepancy exists for the case of the 1407 keV state, where a $\frac{9}{2}^-$ spin assignment has been made previously [2]). The negative δ_{270}, which has already been established, does not permit the observed A_2 value for the 1137–270 keV cascade unless the proposed E1 1137 keV transition is

appreciably (a few per cent) M2 admixed. Either a $\frac{7}{2}^+$, $\frac{9}{2}^+$ or $\frac{11}{2}^+$ assignment would be consistent with the correlation results.

The 1013–1213 correlation leaves $\frac{9}{2}$, $\frac{11}{2}$ and $\frac{13}{2}$ as the possible spin assignments for the 2226 keV level.

From the already established spins and parities of the 1366 and 1213 keV levels and from the correlation measurements on the 912–153 and 912–(153)–1213 keV cascades, the spin and parity of the 2278 keV level must be $\frac{9}{2}^-$ or $\frac{13}{2}^-$. The 912 keV M1 + E2 transition consists of from 20 to 70 % E2.

From the 2089–270 keV correlation an $\frac{11}{2}^+$ assignment can be ruled out for the 2360 keV state, and $\frac{11}{2}^-$ is unlikely since then the 2089 keV gamma would have to be M2 with about a 20 % E3 admixture. A spin of $\frac{9}{2}$ is the most probable value, making the 2089 keV transition M1 + E2 or almost pure E1.

No reliable evidence was obtained to allow spin assignments to be made to the 1048, 1250, 2129 and 2284 keV states.

6. Conclusion

Although uncertainties in the correlation coefficients are large enough at present to prevent in several cases a unique spin assignment on the basis of the angular correlation experiments alone, these experiments complement and provide independent support for assignments based on conversion electron studies. As is evident from the complexity of the decay scheme of ^{119m}Te, correlation experiments performed with scintillation counters alone are not adequate in this and in many other cases. The fact that quantitative coincidence studies can be made with reasonable success with a Ge(Li)-NaI(Tl) system should, hopefully, provide motivation for more experiments of this nature for establishing decay schemes as well as for angular correlation measurements.

The authors wish to thank Dr. W. P. Johnson for his assistance with the cyclotron bombardments and Dr. C. R. Gruhn for his efforts in developing a Ge(Li) detector fabricating laboratory. The kindness of Dr. R. C. Etherton, Southern Illinois University, in allowing us to use his Ge(Li) detector for the early measurements, is gratefully acknowledged. Gratitude is also expressed to Drs. L. M. Beyer and Etherton for helpful discussions and to Mr. W. B. Chaffee, D. B. Beery and R. Hickey for their assistance in the data acquisition.

References

1) G. Berzins and W. H. Kelly, Nuclear Physics **A92** (1965) 65
2) G. Graeffe, E. J. Hoffman and D. G. Sarantities, preprint (1967)
3) J. Svedberg and G. Andersson, Nuclear Physics **48** (1963) 313
4) J. Kantele and R. W. Fink, Nuclear Physics **43** (1963) 187
5) R. M. Singru, S. H. Devare and H. G. Devare, preprint (1966)
6) A. V. Ramayya, Nucl. Sci. Abst. **19** (1965) 2622, thesis, unpublished, D64
7) R. W. Fink, G. Andersson and J. Kantele, Ark. Fys. **19** (1961) 323
8) R. L. Health, IDO-16880 (Aug. 1964)
9) Nuclear Data Sheets, compiled by K. Way *et al.* (National Research Council, Washington D.C.)
10) S. Ofer, Phys. Rev. **114** (1959) 870

NUCLEAR INSTRUMENTS AND METHODS 58 (1968) 309–314; © NORTH-HOLLAND PUBLISHING CO.

A POST-FOCUSING ACCELERATOR FOR A $\pi\sqrt{2}$ SPECTROMETER*

R. J. KRISCIOKAITIS+ and S. K. HAYNES

Department of Physics, Michigan State University, East Lansing, Michigan, U.S.A.

Received 3 July 1967

A post-focusing accelerator for a $\pi\sqrt{2}$ spectrometer is described which enables electrons down to less than 150 eV to be detected quantitatively with almost negligible spurious background. The properties of the accelerator are illustrated with K- and L-Auger lines of ^{113}In from ^{113}Sn.

1. Introduction

Though other types of detectors have been tried, the most successful attempts to detect electrons with known efficiencies substantially below 5 keV in energy have involved the use of either prefocusing or post-focusing acceleration combined with a thin-window gas counter or a photographic plate as detector[1–14]). Whereas, on the one hand, acceleration of the electrons as they leave the source (prefocusing acceleration) has the disadvantage of markedly worsening the ultimate resolution of the spectrometer for low energies, on the other hand, until recently, all attempts at acceleration near the detector had difficulty with a vastly increased background whenever the accelerator potential brought low energy electrons above the window energy cutoff. However, two post-focusing arrangements which seem capable of quantitative intensity measurements to nearly zero energy have recently been reported: one briefly by the present authors[15]) and the other by Slātis[16]). The former will be described in more detail here.

Most previous workers had used 10 kV or more with windows of the order of 0.1 mg/cm^2. The work of Achor[9]) had shown that accelerating voltages of about 5 kV could be used with windows down to 10 μg/cm^2 (100% transparent to about 5 keV), with the only excess background coming from nearly zero energy electrons picked up by the accelerator from the spectrometer volume. The recent work of Mehlhorn and Albridge[14]), though with a thicker window, had shown that the use of a small negative retarding voltage prior to acceleration reduced but did not eliminate the unwanted background. We therefore decided to use low voltages with thin windows and a retardation electrode. The former decision was reinforced thereafter by the work of Geiger et al.[13]) in which 2.4 kV were used with a thin window to detect the M and N conversion lines ($\sim$3 keV) of ^{151}Sm.

In designing the accelerating cell, we kept the following objectives in mind:

1. Elimination of all steep electric field gradients;
2. Minimization of the field in the immediate vicinity of the counter window where leaks were expected;
3. Use of very regular and smooth surfaces;
4. Cleanliness of the surfaces in the acceleration space;
5. Reduction of the penetration of the accelerating field through the resolution defining slit.

2. The acceleration cell and supporting electronics

Fig. 1 shows the combination of slit sizes and geometry which was used to obtain the L-Auger spectrum of ^{113}In ($\simeq$2 to 4 keV). The spectrometer baffles were set to give an incident beam of about 4° spread at the focus. The plastic screws on the side of the cell nearest the source were tightened more firmly than the others to correct for approximately 1 mm deviation of the curving beam at point no. 3.

3. Counter anode and outside wall

The basic counter design is the same as that described by Parker[17]). The anode is a stainless steel wire 0.005 cm in dia. which is raised to the operating potential by a high voltage power supply, the negative terminal of which is connected to the positive terminal of the accelerator power supply and to the counter wall. The counter is operated in the Geiger-Müller region and uses a 67% argon–33% ethylene mixture at 55 mm Hg, with a resulting slope of 12% per 100 V. Teflon tubing is used to isolate the counter from the gas tank. The high voltage connections are made via a non-magnetic coaxial cable†, where the shield is at the accelerating potential and the inside conductor is at the counter potential.

* Research was supported in part by the National Science Foundation.

+ Presently at Harvard University as Research Fellow in Physics on the Cambridge Electron Accelerator, Cambridge, Massachusetts.

† Belden 8239.

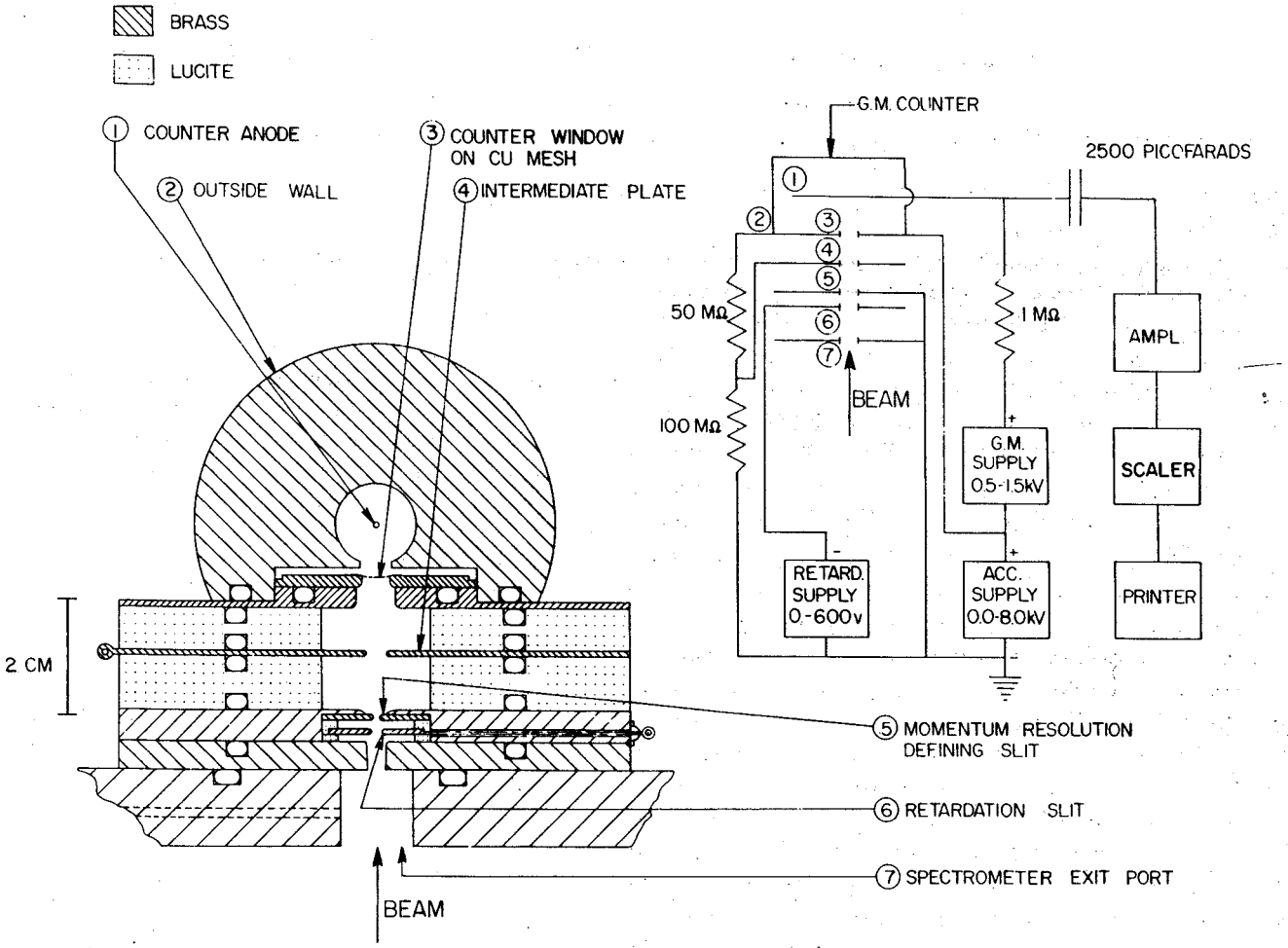

Fig. 1. Post-focusing acceleration cell and voltage connections.

4. Counter window on copper mesh

The windows consisted of collodion of thickness 10 to 20 $\mu g/cm^2$ supported on copper mesh. They had a long lifetime in the spectrometer and permitted vacuums of better than 10^{-5} Torr.

5. Intermediate plate

An intermediate plate was introduced after experimenting with single insulating slabs of several thicknesses, and after a study of the relationship of system vacuum to counter background. We observed early in these investigations that application of accelerating potentials in excess of 3 kV across a single insulator spacer approximately 1 cm thick with a system vacuum of $\sim 10^{-5}$ Torr, led to the appearance of a new class of pulses (distinct from the easily recognisable counter pulses). Their amplitude and frequency seemed to increase with residual gas pressure, with decrease in insulator thickness, and with accelerating potential. Unfortunately, during these tests it was difficult to keep the variables under quantitative control and therefore, the change of the number of such pulses with these variables was not precisely and quantitatively determined.

We felt that these spurious pulses may have had their origin in the accelerating volume, and were possibly due to the formation of positive ions which, when accelerated to the cathode, produced secondary electrons, thus producing a kind of capacitive discharge which could have easily been transmitted into the counting circuit.

Although the spurious pulses which were observed at moderate accelerating potentials and good vacuum were smaller in amplitude than the scaler threshold, discrimination became impossible when the applied voltage exceeded 4 kV. A two-stage accelerator was

then constructed with a higher electric field immediately behind the momentum resolution slit and a lower field in the region of escaping gas in front of the counter. This arrangement is shown in fig. 1 where only $\frac{1}{3}$ of the accelerating potential is applied across the slightly narrower region next to the counter.

6. Slits

Although the momentum resolution defining slit had a width of 1.0 mm, smaller widths can easily be used.

The retardation slit width was 1.5 mm. The roles of the two slits might be interchanged, although this was not tried. The disadvantage of reversing the roles is that the retarding slit would be moved into the accelerator field and therefore would probably require more retardation voltage. The primary disadvantage to its present location is that it offers the incident beam, which misses the opening in the retardation slit, a negatively charged obstacle. The resulting collisions probably produce secondary electrons which are attracted in by the accelerating field and may contribute to the spurious background which will be discussed in the following section.

The basic material used for the electrodes was yellow brass (67% Cu–33% Zn). The counter material was also brass with a somewhat higher content of zinc. The electrode surfaces were finished with fine emery polishing paper, cleaned with Brasso, and washed with benzene. All corners were smoothly rounded to about 1.2 mm radius. Care was taken to avoid the introduction of foreign materials on the electrodes.

7. Operation and performance

Tests performed on the spectrometer following introduction of the accelerating components showed that, in the absence of the accelerating voltage, the beam transmission and instrumental resolution were unchanged. Actually, in the preliminary studies, a 0.5 mm momentum resolution defining slit was used. The change of the width of the momentum resolution defining slit from 0.5 mm to 1.0 mm had no effect on the accelerator performance except that the height of the plateau of the upper curve of fig. 2 increased in the case of the wider slit.

After introducing the intermediate plate, it was observed that the spurious pulses mentioned above occurred only at accelerating potentials above about 6 kV and were still small enough at 8 kV to be rejected by suitable selection of the scaler threshold. The quantitative results of the tests of the accelerator are shown in figs. 2–5. Fig. 2 shows that the counter pulse rate increased with accelerating voltage to a plateau (no

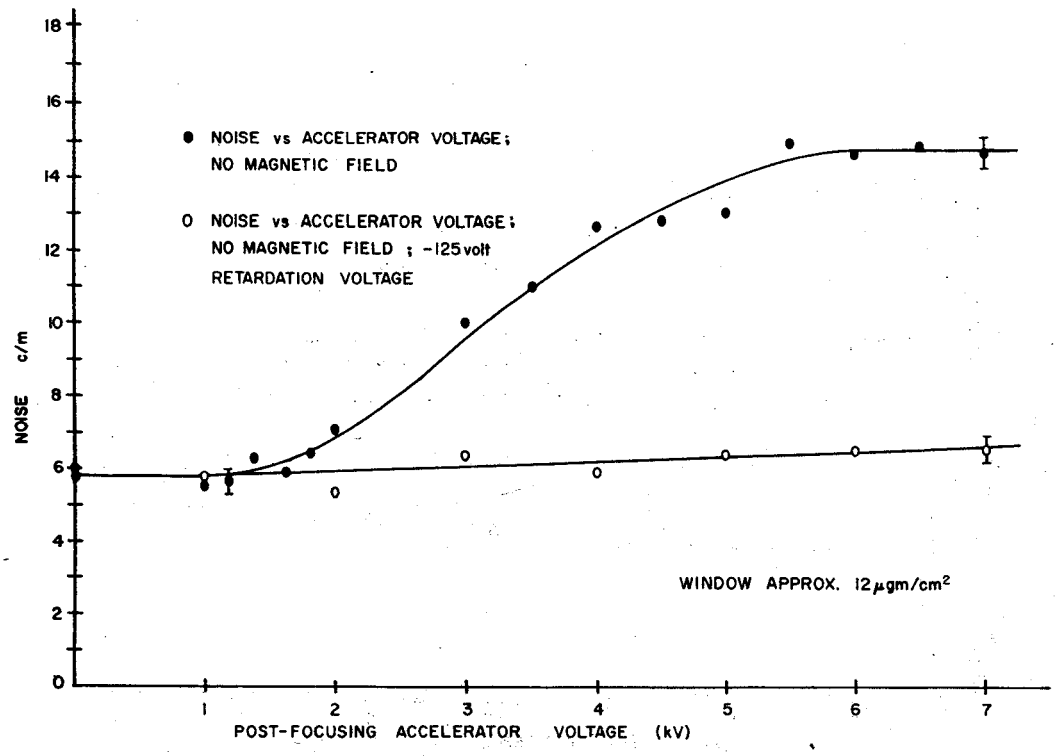

Fig. 2. Noise curves showing retardation effect.

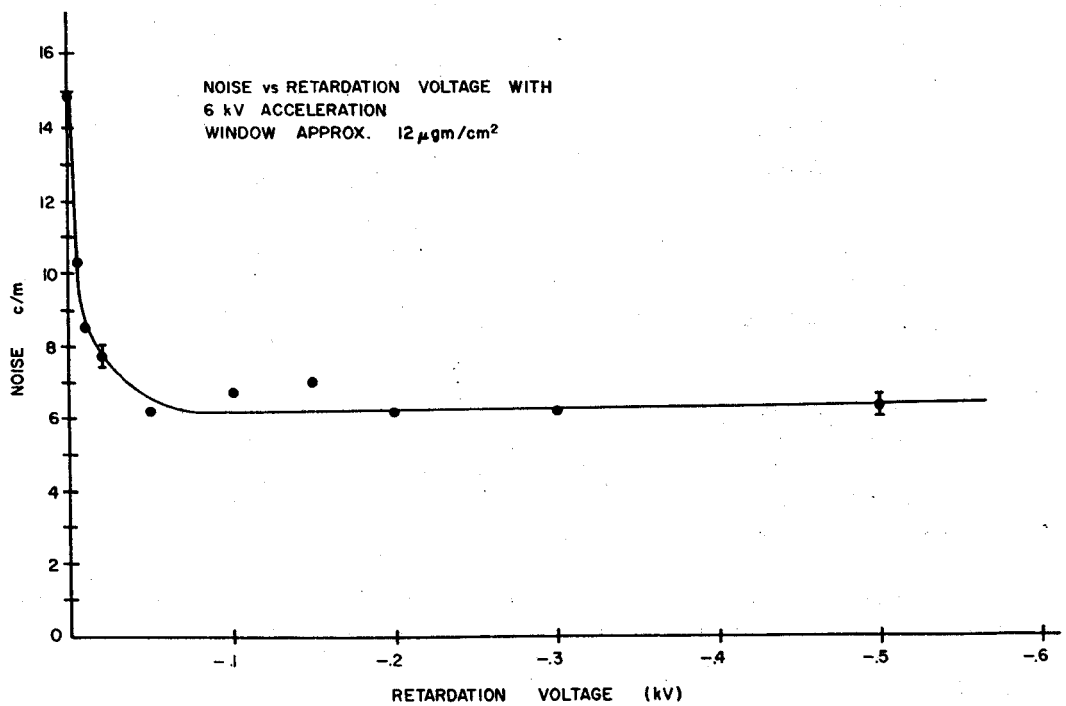

Fig. 3. Noise vs retardation voltage with fixed accelerating potential and no magnetic field.

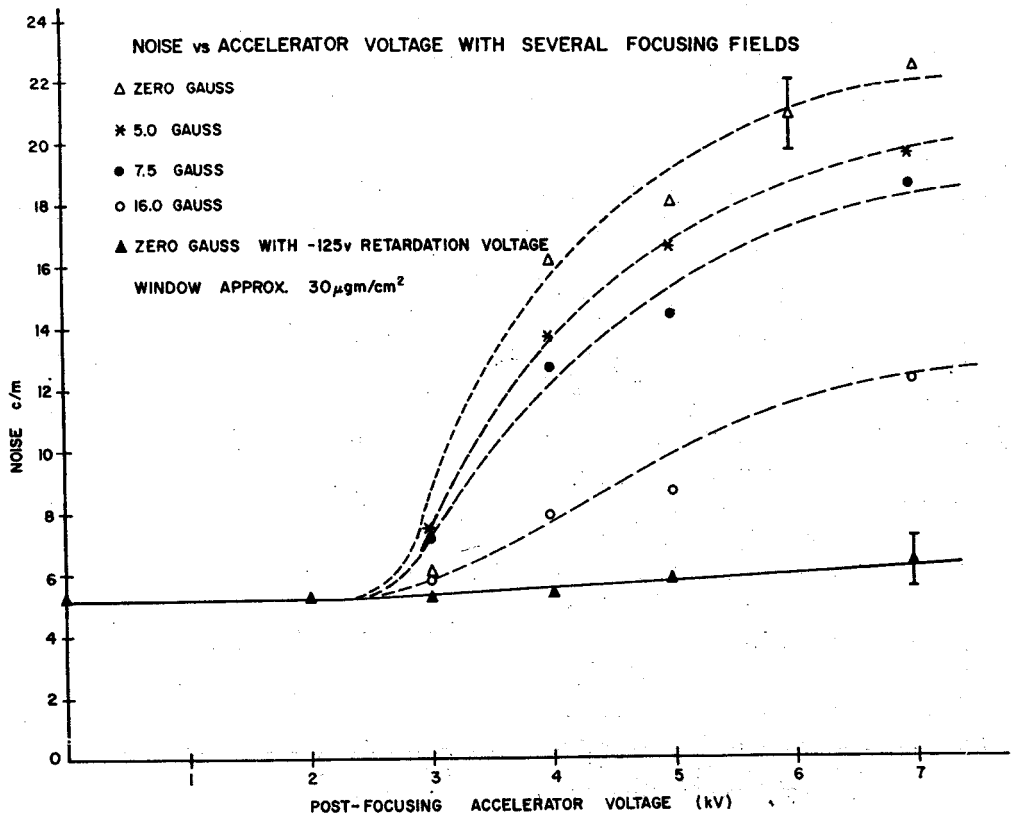

Fig. 4. Noise vs accelerator voltage with several focusing fields.

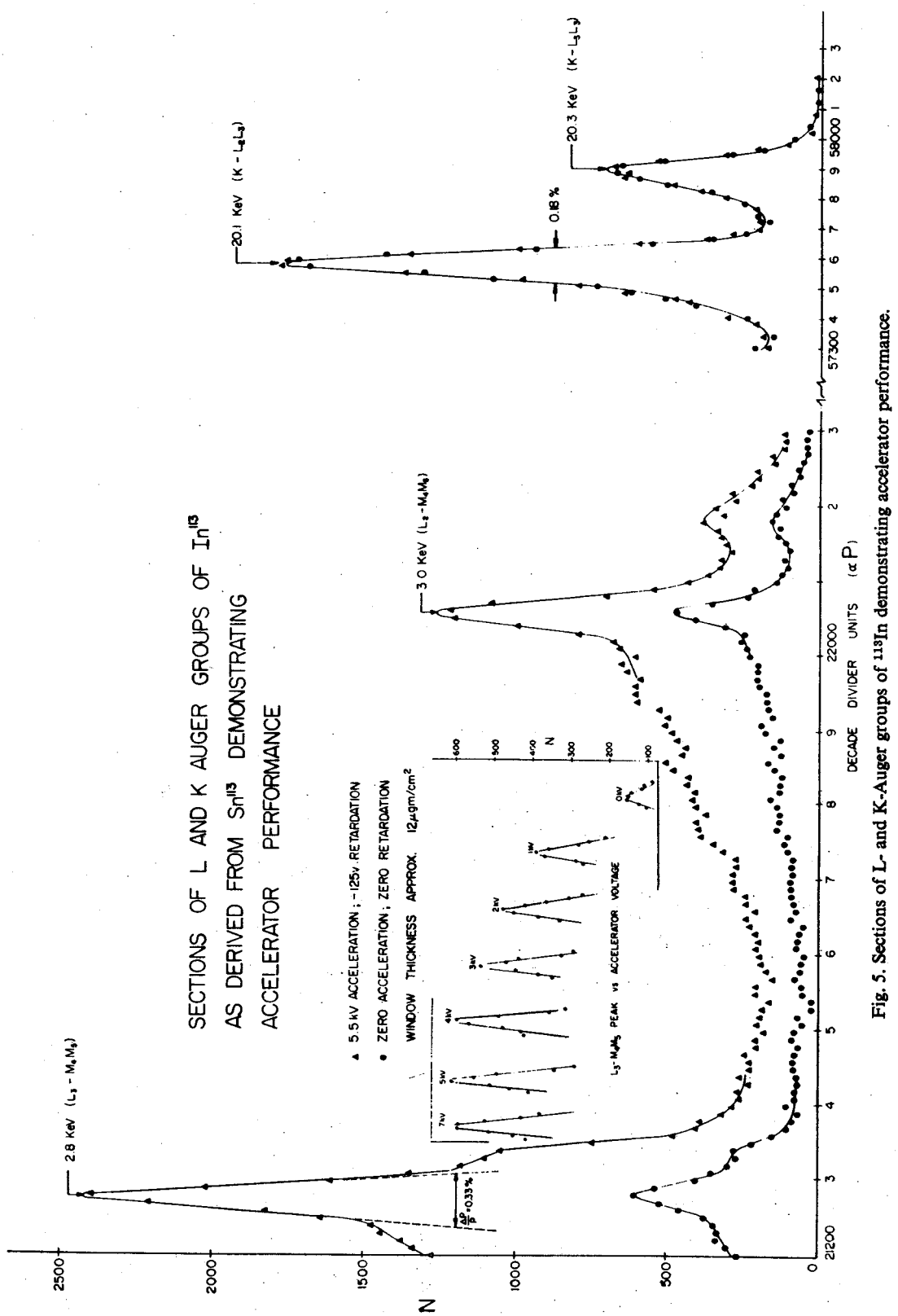

Fig. 5. Sections of L- and K-Auger groups of ^{113}In demonstrating accelerator performance.

magnetic field and no source). With a typical source in the spectrometer, the only change that was produced with no retardation was a small increase in the plateau height of the curve. Fortunately, the application of the retardation potential, as shown in figs. 2 and 3, reduced the excess background almost to natural background level. The lower curve in fig. 2 shows the retardation effect over the full range of accelerator voltages. Thus, one may postulate that the top curve of fig. 2 represents the delivery of low energy electrons from the main vacuum system to the detector. This is strongly substantiated by the fact that these electrons may be repelled by the application of the small retarding potential, and also by the results shown in fig. 4 where increasing spectrometer magnetic field reduces the excess background measured with no retardation.

Further, it is interesting to note that the point at which the unretarded curve leaves the retarded curve, figs. 2 and 4, corresponds very closely to the cut-off energy of the window. This point of divergence of the two curves was, for all windows tried, consistent with the cut-off point computed from the estimated window thickness[18]). It may also be noted that for the 12 $\mu g/cm^2$ window the shape of the curve corresponds very closely to the absorption curves by Lane and Zaffarano[18]). The difference between the lower curve in fig. 2 and natural background is probably due to events occurring in the accelerating space itself.

Considerable time was spent in studying the effects of the post acceleration cell once the spectrometer was allowed to focus an electron beam. We found that at about 20 keV, there seems to be no defocusing, as shown in fig. 5, but there was a spurious contribution to the counting rate on the K-L_2L_3 line which was roughly dependent on the acceleration and the beam strength, e.g., $\approx$2% at 6 kV acceleration. This appears to be substantially smaller than any background previously reported[14]). At lower energies there was no simple way of checking the accelerator performance without an intense isolated line in the region of interest. By running curves of the type shown in fig. 5 (left) it was possible to show, however, both that defocusing is negligible for this resolution and that the peaks were not shifted by the accelerating potential. This was done by a point-to-point comparison of neighbouring shapes for the two cases of acceleration and no acceleration. Examination of the peak to valley ratios of both curves (using a rough absorption correction) yielded an accelerator-induced noise figure of about 1% of beam strength in this energy region. The insert shows graphically the growth of the L_3-M_4M_5 peak from ^{113}In with accelerator voltage. No inconsistencies were found to within the statistical uncertainty of about 5% per point.

Our thanks go to Dr. L. J. Velinsky and Mrs. M. Velinsky for some of their initial work on the design of the post-focusing accelerator.

References

[1]) M. S. Freedman, F. T. Porter, F. Wagner and P. P. Day, Phys. Rev. **108** (1957) 836.
[2]) C. S. Cook, Nucleonics **12**, no. 2 (1954) 53.
[3]) C. H. Chang and C. S. Cook, Nucleonics **10**, no. 4 (1952) 24.
[4]) A. Juillard and A. Moussa, J. Phys. Rad. **19** (1958) 94.
[5]) H. M. Agnew and H. L. Anderson, Rev. Sci. Instr. **20** (1949) 869.
[6]) L. M. Langer and C. S. Cook, Rev. Sci. Instr. **19** (1948) 257.
[7]) D. K. Butt, Proc. Phys. Soc. (London) **63A** (1950) 986.
[8]) G. Giroux and C. Geffrion, Can. J. Phys. **34** (1956) 153.
[9]) W. T. Achor, Ph. D. Thesis (Vanderbilt University, 1958).
[10]) W. Mehlhorn, Z. Physik **160** (1960) 247.
[11]) P. Erman and Z. Sujkowski, Ark. Fys. **20** (1961) 209.
[12]) J. Sant'ana Dionisio, Ann. Phys. **9** (1964) 29.
[13]) J. S. Geiger, R. L. Graham and J. S. Merrit, Nucl. Physics **48** (1963) 97.
[14]) W. Mehlhorn and R. G. Albridge, Nucl. Instr. and Meth. **26** (1964) 37.
[15]) R. J. Krisciokaitis and S. K. Haynes, Bull. Am. Phys. Soc. **10** (1965) 53.
[16]) H. Slätis, Ark. Fys. **29** (1965) 485.
[17]) R. A. Parker, M. S. Thesis (Vanderbilt University, 1960).
[18]) R. O. Lane and D. J. Zaffarano, Phys. Rev. **94** (1954) 960.

3.C

Nuclear Physics A104 (1967) 466—480; © *North-Holland Publishing Co., Amsterdam*

A STUDY OF THE L- AND K-AUGER SPECTRA OF $^{113}_{49}$In from $^{113}_{50}$Sn

RAYMOND J. KRISCIOKAITIS † and SHERWOOD K. HAYNES

Department of Physics, Michigan State University ††, *East Lansing, Michigan, USA*

Received 10 July 1967

Abstract: The L- and K-Auger spectra for ^{113}In derived from the orbital capture decay for ^{113}Sn have been measured by means of an iron-free, $\pi\sqrt{2}$ beta-ray spectrometer. A total of 47 L-Auger lines and groups of lines have been identified and their intensities estimated. Incremental nuclear charge values $\Delta Z = 0.55$ and 0.67 were found to fit the transitions of type $L_{1,2,3}$-$M_{1,2,3}M_{1,2,3}$ and $L_{1,2,3}$-$M_{4,5}M_{4,5}$, respectively. Analysis of the K-Auger spectrum led to identification of nine lines in the K-LL group, as predicted by the intermediate coupling theory. The relative intensities of the K-LL lines indicate closest agreement with calculations by Asaad who takes into account configuration interaction as well as intermediate coupling. The ratios (K-LX)/(K-LL) = 0.431 ± 0.003 and (K-XY)/(K-LL) = 0.0513 ± 0.0007 were also measured.

E | ATOMIC PHYSICS In measured $E_{K,\,L\text{-Auger}}$, $I_{K,\,L\text{-Auger}}$.

1. Introduction

Measurements of L-Auger spectra are important not only as a source of information on the coupling of pairs of M-vacancies but also because an understanding of the L-Auger spectra may make possible the eventual use of L-Auger electrons as detectors of L-subshell vacancies produced in orbital capture. The few L-Auger measurements performed thus far have mainly been confined to the *heavy* elements ††† where the low-energy spectral limit is high enough to permit relatively simple electron detection techniques.

We thought it would be of interest to make a preliminary exploration with a $\pi\sqrt{2}$ iron-free spectrometer [2]) of the experimental problems (low-energy detection [$\approx$ 2 keV], very thin source, good vacuum) associated with observing L-Auger spectra of *medium-Z* elements. In addition to the desirability of a general investigation of the Auger spectra for medium-Z, we thought that the larger K-Auger yield [3]) at medium-Z might make visible L-Auger lines which follow a K-LL Auger process (vacancy satellites) [4, 32]).

The spectrum of L-Auger electrons associated with the decay [5,6]) ^{113}Sn(119 d) EC^{113m}In(1.7 h) was chosen for the study since very high specific activity sources are needed and can easily be obtained for this nucleide.

† Presently at Harvard University as Research Fellow in Physics on the Cambridge Electron Accelerator, Cambridge, Massachusetts.

†† Research was supported in part by the National Science Foundation.

††† See ref. [1]), p. 1532.

Because of the ≈ 2 keV lower energy limit for L-Auger electrons for medium-Z elements, it was necessary to develop a post-focussing accelerator to drive these electrons through the detector window. This device is described elsewhere [7]).

In order to utilize the high resolution of the iron-free, $\pi\sqrt{2}$ spectrometer [1]) at such low energies, the source had to be very thin. We describe in sect. 3 the special source preparation technique employed for this purpose.

We present in sect. 4 the L-Auger spectrum of our best source of ^{113}Sn and ^{113m}In in equilibrium with analysis and interpretation. Since we used the K-L_2L_3 K-Auger line for low-energy calibration, we also measured the complete K-Auger spectrum of the same source. The K-Auger spectrum and analysis are given in sect. 5.

2. Experimental procedure

2.1. SOURCE PREPARATION

Isotopically enriched (≈ 72 %) ^{112}Sn in oxide form was irradiated in the Oak Ridge Research Reactor for seven weeks and subsequently converted by ORNL to metal powder. The isotopic mass separator of the Argonne National Laboratory was then used to reduce the proportion of stable ^{112}Sn and other impurities.

We initially tried direct preparation of our sources by the mass separator. As indicated by Bergstrom *et al.* [8]), there is substantial penetration of the ions into the target (later to be the spectrometer source backing) when deposition is at the 40 to 60 keV beam energy of the separator. Such penetration is sufficient to cause an appreciable low-energy tail for a mono-energetic electron line. Therefore, for electrons in the 2-4 keV range, the beam energy of the mass separator must be substantially reduced.

A direct deposition of a retarded beam at, say, 1.0 keV on the source does not, on the other hand, necessarily assure a solution. At very low (< 1.0 keV) deposition energies retention of the ions on the target may be a problem, besides the fact that even at ≈ 1.0 keV there is still some penetration into the target [8]). After several sources were made by direct deposition which were either too weak or showed substantial source thickness effects, we tried a different technique.

The separated and retarded (≈ 1.0 keV) ^{113}Sn beam was collected on a tantalum strip 5 × 0.394 × 0.013 cm. The strip was then cut along its length into strips roughly 0.072 cm wide. They were connected one at a time to act as filaments in a vacuum evaporator. The residual gas pressure in the evaporator was about 10^{-5} Torr. An Al mask, measuring 0.5 × 18.0 mm, was used to define the source deposit on a ≈ 1.5 mg/cm^2 Al backing. The filament was flashed to very dull red to remove any volatile foreign matter, then the mask and backing were introduced and the filament flashed twice to dull red. These steps sufficed to remove most of the active deposit from the filament. Two such filaments were needed to produce the source which was used for both the L- and K-Auger runs.

2.2. MEASUREMENT

The $\pi\sqrt{2}$ spectrometer was adjusted for a momentum resolution of 0.12 %. The 2 to 4 keV region of the L-Auger spectrum was scanned repeatedly by taking 1000

points at equal momentum intervals. The focussed beam was post-accelerated by a 5.5 keV electrostatic potential [7]. The voltage was increased to 6.5 keV when investigating the region down to 1.0 keV. The counter window was collodion (12-15 $\mu g/cm^2$) supported on a copper mesh. The momentum of the L-Auger spectrum was compared to that of the K-L_2L_3 Auger line with a precision better than 10^{-4}.

The spectrometer vacuum was maintained at 5×10^{-6} Torr. There appeared to be a deterioration of source quality with time as the L-Auger spectrum was run over a period of 550 h. During this time, the slope and peak intensity of the most prominent L_3-M_4M_5 line (fig. 2) decreased by 23 % and 13 %, respectively. The decrease was attributed to contamination of the source surface by vacuum pump oil. Some loss of source material may also have occurred but was estimated to be less than 3 % on the basis of observation of the K-L_2L_3 line. A check on the source quality approximately 1600 h after the run started indicated that the deterioration process was progressing at a decreasing rate and that most of the damage had occurred in the first 400 h or so. In order that source deterioration not affect the shape of one portion of the spectrum more than another, several scans were made over the spectrum. Each scan over the regions with strong lines occupied about 60 h, and during this time change of source could be considered insignificant.

The earth's magnetic field was compensated to $\lesssim 0.2$ mG for the vertical component and 0.1 mG for the horizontal components with the help of four daily checks with a saturable strip magnetometer. Short term drifts of the vertical component of the earth's magnetic field are immediately compensated by the control circuit [2].

The K-Auger spectrum was obtained under conditions closely identical with those of the L-spectrum except that the post-focussing accelerator was not used, and instead of a copper mesh supported window, we used one of density $\approx 40\ \mu g/cm^2$ which needed no support. Also, the spectrometer baffle opening was slightly reduced.

3. The L-Auger spectrum

3.1. ANALYSIS

The L-Auger spectrum of a radioactive nucleide depends both on the form of the Auger spectrum for each of the three L-subshells and also on the numbers of vacancies produced in each subshell by the decay (it is also important whether a secondary L-vacancy is produced by a preceding Auger process or not). The numbers of vacancies clearly depend on the decay scheme.

The chief features of the decay of ^{113}Sn are well established [9-15]. Fig. 1 shows the decay scheme due to Schmorak *et al.* [6]. Studies on the L/K orbital-capture ratio in the decay to the 648 keV state [9-15] and the 393 keV state [16-19] have been somewhat inconsistent, however.

Our measured L-Auger spectrum of ^{113}Sn → ^{113}In is shown in fig. 2 together with the predicted energy ranges of the different L-Auger groups. The analysis is complicated by several factors.

(i) A substantial number of vacancies occurs in all three L-subshells. Because, of the uncertainty of the L/K capture ratio, precise predictions of the numbers are impossible. If capture to the 648 keV state is neglected and the capture energy to the 393 keV state is high, the vacancy probability per disintegration is that shown in table 1. It should be noted for these estimates that the L-vacancies resulting from the K-LL and K-LX Auger processes will not have the same initial energy as those resulting from capture, internal conversion and K_α radiation.

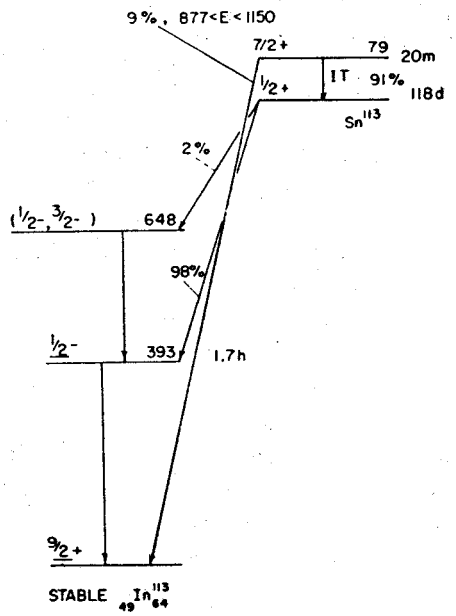

Fig. 1. Decay scheme of ^{113}Sn from Schmorak, Emery and Scharff-Goldhaber [6]).

(ii) Since there is a substantial number of vacancies in each subshell, all of the bands indicated in fig. 2 should be present. Because each band is quite complex, frequent overlap of as many as three bands should give many very closely spaced lines which would be difficult to resolve and identify even if their line shape and expected energies were perfectly known.

(iii) The experimental shape of a line is a combination of natural line shape, spectrometer line shape and source thickness. The spectrometer line shape is known. Because the widths of the different L-, M- and N-shells differ, the estimation of the contribution of the natural line width to the width of any experimental line presupposes identification of the line and knowledge of the widths of the vacancies involved.

(iv) Identification is complicated by the overlapping bands and the resulting close spacing of the lines and by the fact that for any L_i-X_jY_k line the coupling of the X_jY_k vacancies is presumably intermediate rather than pure *jj* and the coupling energy is not very precisely known. Furthermore, most level widths for $Z = 49$

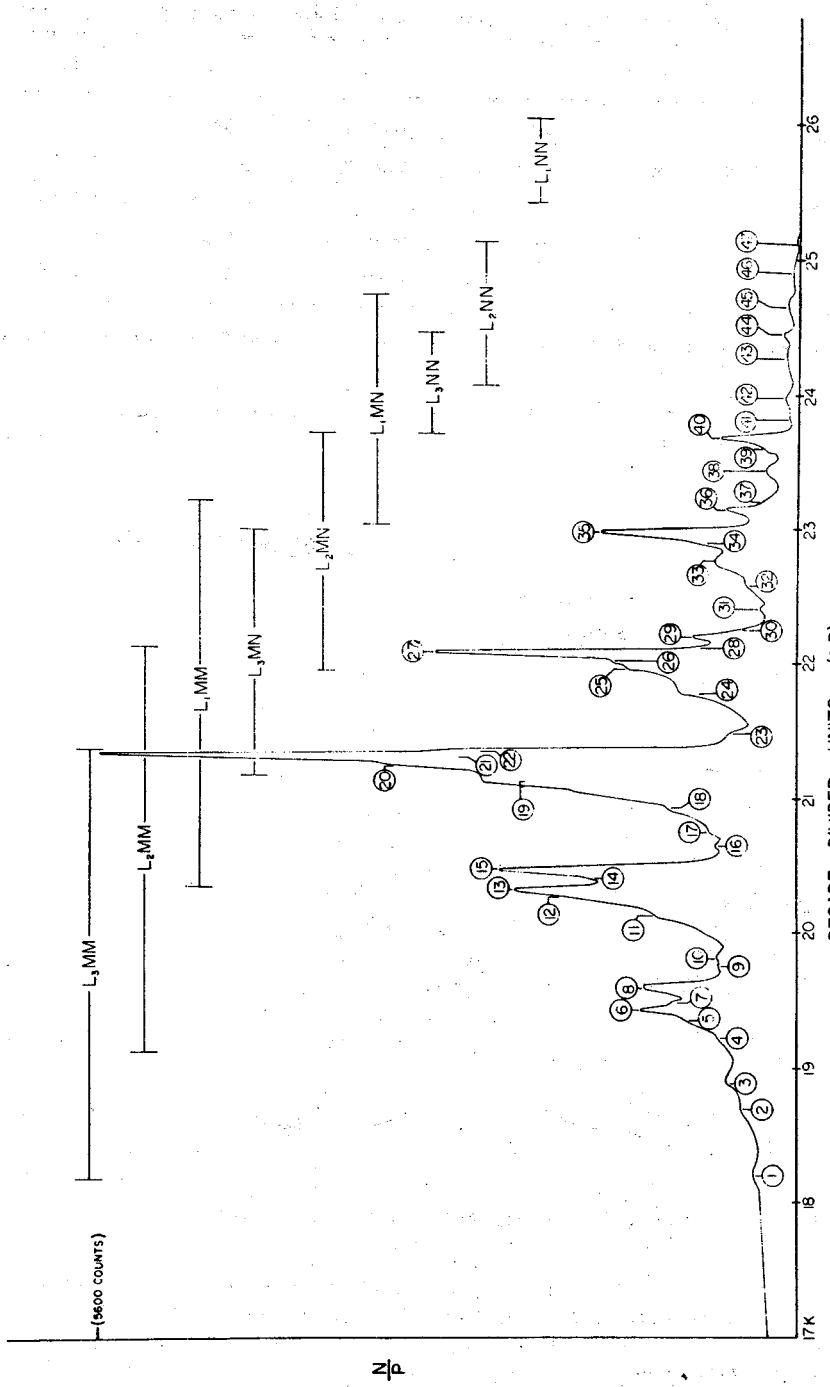

Fig. 2. The L-Auger spectrum of ^{119}In as derived from ^{119}Sn.

TABLE 1

Estimated relative primary vacancy distribution per disintegration for the K, L_1, L_2, L_3 shells

Process creating vacancy	K	L_1	L_2	L_3
electron capture [a])	0.871	0.1043	0.0022	
internal conversion [b]) (393 keV)	0.283	0.0410	0.0061	0.0082
radiative transfer from K [c])			0.2665	0.5240
Auger transfer [c])		0.0850	0.0940	0.1425
sum	1.154	0.2303	0.3688	0.6747

[a]) Calculated using Brysk and Rose [23]) formulae corrected for imperfect overlap and exchange effects as suggested by Bahcall [24]).
[b]) Calculated using tables of internal conversion by Sliv and Band ref. [1]), p. 1969).
[c]) The K fluorescence yield [1]) was assumed $\omega_K = 0.8285 \pm 0.0050$. The radiative and Auger transfer of K-vacancies to the L-shells were determined using the tables of Wapstra *et al.* [25]) and our own measurements of the K-Auger group.

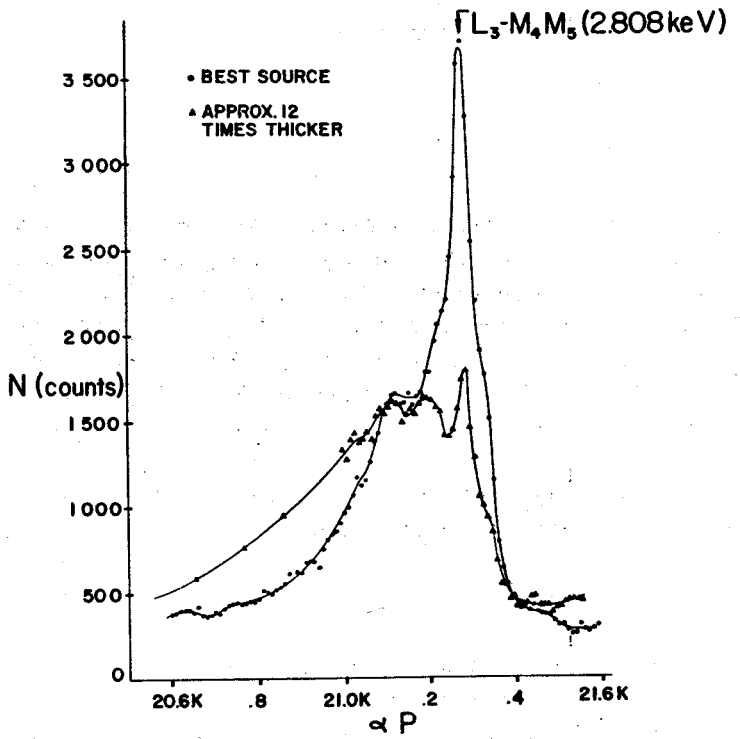

Fig. 3. Illustration of the serious source thickness effects and DEL encountered in this energy region. Both sources were prepared directly in the isotope separator. The thicker source differs from the best source principally because the source material is confined to a smaller area on the source backing. Both spectra are roughly normalized to the same area. The spectrum with the thicker source was obtained at a slightly higher resolution.

TABLE 2
Energies and relative intensities of the L-Auger lines

Line no.	Trans.	Energy calc. (eV)	Energy meas. (eV)	Estimated intensity L_3-M_4M_5 = 100.0	Comments
1	L_3-M_1M_1	2047	2053	<2.5	
2	L_3-M_1M_2	2173	2167	3.0	
3	L_3-M_1M_3	2213	2211	5.0	possible multiplet
4	L_3-M_2M_2	2296	2290	7.0	
5			2320		possibly DEL
6	L_3-M_2M_3	2336	2339	20.5	possible multiplet
7			2352		L_3-M_2M_3I.C. satellite(?)
8	L_3-M_3M_3	2373	2375	27.0	signs of multiplet
9	L_3-M_1M_4	2424			
	L_2-M_1M_3	2420	2418	6.5	
10	L_3-M_1M_5	2432	2431	11.5	
11	L_3-M_2M_2	2504	2506	13.5	
12	L_3-M_2M_4	2550	2542	18.5	L_2-M_2M_3 contr.
13	L_3-M_2M_5	2558	2555	36.5	
14	L_2-M_3M_3	2582	2577	21.0	
15	L_3-M_3M_5	2595	2592	48.0	L_3-M_3M_4 contr.
16	L_2-M_1M_5	2640	2639	9.5	L_2-M_1M_4 contr.
17	L_1-M_1M_2	2680	2666	≈2.5	(?)
18	L_1-M_1M_3	2721	2712	≈2.5	
19	L_2-M_2M_4	2758	2763	50.0	L_2-M_2M_5 contr.
20	L_2-M_3M_4	2795	2792	22.0	
	L_2-M_4M_4	2800			
21	L_3-M_4M_5	2808	2808	100.0	L_2-M_3M_5 contr.
22	L_2-M_5M_5	2816	2821	45.5	
23	L_1-M_3M_3	2843	2860	12.5	double vacancy(?)
	L_1-M_2M_3	2882			
24	L_3-M_2N_3	2940	2939	9.5	L_1-M_1M_5 contr.
25	L_3-M_3N_3	2978	2985	13.0	
26	L_3-M_2N_5	3004	2999	7.0	
27	L_3-M_4M_5	3016	3016	60.0	
28	L_2-M_5M_5	3024	3028	7.5	
29	L_3-M_3N_5	3042	3050	16.5	double vacancy
30	L_1-M_2M_5	3066	3063	4.5	
31	L_1-M_3M_5	3103	3107	<2.5	(?)
32	L_2-M_2N_2	3146	3150		
	L_2-M_2N_3	3148		6.5	
	L_2-M_5N_1	3150	3160		
33	L_3-M_5N_2	3199	3208	15.5	
	L_2-M_2N_5	3212			
34	L_2-$M_3N_{4,5}$	3250	3246	6.0	
35	L_3-$M_5N_{4,5}$	3262	3266	42.5	
36	L_1-M_4M_5	3316	3316	12.0	
37	L_1-M_5M_5	3324	3333	≈2.5	
38	L_2-$M_4N_{2,3}$	3398	3400	≈2.5	
	L_2-$M_5N_{2,3}$	3408			
39	L_1-$M_2N_{2,3}$	3447	3448	<2.5	

TABLE 2 (continued)

Line no.	Trans.	Energy calc. (eV)	Energy meas. (eV)	Estimated intensity L_3-M_4M_5 = 100.0	Comments
40	L_3-M_5N_5	3471	3471	14.5	L_2-$M_{4,5}N_{4,5}$ contr.
41	L_1-$M_2N_{4,5}$	3512	3512	<2.5	
42	L_1-$M_3N_{4,5}$		3560	≈2.5	
	L_3-$N_{2,3}N_{3,3}$				
43	L_3-$N_{2,3}N_{4,5}$		3610	≈2.5	
			3677		
44	L_2-$N_{4,5}N_{4,5}$		3701	≈2.5	
	L_1-$M_5N_{2,3}$				
45	L_1-$M_{4,5}N_{4,5}$		3753	≈2.5	
	L_2-$N_{2,3}N_{2,3}$		3773		
46	L_2-N_3N_5	3836	3836	≈2.5	
47	L_2-$N_{4,5}N_{4,5}$		3904	<2.5	

have not been measured and can only be estimated. As a guide in analysis, we used extrapolated values for the L-widths obtained from Geiger *et al.* [20]) and Listengarten (ref. [21])).

(v) Source thickness effects are suspected in the spectrum of fig. 2 not only by the failure of the spectrum to descend to background between well spaced lines such as the members of the L_3-MM band but also by the long tail below the L-Auger spectrum. Not only does source thickness produce low-energy tails on the lines which vary with energy, but it may also produce extra peaks on the low-energy side of lines through discrete energy losses [20,22]) (DEL). Such DEL peaks were evident in our earlier sources as shown in fig. 3. Though this effect is greatly reduced in our best source (fig. 3) we cannot be absolutely sure it is completely eliminated at energies near 2 keV.

(vi) Attempts to deduce an approximate line shape were further complicated by backscattering. The Al backing was very thick for 2 to 4 keV electrons, and undoubtedly some of the continuum (C) under the lines and a large part of the continuum (C′) at lower energies than the spectrum are due to backscattering. From fig. 2, we estimate $S : C : C' = 826 : 466 : 239$, where S is the area of the lines only. Data on backscattering at these energies are scanty. Danguy *et al.* [26]) find about 20 % at 4 keV for an infinite Al backing which is in reasonable agreement with the results of Kanter [27]) for 10 keV. The ratio $C'/(C+S) \approx 0.18$ is therefore not inconsistent with C' being entirely due to backscattering.

Clearly, the interpretation of this spectrum cannot be carried out in a completely definitive manner. Table 2 gives the measured positions of lines and the most probable transition assignment in *j-j* notation. Also given are the energy values calculated by means of the expression from Bergstrom and Hill [28])

$$E_{(ikl)} = E_i - E_k - E_l - \Delta E_{kl}. \qquad (1)$$

Here i denotes the primary vacancy in any of the three subshells, k and l the resulting vacancies in any of the succeeding subshells of major shells, E_i, E_k and E_l the binding energies of the respective subshells †, and

$$\Delta E_{kl} = \Delta Z[E_{kl}(Z+1) - E_{kl}(Z)];$$

ΔZ was allowed to take values 0.55 and 0.67 for transitions of the type $L_{1,2,3}$-$M_{1,2,3}$ $M_{1,2,3}$ and $L_{1,2,3}$-$M_{4,5}M_{4,5}$, respectively ††. For transitions of the type $L_{1,2,3}$-$M_{1,2,3}M_{4,5}$, estimates were made, for example, by taking an average of L_1-M_1M_5 ($\Delta Z = 0.67$) and L_1-M_5M_1 ($\Delta Z = 0.55$). We applied $\Delta Z = 1.0$ for all others where one or more of the levels had principal quantum numbers greater than 3. The energy calibration in the L-Auger region was based on the location of the K-L_2L_3 line which was assumed to have an energy of 20.144 keV based on a semi-empirical table by Hornfeldt [29]). The energies in this table are estimated to be accurate to about 0.05 %. A work function correction of 4 eV was applied †††.

It should be emphasized that the measured positions of the lines are probably actually center-of-gravity estimates for multiplets. This is due to the fact that for $Z = 49$ the coupling is intermediate between pure j-j and L-S. A rough attempt at line fitting, hazardous as it may be, due to the above mentioned reasons, was nevertheless used in a complementary way to aid in the identification and positioning of the lines. The resulting estimated relative intensities are also given in table 2. For these studies a computer program was written in which we assumed spectral lines of Gaussian shape with an exponential low-energy tail. This was tried only on some of the regions of the spectrum. The results indicated by means of parameters that were obtained graphically (together with empirical data such as positions of lines, estimated widths and heights) that the standard deviation from an optimum fit was 20–30 %. Thus, the column of relative intensities in table 2 should be regarded as possessing errors of at least this magnitude and possibly even greater for the very weak lines.

3.2. DOUBLE VACANCIES

Not all L-vacancies in ^{113}In occur singly. All vacancies which are the direct result of Auger processes will occur in pairs. The most important of these processes are the K-LL, K-LX and the Coster-Kronig L_1-L_3X transitions.

Double vacancies of the LM type give rise to X-ray satellites [33]) and Auger-vacancy satellites [4, 32]) as do the other LX vacancy pairs. Whereas the X-ray satellites have higher than normal energy, those of the Auger electrons have lower than normal energy [32]). Since the expected displacement in our spectrum is only 15 to 20 eV, and the lower side of the strongest lines is somewhat complex, it has not been possible to identify unequivocally any satellites of the LX type.

† Binding energies used were obtained from tables presented in ref. [1]) due to S. Hagstrom *et al.*
†† A higher ΔZ for higher orbital angular momentum value is qualitatively consistent both with K-Auger results [30]) and with the L-Auger data of Sujkowsky and Slatis [31]) and of Haynes *et al.* [32]).
††† Ref. [1]), p. 850.

Auger vacancy satellites arising from an initial LL state have never been observed because the K-Auger yield is small in the high-Z elements. In the past only these cases have been accessible to L-Auger studies because of their higher energy. Since the K-Auger yield for indium is substantially larger, our spectrum has been carefully examined in the light of the known energies and yields of the different LL states resulting from the K-Auger process.

The energy of a normal Auger line was given earlier by expression (1). When a "spectator" vacancy v is associated with both initial and final states, the energy is †

$$E'_{i,v\to j,k,v} = (E_i+E_v+\Delta E_{iv})-(E_v+E_k+E_j+\Delta E_{vk}+\Delta E_{kj}+\Delta E_{jv}). \quad (2)$$

The displacement of the resulting satellite from its parent line is therefore given by

$$\Delta E_a = E'_{i,v\to j,k,v}-E_{i\to jk} = \Delta E_{iv}-\Delta E_{vk}-\Delta E_{jv}. \quad (3)$$

When i and v are both L-levels and k and j are higher levels, E_{iv} can be obtained from Hornfeldt's tables [29]) of K-LL Auger energies and

$$\Delta E_{vk} = E_k(Z+1)-E_k(Z) \quad (4)$$

and a similar expression for ΔE_{jv}. In this case, the ΔE are always positive because the coupling between two L-levels is much greater than that between an L-level and an M-level.

The most intense K-Auger line is K-$L_2L_3(^1D_2)$. It can be easily shown by use of the partial K-L_2L_3 Auger yield that if all the L_2 vacancies resulting from this initial state are filled before the L_3 vacancy, each L_2 Auger line should have a vacancy satellite (from these vacancies only) of intensity about 19 % while if the L_3 level is always filled first, its lines should have satellites of about 10 % intensity. In the case of the L_3-M_4M_5 ($\approx$ 5000 counts) and L_2-M_4M_5 ($\approx$ 2650 counts) lines these intensities would both be about $\approx$ 500 counts (fig. 2) and would be displaced toward higher energy by about 44 eV or 165 decade divider units. Peaks 23 (broad) and 29 correspond fairly closely to the predicted positions, but peak 23 appears to be little larger than that necessary for L_1-M_2M_3, L_1-M_3M_3 and the 165 counts predicted for the satellite from $L_3L_3(^3P_2)$.

On the other hand, peak 29 is not only somewhat broader than a normal peak but has a peak intensity of 500 to 600 counts with L_3-$M_3N_{4,5}$ being the only ordinary Auger transition falling anywhere near it. The latter transition was not found at all in the high-resolution study [31]) of ^{212}Bi and, we therefore doubt if it can account for more than a small part of the intensity in peak 29. Even more conclusively, the 500 counts must appear either associated with the L_3-M_4M_5 or the L_2-M_4M_5 line ††.

† Since two vacancies vk can couple in several ways, and since the component lines would not be observable in the spectrum of fig. 2, E_{vk} is to be taken here as the weighted average over all couplings of v and k.

†† Although simultaneous filling of the two states with the emission of a single electron would not seem probable theoretically, we investigated the 6 to 8 keV energy region which would correspond to such a transition and found only background.

Since most of them do not fall in peak 23, then this would support further that the excess intensity of peak 29 may be accounted for by the vacancy satellite transition of $L_2(L_3)$-$M_4M_5(L_3)$. It is not clear, however, why the L_2 level should tend to fill first in the case of simultaneous L_2 and L_3 vacancies when it can be shown from level widths and Auger yields that an isolated L_3 vacancy has a slightly higher Auger probability than an L_2 vacancy.

As a further check on the existence in the L-Auger spectrum of Auger-vacancy satellites following the K-Auger process, we have calculated the energy displacement and the expected maximum intensity of the satellites associated with all the other strong lines of the spectrum, namely: L_3-M_2M_5 (peak no. 13), L_3-$M_{4,5}N_{4,5}$ (no. 35), L_2-$M_{4,5}N_{4,5}$ (no. 40) and L_1-M_4M_5 (no. 36). While none of these satellites can conclusively be said to be present, there is sufficient intensity at the calculated position to allow for their possible (and in some cases, probable) existence.

4. The K-Auger spectrum

4.1. THE K-LL GROUP

Fig. 4 shows the K-LL spectrum obtained with the same source as was used for the L-Auger spectrum. The lines drawn in for the peaks show the best fits that were

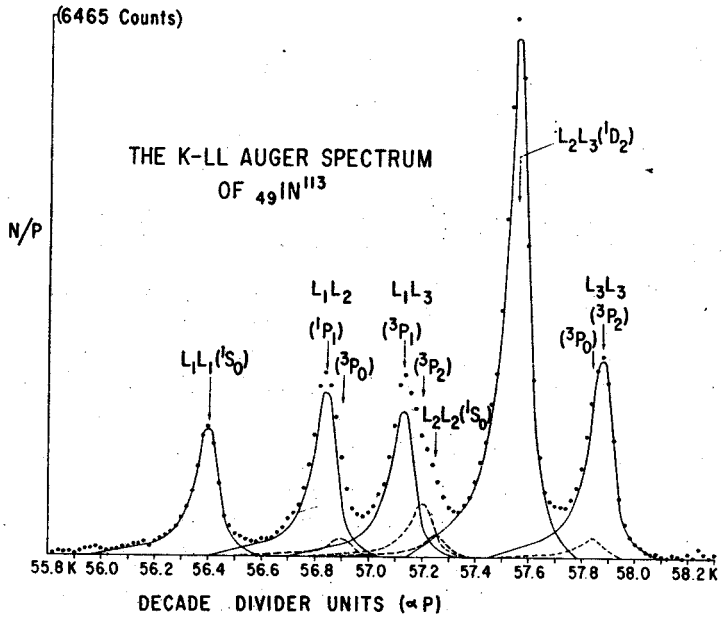

Fig. 4. The K-LL Auger spectrum of ^{113}In from ^{113}Sn.

obtained by the analysis described below and also indicate that there is definite evidence for a spectrum having nine lines as predicted by the intermediate coupling theory [34]).

In the analysis we developed standard lines by using the high-energy side of the K-L_3L_3 line together with the low-energy side of the K-L_1L_1 line as a basic shape, We determined a first approximation to the proper line width for each of the strong lines by combining the instrumental width (0.12 % in momentum and about 49 eV at the K-LL energy) with the natural widths of the Auger lines. We obtained the

TABLE 3
Analysis results of the K-LL group

		Energy (keV)			(eV)
1	2	3	4	5	6
K-$L_1L_1(^1S_0)$	0.18	19.353	19.352	19.353	78
K-$L_1L_2(^1P_1)$	0.22	19.651	19.651	19.653	75
K-$L_1L_3(^3P_1)$	0.30	19.849	19.849	19.849	75
K-$L_2L_3(^1D_2)$	0.18	20.144	20.143	20.144	71
K-$L_3L_3(^3P_2)$	0.20	20.361	20.362	20.363	71

Column 1. Raw structure denoted by the strongest component.
Column 2. Approximate relative widths of the unstripped group.
Column 3. Graphically determined position before stripping.
Column 4. Position of standard lines after stripping.
Column 5. Energies obtained from Hornfeldt [20]).
Column 6. Full width at half height of lines used in stripping.

TABLE 4
Relative intensities of the K-LL group K-$L_1L_1(^1S_0)$ = 1.00

Z	$L_1L_2(^1P_1)$	$L_1L_2(^3P_0)$	$L_1L_3(^3P_1)$	$L_1L_3(^3P_2)$	$L_2L_2(^1S_0)$	$L_2L_3(^1D_2)$	$L_3L_3(^3P_0)$	$L_3L_3(^3P_2)$
49 [a])	1.28±0.03	0.19±0.04	1.15±0.03	0.44±0.04	0.18±0.06	3.90±0.04	0.20±0.04	1.48±0.03
47 [b])	1.3±0.2		1.3±0.2		0.5 ±0.2	3.2 ±0.4	1.8±0.2	
52 [c])	1.13±0.07	0.30±0.05	1.16±0.08	0.51±0.06	With L_1L_3	3.69±0.06	0.30±0.07	1.28±0.07
47 [d])	1.63	0.06	1.30	0.31	0.24	3.53	0.29	1.29
50 [d])	1.52	0.06	1.42	0.31	0.23	3.56	0.29	1.37

[a]) Present measurement.
[b]) Photographic-detection measurement of Johnson and Foster [38]).
[c]) Measurement of Graham *et al.* [39]).
[d]) Calculated by Asaad [36]) using transition amplitudes computed by Callan [37]) with configuration interaction.

latter by using extrapolated values from Geiger *et al.* [20]) and Listengarten [21]), p. 1078, with fig. 15 given on p. 971 of Siegbahn's book [1]) as a guide. The estimated widths are 21 eV, 17 eV and 13 eV, respectively, for the K-L_1L_1, K-L_1, $L_{2,3}$ and K-$L_{2,3}L_{2,3}$ lines.

Obviously, in view of the non-Gaussian shape of the spectrometer lines, there is no simple relationship between instrumental width and natural widths to give the total

width. In developing the standard lines, the relationship suggested by Nordling *et al.* (ref. [35])

$$W^n_{\text{tot}} = W^n_{\text{nat}} + W^n_{\text{inst}},$$

with $n = 1$ was used as a guide. The best fit was obtained using 78 eV, 75 eV and 71 eV for the K-L_1L_1, K-$L_1L_{2,3}$ and K-$L_{2,3}L_{2,3}$ lines, respectively.

From an examination of the raw widths of each of the five major lines, it was evident that three of them, K-L_1L_2, K-L_1L_3, and K-L_3L_3, were significantly wider than the above guide lines would indicate, suggesting a more complex structure. Graphical determinations of the positions of each of these raw lines yielded energy differences from the K-L_2L_3 line that are surprisingly close to the values for the five strongest lines obtained from the semi-empirical tables of Hornfeldt [29]). The energy of the K-L_2L_3 line (20.144 keV) was taken from the same tables and used as reference for the K-Auger spectrum. Inherent in this determination was, of course, an ambiguity due to the fact that the effect of the intermediate coupling satellite lines could not initially be taken into account. However, in the final fitting of the standard lines (including satellites) to the data, we discovered that the positions of the standard lines that were needed to give the best fit corresponded very closely to the positions determined from an examination of the unstripped peaks. We infer, therefore, that the energy positions as given by Hornfeldt for the K-$L_1L_1(^1S_0)$, K-$L_1L_2(^1P_1)$, K-$L_1L_3(^3P_1)$ and K-$L_3L_3(^3P_2)$ lines relative to the K-$L_2L_3(^2D_1)$ line are good to within 2 eV for $Z = 49$.

After many trial strippings of the strong lines using several different standard line shapes, it was evident that the remaining residues fit logically into the expected picture for satellite lines given by the intermediate coupling theory. Final positioning of these satellite lines was carried out by use of the energy figures given by Hornfeldt. The final standard line widths are given in table 3, column 6. The relative intensity determinations are given in table 4 and show reasonable agreement with the results obtained by Asaad [36]) who used transition amplitudes computed by Callan [37]) and took into consideration configuration interaction between the $(2s)^0(2p)^6$ and $(2s)^2(2p)^4$ configurations for the $J = 0$ state. The transition probabilities were obtained using method A of Asaad [36]). Table 4 compares available experimental data for neighbouring elements $Z = 47$ [ref. [38])] and $Z = 52$ [ref. [39])]. The agreement with the results for the $Z = 52$ is good with the exception of our smaller relative intensities for the K-L_1L_2 and K-L_3L_3 satellites.

4.2. THE K-LX AND K-XY GROUPS

Fig. 5 shows the two spectra. The available experimental data on these spectra are scarce, and there is not a single high-resolution spectrum which has been measured and analysed. The analysis is complicated by the fact that the spectrum is very rich in lines (although not as rich as the L-Auger spectrum), and for medium-Z the expected intermediate coupling features add somewhat to the complexity. The resolution of the instrument was not sufficient in this case to warrant a careful stripping but an

approximate analysis was made of the K-LX spectrum with the results shown in table 5.

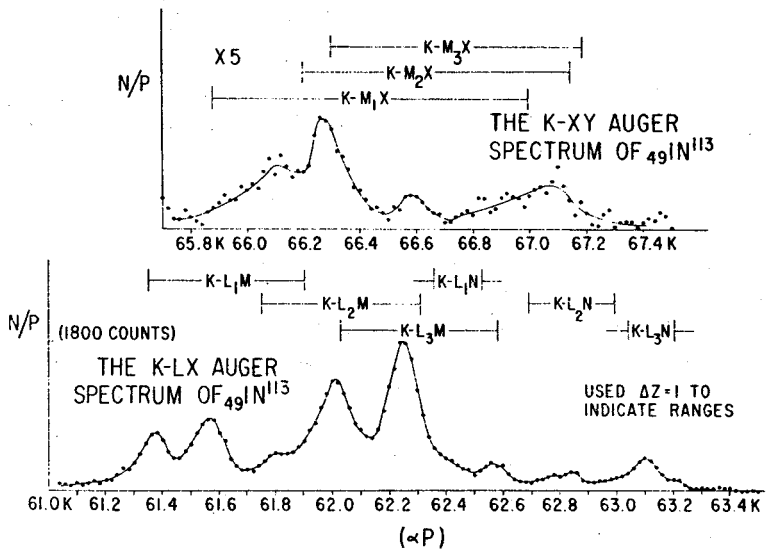

Fig. 5. The K-LX and K-XY groups of ^{113}In from ^{113}Sn.

TABLE 5

Relative intensities of the K-LX and K-XY groups $K\text{-}L_1L_1 = 1.00$

Transition	Present measurement $Z = 49$	Theoretical calculations [a]) $Z = 47$
$K\text{-}L_1M_1$	0.42	0.292
$K\text{-}L_1M_{2,3}$	0.62	0.508
$K\text{-}L_2M_1$	0.20	0.156
$K\text{-}L_1M_{4,5}$, $K\text{-}L_2M_{2,3}$, $K\text{-}L_3M_1$	0.865	1.459
$K\text{-}L_3M_{2,3}$, $K\text{-}L_2M_{4,5}$	1.28	1.672
$K\text{-}L_1N$	0.15	
$K\text{-}L_3M_{4,5}$	0.20	0.247
$K\text{-}L_2N$	0.15	
$K\text{-}L_3N$	0.25	

[a]) Ref. [34]).

Asaad and Burhop have calculated the expected relative intensities for several values of Z using the intermediate coupling scheme [34]). Table 5 shows the comparison of our results with the Asaad and Burhop calculations for $Z = 47$. There is agreement in the general trend of relative intensities, although the individual components agree with theory only in a rough way. The errors in the experimental values are estimate to be approximately $\pm 10\,\%$.

From these spectra we have the integral intensity ratios (K-LX)/(K-LL) = 0.431 ± 0.003 and (K-XY)/(K-LL) = 0.0513 ± 0.0007.

We would like to express sincere appreciation to Argonne National Laboratory for the use of the isotopic mass separator and to Mr. Jerry Lerner for his kind help and advice.

Our thanks also go to Mr. William Johnston for assistance in the data analysis.

A word of gratitude should also be expressed to Messrs. George Fleming and Robert Françoise for their eager aid in the processing and collection of data.

References

1) K. Siegbahn, Alpha-, beta- and gamma-ray spectroscopy (North-Holland Publ. Co., Amsterdam, 1965)
2) L. J. Velinsky, Ph. D. thesis, Michigan State University (1964)
3) Ref. [1]), p. 1534
4) S. K. Haynes, M. Velinsky and L. J. Velinsky, Bull. Am. Phys. Soc. **10** (1965) 1097
5) Nuclear Data Cards, NRC-60-2-99, 100, 105, 106
6) M. Schmorak, G. T. Emery and G. Scharf-Goldhaber, Phys. Rev. **124** (1961) 1186
7) R. J. Krisciokaitis and S. K. Haynes, Nucl. Instr., to be published
8) I. Bergstrom *et al.*, Nucl. Instr. **21** (1963) 249
9) R. C. Greenwood and E. Brannen, Phys. Rev. **122** (1961) 1849
10) W. E. Phillips and J. F. Hopkins, Phys. Rev. **119** (1960) 1315
11) S. B. Burson, H. A. Grench and L. C. Schmid, Phys. Rev. **115** (1959) 188
12) W. T. Achor, W. E. Phillips, J. I. Hopkins and S. K. Haynes, Phys. Rev. **114** (1959) 137
13) R. K. Girgis and R. Van Lieshout, Physica **24** (1958) 672
14) K. S. Bhatki, R. K. Gupta, S. Jha and B. K. Mandan, Nuovo Cim. **6** (1957) 1461
15) D. E. Khulelidze, V. L. Chikhladze and V. G. Onufriev, Bull. Acad. Sci. USSSR (phys. ser.) # **1** (1966), Izv. Akad. Nauk SSSR (ser. fiz.) p. 131
16) C. Manduchi, G. Nardelli, M. T. Russo-Manduchi and G. Zaunoni, Nuovo Cim. **31** (1964) 1380
17) P. Avignon, Ann. de Phys. **1** (1956) 10;
Y. Deschamps and P. Avignon, Compt. Rend. **236** (1953) 478
18) C. D. Broyles, D. A. Thomas and S. K. Haynes, Phys. Rev. **89** (1953) 715
19) R. G. Jung and M. L. Pool, Bull. Am. Phys. Soc. **1** (1956) 172
20) J. S. Geiger, R. L. Graham and J. S. Merrit, Nuclear Physics **48** (1963) 97
21) M. A. Listengarten, Izv. Akad. Nauk SSSR (fiz. ser.) **24** (1960) 1050
22) C. Nordling, E. Sokolowski and K. Siegbahn, Phys. Rev. **105** (1957) 1676
23) H. Brysk and M. E. Rose, Revs. Mod. Phys. **30** (1958) 1169
24) J. H. Bahcall, Phys. Rev. **129** (1963) 2683
25) A. H. Wapstra, G. J. Nijgh and R. Van Lieshout, Nuclear spectroscopy tables (North-Holland Publ. Co., Amsterdam, 1959)
26) Danguy, J. Franeau, I. Corney and M. Despestel, J. de Phys. **26** (1965) 148A
27) H. Kanter, Ann. der Phys. **20** (1957) 156
28) I. Bergstrom and R. D. Hill, Ark. Fys. **8** (1954) 21
29) O. Hornfeldt, Ark. Fys. **23** (1963) 235
30) Ref. [1]), p. 1530
31) Z. Sujkowski and H. Slatis, Ark. Fys. **14** (1958) 101
32) S. K. Haynes, M. Velinsky and L. J. Velinsky, Nuclear Physics **A90** (1967) 573
33) F. R. Hirsh Jr., Phys. Rev. **48** (1935) 722
34) W. N. Asaad and E. H. S. Burhop, Proc. Phys. Soc. **71** (1958) 369
35) C. Nordling, E. Solokowski and K. Siegbahn, Ark. Fys. **13** (1958) 483
36) W. N. Asaad, Nuclear Physics **66** (1965) 494
37) E. J. Callan, Phys. Rev. **124** (1961) 793
38) F. A. Johnson and J. S. Foster, Can. J. Phys. **31** (1953) 469
39) R. L. Graham, I. Bergstrom and F. Brown, Nuclear Physics **39** (1962) 107

Lithium-Drifted Germanium for Charged Particle Spectroscopy*

C. R. Gruhn, T. Kuo, C. Maggiore, **
B. Preedom, L. Samuelson, and J. Chander**
Michigan State University
East Lansing, Michigan

SUMMARY

The Michigan State University Cyclotron Laboratory has undertaken a program of developing lithium-drifted germanium for high-resolution charged particle spectroscopy. The charged particle spectroscopy has been concerned with reactions leading to protons, deuterons, and tritons in the energy range of 25 to 90 MeV. The emphasis of this program has been two-fold in that both the response of the detector and the packaging of the detector are considered.

The side-entry geometry Ge(Li) detector was shown to be capable of 60 keV (FWHM) with 40-MeV protons. The major limitation in the resolution for this geometry is attributed to a non-uniform window (3-12μ) on the surface of the detector. The electrodes of a side entry detector were segmented and a single crystal ΔE - E counter telescope was achieved. The best resolution was achieved with a thin-window surface barrier Ge(Li) detector and measured to be 34 keV (FWHM) for 40 MeV protons. A "thin" slit was used and shown to give cleaner spectra over a limited range in excitation energy. A peak to valley ratio of 5000:1 was obtained using this thin slit. The proton radiation damage of Ge(Li) was studied at 40 MeV and shown to be an appreciable problem by 10^{10} protons/cm^2.

INTRODUCTION

In several recent publications[1,2,3,4] the potential of the Ge(Li) detector as a high resolution spectrometer for medium energy protons (30 - 160 MeV) has been demonstrated. It is the purpose of this paper to report on recent results obtained at the MSU cyclotron laboratory using such detectors.

The motivation of this work is tied directly to the interests of the authors in doing high resolution inelastic proton scattering at 40 MeV and (He^3,p) (He^3,d), and (He^3,t) reactions at 70 MeV. It is not uncommon in these reactions for the more interesting physics to be contained in the weaker excited states. For this reason we have studied problems which not only relate to the resolution, but also to the "tails" of peaks. Our best results on these two points is 0.08% at 40 MeV with a 5000:1 peak to valley ratio.

The choice of using Ge(Li) rather than Si(Li) is based on the following reasons:

1) The range of a proton in Ge is about one half of that in Si. This allows one to use 1-cm drifted detectors for 60-MeV protons such that entry is parallel to the electric field lines in the detector.
2) The resolution of Ge(Li) detectors should ultimately be better than Si(Li) detectors as indicated by:
   a) The cost to form an ion pair in Ge being about 20% less than in Si (2.98 vs. 3.66 MeV).
   b) The Fano factor, thus far measured, being less for Ge than Si (0.129 vs. 0.15)[5,6] and
   c) The maximum transfer of energy in nuclear collisions in Ge being less (x2.5) than in Si.
3) The reaction contribution to the tails should be considerably less structured in energy and thus more easily accounted for as a background source. The

reasons for this are the higher density of states at lower excitation energies and the relatively uniform spread in isotopic abundance.

4) The proton radiation damage effect on the lifetime of a Ge detector appears to be less severe than those observed for Si[7,8].

FABRICATION OF DETECTORS

The starting material was horizontally grown, gallium-doped germanium having a resistivity of 10-20 ohm-cm, an etch-pit density of less than 1000 per cm^2, and a carrier lifetime of 400 microseconds. The lithium diffusion and drift techniques were the same as reported elsewhere[9]. The lithium was drifted typically to depths of about 0.8 cm.

We have used two basic geometries for our Ge(Li) charged particle detectors, side entry and thin window. The side entry geometry shown in Figure 1 is used for long range particles and for particle identification in a single crystal. The cuts in the lithium diffused electrode are made with a 125 micron wire abrasive cutter. Considerable care is taken to insure that the resistivity of the n-type electrode is uniform at the edge presented to the beam. Also the surface presented to the beam is freshly lapped and etched just prior to packaging. The lapping and etching seems to minimize window effects due to poor collection of charge in the surface region.

The thin window geometry shown in Figures 2 and 3 is used for protons in the energy range of 25-55 MeV. The thin window is achieved by fabrication of a p + contact on the intrinsic region. The procedure for the fabrication of this contact is as follows: A drifted piece of Ge crystal is cut to the desired geometry. A 1-cm diameter flat ended quartz rod is chucked in a mill and is used with 600 grit abrasive and water to bore just into the intrinsic region through the p-type region. A p-type rim is thus left free to use for mechanical mounting minimizing injection of charge. This same rim has the added advantage of providing a simple means of encapsulating the p + contact during subsequent etching of the outer surfaces. Crystal damage in the bored hole is removed by lapping with finer grits and then etching. The etch of the bored hole is rinsed and dried carefully prior to evaporation of a thin Au film onto the Ge surfaces of the hole and the exposed intrinsic region. The hole and p + contact are then encapsulated by placing a piece of tape across the p-type rim sealing off the gold p + contact. The crystal is then prepared using standard etch techniques[9]. Finally the diode is mounted in the detector package and cooled.

The window thickness in these two geometries was investigated with alphas (5.48 MeV) from Am^{241}. In the side entry geometry the resulting window on the surface of the detector was observed to be non-uniform and ranged in thickness from 3 to 12 microns. It is assumed that this window is due to the formation of thin inversion layers during the chemistry of the surface. The thin window Ge(Li) yielded windows having a thickness of less than 1μ. On the other hand, it was observed that if the fresh p + contact was allowed to remain at room temperature for 24 hours before cooling, a thick (6μ), window resulted. The thin p + contact could be remade by removing the old contact by etching and recycling through the above p + preparation procedure. If the detector was cooled within one hour after the formation of the p + contact, the usual thin window resulted.

PACKAGING OF GE(LI) DETECTOR FOR CHARGED PARTICLE SPECTROSCOPY

The requirement that the Ge(Li) detector be stored in vacuum and at liquid nitrogen temperature at all times makes the packaging a problem. This is especially true when one requires that the package also function within existing scattering chambers. We have settled on two approaches to the problem. The first approach was to design and construct a scattering apparatus[10], compatable with existing packages of the Chasman design[11]. The second approach was to modify a Harshaw Ge(Li) satellite dewar package such that it would function in the MSU scattering chamber. See Figures 4 and 5. For this latter package

copper tubes were soldered to the dewar vents and flexible polyflo tubing was then used to vent the dewar through the wall of the scattering chamber. Also, the vacuum of the detector package was completely isolated from the scattering chamber vacuum. The dewar was mounted rigidly to the scattering chamber arm. The vacuum cap which covers the crystal seen in Figure 4 was designed with a 6 Havar micron window. The contribution to the resolution for this window for 40-MeV protons is approximately 20 keV (1/3 the mean energy loss in the foil) as calculated assuming a Vavilov distribution. In the case of the thin-window Ge(Li) the p-type rim was mounted and centered on a brass collimator having a 1/4 inch diameter aperture.

The side entry Ge(Li) detector was mounted with the intrinsic region perpendicular to the scattering plane and about 0.3 cm from a 0.25 cm x 0.6 cm aperture in brass. The detector was oriented to minimize the out-scattering of particles. This effect can be a significant contribution to the "tails" of peaks. For example, 40-MeV protons at the end of their range will have an rms radius of 0.05 cm. In Figure 6 we have calculated[12] as a function of range, the rms radius at the end of the range of protons in germanium.

We have also made a study of the design of slits which will minimize the slit scattering contribution to the "tails" of the peaks. The results of this study are summarized in Figure 7. The response of the detector and slits to the $^{12}C(p,p')$ reaction at 40 MeV was measured at a laboratory angle of 45 degrees. The top spectrum shows the response to what was thought to be an "ideal" slit geometry. A broad satellite peak was observed to be associated with each of the excited states of ^{12}C. This satellite peak was then shown to be due to slit scattering by degrading the energy of the scattered particles which are in the region of the thick slit and using the thin slit as the effective collimator. The result is seen in the middle spectrum. The "thin" collimator was then made of Pilot B scintillator and the signal from a photo tube viewing the scintillator was used to turn off the Ge(Li) detector when protons passed through it. This technique greatly reduced the slit scattering contribution to the tail as seen in the bottom spectrum of Figure 7. This technique also allows us to use relatively narrow collimation in order to reduce kinematic broadening effects and at the same time minimize the problem of slit scattering from the thick slits.

Note also in the bottom spectrum with the slit scattering removed, the peaks are quite asymetric. Although we have not established what caused this asymetry, out-scattering from the detector seems to be a likely explanation.

SIDE-ENTRY GE(LI) DETECTORS

There are two major advantages of the side- entry geometry (Figure 1) over the conventional thin-window geometry (Figure 2). First, this geometry allows the detection of particles with longer range and second, the electrodes may be structured such that one can measure the density of ionization along the path of the particle. The chief disadvantage of the side-entry geometry is the non-uniform window on the side through which the particles pass. The best resolution we have measured for this geometry is 60 keV (FWHM) for 40-MeV protons scattered from Au. A contribution of about 40 keV is attributed to this non-uniform window.

This geometry also permits one to achieve particle identification with just the single crystal shown in Figure 1. Signals are taken from regions 1, 2, and 3 through separate preamps. Regions 2 and 3 are used for the identification of deuterons and tritons. He^3's and He^4's are stopped in region 3 and protons in the energy range of interest pass on to region 1.

A particle identification spectrum was obtained using an Ortec particle identifier. See Figure 8. The detector was placed at 30 degrees and about 15 inches from a 1 mil Be target. The response of the system was checked using a 40-MeV proton beam. It was observed that the effective thickness of region 3 depended critically upon the biasing of region 3 relative to region 2. For example, the difference in thickness of region 3 varied by almost a factor of 2 between the biasing of region 3 at 700 V, and region 2 at 1000V; and region 3 at 1000V, with region 2 at 700V. This effect therefore

puts one in a position to "dial" the relative thicknesses of this single crystal counter telescope to fit a particular experiment. The best resolution measured in the resultant total energy spectrum thus far has been 80 keV (FWHM) with 40-MeV protons.

THIN-WINDOW SURFACE-BARRIER GE(LI) DETECTORS

At present the thin-window, surface-barrier Ge(Li) detector offers the greatest resolution potential. This is because the p + contact formed on the intrinsic region is uniform and quite thin (a fraction of a micron). In this section we shall discuss some of the problems we have encountered which limit the resolution of the Ge(Li) detector as a charged particle spectrometer.

It has been our experience with commercially available electronics that it is the later stages of amplification that make the dominant contribution to the electronics noise. For example, it is not uncommon in later stages of amplification to have a maximum voltage of 5 to 10 volts with an rms noise level of 3 to 4 mV thus yielding a precision of 0.04% to 0.06% in the voltage measurement. At 40 MeV this corresponds to a contribution of 16 to 24 keV to the overall resolution. For high resolution experiments at these energies this is not acceptable.

In order to circumvent this problem, the signal from a modified amplifier was input to an Ortec biased amplifier. The biased-off signal was used to drive the second input of a TC200 amplifier. The second output of the TC200 was then analyzed in a Nuclear Data 2200 - 4096 pulse-height analyzer utilizing the digital zero shift (4096). With this configuration of electronics (see Figure 9) we were able to reduce the electronic noise as measured with a pulser at 40 MeV to 6 keV FWHM (.015%). This arrangement works but is not totally satisfactory inasmuch as the resolution was achieved at the expense of the measurable range in excitation energy.

A second source of noise is the energy straggling in the 6 micron Havar window. At 40 MeV this amounts to about 20 keV as calculated assuming a Vavilov distribution. This contribution is expected to be somewhat less than calculated inasmuch as the detector detects some of the recoil electrons and nuclei from the window. The most ideal geometry would be to do away with the external window completely. We shall, in the near future, accomplish this using a scattering apparatus[10] designed to be compatible for use with Ge(Li) detector packages.

A third source of noise arises due to pile-up of low energy signals from the target and faraday cup. Electrons from the target can be removed as a source of noise using a pair of electrostatic deflection plates. Background from the faraday cup can be reduced greatly by simply moving the cup far from the detector and shielding it. In order to aid in the shielding of the detector from the faraday cup we plan to deflect the beam slightly beyond the target with a magnet.

A fourth source of noise is in the statistics of the production of ion pairs. An estimate of the amount of this noise is 9.4 keV at 40 MeV assuming a Fano factor of 0.129.

An optimum resolution of 34 $\pm$2 keV (FWHM) was obtained at 40 MeV. See Figures 10 and 11. The striking features of these spectra are the symmetric peak shapes and the lack of a prominent tail. For example, the width of the peak at 1% of the maximum height is 160 keV, and the peak to valley ratio is typically 5000:1. We calculate that energy straggling in the window and target contributes 120 keV (FW

A breakdown of the various sources of noise which contribute to the measured 34 keV resolution is listed in the following table.

Source	Noise
beam	22 keV
detector and electronics	6 keV
detector package window	20 keV
target	7 keV
statistics	9 keV
total noise	33 keV

Upon inspection of the above table, it is obvious that if the noise in the beam and window are reduced by a factor of 2, resolutions of about 20 keV should be feasible at 40 MeV.

A typical spectrum from a recent inelastic proton scattering experiment is shown in Figure 12. The degrader slit was chosen in thickness such that slit scattered events would fall in the spectrum at those excitation energies where the (p,d) reaction contributes as a background. The detector subtended an angle of about 2 degrees, which, because of kinematic broadening, added about 24 keV in quadrature to the resolution. Note the many weak states in the spectrum, pointing out the need for obtaining even cleaner data.

RADIATION DAMAGE OF GE(LI) DETECTORS BY 40 MEV PROTONS

The radiation damage studies were made with the Ge(Li) detectors in the side-entry geometry. Protons at 42 MeV were scattered from a 15 mil tantalum foil. All protons were counted above 160 keV. After each bombardment the response of the detector was measured with Cs^{137} γ-rays, Co^{60} γ-rays, and the elastic scattering of protons from Ta.

Conventional electronics were used for these experiments. The detector was operated at a bias of 100 V/mm. The response to the γ-rays was made with 7-keV (FWHM) initial limiting resolution in the electronics. The integration and differentiation time constants were set for 1.6×10^{-6} secs.

The resolution was measured as a function of total proton flux presented to the detector. A significant deterioration (12 keV FWHM) in the resolution after about 10^{10} protons/cm^2 total flux was observed. There was no noticeable increase in reverse current after the bombardment, although during the bombardment the reverse current was proportional to the beam current presented to the target and was as large as 500 namps. In Figure 13 we show the charge collection efficiency as a function of total proton flux presented to the detector.

It is interesting to note the charge collection efficiency response was the same for both γ-rays and protons. The charge collection efficiency vs. total flux was observed to fit the following functional form:

$$\varepsilon = 1 - K\Phi$$

where ε is the pulse height normalized to its pre-bombarded value

Φ is the integrated proton flux in protons/cm^2

$K = 3.2 \times 10^{-12} \pm 0.8 \times 10^{-12}$ cm^2/proton.

The above functional form can be easily understood using the Hall[13] and Shockley-Read[14] single-level recombination theory. Their theory predicts that the changes in the free carrier life time, $(1/\tau - 1/\tau_o)$, is a linear function of the number of defects introduced, the capture-cross-section of the defect for minority holes or electrons, the position of the Fermi level and the position of the recombination level in the forbidden gap.

The charge collection efficiency, ε, is easily shown to be related to the free carrier lifetime.

$$\varepsilon \simeq 1 - t/2\,(1/\tau - 1/\tau_o)$$

and $$(1/\tau - 1/\tau_o) \simeq (2K/t)\Phi$$

where t is the charge collection time

τ_o is the carrier lifetime before bombardment

τ is the carrier lifetime after a bombardment of Φ protons/cm^2.

On the basis of this single level theory we measure

$$\eta\sigma e^{\frac{\Delta E}{-kT}} = 12 \times 10^{-12} \text{ cm/proton}$$

where η = the number of recombination levels/cm proton

σ = the capture cross section

ΔE = energy measured from the center of the gap to the recombination level.

In figure 14 we have calculated the fraction of protons lost from the full energy peak due to reactions in the Ge(Li) detector. In making this calculation it was assumed that the cross section was approximately geometric and independent of energy. The calculation is most valid for proton energies much greater than the Coulomb energy for Ge. For 40 MeV protons we estimate the efficiency of the Ge(Li) detector to be $\sim$ 98%.

ACKNOWLEDGEMENTS

We are indebted to our colleagues, Professors E. Kashy, A. Galonsky and S. Austin for their many discussions and encouragement throughout the course of this work. We also wish to thank the MSU Cyclotron technical staff for their practical contributions.

REFERENCES

* This work supported in part by the National Science Foundation, contract #GP-06760.

** National Science Foundation College Research Participant, visiting from Wisconsin State College at Stevens Point, Wisconsin.

1. R. H. Pehl, D. A. Landis and F. S. Goulding, IEEE Trans. Nucl. Sci. NS-13, No. 3, (1966) 274.
2. F. E. Bertrand, R. W. Peele, T. A. Love, R. J. Fox, N. W. Hilland and H. A. Todd, IEEE Trans. Nucl. Sci. NS-13, No.3, (1966) 279.
3. C. R. Gruhn, T. Kuo, B. Gottschalk, S. Kannenberg and N. S. Wall, Physics Letters 24B(1967)266. (In press IEEE)
4. Y. S. Horowitz and N. K. Sherman, BAPS 12(1967)632.
5. H. R. Bilger, Phys. Rev. 163 (1967)238.
6. F. S. Goulding, D. A. Landis and R. H. Pehl, UCRL-17556.
7. H. M. Mann and J. L. Yntema, IEEE Trans. Nucl. Sci. NS-11, No. 3(1964) 201.
8. C. R. Gruhn, Carl Maggiore, J. Chander, BAPS 12(1967).
9. A. J. Tavendale, IEEE Trans. Nucl. Sci. NS-11, No. 3 (1964) 191.
10. K. Thompson and C. R. Gruhn (to be published) BAPS (1968)
11. C. Chasman and R. A. Trestinen, Nucl. Inst. Methods 34(1965)250.
12. W. M. Preson and A. M. Kochler, The Effects of Scattering on Small Proton Beams (preprint).
13. R. N. Hall, Phys. Rev. 87 (1952) 587.
14. W. Shockely and W. T. Read, Phys. Rev. 87(1952)587.

SINGLE CRYSTAL SIDE
Entry Ge(Li) DETECTOR GEOMETRY

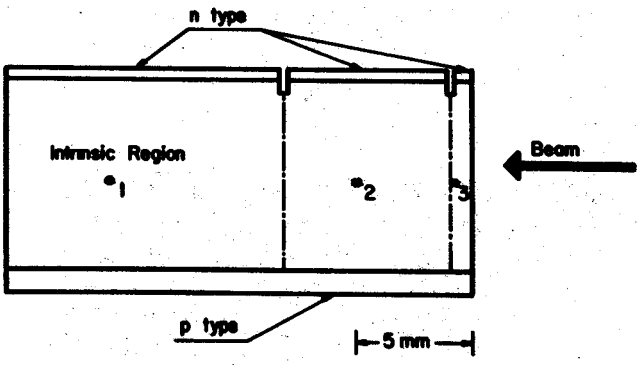

Fig. 1. Basic geometry for detection of particles in side-entry Ge(Li).

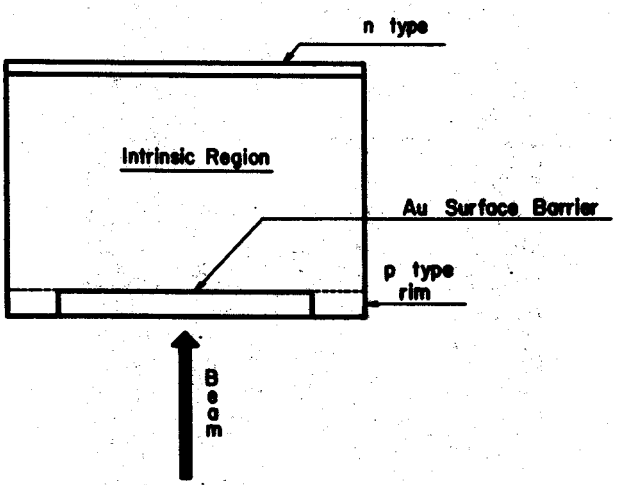

Fig. 2. Thin-window (surface barrier) geometry Ge(Li).

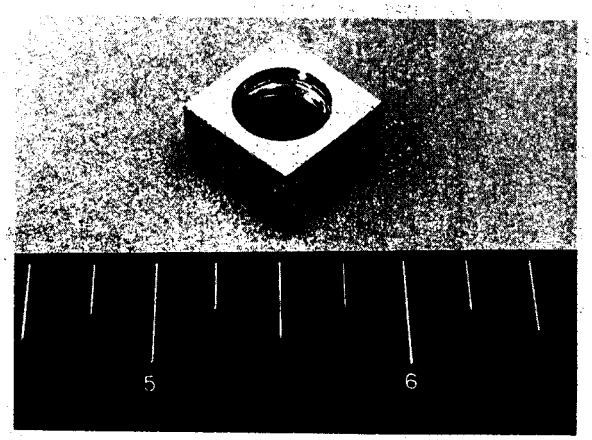

Fig. 3. Ge(Li) detector showing cuts for thin-window geometry.

Fig. 5. Modified Harshaw Satellite Dewar.

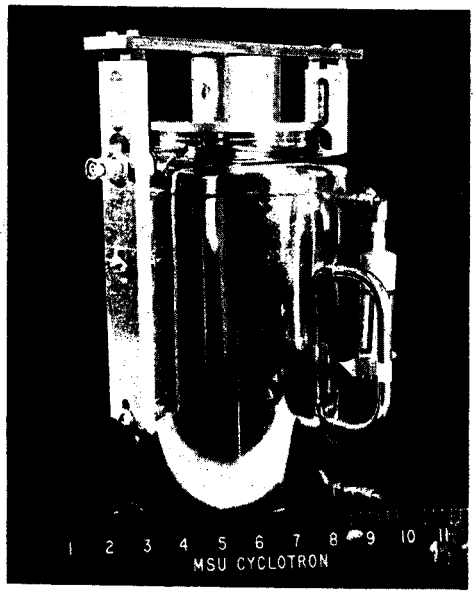

Fig. 4. Modified Harshaw Satellite Dewar

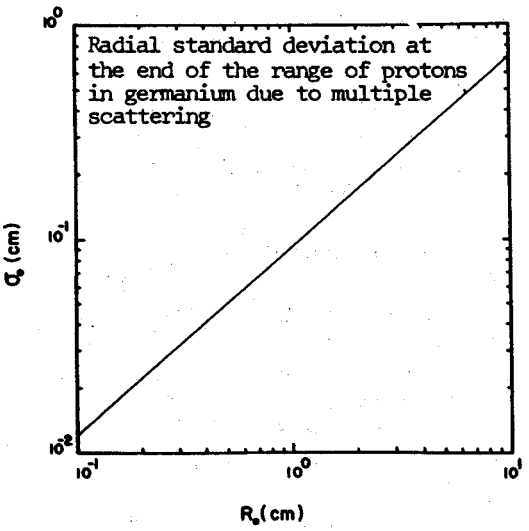

Fig. 6. Results of calculation of the rms radius at the end of the range or protons in germanium plotted as a function of range.

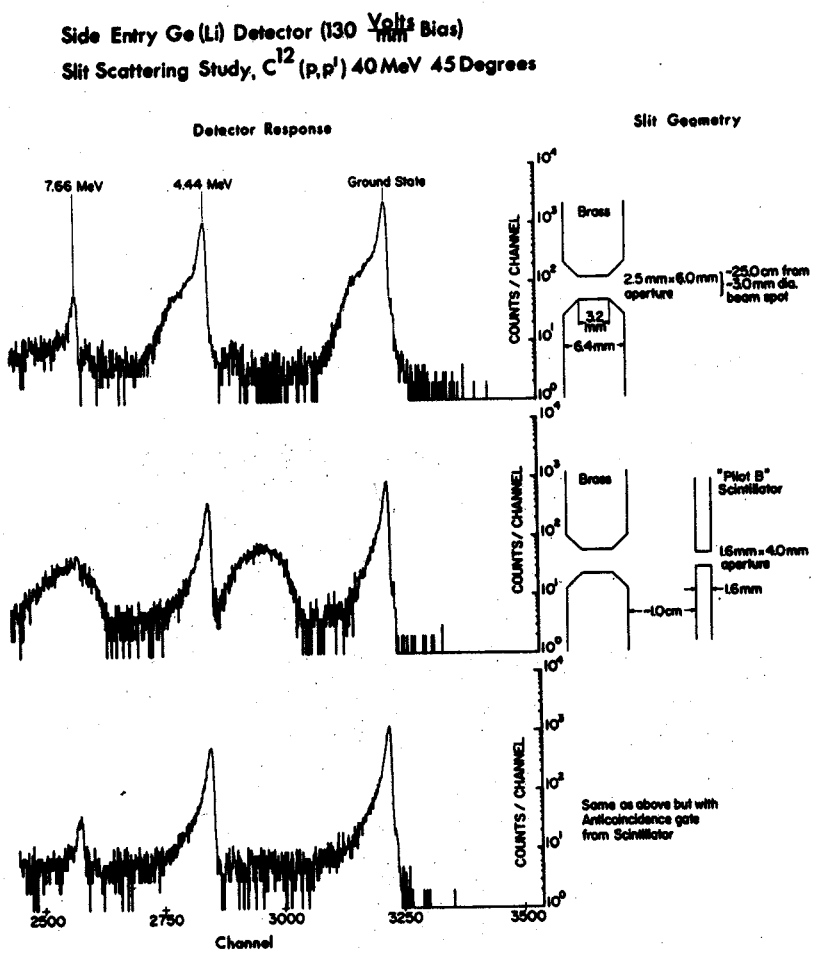

Fig. 7. Summary of slit scattering study.

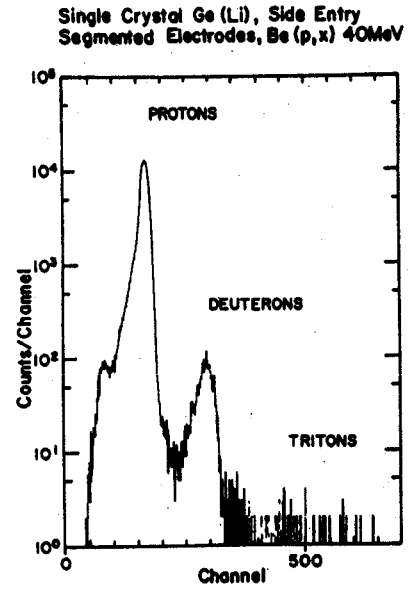

Fig. 8. Single-crystal Ge(Li)-detector particle-identification spectrum.

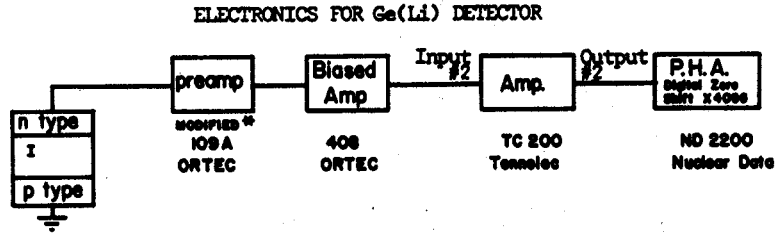

Fig. 9. Electronics used for high resolution proton detection.

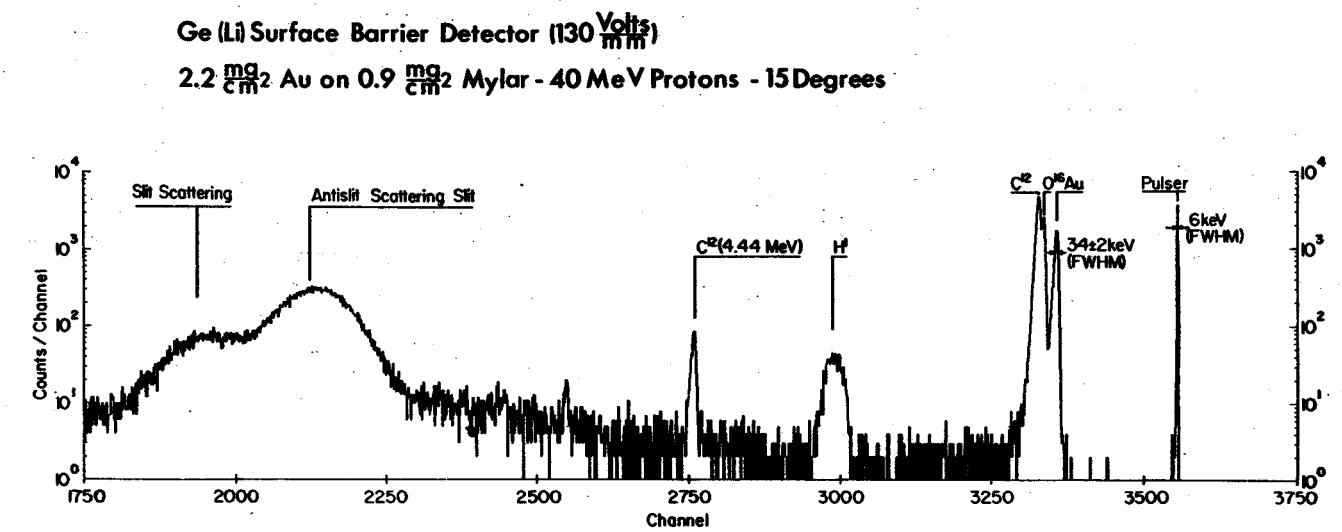

Fig. 10. Resolution check using inelastic proton scattering from gold on mylar with 40-MeV protons.

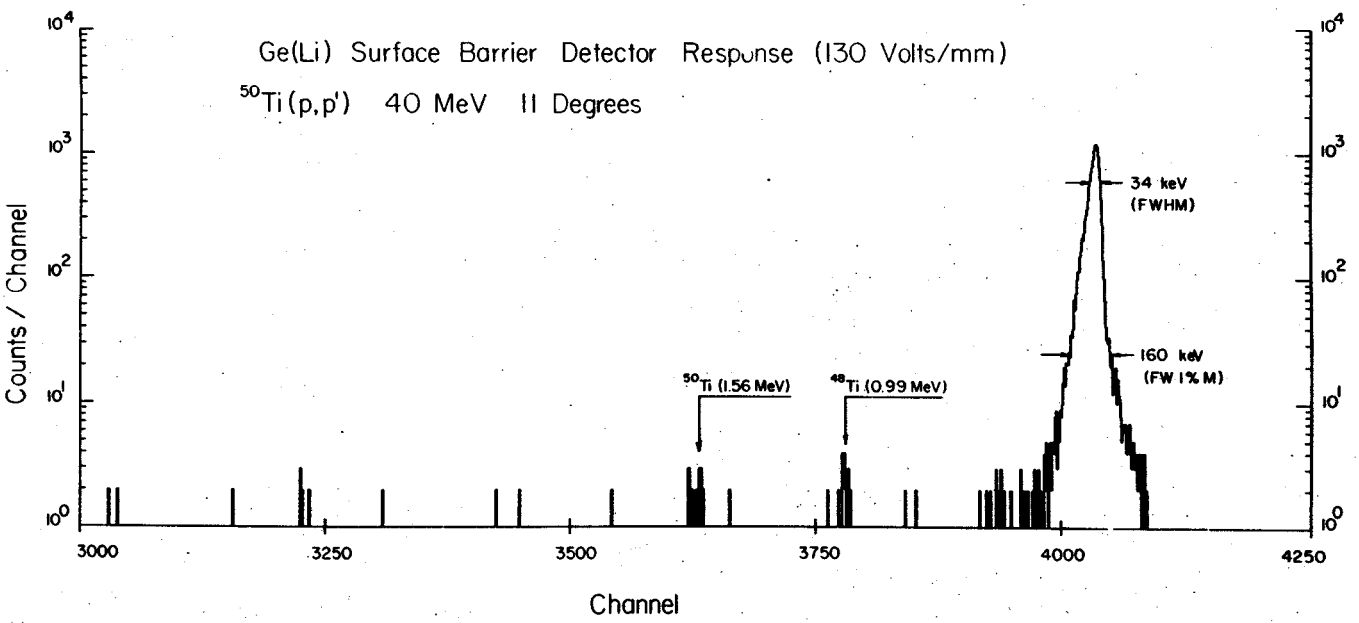

Fig. 11. Peak shape check using inelastic proton scattering from Ti^{50} with 40-MeV protons.

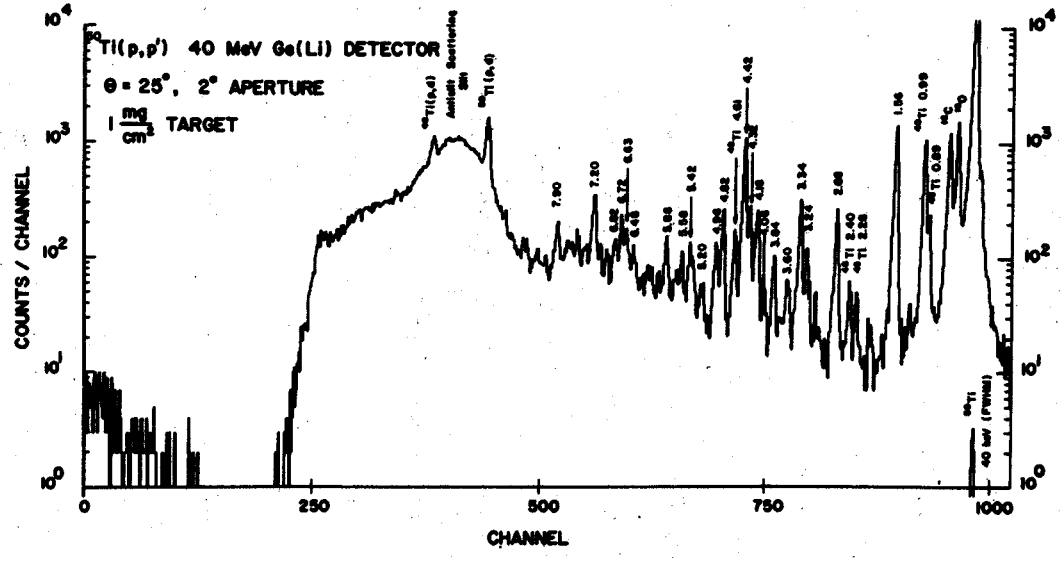

Fig. 12. Typical spectrum, inelastic proton scattering from Ti^{50} with 40-MeV protons.

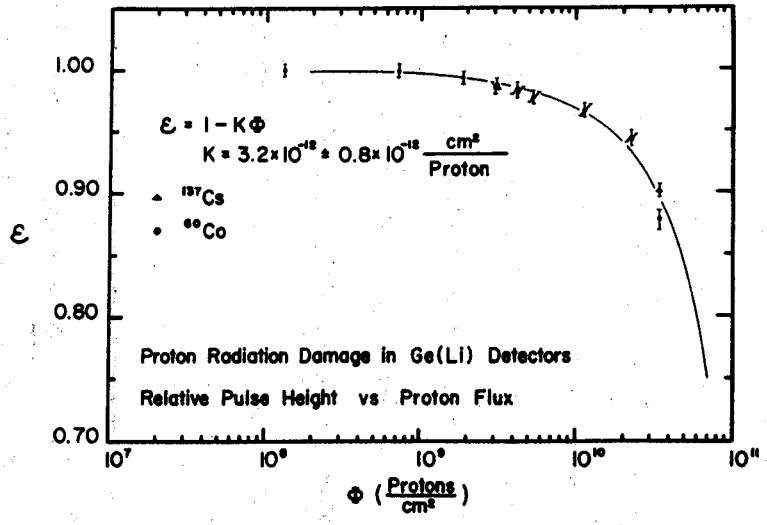

Fig. 13. Proton radiation damage study of Ge(Li). Relative pulse height plotted as a function of proton flux.

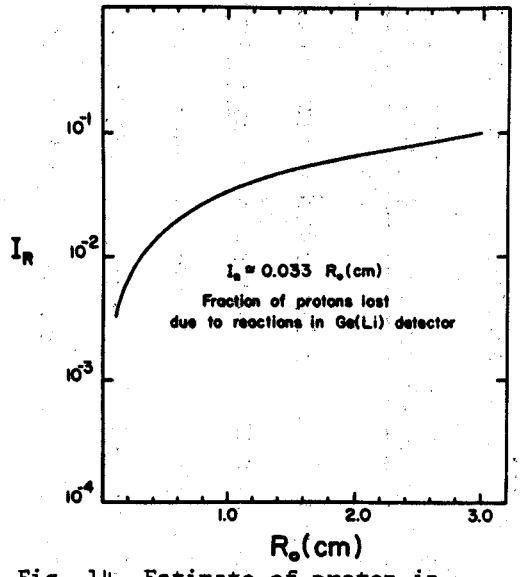

Fig. 14. Estimate of proton induced reactions in Ge as a function of proton range.